CHEMICAL AND BIOLOGICAL SENSING WITH CARBON NANOTUBES IN SOLUTION

A Dissertation

Presented to the Faculty of the Graduate School

of Cornell University

in Partial Fulfillment of the Requirements for the Degree of

Doctor of Philosophy

by

Lisa Larrimore Ouellette

January 2008

CHEMICAL AND BIOLOGICAL SENSING WITH CARBON NANOTUBES IN SOLUTION

Lisa Larrimore Ouellette, Ph.D.

Cornell University 2008

Carbon nanotubes—individual rolled-up graphene sheets—have emerged as exciting tools for probing the biomolecular world. With diameters of about a nanometer, they are roughly the same size as DNA molecules or cell membranes. Nanotubes can be either metallic or semiconducting, and the electronic properties of either type rival the best materials known. The extreme sensitivity of semiconducting nanotubes to their environment, coupled with their small size and ability to operate in a variety of electrolyte solutions, gives us a versatile probe for studying biochemical systems.

Although nanotubes have previously been used to electrically detect a variety of molecules and proteins in solution, the mechanisms behind this detection are not always well understood. In this thesis, we have endeavored to improve our understanding of the nanotube interaction with a variety of analytes in solution. We present experiments exploring the nanotube response to redox-active transition metal complexes, DNA molecules, charged microspheres, and living cells.

In our experiments with redox-active complexes, we find that the nanotube is highly sensitive to the oxidation states of the molecules. We also show that this response is not related to the interaction of the molecules with the nanotube; rather, the nanotube acts as a tiny reference electrode and measures the chang-

ing electrostatic potential of the solution, which changes due to the properties of the molecules. This new result has important implications for the interpretation of other nanotube sensing experiments, and could also lead to novel nanoscale electrochemistry experiments.

By studying the nanotube response to local electrostatic gating by DNA, microspheres, and cells, we discover that the proximity of the nanotube to the analyte is of critical importance to prevent changes in the electric field from being screened by ions in the solution. Because of this effect, we are unable to observe a consistent signal from the DNA or microspheres, but we explore possibilities for better immobilizing small objects near a nanotube device. In our experiments with living cells, we see that placing these cells on suspended nanotubes does cause a large electrical response. We discuss attempts to understand the origin of this signal, as well as future directions for this work.

BIOGRAPHICAL SKETCH

Lisa Larrimore was born in 1980 in Bryn Mawr, Pennsylvania. She attended Swarthmore College for her undergraduate degree, where she worked as a science and writing mentor, organizing a homework clinic for introductory physics students and being selected into the Writing Associates program. She participated in summer research programs at NIST (Gaithersburg, MD) and CERN (Geneva, Switzerland), and she spent a semester at the University of Melbourne in Australia. She also worked with Swarthmore Professor Amy Bug to develop a computational model of positronium, and her senior honors thesis was a finalist for the APS Apker Award. She graduated with high honors in 2002, with a major in Physics and a minor in Mathematics.

Lisa then began graduate work at Cornell, where her work on carbon nanotubes with Professor Paul McEuen has been supported by a Cornell Graduate Fellowship and a NSF Graduate Research Fellowship. In 2006, Lisa traveled to Göttingen, Germany, where she spent six months at Eberhard Bodenschatz's laboratory at the Max Planck Institute for Dynamics and Self-Organization, conducting experiments with the amoeba *Dictoystelium*.

At Cornell, Lisa has become actively involved in science outreach activities, and for two years she co-chaired Cornell's Expanding Your Horizons science conference for middle-school girls. Other highlights of her time in Ithaca include learning to rock climb, winning the 2005 Graduate Iron Chef Competition, and her marriage to Nicholas Ouellette in 2004.

In memory of my Grammie,

Kathleen Ann “Betty” Hebeler

ACKNOWLEDGEMENTS

This thesis would not have been possible without the generous support I have received throughout the last five years in Ithaca. Many people have contributed to the research projects presented here, and many others have provided much-needed encouragement through the inevitable frustrations of graduate school. Although mere words are inadequate to express my gratitude, it gives me great pleasure to have this small opportunity to thank everyone who contributed to this work.

I feel incredibly lucky to have had the opportunity to work with my advisor, Paul McEuen. Paul is an outstanding scientist, and even though he is a novice to the field of biology, he always impressed me with his experimental insights as we tried to understand our results and choose what directions to pursue. He is also an amazing teacher: I always looked forward to his group meeting talks, and whether they were about nanotubes or solar energy, I was sure to come away with new insights about the world. But Paul is not only one of the most intelligent and accomplished scientists I know; he is also one of the kindest and most generous people I have ever worked with. Every time I went to Paul's office to discuss some concern, either academic or personal, I left feeling much better than when I went in. Spending time with Paul was always a pleasure, whether he was enthusiastically leading group hiking and cross-country skiing trips or inviting us to his house to try out his unicycle and play with his dogs. I look forward to returning to Ithaca for McEuen group parties in the years to come.

I owe a huge debt of gratitude to the rest of the McEuen group: Jonathan Alden, Ken Bosnik, Markus Brink, Scott Bunch, Luke Donev, Nathan Gabor, Shahal Ilani, Ethan Minot, Jiwoong Park, Ji-Yong Park, Patrycja Paruch, Samantha Roberts, Sami Rosenblatt, Vera Sazonova, David Tanenbaum, Yaqiong Xu, Yuval Yaish,

Alex Yanson, Arend van der Zande, Xinjian Zhou, Zhaohui Zhong, and Jun Zhu. Not only has this group taught me most of what I know about experimental physics, but they have also enriched my life outside the lab. My time in Ithaca would not have been the same without learning to rock climb from Ethan and Patrycja, swimming in gorges with Arend, learning German with Vera and Patrycja (with great help from Markus), dancing with Luke and others at my own and at Nathan's weddings, or just having everyone over for a barbeque on a summer weekend. Whenever I needed a hand, whether with fixing a piece of lab equipment or moving all the furniture out of my house, my labmates were all very willing to help. The hardest part about leaving Ithaca is leaving this wonderful family. I would especially like to thank Samantha for her collaboration and friendship over the past months; her optimism and perseverance is inspiring, whether she is overcoming fabrication hurdles or climbing Denali, and I have no doubt that she will soon be telling me all about how chromaffin cells interact with nanotubes.

I would also like to thank all of my collaborators from other groups and departments at Cornell. I think that the ease of interdisciplinary research is one of Cornell's great strengths, and I have enjoyed the opportunity to interact with and learn from people from so many backgrounds. I owe a special thanks to Suddhasattwa Nad (from Héctor Abruña's group), who contributed so much to the results in Chapter 7 of this thesis and to my own understanding of electrochemistry, and to Kassandra Kisler (from Manfred Lindau's group), who dealt with the cell culture and manipulation for many of the experiments in Chapter 9. Wei Wang (from Jiwoong Park's group) taught me how to measure the photocurrent through a nanotube (as discussed in Section 6.2.2), which I suspect will become a powerful tool for studying nanotubes in solution. Finally, Erik Herz

(from Uli Wiesner's group) joined me in an attempt to dielectrophoretically trap metal-coated CU dots with carbon nanotubes, and I discuss these results in Section 3.2.3.

The opportunity to spend six months at Eberhard Bodenschatz's Max Planck Institute last fall was another highlight of my graduate studies. Carsten Beta and Katharina Schneider taught me all about keeping *Dictyostelium* cells happy, and Eberhard and Barbara Kasemann made sure I had all the equipment I needed for my experiments with carbon nanotubes. *Vielen Dank* as well to the rest of the Bodenschatz group—including Amgad Squires, Dario Vincenzi, Gabriel Amselem, and Stephan Weiss—for the scientific discussions as well as the evenings in Göttingen's cafes and travels to different German towns.

I would also like to thank the other Cornell physics professors who have helped me throughout my studies. As the two Directors of Graduate Studies during my time here (and my instructors in Advanced Lab), Jim Alexander and Ritchie Patterson welcomed me to the department and always made time for my questions and comments. Coming to Cornell, I missed the personal interactions and the focus on teaching that I had experienced at Swarthmore College, but some of my classes here were particularly memorable for the enthusiasm and dedication of my professors; I would particularly like to thank Jim Sethna (Statistical Mechanics), Neil Ashcroft (Solid State Physics), Tomas Arias (Computational Physics), and Don Holcomb (Physics Teaching and Learning). Many thanks to my committee members Veit Elser and Carl Franck, whose questions and interest in my work made my A and B exams much more fun. Helping Carl build crystal radios with kids and teaching them about electromagnetic waves has been one of my favorite outreach activities over the past years.

The wonderful support staff at Cornell—both scientific and administrative—also deserve a hearty thanks. The CNF staff, including Rob Ilic, Mike Skvarla, Garry Bordonaro, and Jim Clair, have provided invaluable training, maintenance, and support on all of the tools I have needed to make my nanotube devices. Jon Shu's help with the CCMR AFM and Bob "Sned" Snedeker's watchful guidance in the student machine shop were also greatly appreciated. Thank you also to Lisa Margosian, Nick Brown, Douglas Milton, Judy Wilson, Deb Hatfield, and everyone else who has helped me navigate the hurdles of Cornell bureaucracy.

Helping other people understand science has also been an important part of my time at Cornell, and I have been involved in a number of science outreach activities. Most of these have been organized by Nev Singhota and the CCMR outreach team or by Monica Plisch and the CNS; they have given me some excellent opportunities to share my excitement about science with others, including running a workshop to teach 20 fifth-grade teachers about hands-on electromagnetism experiments, leading a classroom of deaf students through microscope activities, mentoring an undergraduate during her summer research, and developing a javascript-based workshop about quantum mechanics for high school students in collaboration with a high school physics teacher. Thanks also to my fellow EYH co-chairs, Karen Masters and Kristin Price in 2004, and Amélie Saintonge and Lindsay Batory in 2005, who helped me run the EYH conference to inspire the next generation of female scientists.

One of the reasons I came to Cornell was that the graduate students here seemed to actually enjoy their lives, and I would like to thank everyone who helped make the physics department such a great community. I enjoyed getting to know many of my fellow students as president of the Physics Grad Society from 2003–2004,

especially my fellow PGS officers, Jeremy Urban, Scott Verbridge, and Gil Paz. I would also like to thank my fellow 2005 Graduate Iron Chef Champions, Pierre Thibault, Scott Forth, and Nick Ouellette, as well as the 2006 and 2007 physics teams for continuing to remind the Hotel School that physicists *can* cook.

Special thanks go to my family for their constant love and encouragement. My parents, Patricia and Dale, have shaped who I am today and supported me through every endeavor, and I have greatly appreciated their efforts to try to understand carbon nanotubes. I can only hope to emulate their success as parents in the coming years. My brother Jeff is one of the most generous, insightful, and interesting people I know, and it has been wonderful having him and his wife Laura in Ithaca for the past two years. I also thank my parents-in-law, Helen and Michael, for sharing their wisdom and support.

Finally, my loving thanks to Nick for being with me through all the triumphs and tribulations of the past seven years, from applying to graduate schools to finishing my dissertation. Nick has listened to countless practice talks, taught me to use Maya to make 3D figures, and proofread this entire thesis. More importantly, however, he has been there to provide a hug or kind words when I need them most. I look forward to exploring the next chapter of our lives together.

Ithaca, August 2007

TABLE OF CONTENTS

LIST OF TABLES

LIST OF FIGURES

Chapter 1

Introduction

Understanding the biological and chemical worlds at the molecular level is increasingly important for many fields today, including genomics, biomedical diagnostics, and chemical monitoring. Current molecular sensing methods, however, generally rely on complex, expensive, and time-consuming optical techniques. DNA sequencing, for example, requires using a polymerase chain reaction (PCR) to purify and amplify a sample, labeling the sample with fluorescent dyes, and optically obtaining a signal from a large number of molecules (Nelson and Cox, 2004). These complexities will be inherent in any optical detection technique, since the molecules of interest are roughly one hundred times smaller than the wavelength of light.

Because many biological and chemical processes involve electrostatic interactions, the possibility of label-free, real-time electronic detection methods has emerged as an exciting alternative to optical techniques. The rapidly growing field of bioelectronics focuses not only on biosensing, but also on integrating biochemical systems with electronic elements to create functional devices such as biofuel cells (Willner, 2002). To interface with the biomolecular world, one would like electrically sensitive objects on the same scale as the molecules of interest: proteins are typically 10 nanometers in size, DNA has a diameter of 2 nanometers, and many molecules are smaller than a nanometer.

Carbon nanotubes are ideal candidates for probing this tiny world. To picture a nanotube, first imagine a sheet made of carbon atoms in a honeycomb arrangement, known as graphene. (Many of these sheets stacked on top of each other makes

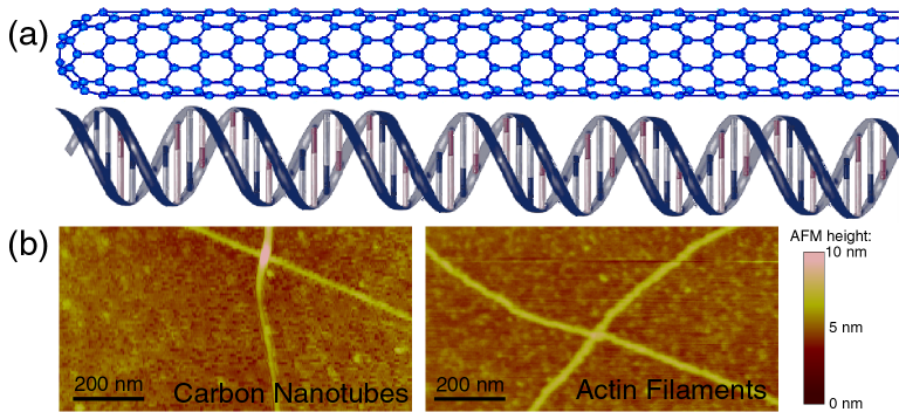

Figure 1.1: Carbon nanotubes have roughly the same diameter as biomolecules like DNA and actin filaments, making them exciting tools for probing the biomolecular world. (a) A cartoon showing the relative size of a carbon nanotube and a strand of DNA. (b) Atomic force microscope (AFM) images of carbon nanotubes and actin filaments, which are part of a cell's cytoskeleton.

graphite.) A carbon nanotube is formed by curling that sheet into a tube. Of course, real graphene sheets are much too small to roll up like that, but nanotubes are actually relatively easy to make in the laboratory. And with diameters of about a nanometer, they are roughly the same scale as the molecules we want to study: in Figure 1.1, we see that a carbon nanotube has about the same diameter as a strand of DNA or a filament of actin.

Nanotubes also have remarkable electronic properties. Depending on the way you roll up the graphene sheet, the resulting nanotube can either be metallic, so that it is a tiny conducting wire, or semiconducting, so that the current through it depends strongly on its external environment. Because of this sensitivity to their surroundings, coupled with their small size and ability to operate in many electrolyte solutions, semiconducting nanotubes are excellent probes for studying biological and chemical systems.

Before we can use a carbon nanotube to sequence DNA or to characterize a

particular chemical solution, however, it is first important to study the nanotube itself and to understand the ways in which it interacts with nearby molecules. Improving this basic understanding of the characteristics of nanotubes in solution is the focus of this thesis.

We begin in Chapter 2 with an overview of the physical properties of carbon nanotubes. We describe the structure of nanotubes and methods for fabricating them. We then see how the electronic properties of nanotubes can be derived from the band structure of graphene, and how transistors can be constructed using semiconducting nanotubes. These transistors can operate either in air or, importantly for sensing applications, in an electrolyte solution.

Before discussing electrolyte-gated nanotube transistors, we present a physical overview of electrolyte solutions in Chapter 3. We discuss their electrical properties, including their bulk resistance and the electrical double layer that forms at metal-solution interfaces, and we explain how electrolytes can be modeled using basic circuit elements. We also provide an overview of Debye-Hückel theory, which describes how the electrostatic potential is distributed near charged objects in solution, such as molecules that we would like to detect with our nanotubes. In the second half of the chapter, we discuss the forces on objects in solution, such as viscous drag or dielectrophoresis, which are important for understanding microfluidic flows and manipulating objects of interest.

With this understanding of electrolyte solutions, we return to electrolyte-gated nanotube transistors in Chapter 4. We discuss how the these devices can be understood with our basic circuit model of electrolytes, and how they differ from nanotube transistors operated in air, which both improves their performance and causes some new experimental problems. We also explain the nanotube's relation

to the electrostatic potential in solution, which will have important implications for the results in Chapter 7.

We next provide a review of previous work with nanotube sensors in Chapter 5. We discuss experiments sensing gas molecules and molecules like proteins that have been dried on top of nanotube devices, but we will focus on experiments in which molecules were sensed in an electrolyte environment. We will see that although nanotubes have been used to detect a variety of analytes, the origin of the observed signal is not always well-understood.

In Chapter 6, we describe the experimental setup for the measurements presented in this thesis. We explain how the nanotube devices were fabricated and how we can see the nanotubes using an atomic force microscope or by looking at their photocurrent response. We describe how the nanotubes were integrated with a microfluidic setup, and how these devices were measured with an electrolyte gate. We will also discuss the complications of measurements in an electrolyte that were mentioned in Chapter 4—hysteresis and leakage currents through the solution—as well as our techniques for mitigating these problems.

We then present results from experiments with redox-active transition metal complexes in Chapter 7. We find that the observed signal in our nanotube devices is not due to a local interaction between the nanotubes and the molecules, as might be expected, but rather to the changing chemical potential in the solution due to the molecules. This non-local effect has important implications for the interpretation of other nanotube sensing experiments, and also suggests the exciting possibility of using a nanotube as a tiny reference electrode to monitor the electrostatic potential in a solution. We describe plans for a future experiment that could explore this possibility.

Having identified this non-local effect, we turn in Chapter 8 to when one might find a signal that is actually due to a local nanotube-analyte interaction. We describe experiments in which we searched for an electrical interaction between nanotubes and DNA and highly-charged microspheres. In all of these experiments, screening by ions in the solution prevented us from measuring a signal with the nanotube. We discuss the significance of these results for other sensing experiments as well as a number of ways in which DNA might be better confined near a nanotube.

In Chapter 9, we examine the interaction between carbon nanotubes and living cells. In our initial experiments, in which nanotubes had *Dictyostelium discoideum* amoebae crawling over them or chromaffin and mast cells placed on top of them, the separation of the cells from the substrate and electrostatic screening again prevented any signal from being observed. When chromaffin or mast cells were placed on suspended nanotubes, however, we often saw a large change in the nanotube conductance. We discuss the possible origins of this signal, as well as questions about this system that remain to be answered.

Finally, in Chapter 10, we summarize the results presented in this thesis, and discuss the future directions for this work.

Chapter 2

Carbon Nanotubes

Carbon nanotubes are hollow carbon cylinders with diameters of about a nanometer and lengths typically on the order of microns, although nanotubes up to 4-centimeters long have been reported (Zheng *et al.*, 2004b). Since they are small, stiff, strong, and extremely good conductors or semiconductors, nanotubes have been the object of intense study, both basic and applied, since their discovery by Ijima (1991). Based on the number of papers receiving many citations, carbon nanotubes are currently the "hottest" topic in physics (Giles, 2006). Individual nanotubes have been used, for example, as test systems for one-dimensional electron theories (Bockrath *et al.*, 1999), as photonic devices (Misewich *et al.*, 2003), and as nanoelectromechanical resonators (Sazonova *et al.*, 2004). The small size and excellent electronic properties of carbon nanotubes also make them very good chemical detectors, as first demonstrated by Kong *et al.* (2000). This application of nanotubes as sensors, both chemical and biological, will be the focus of this thesis.

In this chapter, we will review the properties of carbon nanotubes that will be relevant for this thesis. In Section 2.1, we describe their structure and the different methods of producing them, including the method that is used for our experiments. We then examine nanotube electronic properties in Section 2.2, where we will see that depending on their physical structure, they can be either metallic or semiconducting. Then, in Section 2.3, we see how semiconducting nanotubes can be used to make high-performance transistors.

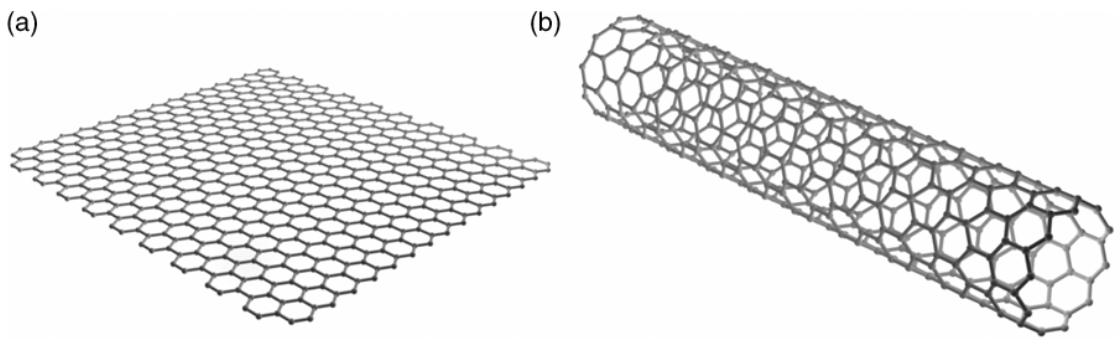

Figure 2.1: Graphene sheet and single-walled carbon nanotube. (a) Graphene consists of carbon atoms covalently bonded in a honeycomb lattice. (b) A carbon nanotube is equivalent to a sheet of graphene that has been rolled into a cylinder.

2.1 Nanotube Structure and Growth

The carbon atoms in a nanotube are covalently bonded in a honeycomb lattice, so a nanotube is equivalent to a graphene sheet that has been rolled into a cylinder, as seen in Figure 2.1. Carbon nanotubes are extremely stable, and they can form whenever a source of carbon is heated in the presence of catalyst particles to help initiate the structure. Multiwalled nanotubes (many concentric graphene cylinders) with many defects have been found naturally in 10,000 year-old ice core samples and in common flames (Murr *et al.*, 2004), as well as in a 400-year-old Damascus saber (Reibold *et al.*, 2006), but more controlled fabrication methods are used to make nanotubes for laboratory study. The first reported nanotubes were formed by arc discharge, in which graphite is heated with a large current (Ijima, 1991). Graphite can also be heated by shining a laser on it inside a hot (around 1000 °C) furnace, a technique known as laser ablation (Guo *et al.*, 1995). In both arc discharge and laser ablation, the catalysts are metal particles—such as iron, cobalt, or nickel—that are mixed with the graphite.

An alternative method for growing carbon nanotubes, which was used for the

experiments presented in this thesis, is chemical vapor deposition (CVD), in which a hydrocarbon gas like methane or ethylene is flowed through a 700–950 °C furnace (Kong *et al.*, 1998a). CVD is currently the best method for the growth of single-walled nanotubes with minimal defects, and the locations of the nanotubes can be controlled by first photolithographically patterning the substrate.

It remains difficult, however, to control how many nanotubes will grow from a particular catalyst site or what their electronic properties will be, and much current research is focused on methods for sorting nanotubes and controlling their placement, such as DNA templating (Keren *et al.*, 2003; Zheng *et al.*, 2003b) or dielectrophoresis (Krupke *et al.*, 2003). There has also been recent progress in selectively destroying only the metallic nanotubes on a sample with a plasma reaction (Zhang *et al.*, 2006), and in using pieces of one nanotube as a template for growth of identical nanotubes (Smalley *et al.*, 2006). Further improvements will need to be made in these directions before individual nanotubes can be integrated into large-scale circuits and used in commercial applications, but the low yield from current fabrication methods is sufficient for basic research like the experiments presented here.

2.2 Electrical Properties and Band Structure

The electronic properties of a carbon nanotube are determined by its physical structure: depending on the angle of orientation of its carbon lattice relative to its axis (known as the chiral angle), a nanotube can be either semiconducting (with a moderate bandgap around 0.5 eV or a small bandgap around 0.01 eV) or metallic. The electronic properties of both metallic and semiconducting nanotubes can rival or exceed the best materials known (McEuen and Park, 2004).

Since a nanotube is a cylindrical graphene sheet, the electronic properties of nanotubes can be calculated from the band structure of graphene. In this section, we examine this band structure and see how it leads to both metallic and semiconducting nanotubes.

Figure 2.2 shows the real-space lattice and reciprocal lattice of graphene, as well as the construction of a nanotube from a graphene sheet. The real-space crystal is a two-dimensional honeycomb lattice of carbon atoms with lattice vectors $\vec{a}_1 = (\frac{a\sqrt{3}}{2}, \frac{a}{2})$ and $\vec{a}_2 = (\frac{a\sqrt{3}}{2}, -\frac{a}{2})$, where the lattice constant is $a = 2.46$ Å. Each nanotube is uniquely defined by the chiral vector $\vec{C}$ that connects the two points on the graphene lattice that are rolled to touch each other when the nanotube is formed; an (n, m) nanotube has $\vec{C} = n\vec{a}_1 + m\vec{a}_2$ (Saito *et al.*, 1998).

The band structure of graphene was first calculated by Wallace (1947) using the tight-binding approximation, in which one assumes that interactions between carbon atoms only cause perturbations to electrons in atomic wave functions. Wallace's calculation has been improved by including the overlap of atomic wavefunctions of different atoms (Saito *et al.*, 1992; Hamada *et al.*, 1992) as well as third-nearest-neighbor interactions (Reich *et al.*, 2002). In Appendix A we show a simpler first-nearest-neighbor tight-binding calculation of the graphene band structure, which is sufficient for a basic understanding of the electrical properties of nanotubes. The resulting band structure from this calculation is shown in Figure 2.3(a), in which we see that the valence and conduction bands meet only at the K points in reciprocal space, which are marked in Figure 2.2(c).[1] Because of this unusual structure, graphene is known as a zero-bandgap semiconductor. Near the

[1]When more interactions are included in the calculation, one sees that the band structure is actually not symmetric around the Fermi energy, but the behavior near the K points is the same.

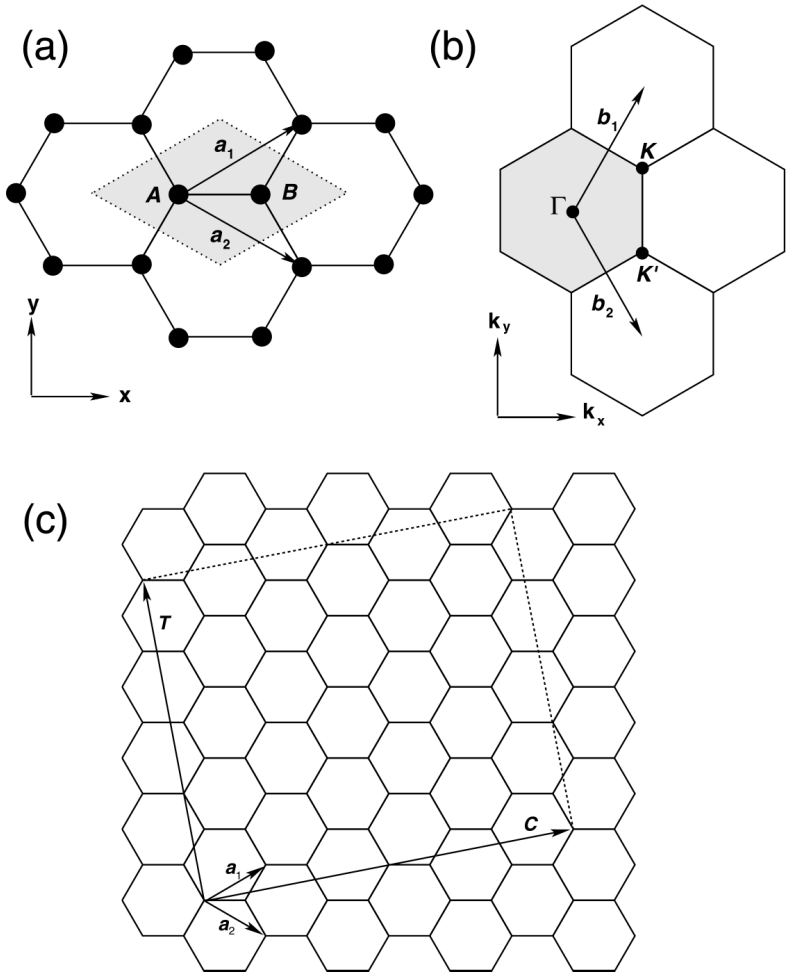

Figure 2.2: Graphene lattice and construction of a carbon nanotube. (a) On the real-space graphene lattice, the lattice vectors are $\vec{a}_1 = (\frac{a\sqrt{3}}{2}, \frac{a}{2})$ and $\vec{a}_2 = (\frac{a\sqrt{3}}{2}, -\frac{a}{2})$, where the lattice constant is $a = 2.46$ Å. The unit cell, containing carbon atoms A and B, is shaded. (b) In reciprocal space, the lattice vectors are $\vec{b}_1 = (\frac{2\pi}{a\sqrt{3}}, \frac{2\pi}{a})$ and $\vec{b}_2 = (\frac{2\pi}{a\sqrt{3}}, -\frac{2\pi}{a})$. The first Brillouin zone is shaded, and the high-symmetry Γ, K, and K' points are marked. (c) A nanotube can be constructed by rolling up a graphene sheet. The chiral vector $\vec{C}$ points from the origin to the point which is rolled up to the origin. Here, $\vec{C} = 4\vec{a}_1 + 2\vec{a}_2$, so this is known as an $(n, m) = (4, 2)$ nanotube. The translation vector $\vec{T}$ points along the nanotube axis. Adapted from Saito *et al.* (1998).

K points, the energy varies roughly linearly with the wavevector $\vec{k}$: if we measure $\vec{k}$ with respect to a K point, we can write the energy near that point (*i.e.*, in the limit $ka \ll 1$) as

$$E(\vec{k}) = \pm\frac{\sqrt{3}}{2}\gamma_0 ka \approx \pm(2.3 \text{ eV})ka, \tag{2.1}$$

where $\gamma_0 \approx -2.7$ eV is the first-nearest-neighbor overlap energy (Reich *et al.*, 2002).

As illustrated in Figure 2.3(b), rolling up a graphene sheet with chiral vector $\vec{C}$ imposes a periodic boundary condition

$$\vec{C} \cdot \vec{k} = 0 \mod 2\pi, \tag{2.2}$$

where $\vec{k}$ is again measured from the origin. This results in one-dimensional energy bands that are given by cuts made through the two-dimensional band structure, as shown in Figure 2.3(c). The resulting nanotube will have a band gap and be semiconducting unless the allowed $\vec{k}$ vectors pass through the K points, in which case the nanotube is a one-dimensional metal with two linearly-dispersing bands. Mathematically, a nanotube will be metallic if and only if the $\vec{k}$ vector of the K point is an allowed wavevector for that tube; *i.e.*, if it meets the periodic boundary condition of Equation 2.2. Since

$$\vec{C} \cdot \vec{k}_K \equiv (n\vec{a}_1, m\vec{a}_2) \cdot (\frac{2\pi}{a\sqrt{3}}, \frac{2\pi}{3a}) = 2\pi\left(\frac{2}{3}n + \frac{1}{3}m\right), \tag{2.3}$$

this condition for a metallic nanotube ($\vec{C} \cdot \vec{k}_K = 0 \mod 2\pi$) is equivalent to $2n + m = 0 \mod 3$, or, equivalently (since $3n = 0 \mod 3$), $n - m = 0 \mod 3$. Assuming that all (n, m) combinations are equally likely, we therefore expect 2/3 of nanotubes to be semiconducting, and 1/3 (including all (n, n) "armchair" nanotubes) to be metallic.

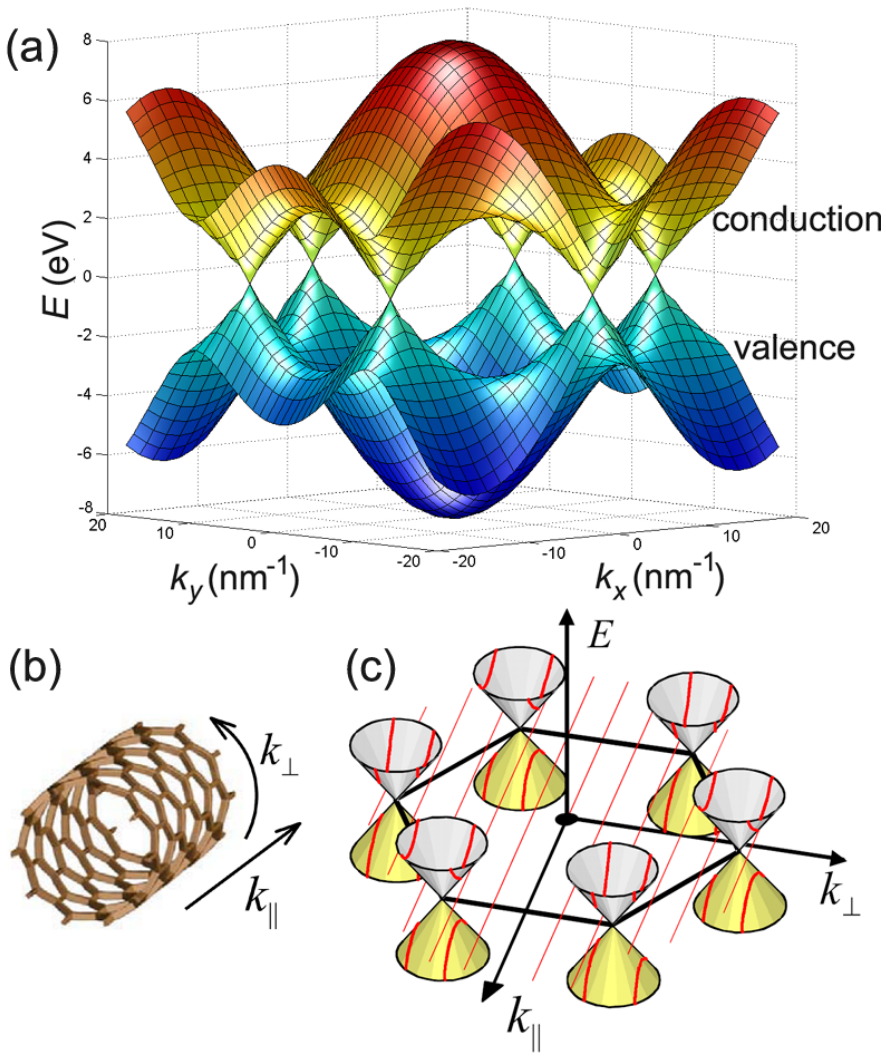

Figure 2.3: Graphene and nanotube band structure. (a) The band structure of graphene, as calculated in Appendix A, is plotted versus wavevector. The valence and conduction bands meet at each K point of the reciprocal lattice. (b) Rolling a graphene sheet into a nanotube quantizes the wave states perpendicular to the nanotube axis. From Minot (2004). (c) The allowed electron states in a nanotube are determined by the intersections between the allowed wavevectors and the graphene band structure, which, near the Fermi energy E_F, is well-approximated by a series of cones. From Fuhrer *et al.* (2002).

The allowed $\vec{k}$ vectors for a nanotube of diameter d are separated by a distance $2/d$ in reciprocal space, and for semiconducting nanotubes, the K point always lies 1/3 of the way between two of these vectors (Saito and Kataura, 2001). Since the states near the Fermi energy are the states closest to the K point, we can insert $k = 2/(3d)$ into Equation 2.1 and multiply by 2 to find the energy gap for a semiconducting tube:

$$E_g = \frac{2}{\sqrt{3}} \frac{\gamma_0 a}{d} \approx \frac{0.75 \text{ eV}}{d \text{ [nm]}}. \tag{2.4}$$

This link between the physical and electronic structure of carbon nanotubes was experimentally verified by both Odom *et al.* and Wildöer *et al.* in 1998. Both groups used scanning tunneling microscopes (STMs) to measure the chiral angle and diameter of individual single-walled carbon nanotubes, allowing (n, m) to be determined. They also measured the electronic properties of each tube, including the band gaps of semiconducting nanotubes, and their results agreed with the theory presented above.

Before we move on to see how semiconducting nanotubes can be used to make field-effect transistors, it is worth noting that there are corrections to this simple picture of nanotube band structure, even for an idealized nanotube with no defects. For small-diameter nanotubes, the curvature of the nanotube wall becomes important, and nanotubes with $n - m = 3j$ for nonzero integer j turn out to have a small bandgap (around 0.01 eV) that scales with $1/d^2$ (Hamada *et al.*, 1992; Kane and Mele, 1997); these small-bandgap nanotubes were first observed by Zhou *et al.* (2000). A nanotube's band structure is also modified by strain (Yang and Han, 2000), as experimentally confirmed by Minot *et al.* (2003). The band diagram becomes even more complicated when defects and interactions with a substrate are introduced. For sensing applications, however, the important fact is simply that

many nanotubes are semiconducting, and not the exact size of their band gap.

2.3 Nanotube Field-Effect Transistors

Tans *et al.* (1998) first reported the fabrication of a transistor made with a semiconducting single-walled carbon nanotube, which had a geometry like that illustrated in Figure 2.4(a). The nanotube is connected to two metal electrodes, known in transistor terminology as the source and the drain; by applying a small voltage bias V_{sd} across the nanotube and measuring the resulting current, one can determine the nanotube conductance. The nanotube is separated from a conducting back gate, such as a doped silicon substrate, by an insulating dielectric like SiO_2.

The low-bias conductance of a semiconducting nanotube is plotted versus the voltage applied to the back gate in Figure 2.4(b). The nanotube conducts well at low gate voltages and shuts off at high gate voltages. The voltage at which a transistor turns off, which is around 2.5 V here, is known as the threshold voltage of the device.

We can understand this behavior by looking at the band diagram for a semiconducting nanotube, as shown in Figure 2.4(c). Whether the nanotube is conducting at a given gate voltage depends on two separate issues: the position of the Fermi level at the contacts, and its position for the bulk of the nanotube.

The Fermi level at the contacts is determined mainly by the work function of the contact metal. For the metals we use (gold, palladium, or platinum), the Fermi level typically lies below the valence band end, causing p-type conduction at $V_{\mathrm{g}} = 0$ through the unoccupied valence states, as shown in the middle panel of Figure 2.4(c). Transistors with n-type behavior at $V_{\mathrm{g}} = 0$ can be made by techniques such as contacting the nanotube with a material like calcium that has a

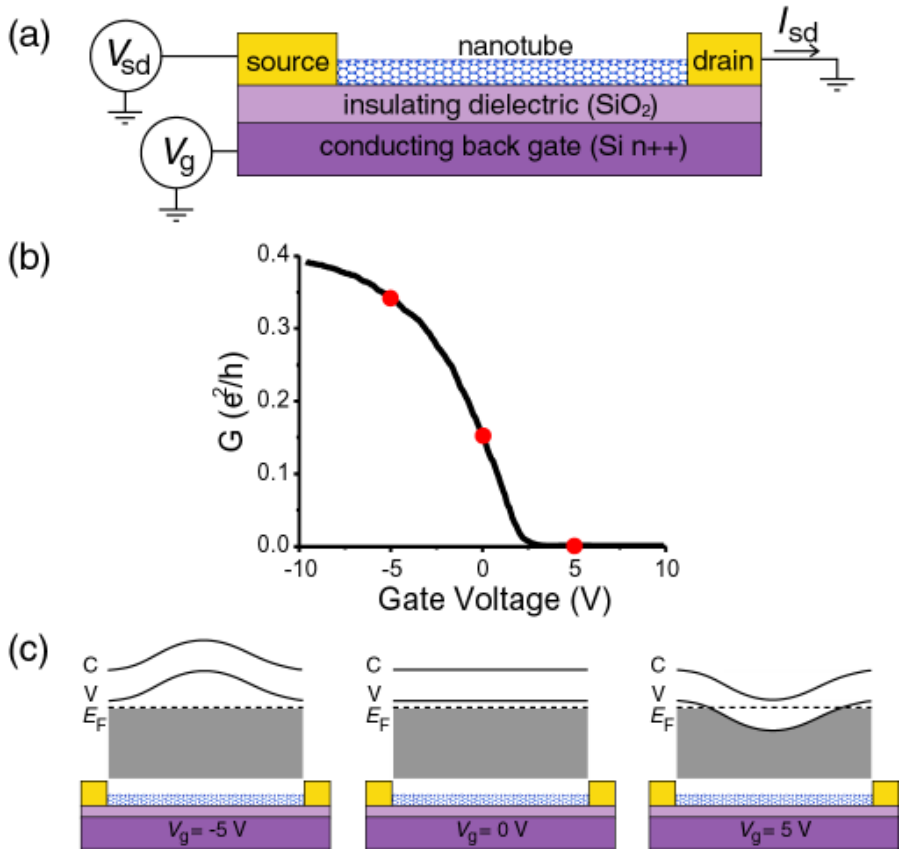

Figure 2.4: Nanotube field-effect transistor (modeled after a figure from Minot, 2004). (a) Side view of a back-gated nanotube transistor. The nanotube is contacted on either end by metal electrodes, allowing one to apply a source-drain voltage bias $V_{\rm sd}$ across it and to measure its conductance as a function of the back-gate voltage $V_{\rm g}$. The nanotube is separated from the gate by an insulating layer, typically SiO_2. (b) Conductance through a semiconducting nanotube as a function of gate voltage. (c) Nanotube band diagram for different gate voltages (marked with dots in the G vs. $V_{\rm g}$ curve) as a function of position along the nanotube axis. At $V_{\rm g} = 0$, the Fermi level typically lies below the valence band edge due to the work function of the metal contacts, so the nanotube is conducting. Increasing or decreasing $V_{\rm g}$ bends these bands, except where it is screened by the metal contacts. At $V_{\rm g} = -5$ V, the Fermi level is deeper in the valence band, allowing higher conduction. At $V_{\rm g} = 5$ V, the Fermi level lies in the band gap, turning the transistor off.

lower work function than the nanotube (Nosho *et al.*, 2005). (The p-type behavior at $V_g = 0$ is also related to charges on the oxide surface and adsorbed oxygen on the nanotube, and annealing the device in vacuum to remove the oxygen will also result in n-type conduction.)

The position of the Fermi level for the bulk of the nanotube is determined by the voltage applied to the gate. Decreasing the gate voltage pushes electrons away from the nanotube and into the contacts, lowering the Fermi energy deeper into the valence band (except where the voltage is screened by the metal contacts), and thus increasing conduction, as seen in the left panel of Figure 2.4(c). Increasing the gate voltage pulls more electrons onto the nanotube from the contacts, raising the Fermi energy into the band gap and stopping conduction, as seen in the right panel of Figure 2.4(c).

If the gate voltage is raised high enough ($V_g > 10$ V for this device), the Fermi level can be raised into the conduction band, and conduction can occur when electrons tunnel from the valence band at the contacts to these conduction band states. Because of this tunnel barrier, the n-type conduction at high V_g is smaller than the p-type conduction at low V_g. This n-type conduction in air was rarely seen for the devices prepared for the experiments in this thesis, but it was sometimes seen once the devices were gated through an electrolyte solution, as we will discuss in Chapter 4.

The number of electrons added to the nanotube for a given gate voltage is determined by the capacitance between the nanotube and the gate. There are two components to this capacitance: the classical electrostatic capacitance between the nanotube and the gate, C_E, which depends on the geometry and dielectric properties between the nanotube and the gate, and the quantum capacitance of

the nanotube, C_{Q}, which depends on the nanotube density of states (some energy is required to add an electron to the next available state in the nanotube). The back gate can be approximated as a perfect metal, so its quantum capacitance is ignored. The total capacitance is then the series combination of these components, $C = (C_{\mathrm{Q}}^{-1} + C_{\mathrm{E}}^{-1})^{-1}$, so that the smaller capacitance will dominate the nanotube charging. For a nanotube separated from a back gate by a 200-nm-thick SiO_2 layer (with dielectric constant $\kappa = 4$), the electrostatic capacitance per length is $C_{\mathrm{E}} \approx 3 \times 10^{-17}$ F/μm, while the quantum capacitance can be estimated as $C_{\mathrm{Q}} \approx 4 \times 10^{-16}$ F/μm, so the electrostatic capacitance will dominate the total capacitance (Rosenblatt, 2006).

Returning to Figure 2.4(b), we see that the maximum conductance is about 0.4 e^2/h; we use e^2/h as our conductance unit because conductance quantization becomes important in a one-dimensional channel. As explained earlier in Figure 2.3(b,c), rolling a graphene sheet into a nanotube quantizes the wave states perpendicular to the nanotube axis, making the nanotube a one-dimensional conductor. The Landauer formula tells us that the conductance G of a one-dimensional channel is

$$G = \left(\frac{e^2}{h}\right) \sum_i T_i, \tag{2.5}$$

where T_i is the transmission probability of the ith channel (see review in Datta, 1995). Electrons can travel along a nanotube via four degenerate channels—they can be spin up or spin down, and they can move around the nanotube clockwise or counterclockwise—so the maximum conductance for a single nanotube is $4e^2/h \approx 155\ \mu\mathrm{S} \approx (6.5\ \mathrm{k}\Omega)^{-1}$.

Conductances near this maximum theoretical value have been measured for both metallic (Kong *et al.*, 2001b) and semiconducting (Javey *et al.*, 2003) nano-

tubes, implying ballistic transport. The devices used for the experiments in this thesis typically had conductances closer to 10 μS = (100 kΩ)$^{-1}$, which is primarily due to scattering by acoustic phonons (Zhou *et al.*, 2005).

Finally, we would like to define two measurements of nanotube device performance, which we will use to compare devices. First, the transconductance is defined as

$$g_m \equiv \frac{\mathrm{d}I}{\mathrm{d}V_\mathrm{g}}, \tag{2.6}$$

which is proportional to the capacitance between the nanotube and the gate. The maximum theoretical transconductance is the same as the maximum theoretical conductance, $4e^2/h \approx 155$ μA/V (Rosenblatt, 2006), but the highest observed transconductance in a back-gated nanotube transistor is approximately 30 μA/V, which was achieved using a high-dielectric-constant material that increased the nanotube-gate capacitance (Javey *et al.*, 2004).

Below the threshold voltage, device performance is measured by the subthreshold swing, defined as

$$S \equiv -\left[\frac{\mathrm{d}(\log G)}{\mathrm{d}V_\mathrm{g}}\right]^{-1}, \tag{2.7}$$

which has a minimum (best) value of 60 mV/decade at room temperature (Rosenblatt, 2006). Using high-κ dielectrics, Javey *et al.* (2002) have fabricated back-gated nanotube transistors with subthreshold swings of 70 mV/decade.

In Chapter 4, we will see that nanotube transistors are able to be gated through an electrolyte solution as well as through a back gate, and that these electrolyte-gated nanotubes have very high device performance. Before discussing putting an electrolyte on a nanotube, however, we will spend the next chapter learning about the properties of electrolytes themselves.

Chapter 3

Electrolyte Solutions

As we will see in Chapter 4, nanotube transistors are able to operate very effectively in an electrolyte solution, which will be important for sensing applications. To understand their behavior, however, we first need to understand the electrical properties of electrolytes themselves, which we will consider in Section 3.1 below. In Section 3.2 of this chapter, we will then consider the forces on objects in an electrolyte, such as viscous drag and dielectrophoresis, which will be important for understanding or controlling the motion of these objects near our nanotubes.

3.1 Electrical Properties of Electrolytes

The electrical processes that occur in solution fall largely in the domains of electrochemistry, physical chemistry, and interfacial science, and a complete explanation of these process requires a thorough understanding of chemistry and chemical reactions. For introductions to these fields, the reader is directed to references such as Bard and Faulkner (2001), Harned and Owen (1958), and Butt *et al.* (2003). In this section, however, we will reduce this topic as much as possible to a physicist's language of electric fields, potentials, resistors, and capacitors.

We will first briefly discuss the bulk properties of electrolytes in Section 3.1.1 before turning to how potentials are distributed near metal-liquid interfaces in Section 3.1.2. We will then clarify the different kinds of potentials in solution in Section 3.1.3. In Section 3.1.4, we then combine these results to explain how an electrolyte solution can be modeled as a simple circuit. Finally, in Section 3.1.5, we will introduce the Debye-Hückel theory, which explains how the potential in a

solution is distributed around charged objects, such as molecules we would like to detect with our nanotubes.

3.1.1 Bulk Electrolyte Properties

Electrolytes, or conducting solutions, include a wide range of solvents and constituent ions (see Barthel *et al.* (1998) for their classification). For the work in this thesis, we are concerned with aqueous electrolytes, in which inorganic salts like NaCl are dissolved in water. Solid NaCl does not conduct electricity, but when placed in water, the NaCl crystal dissolves into separate Na^+ and Cl^- ions as the polar water molecules surround each element and break their ionic bonds. (Because it dissolves into ions with charge ± 1, NaCl is known as a 1:1 salt.) Once it has charged ions floating around, the NaCl solution can conduct electricity just like a metal with free electrons.

The electrical properties of a bulk electrolyte can generally be approximated quite well by its resistivity, ρ (Bard and Faulkner, 2001). Depending on the concentration of conducting ions, the solution can either be highly conductive or relatively resistive. A 100 mM NaCl solution has $\rho = 0.9\ \Omega \cdot \mathrm{m}$, while 1 mM NaCl has $\rho = 81\ \Omega \cdot \mathrm{m}$. The *CRC Handbook of Chemistry and Physics* provides the "equivalent conductivity," Λ, for a variety of electrolytes, which has units of $\mathrm{m}^2/\Omega \cdot \mathrm{mol}$. The conductivity is then $\sigma = \Lambda \cdot c_0$, where c_0 is the bulk salt concentration, and the resistivity is $\rho = 1/\sigma$. For most solutions, $\Lambda \approx 100 \times 10^{-4} \mathrm{m}^2/\Omega \cdot \mathrm{mol}$ (for NaCl of concentrations 0.5–100 mM, $\Lambda = 107\text{–}126 \times 10^{-4} \mathrm{m}^2/\Omega \cdot \mathrm{mol}$, and for all solutions listed, Λ is in the range $50\text{–}425 \times 10^{-4} \mathrm{m}^2/\Omega \cdot \mathrm{mol}$) (Lide, 2006). Because of this similarity in Λ, for most of the solutions we are interested in, we can obtain a good

estimate of the resistivity using

$$\rho \approx \frac{100}{c_0\ [\mathrm{mM}]}\ \Omega \cdot \mathrm{m}. \tag{3.1}$$

We can then estimate the resistance of a section of solution with length l and cross-section A using $R_{\mathrm{soln}} = \rho l/A$.

Since our entire circuit is not made out of solution, however, we must consider what happens when an electrolyte with ion charge carriers meets a metal with electron charge carriers; in Section 3.1.2, we will see that our story then becomes much more complicated.

3.1.2 Metal-Liquid Interfaces and Electrical Double Layers

Any charged surface in a solution, including a metal electrode, will create an electric field and attract oppositely charged ions from the solution, forming what is known as the electrical double layer. The two layers of charge—the surface charge and the layer of counterions—can be approximated very well as a parallel plate capacitor (Bard and Faulkner, 2001). It is also possible for charges to move between the solution and the metal, as we will discuss in Section 3.1.4, but we will first consider how to model this double-layer capacitance.

The simplest model of the electrical double layer is the Helmholtz model, in which a single layer of counterions in the electrolyte adsorb to the surface and neutralize its charge (Hermann Helmholtz assumed that like for a metal, the solution counter-charge is located at the surface). As seen in Figure 3.1(a), the electrostatic potential will drop linearly across the counterion layer. We can write the capacitance per area as $C_{\mathrm{H}} = \epsilon\epsilon_0/x_H$, where $\epsilon_0 = 8.85$ pF/m is the vacuum permittivity, ϵ is the dielectric constant ($\epsilon \approx 80$ in water), and x_H is the separation between

the charge layers, which is roughly the size of the counterions. For a typical cation of radius 2 Å, this gives 3.5 F/m^2; experimentally observed values, however, are about an order of magnitude smaller (0.1–0.4 F/m^2) and can vary with surface potential and solution concentration (Bard and Faulkner, 2001).

For a more sophisticated model, we turn first to the Poisson equation, which gives the general relation for the electrostatic potential $\phi(\vec{x})$ due to a local electric charge density $\rho(\vec{x})$:

$$\nabla^2\phi(\vec{x}) = -\frac{\rho(\vec{x})}{\epsilon\epsilon_0}. \tag{3.2}$$

In a solution, where moving charges cause fluctuations in $\rho(\vec{x})$, this becomes difficult to solve. If we assume, however, that these ions are Boltzmann-distributed in the potential $\phi(\vec{x})$, we can write the local cation and anion concentrations as $c^+(\vec{x}) = c_0 e^{-e\phi(\vec{x})/k_\mathrm{B}T}$ and $c^-(\vec{x}) = c_0 e^{e\phi(\vec{x})/k_\mathrm{B}T}$, where c_0 is the bulk salt concentration, k_B is Boltzmann's constant, T is the temperature, and e is the electron charge. (We have also assumed for simplicity that our solution only contains a salt like NaCl that dissolves into two monovalent ions.) We can then write the local charge density as $\rho(\vec{x}) = e[c^+(\vec{x}) + c^-(\vec{x})] + \rho_\mathrm{fixed}(\vec{x})$, where $\rho_\mathrm{fixed}(\vec{x})$ is the charge density of any fixed charges, like macromolecules or metal electrodes. Substituting this into Eq. 3.2 gives the Poisson-Boltzmann equation:

$$\nabla^2\phi(\vec{x}) = \frac{c_0 e}{\epsilon\epsilon_0}\left(e^{e\phi(\vec{x})/k_\mathrm{B}T} - e^{-e\phi(\vec{x})/k_\mathrm{B}T}\right) - \frac{\rho_\mathrm{fixed}(\vec{x})}{\epsilon\epsilon_0}. \tag{3.3}$$

Louis Gouy and David Chapman independently solved Eq. 3.3 around 1910 for the case of an infinite charged plane of potential ϕ_0 and found that rather than a sharp linear drop, the potential falls off roughly exponentially at low potentials, with the drop off becoming more rapid as ϕ_0 increases (Bard and Faulkner, 2001). They therefore proposed that the counterions are spread out in a diffuse layer near

the surface, with their concentration dropping off farther from the electrode as electrostatic forces become smaller compared to thermal effects. A cartoon of this model is seen in Figure 3.1(b). In this model, the capacitance across the double layer for our 1:1 salt can be written as (Bard and Faulkner, 2001)

$$C_{\mathrm{GC}} = \sqrt{\frac{2e^2\epsilon\epsilon_0 c^0}{kT}}\cosh\left(\frac{e\phi_0}{2kT}\right), \tag{3.4}$$

or, at room temperature,

$$C_{\mathrm{GC}}[\mathrm{F/m^2}] = 2.3\sqrt{c_0[\mathrm{M}]}\cosh(19.5\phi_0[\mathrm{V}]). \tag{3.5}$$

This capacitance rises almost exponentially as ϕ_0 increases, an unphysical result which arises because the Gouy-Chapman model ignores the finite size of the ions, allowing them to approach arbitrarily close to the surface (Kitahara and Watanabe, 1984).

A solution to this difficulty, first suggested by Otto Stern in 1924, is to combine the Helmholtz and Gouy-Chapman models, as seen in Figure 3.1(c), in what is often called the Gouy-Chapman-Stern (GCS) model. Stern pointed out that both the ion size and the thermal energy are important, and that the total capacitance should be the combination of these effects: $C_{\mathrm{GCS}}^{-1} = C_{\mathrm{H}}^{-1} + C_{\mathrm{GC}}^{-1}$. Since the capacitance is dominated by the smaller of these two effects, Stern's solution maintains the correct behavior of the capacitance at low surface potential but becomes a constant at higher potentials, rather than exponentially increasing (Bard and Faulkner, 2001). In 1947, David Grahame modified Stern's model to distinguish between the chemically adsorbed ions (either anions or cations, though usually the more weakly hydrated anions) that lose their hydration shell and are thus closer to the metal (at what is known as the inner Helmholtz plane) and the hydrated ions (cations are generally more strongly solvated) at the outer Helmholtz plane (Kitahara and

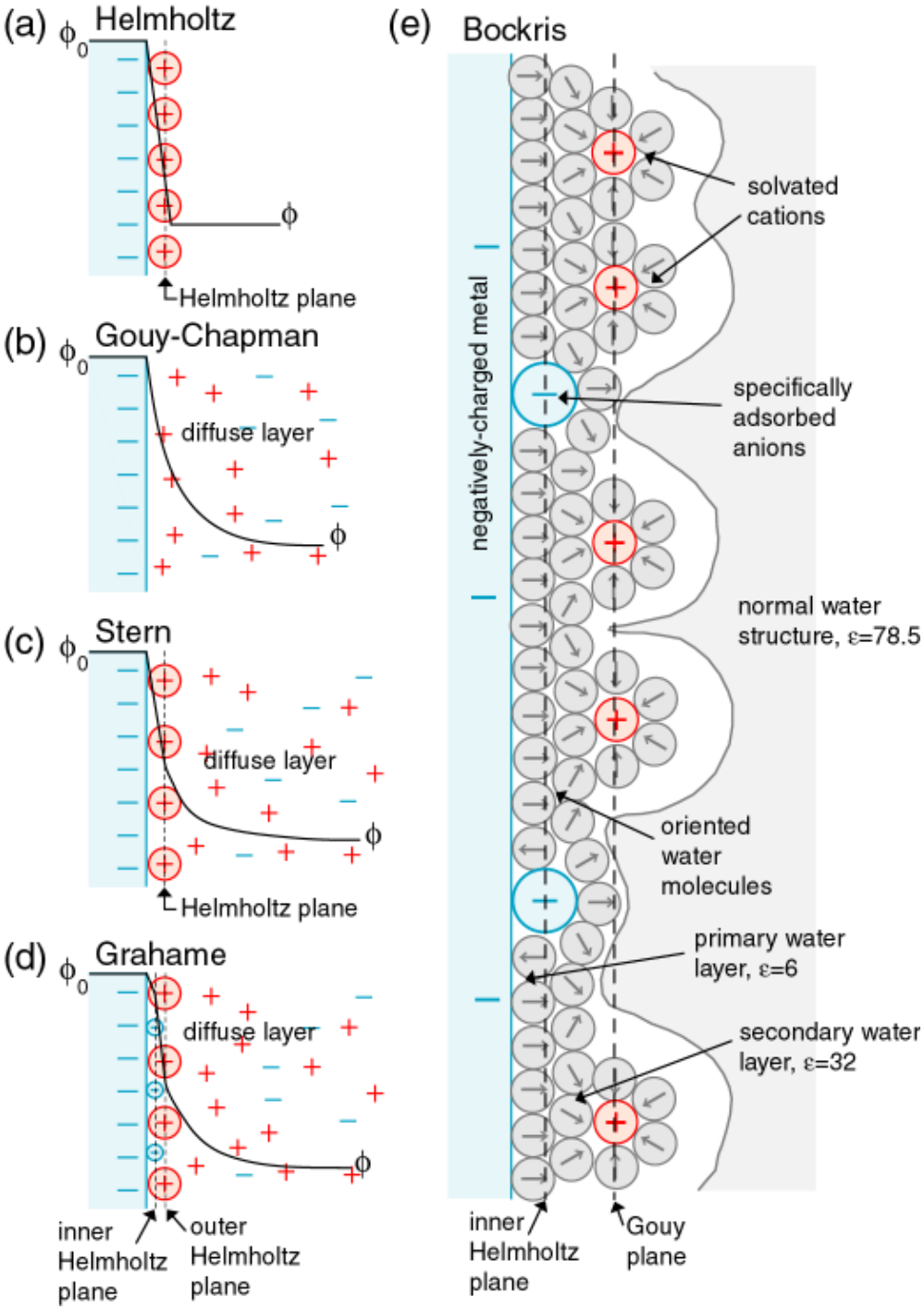

Figure 3.1: Models of the electrical double layer at a negatively charged metal with potential ϕ_0, adapted from figures in Kitahara and Watanabe (1984). The arrangement of ions and decay of solution potential ϕ is illustrated for the five models discussed in the text.

Watanabe, 1984; Christensen and Hamnet, 1994); this modification is shown in Figure 3.1(d).

Finally, our understanding of the electrical double layer has been further improved by Bockris *et al.* (1963), who suggested a more detailed model in which a layer of oriented water molecules separates the hydrated counterions and the metal. They note that the value of ϵ close to the surface should be reduced because the water molecules cannot freely rotate; the dielectric constant has been calculated as $\epsilon \approx 6$ in the first layer of adsorbed water and $\epsilon \approx 30$ in second layer, as indicated in Figure 3.1(e). With this adjustment, the model reproduces not only the correct qualitative dependence of capacitance on surface potential, but also capacitance values in the correct range of 0.1–0.4 F/m^2. There are still a number of discrepancies between this corrected Gouy-Chapman-Stern model and experimental results (for example, ion-ion correlations are unaccounted for), but it remains the standard model of the double layer at a charged surface (Bard and Faulkner, 2001).

Figure 3.2 gives a sense of how these various models compare with experimentally measured capacitances. We see that the GCS theory certainly gives the right order of magnitude and that it captures the dip in capacitance that occurs at $\phi_0 = 0$, but there are clearly features, including differences between electrolytes, that are not captured by this model. One problem is that the Helmholtz distance x_H is not truly independent of potential, but there is no simple theory to provide a better estimation (Bard and Faulkner, 2001). To understand our experiments, however, knowing that the capacitance is generally on the order of 0.1 F/m^2 is sufficient.

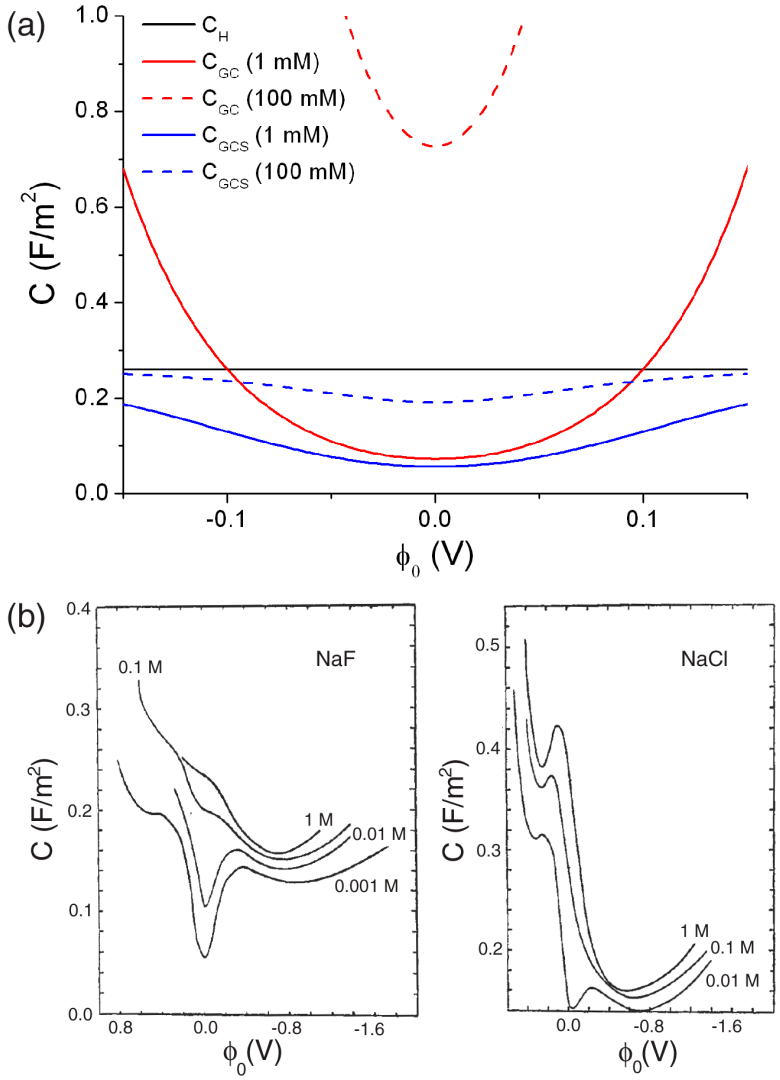

Figure 3.2: Models and data for the double-layer capacitance between an electrolyte and a charged metal. (a) The capacitance as a function of potential is plotted for the Helmholtz model ($C_{\rm H} = \epsilon\epsilon_0/x_H$, assuming $\epsilon = 6$ and $x_H = 0.2$ nm), the Gouy-Chapman model ($C_{\rm GC}$, from Eq. 3.5), and Gouy-Chapman-Stern model ($C_{\rm GCS}^{-1} = C_{\rm H}^{-1} + C_{\rm GC}^{-1}$). (b) The measured differential capacitance for NaF and NaCl solutions in contact with a mercury electrode, as a function of the potential on the electrode minus the potential of zero charge (Grahame, 1947).

3.1.3 Potentials in Solution

Thus far, we have been discussing how the *electrostatic* potential ϕ is distributed in a solution, but there are actually several potentials that we need to keep track of. When a voltage V_0 is applied to an electrode in solution, this sets not the electrostatic potential, but the *electrochemical potential* $\mu_{\mathrm{e-c}} = eV_0$ of the solution, which is composed of the electrostatic and *chemical* potentials:

$$\mu_{\mathrm{e-c}} = e\phi + \mu_{\mathrm{c}}. \tag{3.6}$$

The chemical potential is determined by the particular chemicals in the solution, which will transfer electrons with the wire until they reach an equilibrium.

Because the electrochemical and chemical potentials are fixed, the electrostatic potential is determined by the difference between them. For high enough salt concentrations (low enough ρ_{soln}), we can treat the electrostatic potential as constant throughout the bulk of the solution.

Throughout this thesis, and especially in Chapter 7 for our experiments with redox-active molecules, we will find that keeping track of the differences between these potentials is critical to understanding the behavior of nanotubes in solution.

3.1.4 Randles Circuit for an Electrode in Solution

In Section 3.1.2, we only considered the capacitance across a charged surface in solution due to the electrical double layer, but in general, there will also be charge transfer across the metal-liquid interface, especially at larger electrode potentials. This Faradaic process cannot be represented as a simple combination of resistors and capacitors whose values are independent of frequency; the most common representation is a charge-transfer resistance R_{ct}, which depends on electrochemical

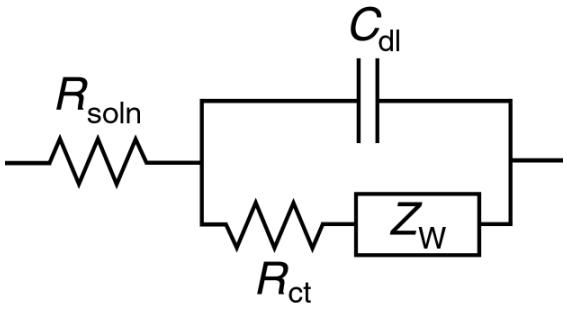

Figure 3.3: Randles equivalent circuit for an electrode in solution. The electrolyte will have a resistance $R_{\rm soln}$ that depends on the resistivity of the solution (see Eq. 3.1). Current can pass through the metal-liquid interface by charging the double-layer capacitance $C_{\rm dl}$ (see Fig. 3.2), or by Faradaic charge transfer; the latter process is represented by a charge-transfer resistance $R_{\rm ct}$ in series with the frequency-dependent Warburg impedance $Z_{\rm W}$.

rate constants, in series with a frequency-dependent "Warburg" impedance $Z_{\rm W}$, which is related to the diffusion of redox-active molecules to the electrode (Christensen and Hamnet, 1994). The Warburg impedance is largest at low frequencies, when charge transfer will be limited by the rate of diffusion of new molecules to the electrode (referred to as "mass transport"); at higher frequencies, a molecule that transfers its charge will not have time to diffuse away before the potential is reversed (Bard and Faulkner, 2001).

Estimating $R_{\rm ct}$ is difficult, as it depends on the particular chemical species in solution and the type of electrode used. It should scale with the exposed surface area of the electrode, $R_{\rm ct} = R'_{\rm ct}/A$, where A will be somewhat larger than the macroscopic geometrical area due to surface roughness.

Li *et al.* (1992) studied the interaction of Cl^- ions with a platinum electrode, and for electrode potentials around 1 V and NaCl concentrations ranging from 0.8–4 M, they observed $R'_{\rm ct}$ values around 10^{-3}–10^{-5} $\Omega{\cdot}{\rm m}^2$. They also observed

that $1/R'_{\rm ct} \propto [{\rm Cl}^-]$, so extrapolating their data to a lower concentration of 1 mM, we might expect $R'_{\rm ct} \approx 0.1\ \Omega{\cdot}{\rm m}^2$, although this will still vary greatly with electrode potential as different chemicals are able to react with the electrodes. It is also unclear how this value would change for NaCl interacting with the gold gate wires that we commonly used for our experiments instead of the platinum electrode used by Li *et al.* The Warburg impedance will also vary with electrode material, electrode potential, sweep rate, and solution composition, although Li *et al.* (1992) generally found it to be of the same order of magnitude as $R_{\rm ct}$.

We note that both $R_{\rm soln}$ and $R_{\rm ct}$ scale inversely with the solution concentration, so that their relative magnitude should remain approximately the same. We will estimate values for each of these resistances in Section 4.1.

3.1.5 Debye-Hückel Theory

We have now discussed the theories relating to the electrostatic potential near a planar surface, like an electrode, but we are also interested in the potential near smaller charged objects, like a DNA molecule or cell placed near the nanotube. For non-planar charged surfaces, the Poisson-Boltzmann equation (Eq. 3.3) is generally not analytically solvable, but in 1923, Peter Debye and Erich Hückel linearized this equation by Taylor-expanding the exponentials and dropping all but the first order terms in ϕ. This approximation is valid as long as $e|\phi| < k_{\rm B}T$, which at room temperature means $\phi < 25$ mV, although in most cases their results are valid up to 80 mV; in general, we can use Debye-Hückel theory in solutions with concentrations under 0.1 M if there are no large external potentials (Butt *et al.*, 2003). Applying their approximation to Eq. 3.3, we obtain

$$\nabla^2\phi(\vec{x}) = \frac{2c_0e^2}{\epsilon\epsilon_0 k_{\rm B}T}\phi(\vec{x}) - \frac{\rho_{\rm fixed}(\vec{x})}{\epsilon\epsilon_0}. \tag{3.7}$$

We then define the Debye length λ_{D} as

$$\lambda_{\mathrm{D}} = \sqrt{\frac{\epsilon\epsilon_0 k_{\mathrm{B}} T}{2 c_0 e^2}} \tag{3.8}$$

to rewrite Eq. 3.7 as

$$\nabla^2 \phi(\vec{x}) = \frac{\phi(\vec{x})}{\lambda_{\mathrm{D}}^2} - \frac{\rho_{\mathrm{fixed}}(\vec{x})}{\epsilon\epsilon_0}, \tag{3.9}$$

which is known as the Debye-Hückel equation.[1]

In the Debye-Hückel approximation, potentials will decay as $e^{-r/\lambda_{\mathrm{D}}}$; beyond this distance, ions are electrostatically screened from each other. For example, the potential at a distance x from a planar charged surface of potential ϕ_0 is given by $\phi(x) = \phi_0 e^{-x/\lambda_{\mathrm{D}}}$, which is equivalent to the small-potential limit of the Gouy-Chapman model. We can also solve Eq. 3.9 in the case of a pointlike charge Q to find that the potential decays as

$$\phi(r) = \frac{Q}{4\pi\epsilon\epsilon_0 r} e^{-r/\lambda_{\mathrm{D}}}. \tag{3.10}$$

Before we discuss calculating the Debye length, we must note that Eq. 3.8 gives λ_{D} for a simple 1:1 salt like NaCl, but in general, the Debye length is

$$\lambda_{\mathrm{D}} = \sqrt{\frac{\epsilon\epsilon_0 k_{\mathrm{B}} T}{2 I e^2}}, \tag{3.11}$$

where I is the ionic strength, given by

$$I = \frac{1}{2} \sum_i z_i^2 c_i, \tag{3.12}$$

with z_i and c_i representing the charge and concentration of the i^{th} chemical species. For a salt that dissolves into two monovalent ions, I is equivalent to the concentration, but I will be higher than the concentration for a more complicated salt;

[1]Note that many books (generally written by chemists) will use "the Debye-Hückel equation" to refer to a different equation for activity coefficients.

for example, for a solution of KH_2PO_4 at concentration c_0, the ionic strength is

$$\begin{aligned} I &= \frac{1}{2}\left(z_{K^+}^2 c_{K^+} + z_{H^+}^2 c_{H^+} + z_{PO_4^{3-}}^2 c_{PO_4^{3-}}\right) \\ &= \frac{1}{2}\left(1^2 c_0 + 1^2(2c_0) + 3^2 c_0\right) = 6c_0. \end{aligned} \tag{3.13}$$

To calculate the Debye length, we introduce a factor of Avogadro's number ($N_A = 6.02 \times 10^{23}$ molecules/mole), since concentration is typically measured in moles/liter (M). We then find that at room temperature in water,

$$\lambda_{\mathrm{D}} \approx \frac{0.3 \text{ nm}}{\sqrt{I \text{ [M]}}}. \tag{3.14}$$

Thus, for a 1 mM NaCl solution, we expect a Debye length of $\lambda_{\mathrm{D}} \approx 10$ nm. We note that the ion concentration in an aqueous solution cannot actually fall below 0.2 μM (since water can dissociate into H_3O^+ and OH^- ions), which puts a theoretical upper limit on the Debye length of 670 nm. Practically, however, the upper limit in distilled water is only a few 100 nm, due to ionic impurities and pH variations, which corresponds to an ionic strength around 1 μM (Butt *et al.*, 2003).

3.2 Forces on Objects in Solution

In Section 3.1, we discussed how the electrostatic potential will be distributed through an electrolyte and across interfaces, which will be important for understanding how a carbon nanotube can be gated through an electrolyte and how charged objects near the nanotube will affect it. We are also interested in how these objects move around in the solution, *i.e.*, what forces act on them and how we can use these forces to manipulate them. In this section, we will consider the forces that affect a variety of types of objects: small chemicals, larger biomolecules like DNA, inorganic microspheres, solutions of different phases (like oil droplets in water), and living cells.

First, in Section 3.2.1, we will discuss the forces that act on any object in solution, like viscous drag and Brownian/diffusive forces. Then, in Section 3.2.2, we will consider the forces that become important when there are electric fields in the solution, like electrophoresis, dielectrophoresis, electrothermal forces, and AC electro-osmosis. Finally, in Section 3.2.4, we will explain what happens when the solution contains different fluids, such as in an emulsion of oil in water.

3.2.1 Fluid Forces: Drag and Diffusion

Although the motion of an object in a fluid is in theory well-defined as a boundary condition on the Navier-Stokes equations, even the motion of a simple sphere remains an unsolved problem and the object of current research (Maxey and Riley, 1983; Bagchi and Balachandar, 2003). The Navier-Stokes equations become much simpler, however, when the inertial forces in the flow are small compared to the viscous forces (*i.e.*, when the flow is laminar instead of turbulent), as is almost always the case in microfluidics. This condition is quantified by the Reynolds number, Re, which can be defined as

$$\mathrm{Re} = \frac{UL}{\nu}, \tag{3.15}$$

where U is a velocity scale (in our case, the mean fluid velocity), L is a length scale (the width of our microfluidic channel), and ν is the fluid kinematic viscosity ($\nu \approx 10^{-6}$ m^2/s for room temperature water). Since our flow velocities are always less than 1 mm/s and our channel widths are less than 100 μm wide, the Reynolds number in our flows will be $\mathrm{Re} < 0.1$, which is well below the beginning of the turbulence transition in a channel at $\mathrm{Re} \approx 10^3$ (Tritton, 1988).

For very small Reynolds number ($\mathrm{Re} < 1$), the Navier-Stokes equations can be

simplified to an equation for "creeping flow,"

$$\nabla p = \eta \nabla^2 \vec{u}, \tag{3.16}$$

where p and $\vec{u}$ are the pressure and velocity fields in the fluid and η is the fluid dynamic viscosity, which is 10^{-3} kg/m·s for water at standard conditions. In a channel, this equation can be solved to show that the velocity profile is parabolic (Tritton, 1988).

Equation 3.16 was also solved by George Stokes for the case of flow past a sphere; he found that the viscous drag on a sphere of radius a and velocity $\vec{v}$ (relative to the fluid) is

$$\vec{F}_{\text{drag}} = -k_{\text{drag}} \vec{v} = -6\pi\eta a \vec{v}. \tag{3.17}$$

For example, for the 200-nm microspheres described in Appendix E, the drag force in a 100 μm/s flow will be 0.2 pN if we hold the sphere fixed by some other force. Equation 3.17 can also be used for non-spherical objects like polymers if the "hydrodynamic radius" is used for a; this value is often determined from experimental measurements, as discussed in Appendix D for the case of DNA molecules.

Thus far, we have only considered hydrodynamics, or the bulk motion of the fluid. But any particle in solution will also experience random thermal motion, which can be more important than motion due to other forces. Historically, "diffusion" has been used to describe the random motion of small molecules, while "Brownian motion" has been used for larger objects, but the two effects are really the same; Einstein showed in 1905 that any size object has an average kinetic energy of $kT/2$ along each axis, which causes this diffusive motion (Berg, 1993).

We can write the mean-squared displacement of the particle due to diffusion as

$$\left\langle x^2 \right\rangle = 2Dt \qquad \text{(1 dimension)}, \tag{3.18}$$

$$\left\langle r^2 \right\rangle = 6Dt \qquad \text{(3 dimensions)}, \tag{3.19}$$

where D is called the diffusion constant of the particle. Einstein also showed that there is a simple relation between the diffusion constant and the drag coefficient (Berg, 1993):

$$D = \frac{k_{\mathrm{B}}T}{k_{\mathrm{drag}}}. \tag{3.20}$$

We can therefore use the Stokes equation (Eq. 3.17) to write the diffusion constant for a spherical bead of radius a as

$$D = \frac{k_{\mathrm{B}}T}{6\pi\eta a}. \tag{3.21}$$

Our 200-nm beads will thus have a diffusion constant of about $D = 2 \cdot 10^{-12}$ m^2/s, and a mean-squared-displacement of 3 μm in 1 second, or 80 μm in 10 minutes. For comparison, a small molecule with a typical diffusion constant $D = 5 \cdot 10^{-10}$ m^2/s (Bard and Faulkner, 2001) will have a mean-squared-displacement of 50 μm in 1 second, or over 1 mm in 10 minutes.

While Eq. 3.19 is useful for estimating the displacement of a particle due to diffusion, it does not tell us the force on the particle; indeed, the time-averaged diffusive force will always be zero. We can, however, define the threshold force which causes a displacement greater than the uncertainty in the position due to random motion, corresponding to three standard deviations from the mean position (Ramos *et al.*, 1998):

$$F_{\mathrm{diff}} = \frac{(6\pi\eta a)(3\sqrt{6Dt})}{t} = 18\sqrt{\frac{\pi\eta a k_{\mathrm{B}}T}{t}}. \tag{3.22}$$

A non-diffusive force would need to be greater than this to result in a motion that is clearly separate from diffusion. For our 200-nm beads, this force is 20 fN over 1 second, or 0.8 fN over 10 minutes, while for a small molecule, it is 310 pN over 1 second, or 13 pN over 10 minutes.

There will also be a sedimentation force on any object in fluid due to the upward buoyant force and downward gravitational force. For a particle of density ρ_p and volume V_p in a medium of density ρ_m, this force is

$$\begin{aligned} F_\mathrm{sed} &= F_\mathrm{buoy} - F_\mathrm{grav} \\ &= V_\mathrm{p}\rho_\mathrm{m}g - V_\mathrm{p}\rho_\mathrm{p}g \\ &= V_\mathrm{p}(\rho_\mathrm{m} - \rho_\mathrm{p})g, \end{aligned} \tag{3.23}$$

where $g \approx 9.8$ m/s^2 is the acceleration due to gravity. For the 200-nm polystyrene microspheres discussed in Appendix E, whose density is roughly matched to water ($\rho_\mathrm{bead} = 1.05$ g/mL and $\rho_\mathrm{water} = 1$ g/mL), this force is about 2 aN, or much smaller than the other forces we are considering. Larger beads feel larger sedimentation forces: the downward force is 0.3 fN on a 1-μm polystyrene bead, and 0.3 pN on a 10-μm bead. The downward force on a living 10-μm cell will be just slightly higher (0.4 pN), since cells typically have a density around 1.06–1.08 g/cm^3. If a drop of buffer containing suspended cells is placed on a substrate, this force is large enough to pull all the cells down to the substrate surface.

While we have not reviewed every force that can act on particles in solution (for example, hydrodynamic interactions between particles can become important if there are many particles around), we have covered the most important forces that should be considered in our experiments. To conclude this section, we provide a comparison in Figure 3.4 of the three forces discussed—drag, diffusion, and

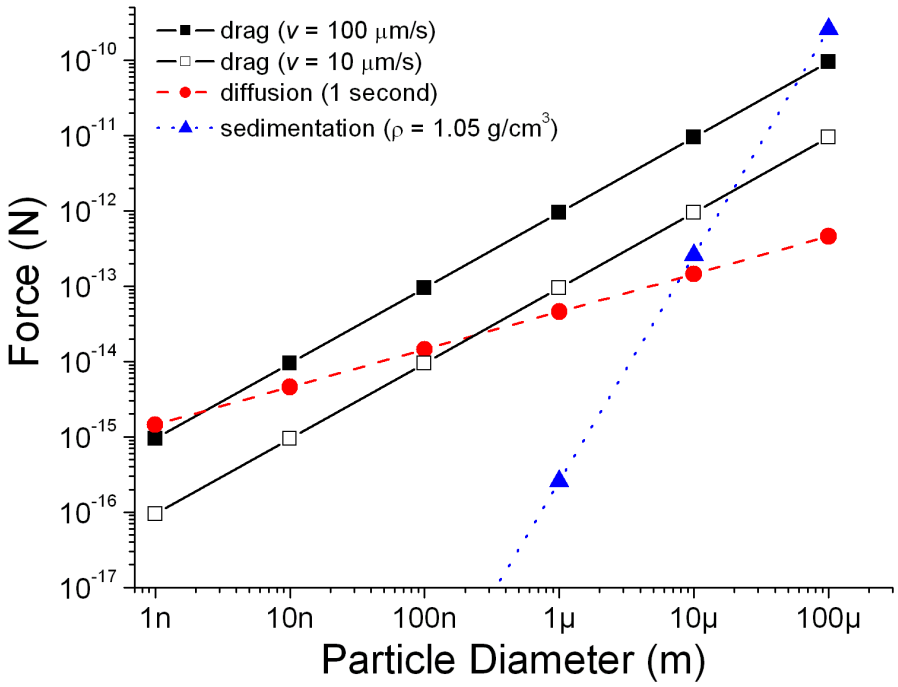

Figure 3.4: Comparison of forces due to drag, diffusion, and sedimentation on polystyrene beads as a function of diameter. F_{drag} is calculated from Eq. 3.17 for velocities of 100 μm/s and 10 μm/s, F_{diff} is calculated from Eq. 3.22 over a time of 1 second, and F_{sed} is calculated from Eq. 3.23.

sedimentation—as a function of the diameter of a polystyrene bead. F_{drag} is calculated from Eq. 3.17 for velocities of 100 μm/s and 10 μm/s (recall that $F_{\text{drag}} \propto v$), F_{diff} is calculated from Eq. 3.22 over a time of 1 second ($F_{\text{diff}} \propto t^{-1/2}$), and F_{sed} is calculated from Eq. 3.23 (using $\rho_{\text{p}} = 1.05$ g/mL and $\rho_{\text{l}} = 1$ g/mL). As the table demonstrates, the drag force is always significant, but it can become less important than diffusion for small particles at low flow speeds. Sedimentation is negligible for small particles, but starts to become significant when the particle size is over 10 μm, and is the dominant force for very large particles.

3.2.2 Electrical Forces: Basic Theory

In this section, we consider what happens when we add electric fields to the fluid. There will be some additional forces on a particle due solely to these fields, such as electrophoresis and dielectrophoresis, and there will also be electrohydrodynamic forces due to the interaction of the fields with the fluid flow. In this section, we will provide a basic overview of these forces, followed by some of our own results using these forces to control DNA and particle motion in Section 3.2.3. We will consider when these forces become important compared to the forces discussed in Section 3.2.1, but for a more detailed review, see Castellanos *et al.* (2003).

Any object with a charge q in an electric field $\vec{E}$ will experience a force

$$\vec{F} = q\vec{E}. \tag{3.24}$$

The movement of an object under this force is known as *electrophoresis*, and this technique is often used to separate mixtures of ions, proteins, or nucleic acids; for example, measuring the migration of tagged DNA strands through a porous gel with electrodes on either end is one of the most common methods of sequencing DNA (Nelson and Cox, 2004).

Electrophoresis is less useful, however, for controlled manipulation of small beads or biomolecules, whose net charge is quickly screened by ions in solution. A more powerful technique takes advantage of these objects' polarizability, and the force on a dipole $\vec{p}$ in a field $\vec{E}$:

$$\vec{F} = (\vec{p} \cdot \nabla)\vec{E}. \tag{3.25}$$

This force on a polarizable particle in a nonuniform electric field is known as *dielectrophoresis*, or DEP. Figure 3.5 illustrates the dielectrophoretic force for the case when the particle is more polarizable than the medium, which is known as

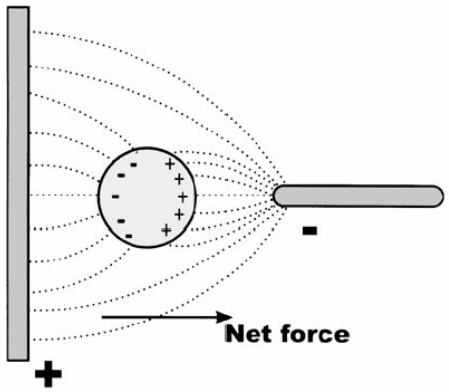

Figure 3.5: Dielectrophoresis (DEP) schematic, from Hughes (2000). DEP is the force on a polarizable particle in a nonuniform electric field. Note that the force on this particle will be the same even if the DC field polarity is switched, or if the field is AC. The case illustrated is called positive DEP; if the particle were less polarizable than the medium, it would feel a negative DEP force towards the opposite electrode.

positive DEP. In this case, the DEP force points up the field gradient to the region of highest field; it does not depend on the field polarity, so the field can be either AC or DC (Hughes, 2000).

The time-averaged DEP force in an AC electric field is given from Eq. 3.25 as

$$\left\langle \vec{F}_{\mathrm{DEP}} \right\rangle = \frac{1}{2}\mathrm{Re}[(\vec{p}\cdot\nabla)\vec{E}]. \tag{3.26}$$

For a spherical particle of radius a, this becomes

$$\left\langle \vec{F}_{\mathrm{DEP}} \right\rangle = 2\pi\epsilon_m a^3 \mathrm{Re}[K(\omega)]\nabla|\vec{E}_{\mathrm{rms}}|^2, \tag{3.27}$$

where $K(\omega)$ is the frequency-dependent Clausius-Mossotti factor

$$K(\omega) = \frac{\epsilon_{\mathrm{p}}^* - \epsilon_{\mathrm{m}}^*}{\epsilon_{\mathrm{p}}^* + 2\epsilon_{\mathrm{m}}^*}, \tag{3.28}$$

with ϵ_{p}^* and ϵ_{m}^* indicating the particle and medium complex permittivities, respectively (Green *et al.*, 2000). The complex permittivity is

$$\epsilon^* = \epsilon - i\sigma/\omega, \tag{3.29}$$

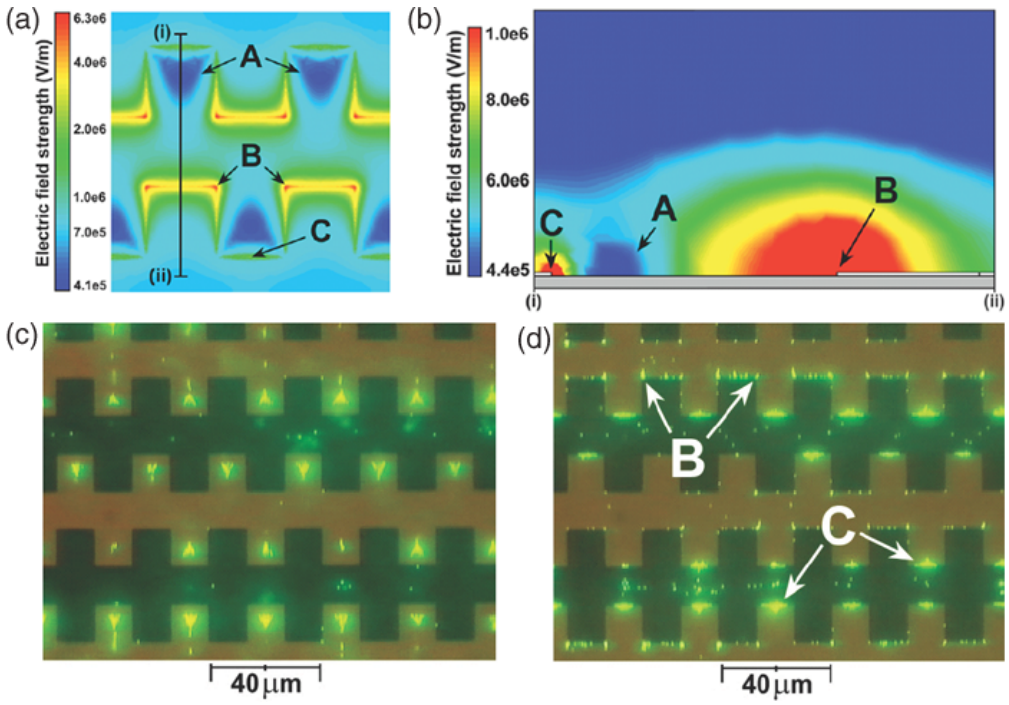

Figure 3.6: Positive and negative DEP for latex spheres, from Green *et al.* (2000). (a) Numerically-calculated electric field 100 nm above castellated electrodes. (b) Electric field in the vertical slice between points (i) and (ii) in (a). (c) Negative DEP is observed for 557-nm latex spheres when the applied signal is 8 volts peak-to-peak at 8 MHz. (d) When the field frequency is reduced to 700 kHz, positive DEP occurs.

where ϵ is the permittivity (or dielectric constant), σ is the conductivity, and ω is the frequency. For a spherical particle, $-\frac{1}{2} < \mathrm{Re}[K(\omega)] < 1$; when $\mathrm{Re}[K(\omega)] > 0$, the particle will experience positive DEP, and when $\mathrm{Re}[K(\omega)] < 0$, the particle will experience negative DEP (Ramos *et al.*, 1998).

Figure 3.6 illustrates that submicron latex spheres can exhibit both positive and negative DEP, depending on the frequency of the applied field. The electric field was numerically calculated above a microelectrode array, and the beads are observed to collect at either the high-field positions (positive-DEP) or the low-field positions (negative-DEP).

In many cases, however, only positive DEP is observed, even when one might expect the Clausius-Mossotti factor to be negative. For example, even though DNA has a low polarizability and one might expect to observe negative DEP, experiments with DNA have generally revealed positive DEP (Asbury and van den Engh, 1998; Asbury *et al.*, 2002; Hölzel, 2002; Dewarrat *et al.*, 2002). This behavior can be understood by including the effects of the charge double layer, which are more important for small particles; this highly polarizable double layer dominates the DEP properties of DNA molecules (Gascoyne and Vykoukal, 2002).

In addition to the electric forces on the particle such as electrophoresis and dielectrophoresis, there will also be electric forces on the fluid, which can then affect a particle's motion. These are collectively known as *electrohydrodynamic* forces. The electric field will generate power in the fluid, and the resulting temperature gradient will also create gradients in density, permittivity, and conductivity. Gradients in density change the buoyant force on the particles and can result in convection, and gradients in permittivity and conductivity cause *electrothermal* forcing of the fluid (Castellanos *et al.*, 2003). The viscous drag on particles caused by this fluid flow is generally small, however, compared with other electrical forces.

A more significant electrohydrodynamic effect is known as *AC electro-osmosis*, which can be larger than the dielectrophoretic force at low frequencies. Classical electro-osmosis describes the motion of the double-layer counterions along narrow channels in response to an applied field across the channel; this effect occurs in the ion channels in cell membranes and in ion separation methods like capillary electrophoresis. AC electro-osmosis, a term coined by Ramos *et al.* (1999), refers to the motion of ions in a double layer in response to AC fields. As illustrated in Figure 3.7(a), AC electro-osmosis occurs at frequencies that are low enough

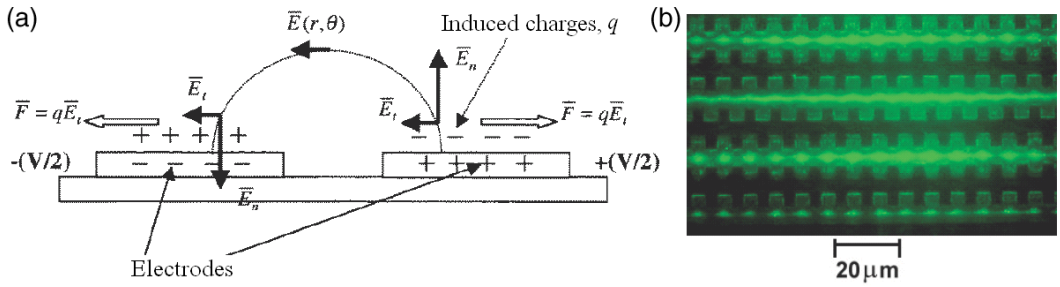

Figure 3.7: AC electro-osmosis schematic and images. (a) As illustrated by Ramos *et al.* (1998), at frequencies below the charge relaxation time, a double layer of counterions will form of each electrode, as discussed in Section 3.1.2. The component of the electric field tangential to the electrodes causes a force on these ions, which drag the fluid along with them towards the center of each electrode. This force, known as AC electro-osmosis, will point in the same direction when the voltage between the electrodes is reversed. (b) Green *et al.* (2000) observed AC electro-osmotic forces pushing their 557-nm latex beads towards the centers of their electrodes at frequencies of the order of 1-10 kHz; note that these trapping locations are different from the ones for positive or negative DEP shown in Figure 3.6.

for an electrical double layer to form at each electrode. For the planar electrode geometries typically used in dielectrophoresis experiments, the ions in the double layer feel a force towards the center of the electrodes due to the applied field, and the motion of the ions drags the fluid in the same direction. Note that the force is always towards the electrode centers, regardless of the electric field polarity (Castellanos *et al.*, 2003).

Green *et al.* (2000) observed the electro-osmotic force pushing submicron latex beads towards the centers of their electrodes at low frequencies (1-10 kHz), as seen in Figure 3.7(b); note that these trapping locations are different from the ones for positive and negative DEP shown in Figure 3.6.

3.2.3 Electrical Forces: Experiments

We saw in Section 3.2.2 that DEP can be be a powerful tool for trapping submicron particles, which could give us a useful handle for bringing objects closer to our nanotube devices. In this section, we present some preliminary experiments in which we used DEP to trap DNA molecules and different microspheres, and we discuss the possibility of using a carbon nanotube as a DEP electrode.

Figure 3.8(a) shows some of our results using DEP to trap double-stranded M13 and lambda DNA molecules, which are described in more detail in Appendix D. An AC voltage was applied between two 15 μm-wide gold electrodes with a 4 μm gap between them. We observed positive DEP for frequencies ranging from about 20 kHz to over 1 MHz, and saw that the voltage required to trap the particles increased with frequency. At lower frequencies of 1–10 kHz, we observed AC electro-osmosis as the DNA molecules trapped at the electrode centers. At higher frequencies, the voltage required to trap the particles caused destructive electrochemistry at the electrodes. In Figure 3.8(b), we see a similar frequency-dependence of the trapping voltage for different kinds of microspheres, which are described in Appendix E.

Carbon nanotubes could be used as an important tool in dielectrophoretic trapping, especially for small objects that become harder to trap as their Brownian motion becomes larger relative to the DEP force. (The DEP force, like the sedimentation force, scales as $F_{\mathrm{DEP}} \propto a^3$ with the particle radius a, whereas diffusion only scales as $F_{\mathrm{diff}} \propto a^{1/2}$.) Equation 3.27 shows that the DEP force scales as $\nabla|\vec{E}_{\mathrm{rms}}|^2$, so increasing the trapping force requires increasing the voltage (which can result in undesirable electrochemical or electrothermal effects) or by increasing the field gradient. The latter has been done already by making ever-smaller

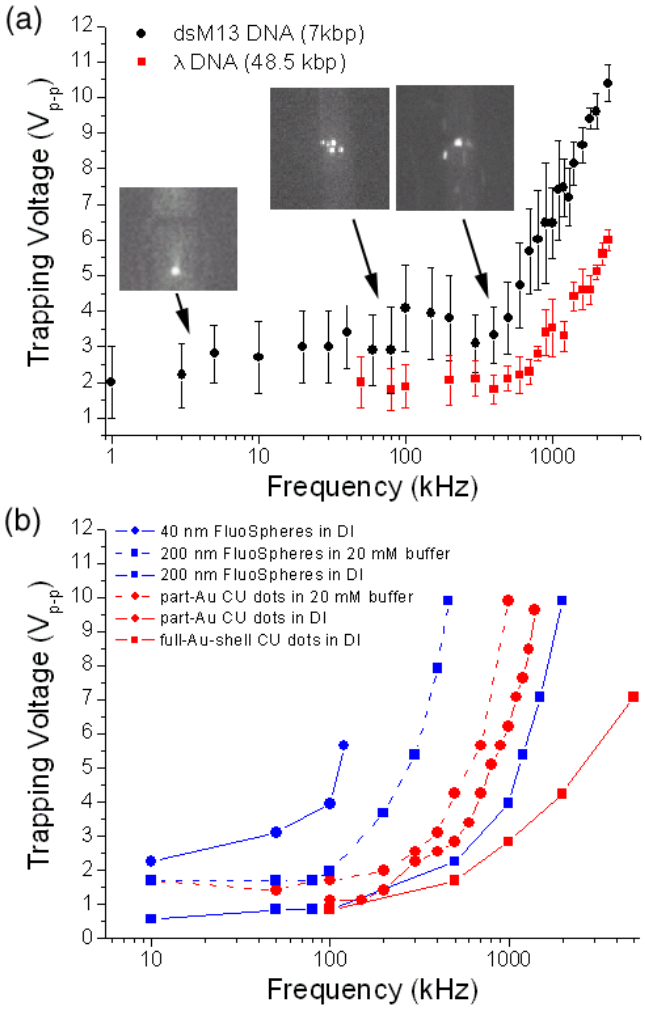

Figure 3.8: Frequency dependence of DEP trapping voltage (measured peak-to-peak) for DNA and microspheres, using 15 μm-wide gold electrodes with a 4 μm gap between them. The flow speed was approximately 100 μm/second. (a) Trapping double-stranded M13 and λ DNA in a buffer solution (see Appendix D for DNA properties). As seen in the inset fluorescence images, at frequencies from 20 kHz to 3 MHz, we observed positive DEP on the electrode edges, and at lower frequencies of 1–20 kHz, we observed AC electro-osmosis. (b) DEP with CU dots (both partly and fully coated with gold, each with a diameter around 150 nm) and polystyrene FluoSpheres (40-nm and 200-nm) from Molecular Probes (see Appendix E for bead properties). Measurements were performed in both DI water and in 20 mM Tris acetate buffer (pH 8.3).

arrays of metal electrodes, but the ultimate limit for a small electrode is a carbon nanotube.

Zheng *et al.* (2004a) used this idea to dielectrophoretically trap polystyrene beads (20–100 nm) and gold nanoparticles (2–10 nm) between gold electrodes that had carbon nanotubes crossing all or part of the 5–10 μm gap between them. We attempted to repeat their experiment with 200-nm polystyrene beads and 150-nm CU dots (see Appendix E for the bead properties). We used very similar devices and identical field parameters (500 kHz, 4-20 V_{p-p}), trying both their protocol for drying the beads on the chip while the voltage is applied and for turning off the voltage and rinsing the chip before the solution dried. We observed positive DEP trapping on the edges of the electrodes, but we observed no selective trapping on the nanotubes, either with fluorescence microscopy during the experiment or with an AFM after the beads had dried on the chip. We do not understand why we were unable to replicate the results of Zheng *et al.* (2004a), but perhaps using smaller microspheres or varying the trapping frequency would help. Tuukkanen *et al.* (2006) recently used a somewhat similar geometry with multiwalled carbon nanotubes to trap small pieces of DNA (150-bp and 1060-bp) using frequencies around 1 MHz.

To conclude this section, we note that electric fields can create much stronger forces on particles in solution than the drag force and other forces discussed in Section 3.2.1, which provides a handle for manipulating the particles. In particular, dielectrophoresis can be used to trap polarizable particles at locations of strong field gradients, and it may be particularly powerful when one of the electrodes used is a carbon nanotube. DEP trapping is best done at frequencies above 20 kHz, since at low frequencies electro-osmotic forcing will dominate the system.

3.2.4 Interfacial Forces

In the previous sections, we have discussed the forces on solid objects in solution. But when the objects in solution are able to deform, like drops of oil or a cell membrane, then interfacial forces also become important. We will investigate the magnitude of these forces by looking at the specific case of how a drop of oil in an aqueous solution would interact with a carbon nanotube, which may be relevant for future experiments.

Carbon nanotubes are hydrophobic, and have only been solubilized in water through chemical modification or by non-covalently wrapping them with polymers like polyvinyl pyrrolidone (PVP) (O'Connell *et al.*, 2001) or single-stranded DNA (Zheng *et al.*, 2003a), surfactants like sodium dodecyl sulfate (SDS) and Triton X-100 (Islam *et al.*, 2003), or starches (Star *et al.*, 2002). This means that it is much more energetically favorable for the nanotube to be surrounded by other nonpolar molecules, such as oil or inside a cell membrane, than to be only surrounded by water.

The nanotube-water interfacial energy has not, to our knowledge, been measured, but for the rough calculations in this section, we will assume that it is similar to the oil-water interfacial energy, which is around $\gamma = 35$ mJ/m^2 for the oil toluene (Lin *et al.*, 2003). That means that every section of surface area S between the nanotube and the water results in an energy γS, so a 1-μm-long nanotube with diameter $d = 1$ nm that is completely surrounded by water has an interfacial energy of 10^{-16} J.

If a drop of oil of radius R were then able to encase the nanotube, it would cause a change in the Helmholtz free energy of

$$\Delta E = \gamma \Delta S \approx -\gamma(2\pi d R). \tag{3.30}$$

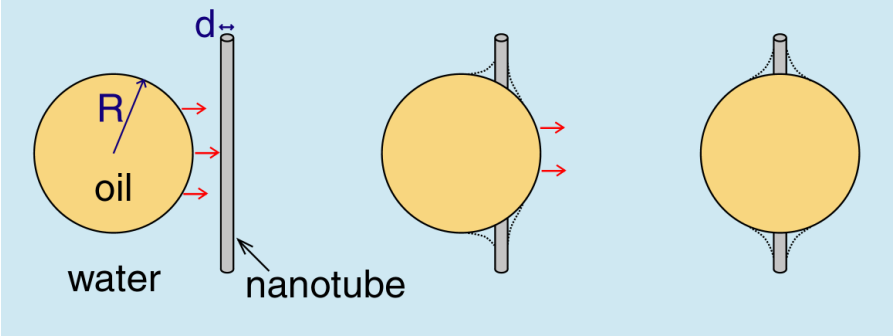

Figure 3.9: Oil droplet sticking to a nanotube. Because nanotubes are hydrophobic, they can lower their interfacial energy by being in the middle of a droplet of oil instead of being entirely surrounded by water. As indicated by the dotted lines, the lowest energy configuration is for the oil droplet to form a lemon-like "unduloid," rather than a sphere, around the nanotube.

We can then roughly estimate the force on the droplet as $F = \Delta E/R$, which turns out to be $2 \cdot 10^{-10}$ N, independent of droplet size. From Figure 3.4, we see that the drag force on even a large droplet with $R = 5$ μm is only 10^{-11} N in a 100 μm/s flow, so it would likely be difficult to remove the oil from the nanotube, although it may be possible to change the nanotube interfacial energy by placing a voltage on it to make it more hydrophilic.

This situation of a drop of oil sticking to a nanotube is illustrated in Figure 3.9. It turns out that the simple intersection of a sphere and a cylinder depicted is not the lowest-energy configuration; the oil can lower its interfacial energy more by eliminating the high-curvature regions at the intersection to form a more lemon-like shape, as indicated by the dotted lines in Figure 3.9. This surface of constant curvature is known as a "Delaunay surface" or "unduloid" (Kapouleas, 1990), and it may be familiar as the shape formed by beads of dew on a spider web, which can lower their energy by minimizing their surface area just like the oil on a nanotube.[2]

[2]We thank Cornell Professor Veit Elser for helping us identify this shape.

The force keeping the oil on the nanotube will therefore be slightly increased from the force found with our rough calculation.

Although we have not yet performed experiments with oil droplets and nanotubes, this seems to be a promising direction for future research. The high affinity of nanotubes for hydrophobic environments discussed in this section will also be relevant for the experiments presented in Chapter 9, when individual cells are placed on suspended nanotubes in solution, as we will discuss further in that chapter.

Chapter 4

Electrolyte-Gated Nanotube Transistors

We have seen in Section 2.3 that semiconducting nanotubes can be used to make high-performance transistors in air, but we would like to use nanotubes with biochemical systems in solution. In 2001, Krüger *et al.* showed that multiwalled carbon nanotubes can be used as field-effect transistors in an electrolyte environment, and these results were extended for single-walled nanotubes by Rosenblatt *et al.* (2002). Rather than gating the nanotube by applying a voltage to a back gate (which is strongly screened by an aqueous solution), these groups gated their devices through a wire placed in the solution, which we shall refer to as the electrolyte-gate wire. A cartoon of this setup can be seen in Figure 4.1(a).

In this chapter, we will first show how we can approximate the electrolyte-gate setup as a basic circuit of resistors and capacitors in Section 4.1, and we will discuss how the electrolyte-gate wire can add charges to the nanotube. In Sections 4.2 and 4.3, we will then discuss two experimental problems that arise from this configuration: hysteresis and leakage currents.

4.1 Circuit Model of an Electrolyte-Gated Nanotube

In Section 2.2, we developed the tools to reduce our electrolyte-gated nanotube to a basic circuit, which we illustrate in Figure 4.1. The interface between the electrolyte and each conducting element can be modeled using the Randles circuit model (see Fig. 3.3) as a double layer capacitance, $C_{\rm dl}$, in parallel with a resistor due to charge transfer, $R_{\rm ct}$ (we will ignore the Warburg impedance for now). Note that the resistance should scale inversely with area ($R_{\rm ct} = R'_{\rm ct}/A$), while

the capacitance should scale with area ($C_{\mathrm{dl}} = C'_{\mathrm{dl}}A$). For most interfaces in solution, $C'_{\mathrm{dl}} \approx 0.1$ F/m^2, as discussed in Section 3.1.2. The solution will also act as a resistor, R_{soln}, with its resistivity ρ_{soln} given by Eq. 3.1.

As discussed in Section 3.1.3, the voltage V_{g} applied to the electrolyte-gate wire will set the electrochemical potential $\mu_{\mathrm{e-c}}$ of the solution, and the electrostatic potential ϕ will be determined by the difference between $\mu_{\mathrm{e-c}}$ and the chemical potential μ_{c}:

$$e\phi = \mu_{\mathrm{e-c}} - \mu_{\mathrm{c}}. \tag{4.1}$$

We can generally treat the electrostatic potential as constant throughout the solution, and it is this potential, along with the capacitance between the nanotube and the gate, that will determine how many electrons are added to the nanotube.

In Section 2.3, we saw that for a back-gated nanotube, the charge ΔQ added to the nanotube is given by $\Delta Q = CV_{\mathrm{g}}$, where $C = (C_{\mathrm{E}}^{-1} + C_{\mathrm{Q}}^{-1})^{-1}$ is the combination of the electrostatic capacitance C_{E} between the nanotube and the back gate and the quantum capacitance C_{Q} of the nanotube; the quantum capacitance of the back gate can be ignored. The solution, however, has a non-negligible quantum capacitance. We instead write the charge added to an electrolyte-gated nanotube as

$$\Delta Q = C_{\mathrm{E}}\Delta\phi, \tag{4.2}$$

where C_{E} is the electrostatic capacitance between the nanotube and the solution and $\Delta\phi$ is the difference in electrostatic potential between the nanotube and the solution. For a 1-nm-diameter nanotube, the electrostatic capacitance is given by $C'_{\mathrm{E}} = \pi(1\text{ nm})(0.1\text{ F/m}^2) = 0.3\text{ fF}/\mu\text{m}$, so if the nanotube is 1 μm long, changing the solution electrostatic potential by about 0.5 mV would add one electron to the nanotube.

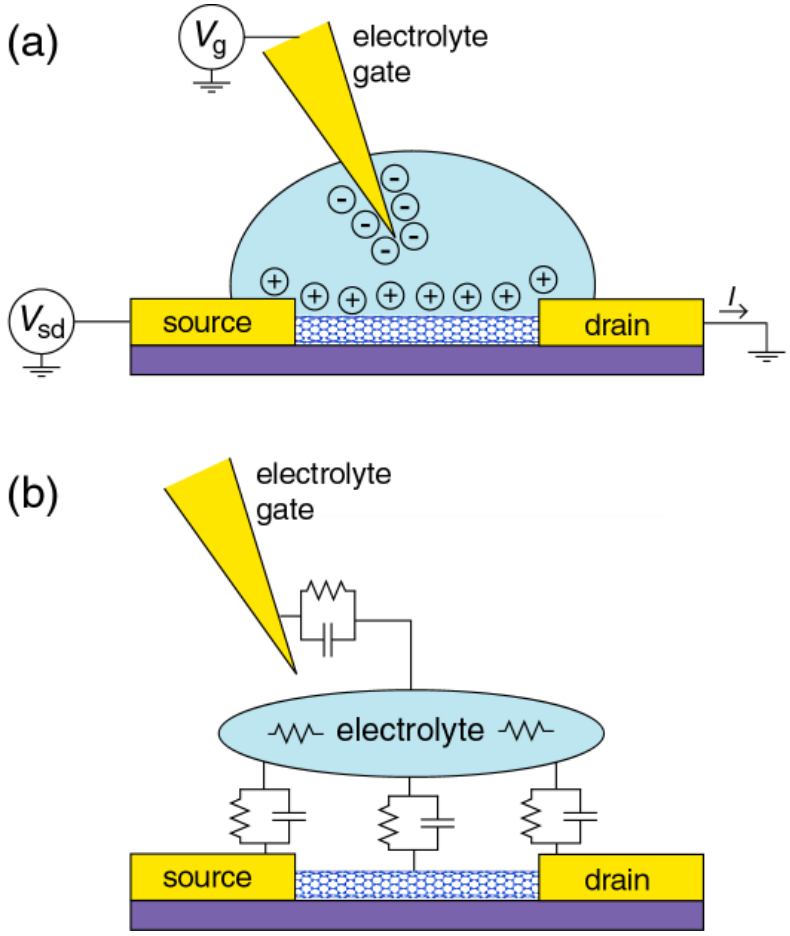

Figure 4.1: Electrolyte-gated nanotube transistor. (a) Schematic of an electrolyte-gated nanotube transistor. Like for the back-gated transistor in Figure 2.4(a), the nanotube is contacted by metal electrodes, allowing one to measure its conductance. The gate voltage V_g is applied to a wire that is placed in the solution, and this voltage affects the nanotube via ions in the electrolyte. If the gate wire is positively charged, it will attract negative ions to form a double layer, as illustrated in Figure 3.1. (b) Circuit model for an electrolyte-gated nanotube. Between the electrolyte and each conducting element is a capacitor C_{dl} due to the ion double layer and a resistor R_{ct} due to the charge transfer barrier. The solution also has its own resistivity ρ.

Because the capacitance between a nanotube and an electrolyte gate is so high compared to a typical back-gated device, electrolyte-gated nanotube transistors can achieve transconductances of $g_m = 20$ μA/V and subthreshold swings of 80 mV/decade (Rosenblatt *et al.*, 2002), values comparable to the devices with high-κ dielectric top gates discussed in Section 2.3, but involving much simpler fabrication.[1]

By using an electrolyte-gate wire to set the electrochemical potential of solution (and thus the electrostatic potential), we are able to gate our nanotube transistor, but we will also face two experimental difficulties that are evident in an examination of the circuit model in Figure 4.1(b). First, when the potential on the gate wire is changed, there will be some time scale associated with the distribution of this potential throughout the circuit that will depend on the magnitude of the resistors and capacitors in our circuit, which leads to hysteresis in our nanotube response. Second, there will also be a current flowing through the circuit elements from the gate wire to the nanotube and contact electrodes; this is known as a leakage current. We will briefly discuss these two phenomena in the following sections.

4.2 Hysteresis

The nanotube conductance versus gate voltage shown earlier in Figure 2.4 was simplified in that the conductance was shown while sweeping the gate voltage

[1]Excellent (and tunable) device properties (transconductances around 5 μA/V and near-ideal subthreshold swings) have also been achieved by drying solid polymer electrolytes with different dopant concentrations on top of nanotubes and then piercing the electrolyte with a wire to apply the gate voltage (Lu *et al.*, 2004; Siddons *et al.*, 2004). While this setup is preferable for most electronic applications, it is less relevant for the sensing applications considered here.

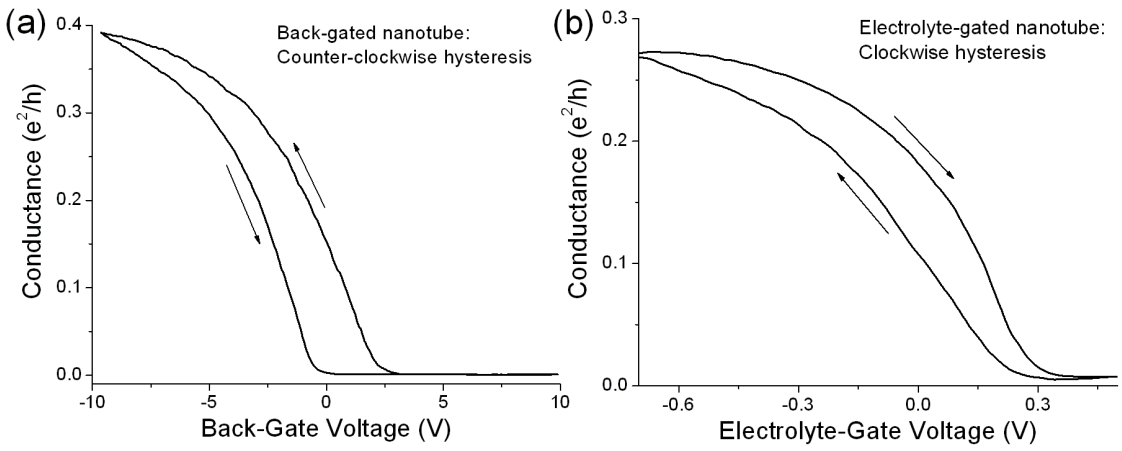

Figure 4.2: Examples of hysteresis in (a) back-gated and (b) electrolyte-gated nanotubes.

in only one direction; when it is swept in the reverse direction, some hysteresis is always observed, as seen in Figure 4.2. This hysteresis is often not shown because it is usually not relevant in interpreting the results of a nanotube sensing experiment, but it is worth understanding its origins.

For a back-gated nanotube in air, the hysteresis is counterclockwise, *i.e.*, the system corrects for the applied gate voltage over some time scale. This hysteresis can be decreased by baking the device in vacuum or coating it with PMMA, or increased by measuring it in a more humid environment, as reported by Kim *et al.* (2003). They suggest that the hysteresis is due to charge trapping by water molecules around the nanotube, although other models argue that there are charge traps in the SiO_2 or at the Si/SiO_2 interface (Robert-Peillard and Rotkin, 2005). In either case, the basic idea is that when the back gate is held at positive gate voltage, electrons are slowly trapped near the nanotube, so that after some time the nanotube sees a more negative potential than is simply due to the gate voltage (and vice versa for the opposite sweep direction).

For an electrolyte-gated device, however, the hysteresis is clockwise: the nanotube "remembers" the last gate voltage it saw. This is because it takes some time for the potential to be distributed in solution, and this time scale will depend on the resistors and capacitors in our circuit model of Figure 4.1(b). In Section 6.4.2, we will see that the hysteresis can be decreased by decreasing the rate at which the gate voltage is swept or by increase the concentration of ions in the solution.

We also note in Figure 4.2 that we are able to turn the electrolyte-gated nanotube on and off using a much smaller range of gate voltage than the for the back-gated nanotube. This is related to the higher capacitance between the nanotube and the gate for an electrolyte-gated device, as discussed in Section 4.1. It is fortunate that we can measure the conductance behavior of a nanotube in solution with such a narrow range of gate voltages, since we are unable to increase the voltage applied to the electrolyte-gate wire beyond this narrow range. This is primarily due to the leakage currents in the solution, which we will discuss in the following section.

4.3 Leakage Currents

The leakage current between the gate wire and drain electrode arises from the charge-transfer resistances, as well as capacitive currents through the double layer. This leakage is typically much higher than for back-gated devices. Figure 4.3 shows the leakage current through a back-gate and through an electrolyte-gate plotted on the same scale.

For our experiments, it will generally suffice to be aware of this effect and to make sure that this leakage current does not overwhelm the current measured through the nanotube. To limit the leakage currents, it is preferable to make the

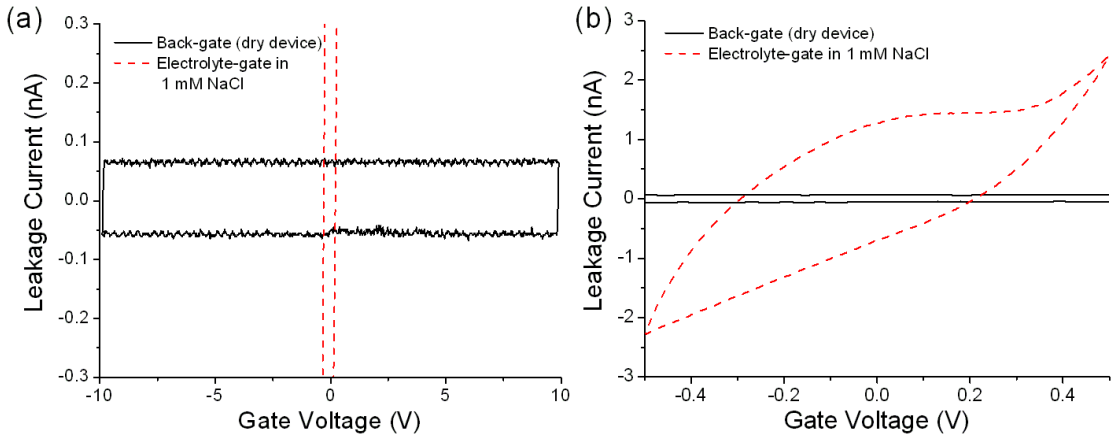

Figure 4.3: Back-gate vs. electrolyte-gate leakage currents, with the same data plotted on two different scales in (a) and (b). While the back-gate leakage current is typically only a small capacitive current through the oxide layer, the electrolyte-gate leakage current is much larger. In both cases, the leakage current was measured with the gate voltage applied through a 10 MΩ resistor.

area of the source and drain electrodes that is exposed to the electrolyte as small as possible; this will also allow the electrolyte-gate wire to control the potential of the solution. We will estimate the magnitude of the leakage current for our circuit model and discuss specific techniques for reducing these unwanted currents in Section 6.4.3.

Chapter 5

Previous Work with Nanotube Sensors

As mentioned in the Introduction, the small size and high sensitivity of carbon nanotubes makes them excellent sensors for biological and chemical systems. In this chapter, we review the previous work with nanotube sensors.[1] We will see that for transistors made from bare (non-functionalized) semiconducting nanotubes, many chemicals and biomolecules cause the entire G vs. V_g response curve to be translated with respect to V_g, which we can describe as a shift in the threshold voltage of the device.

While it is clear that a variety of analytes cause a threshold voltage shift in nanotube devices, the origin of this response is not always well-understood. A number of mechanisms have been proposed to explain the response in different situations, including direct charge transfer between the analyte and the nanotube, local capacitive gating of the nanotube by a charged analyte, and more subtle interactions of the analyte with things other than the nanotube, such as the metal electrical contacts. In the following sections, we will first present the published data on sensing with nanotube transistors, along with the original explanations. Then, in Section 5.5, we will look more closely at these explanations, particularly in the cases of nanotube sensing in electrolytes that are most relevant to the results presented in this thesis.

[1] Nanotubes have been used in bulk in a number of sensing experiments, such as to create high-surface-area electrodes for sensing glucose (Sotiropoulou and Chaniotakis, 2003; Wang *et al.*, 2003) or DNA (Cai *et al.*, 2003; Li *et al.*, 2003), but we will focus on nanotubes that have been used in a transistor geometry.

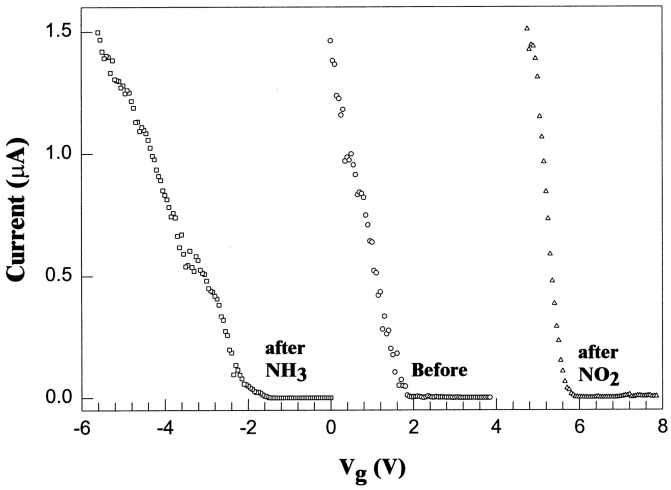

Figure 5.1: Nanotube response to gaseous NH_3 and NO_2, from Kong *et al.* (2000). Each gas causes a large threshold voltage shift in the I vs. V_g curve. These measurements were carried out successively after sample recovery.

5.1 Sensing Gas Molecules

The first nanotube sensing experiment was performed by Kong *et al.* (2000) in Hongjie Dai's Stanford laboratory, where they found that exposing a back-gated nanotube transistor to gaseous NO_2 caused an increase in threshold voltage $\Delta V_{\text{th}} \approx 4$ V, while exposure to NH_3 caused a decrease in threshold voltage $\Delta V_{\text{th}} \approx -4$ V, as shown in Figure 5.1. Since NO_2 is a strong oxidizer, they attributed the increase in threshold voltage to charge transfer from the nanotube to NO_2 molecules (p-doping the nanotube). NH_3 has a lone electron pair that it can donate (n-doping the nanotube), but their density-functional theory calculations showed no affinity between NH_3 molecules and the nanotube, so they suggest that it is affecting the nanotube indirectly through the SiO_2 substrate or through preadsorbed oxygen on the nanotube.

Kong and Dai (2001) have also observed similar n-doping effects from other amine compounds, and Bradley *et al.* (2003b) from Nanomix Inc. found the same results using nanotube devices in which the metal contacts were covered with SiO_2, showing that the effect is not related to these contacts. Liu *et al.* (2005) used these results to modulate the band structure of single-walled nanotubes spatially by covering parts of the nanotubes and letting the exposed areas be doped by gaseous NO_2 or NH_3.

In an application of this sensing mechanism, Novak *et al.* (2003) showed that dimethyl methylphosphonate (DMMP), an electron donor which is very similar to the gaseous nerve agent sarin, causes a threshold voltage shift $\Delta V_{\text{th}} \approx -2$ V, and that this detection can be made specific by coating the nanotube with a chemoselective polymer film. Polymer coatings have also been used to differentiate between NO_2 and NH_3 (Qi *et al.*, 2003). And while bare nanotubes show no response to CO_2 or H_2, nanotubes can be coated with a polymer to show a CO_2 response (Star *et al.*, 2004a) or with Pd nanoparticles to show a H_2 reponse (Kong *et al.*, 2001a).

Oxygen gas has also been shown to have a dramatic influence on the electrical characteristics of bare nanotubes; while nanotubes are p-type in air or in pure oxygen environments, they become n-type in ultrahigh vacuum (Collins *et al.*, 2000). This was initially ascribed to charge transfer from nanotubes to adsorbed O_2, but more recent studies from Phaedon Avouris's group have suggested that the O_2 instead changes the energy alignment at the metal-nanotube contacts (Derycke *et al.*, 2002; Cui *et al.*, 2003).

The nanotube G vs. V_{g} curve has also been shown to change in response to alcohol vapors like ethanol, although this response is not yet understood (Someya

et al., 2003).

A different kind of nanotube gas sensing experiment has been developed by Eric Snow and his colleagues at the Naval Research Laboratory. Rather than studying the conductance response of the nanotubes, they look at the change in the capacitance between the nanotube and the silicon back gate, and they find that for most vapors the change in this capacitance is 10–100 times larger than the corresponding change in conductance (Snow and Perkins, 2005). They conclude that the adsorbed gas molecules form a polarizable layer that increases the nanotube capacitance, and they show that the signal scales roughly with the molecular dipole moment (Snow *et al.*, 2005). They also find that this signal is dominated by adsorption at defect sites, and that they can increase their sensitivity through the controlled introduction of defects by oxidation (Robinson *et al.*, 2006).

5.2 Sensing Molecules Dried from Solution

The successes of using nanotubes to sense gaseous molecules has led to experiments with other analytes. One technique, which has primarily been used by researchers at Nanomix Inc., is to coat carbon nanotube transistors with some solution of molecules and to measure the change in conductance versus back-gate voltage after the solution has dried on top of the nanotube. Examples of the response of nanotubes to different molecules are shown in Figure 5.2.

Klinke *et al.* (2005) have coated nanotubes with dried solutions of amine-containing molecules, which, like the amine-containing gases, n-doped the nanotubes. In Figure 5.2(a), we see that the reduced form of polyaniline, which has all of its nitrogen atoms in the amine form with sp^3 hybridization, converts an originally p-type device to strong n-type behavior. After the device has been immersed

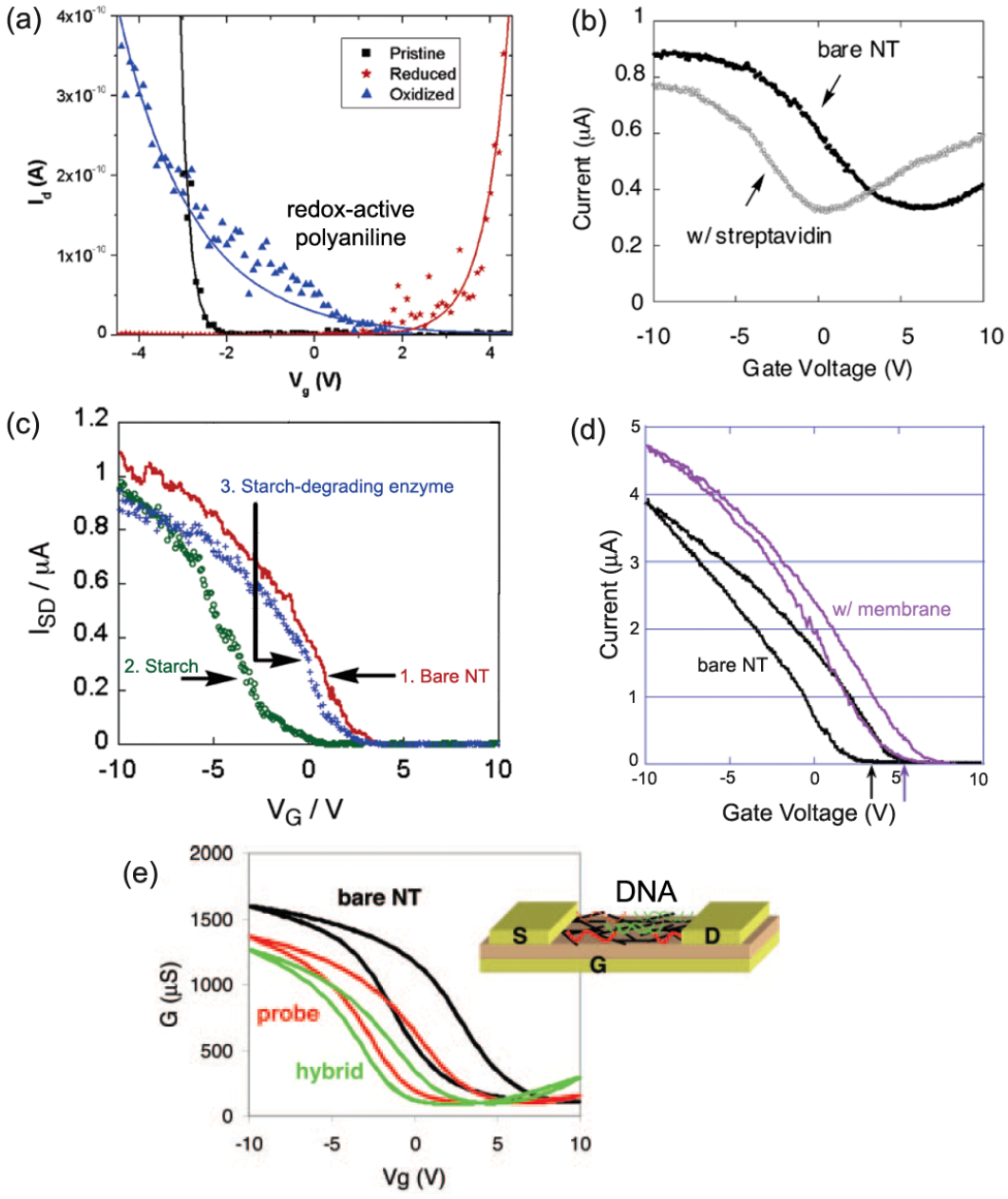

Figure 5.2: Previous work sensing molecules dried from solution. Nanotube response is shown for (a) redox-active polyaniline (Klinke *et al.*, 2005), (b) streptavidin (Star *et al.*, 2003a), (c) starch and a starch-degrading enzyme (Star *et al.*, 2004b), (d) a cell membrane (Bradley *et al.*, 2005), and (e) DNA (Star *et al.*, 2006).

in a solution that oxidizes the polyaniline molecules, converting the nitrogens to imine groups with sp^2 hybridization, the device is converted back to *p*-type.

The experiments at Nanomix have all involved drying various biomolecules on transistors made from individual nanotubes or nanotube networks. Star *et al.* (2003a) found that the dried protein streptavidin causes a negative threshold voltage shift, as shown in Figure 5.2(b), which they attribute to electron transfer from the protein to the nanotube. (They were also able to detect protein binding after functionalizing their nanotubes with biotin, the substrate for streptavidin, which reduced the overall conductance rather than shifting the G vs. V_g curve; we are, however, more interested in non-functionalized nanotubes.) In another experiment, they found that dried starch also causes a negative threshold voltage shift (attributed to the electron-donating abilities of the hydroxyl groups), which can be reversed by soaking the device in a buffer containing an enzyme that degrades starch, as shown in Figure 5.2(c) (Star *et al.*, 2004b).

In the first experiment to integrate nanotubes with cell membranes, Bradley *et al.* (2005) deposited the membrane from *Halobacterium salinarum* on top of transistors made from networks of carbon nanotubes. This membrane contains the protein bacteriorhodopsin, which has a permanent dipole moment; the researchers were thus able to assemble the membrane in different orientations on top of the nanotubes by applying different voltages to the silicon substrate during deposition. They found that the membrane shifted the transistor threshold voltage in different directions depending on which side of the membrane contacted the nanotubes: the cytoplasmic side caused a positive shift (as shown in Figure 5.2(d)), and the extracellular side caused a slight negative shift. They conclude that the electrostatic field associated with the bacteriorhodopsin dipole induces

charge in the nanotubes, shifting the Fermi level and thus the threshold voltage, and they use the differences in threshold voltage shifts to conclude that the electric dipole of the bacteriorhodopsin is located 2/3 of the way from the extracellular to the cytoplasmic side of the membrane.

The Nanomix group has also measured the electrical characteristics of nanotubes with DNA dried on top. As seen in Figure 5.2(e), incubating nanotubes with single-stranded "probe" DNA causes a negative threshold voltage shift, which is increased after the nanotubes are also incubated with the complementary hybrid to the first DNA strand (Star *et al.*, 2006). This shifts are ascribed to electron transfer through π-stacking interactions between exposed aromatic nucleotide bases in the single-stranded DNA and the nanotube sidewalls. Further studies by Tang *et al.* (2006), however, indicate that DNA hybridization on the gold source and drain electrodes, not on the nanotube itself, is the source of the conductance change; they suggest that the DNA changes the energy level alignment between the nanotube and the gold.

5.3 Sensing Molecules in Solution

While simply drying a solution of molecules on a nanotube device can provide some information about the molecule, we would prefer to study biomolecules in their natural wet environment. Furthermore, the approach of drying molecules on a nanotube cannot be used for real-time electrical monitoring. Covering a nanotube device with an aqueous solution, however, screens the voltage from the back gate, preventing one from using it to obtain any useful information about the device.

One approach for using a nanotube to study molecules in solution is to use a solution with a very low conductivity that will not screen the back gate voltage.

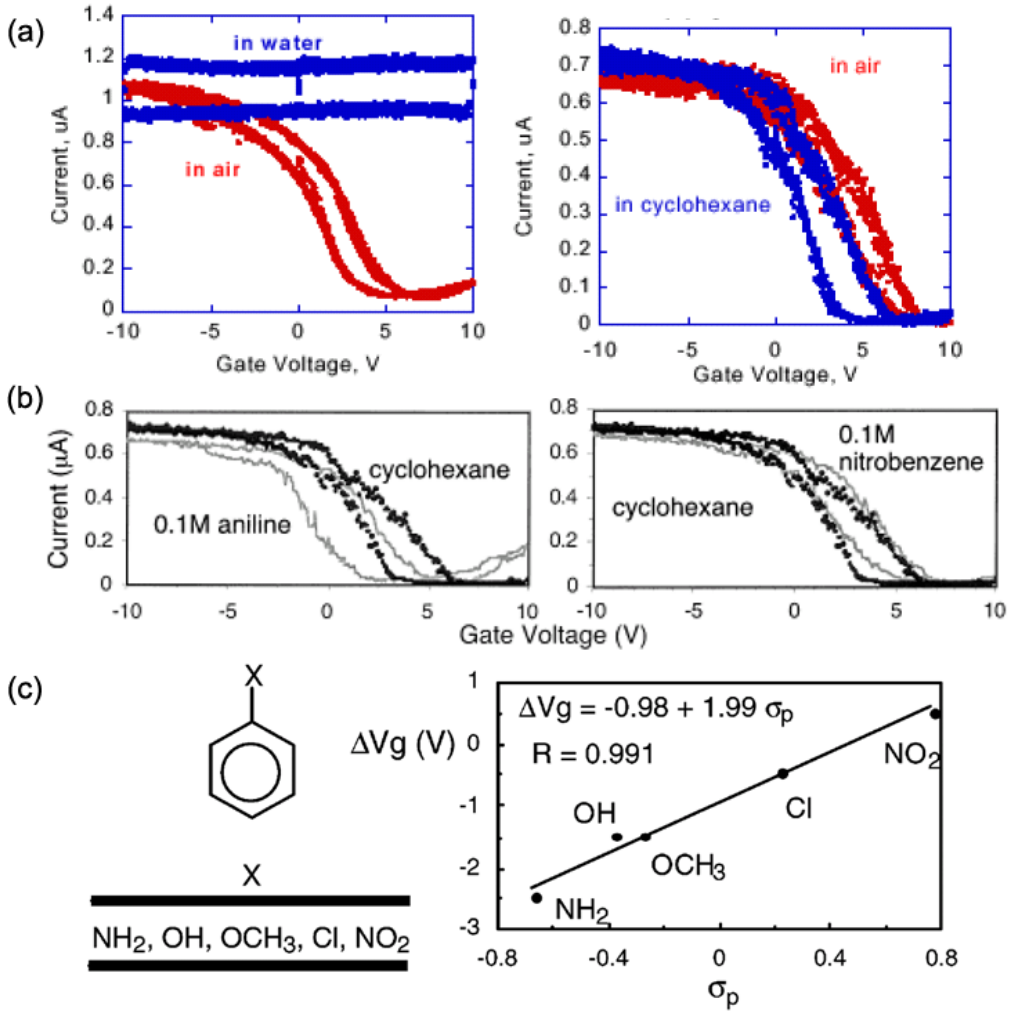

Figure 5.3: Sensing aromatic compounds in solution with a back gate, from Star *et al.* (2003b). (a) Coating a nanotube device with water screens the voltage from the back gate so that it cannot be used to modulate the device conductance. In a low-conductivity solution like cyclohexane, however, the G vs. V_g curve appears similar to the curve taken in air. (b) Adding aromatic compounds to the cyclohexane shifts the threshold voltage. (b) There is a linear correlation between the threshold voltage shift and the Hammett σ constant, which is a measure of the electron-donating character of the molecules.

As seen in Figure 5.3(a), although coating a device in water prevents one from modulating its conductance with the back gate, coating it with low-conductance cyclohexane only causes a shift in the threshold voltage. Star *et al.* (2003b) added aromatic compounds to the cyclohexane and measured the resulting threshold voltage shift, as seen in Figure 5.3(b). They suggest that the aromatic compounds should interact with the nanotube sidewalls through π-π stacking, and they indeed found a linear correlation between the electron-donating character of a compound (as measured by its Hammett σ constant) and the resulting ΔV_{th}, as shown in Figure 5.3(c).

Most biomolecules of interest, however, naturally occur in conducting aqueous solutions, rendering this approach less useful. But as we saw in Chapter 4, nanotube transistors can also be gated through an electrolyte solution using a gate wire. Figure 5.4 shows the response of electrolyte-gated nanotubes to different analytes.

Bradley *et al.* (2003a) found that increasing concentrations of ammonia in water cause increasingly negative threshold voltage shifts, as shown in Figure 5.4(a), which they regard as the effect of electrostatic gating, in which adsorbed ammonia charges the nanotube. They do not state what they use to apply a gate voltage to the solution, though in later work they use a platinum wire (Bradley *et al.*, 2004).

Krüger *et al.* (2003) found that the peak in the resistance of individual multi-walled nanotubes versus the voltage on a platinum electrode shifts for electrolytes with different salts, as seen in Figure 5.4(b). $KMnO_4$, a strong oxidizing agent, causes a positive shift relative to $LiClO_4$, while H_3PO_3, a strong reducing agent, causes a negative shift. They suggest that these redox-active molecules are oxidizing and reducing the nanotube, shifting the position of its Fermi level.

A number of experiments have been done to investigate nonspecific protein

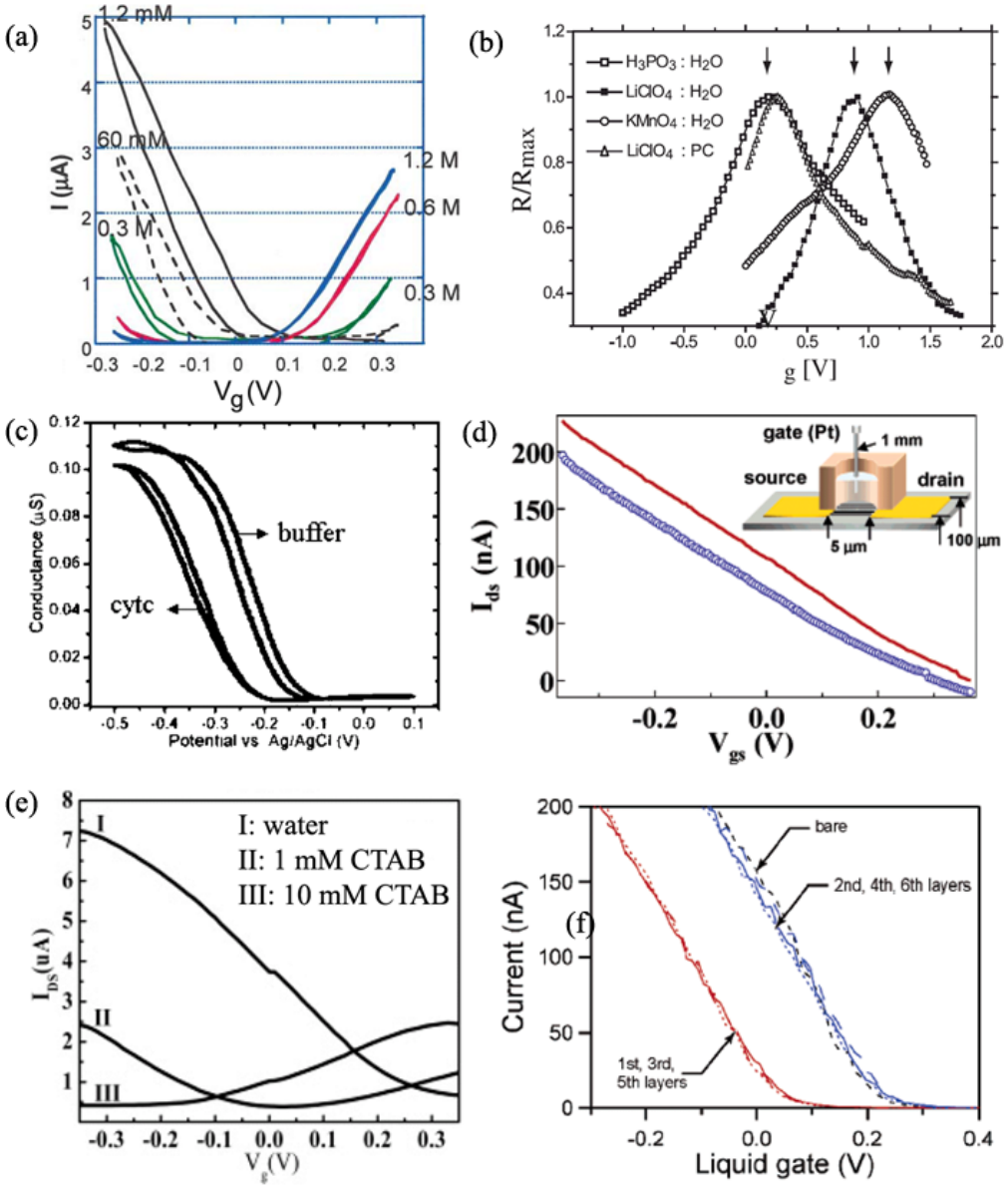

Figure 5.4: Examples of previous work using electrolyte-gated nanotube sensors. Nanotube response is shown for (a) various concentrations of ammonia (Bradley *et al.*, 2003a), (b) different salt solutions (with the response plotted as resistance, not conductance) (Krüger *et al.*, 2003) (c) the protein cytochrome c (Boussaad *et al.*, 2003), (d) the protein hCG, (e) the surfactant CTAB (Fu and Liu, 2005), and (f) alternating layers of positively and negatively charged polyelectrolytes (Artyukhin *et al.*, 2006).

adsorption on electrolyte-gated nanotube transistors.[2] In Figure 5.4(c), we see that the protein cytochrome c (in a 10 mM phosphate buffer background) causes a negative $\Delta V_{\rm th}$ relative to a silver "quasi-reference" wire (Boussaad *et al.*, 2003), and Bradley *et al.* (2004) found that nonspecific streptavidin binding (in a 15 mM phosphate buffer) causes a negative $\Delta V_{\rm th}$ relative to a platinum wire. Both groups attribute these shifts to electrostatic gating of the nanotube by surface charges from adsorbed proteins. Chen *et al.* (2004) have also found that nonspecific protein binding in 10 mM phosphate buffer causes the conductance at a given gate voltage to decrease (see, *e.g.*, Figure 5.4(d)). They also found, however, that except for extremely strongly charged proteins, this change disappeared if they first passivated the Pd or Pd/Au source and drain contacts using a self-assembled monolayer (SAM) of thiols, even though proteins still adsorbed in large numbers on the bare nanotube surfaces. They therefore conclude that the conductance change is caused by electronic effects at the metal-nanotube contact, and not by interactions between the proteins and the nanotube.

The response of transistors made from nanotube thin films to surfactants has been investigated by Fu and Liu (2005), using a silver electrolyte-gate wire. As shown in Figure 5.4(e), the cationic (positively-charged) surfactant cetyltrimethylammonium (CTAB) causes a negative threshold voltage shift, which increases with concentration. This change was not observed for anionic surfactants, but a change was observed if the usually-negative SiO_2 surface was first made positively charged.

[2]The fact that many proteins adsorb strongly to nanotubes also opens up a very different technique for studying biomolecules: using nanotubes as a sample mount to hold difficult-to-crystallize proteins in a diffraction microscopy setup. Since the structure of an individual double-walled nanotube has been reconstructed from its diffraction pattern (Zou *et al.*, 2003), it seems feasible to also image an individual protein, if enough data can be taken before the protein is destroyed by radiation damage (Larrimore, 2005).

Fu and Liu conclude that oppositely-charged surfactants adsorb to the SiO_2 surface, and that these additional charges either electrostatically gate the nanotube or affect the metal-nanotube junctions.

Artyukhin *et al.* (2006) have further investigated altering nanotube conductance through local electrostatic gating by putting alternating layers of positively and negatively charged polyelectrolytes over nanotube transistors (in a 1 mM NaCl background), which cause alternating threshold voltage shifts, as seen in Figure 5.4(f). They assume that this is a local capacitive effect: when a positively charged layer is near the nanotube, a more negative gate voltage must be applied to compensate for this charge. They do not discuss the possible effects of the polyelectrolyte interacting with the platinum source and drain electrodes, but their results do agree very well with a model with no free parameters. They also find that at high background salt concentration (100 mM NaCl), the initial positive polyelectrolyte layer counterintuitively causes a positive threshold voltage shift, but that this agrees with their model when the surface charge of the SiO_2 is taken into account. Their modeling and measurements show that increasing the NaCl concentration causes a negative threshold voltage shift. This effect will be discussed in more detail in Section 6.4.1.

The first work integrating artificial membranes with nanotube transistors in solution has been recently performed by Zhou *et al.* (2007), in a collaboration between the Craighead and McEuen groups at Cornell. They introduced phospholipid vesicles into microfluidic channels above nanotube devices, and these vesicles ruptured and fused to form a uniform supported lipid bilayer. Much of their work involved using fluorescence measurements to probe the interaction of the bilayer and the nanotube, but they also performed some electrical measurements, such as

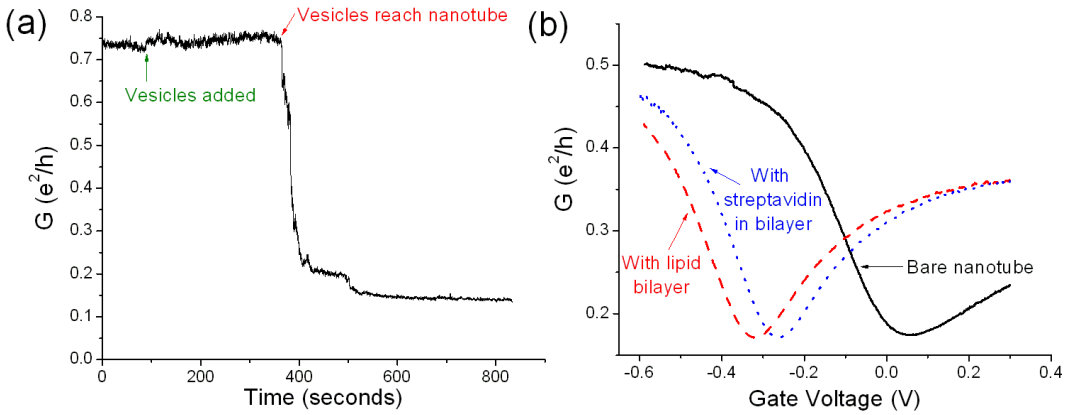

Figure 5.5: Nanotube response to a supported lipid bilayer, from Zhou *et al.* (2007). (a) Conductance versus time as a supported lipid bilayer forms over a nanotube transistor. There was little change in conductance when the vesicles were added to the microfluidic channel over the transistor, but there was a large drop once the vesicles reached the nanotube and formed a bilayer through rupture and fusion. (b) The conductance drop after formation of the bilayer corresponds to a negative threshold voltage shift. In this case, the bilayer was functionalized with biotin and has a net negative charge. When the device was incubated with negatively charged streptavidin (which binds to biotin), the threshold voltage shifted back in the positive direction. A large negative threshold voltage shift was also observed for neutral bilayers (data not shown). Measurements were performed in a 1 μM phosphate buffer solution.

those seen in Figure 5.5. The vesicles caused little change in the nanotube conductance when they were first introduced to the channel, but a huge conductance drop occurred as they formed a bilayer over the nanotube, corresponding to a negative threshold voltage shift. As seen in Figure 5.5(b), the large negative shift observed for positively charged biotin-functionalized bilayers was reduced when negatively-charged streptavidin bound to the bilayer, suggesting that local electrostatic gating is contributing to this signal. But nearly as large of a negative shift was observed when a neutral bilayer was formed over the device, and the origin of this shift remains unclear.

To conclude our review of nanotube sensing in solution, we note that electrolyte-gated nanotube transistors have also been used to sense binding of proteins to nanotubes that have been functionalized with the protein receptors (Besteman *et al.*, 2003; Chen *et al.*, 2003; So *et al.*, 2005). Besteman *et al.* (2003), for example, detected the attachment of glucose oxidase to a nanotube, and then used the functionalized nanotube transistor as an electronic pH sensor. We are more concerned, however, with non-functionalized nanotube sensors.

5.4 Non-Carbon Nanotubes and Nanowires

While we have seen that carbon nanotube transistors have been used for a variety of sensing experiments, carbon nanotubes are not the only one-dimensional object that could be used to probe nanoscale systems. The first non-carbon nanotubes were synthesized from lamellar molybdenum and tungsten disulfides in 1992, and nanotubes have since been synthesized using a variety of materials (including germanium silicide, boron nitride, and transition metal dihalcogenides and oxides) and have been predicted for many more (Ivanovskii, 2002).

The electronic properties of these nanotubes are determined from the band structure of the lamellar material they are formed from. While graphene's zero-gap band structure is unique, with the result that carbon nanotubes can be either metallic or semiconducting, for sensing applications it could be better to have a material that only forms semiconducting nanotubes. Boron nitride nanotubes, for example, are always wide-band-gap semiconductors. The problem with using non-carbon nanotubes for sensing, however, is that they are less structurally stable and much more difficult to synthesize than carbon nanotubes; there has therefore not yet been progress on this front.

Another option for forming one-dimensional sensors is to grow nanowires that have the desired electrical properties, an area of research that has been led for over 15 years by the Lieber group at Harvard. While nanotubes are hollow tubes with atomically-thin walls, nanowires are solid wires that can be grown from a variety of semiconductors, including Si, Ge, Si/Ge, GaAs, and InP (Gudiksen *et al.*, 2002); of these, doped silicon nanowires have been used the most extensively. Silicon nanowires are thicker than nanotubes, with typical diameters of 20–50 nm, but like nanotubes, they have excellent electronic properties (Cui and Lieber, 2001).

While nanowires could theoretically be used in the same ways as the non-functionalized nanotubes described in the previous sections, most of the nanowire sensing experiments thus far have taken advantage of the research that has already been done into chemical modification of oxide surfaces to attach specific receptors to the nanowire surface. In the first nanowire sensing experiment, Cui *et al.* (2001) modified the surface of silicon nanowires to make them sensitive to pH, streptavidin, or calcium ions due to changes in the nanowire surface charge. Nanotubes have also been modified with receptors to detect DNA (Hahm and Lieber, 2004), individual viruses (Patolsky *et al.*, 2004), and cancer markers (Zheng *et al.*, 2005).

In all of these experiments, the analyte was in solution, but there was no electrolyte-gate wire, and it is not clear whether the back gate was grounded or floating. For the experiments with viruses and cancer markers, the Ni metal contacts to the nanowire were passivated with a 50-nm Si_3N_4 coating; for the other experiments, the Al or Ti/Au contacts were exposed to the solution and could have set the electrochemical potential. The observed signal is in all cases attributed to a change in the nanowire surface charge: for a p-type nanowire, a more negative surface charge causes a conductance increase, while a more positive charge causes

a conductance decrease.

The Lieber group has also grown individual live neuron cells such that their axons and dendrites cross over multiple unmodified nanowires, and they were able to cause the neurons to fire and to record these firings as nanowire conductance spikes (Patolsky *et al.*, 2006). Polylysine was patterned over the nanowires to promote adhesion and direct neuron growth, and the cells could be stimulated by applying a voltage pulse to a microelectrode sealed inside (relative to a grounded electrode in the solution outside the cell). The nanowire response is nicely correlated with the intracellular potential peaks, although the origin of this response is not investigated.

5.5 Discussion and Analysis

In this chapter we have examined many examples of chemical and biological sensing with non-functionalized carbon nanotube transistors, as well as some similar experiments with silicon nanowires. It is important to remember that in some cases, such as the experiments of Chen *et al.* (2004) and Tang *et al.* (2006), the change in nanotube conductance was shown to stem from the metal contacts, and not the nanotube itself. When the analyte does affect the nanotube, it can modify the conductance in two general ways: the carrier mobility can be decreased, causing a suppression of conductance at all gate voltages, $G_{\mathrm{new}}(V_{\mathrm{g}}) = G_{\mathrm{old}}(V_{\mathrm{g}})/a$, or the carrier density can be changed, causing a shift in the conductance with respect to gate voltage, $G_{\mathrm{new}}(V_{\mathrm{g}} + \Delta V_{\mathrm{th}}) = G_{\mathrm{old}}(V_{\mathrm{g}})$ (Gruner, 2006). The former is commonly seen in experiments with functionalized nanotube sensors, but we have seen that almost all experiments with non-functionalized nanotubes result in the latter signal.

A change in carrier density in a nanotube can be caused either by electron transfer from the analyte to the nanotube or by capacitive gating, in which the analyte changes the local electric field (Artyukhin *et al.*, 2006). These two cases are illustrated in Figure 5.6. In the first case, when a total charge Δq is transferred to the nanotube, it will cause a threshold voltage shift ΔV_{th} given by $\Delta q = C\Delta V_{\mathrm{th}}$, where C is the combination of the electrostatic and quantum capacitances. In the second case, the analyte changes the carrier density not by directly transferring electrons to or from the nanotube, but by changing the electrostatic potential near the nanotube, which pulls more electrons onto the nanotube from the contacts (or vice versa); this effect changes the nanotube conductance in the same way as gating the transistor through a back gate or through the electrolyte, as discussed in Section 2.3.

While calculating the expected threshold voltage shift due to electron transfer is relatively straightforward, determining when this is the correct explanation is more complicated, and there is no way to distinguish this mechanism from local capacitive gating by simply examining the nanotube response. If the nanotube device is suspended, then the two mechanisms will shift the threshold voltage in opposite directions, as seen in Figure 5.6, so one might simply need to know the analyte's charge. All of the experiments reported in this chapter, however, were performed with nanotubes lying on an SiO_2 surface, and Artyukhin *et al.* (2006) have shown that this complicates the capacitive gating signal. Arguments for what mechanism is dominating have therefore been based on other knowledge of the analyte. For example, the correlation between the shift caused by aromatic compounds in cyclohexane and their Hammett σ constants (which measure their electron donating character) strongly suggests an electron transfer mechanism (Star *et al.*, 2003b).

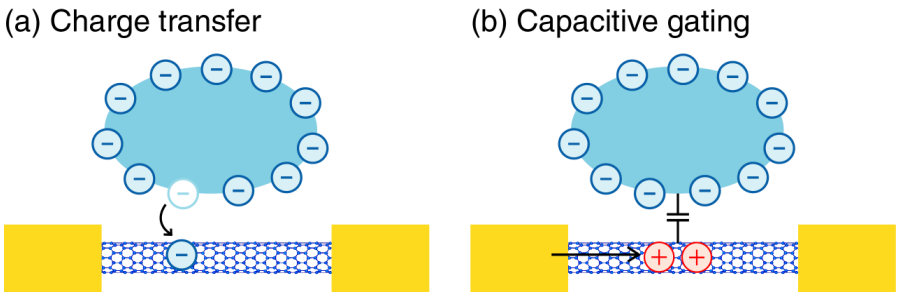

Figure 5.6: Changing nanotube carrier density via charge transfer versus capacitive gating. A charged analyte (negatively-charged, in this illustration) can affect a nanotube by two general mechanisms. (a) Transferring a charge Δq directly from the analyte causes a threshold voltage shift $\Delta V_{\text{th}} = \Delta q/C$, where C is the capacitance between the nanotube and the electrolyte. The negative charge transfer illustrated here will cause a negative threshold voltage shift. (b) Capacitive gating occurs when a charged analyte alters the local electrostatic potential around the nanotube, which pulls more charges onto the nanotube from the contacts. For a nanotube surrounded only by electrolyte (like a suspended nanotube), the more negative potential caused by a negative analyte will result in a positive threshold voltage shift, since a more positive gate voltage is needed to compensate. The direction of the response can be more complicated, however, when the nanotube is sitting on a charged surface like SiO_2, as seen by Artyukhin *et al.* (2006).

Electron transfer has not, however, been conclusively demonstrated between an analyte and a nanotube in an electrolyte solution (as opposed to the low-conductance cyclohexane). In most cases, this explanation was presented simply because it seems plausible: since Krüger *et al.* (2003) were working with strongly redox-active molecules, they assumed that the shifts were due to charge transfer, and since a theoretical calculation has shown that an NH_3 molecule can donate 0.04 electrons to a nanotube, Bradley *et al.* (2003a) use this to explain their NH_3 experiments. Our experiments described in Chapter 7, however, have called these explanations into question (Larrimore *et al.*, 2006). The Nanomix group uses the same electron transfer argument to explain the shift caused by amine-containing streptavidin (Bradley *et al.*, 2004), as do Boussaad *et al.* (2003) in explaining the shift caused by the protein cytochrome c, although in the latter case the agreement they see depends on the assumption that *all* of the protein charge is transferred to the nanotube, which is highly unlikely. These explanations are also weakened by the work of Chen *et al.* (2004), in which they found the conductance change due to adsorbed proteins disappeared if the contacts were passivated.

The other mechanism we have discussed for changing nanotube carrier density is capacitive gating, which was first suggested in a sensing experiment with an electrolyte-gated nanotube by Fu and Liu (2005) in their work with surfactants, since the molecules they used had no free or lone-paired electrons to donate to the nanotube. While this explanation gave them the right qualitative threshold voltage shifts, quantitative agreement was not demonstrated until the work of Artyukhin *et al.* (2006) with polyelectrolyte layers. Their model for the change in electrostatic potential at the surface (which is equivalent to the threshold voltage shift) was obtained by solving the Debye-Hückel equation, Eq. 3.9. If we simplify

this model to a single film of charge σ and thickness d, we can write the expected threshold voltage shift as

$$\Delta V_{\mathrm{th}} = \frac{\lambda_{\mathrm{D}}\sigma/2\epsilon\epsilon_0}{\frac{\epsilon_{\mathrm{f}}\lambda_{\mathrm{D}}}{\epsilon\lambda_{\mathrm{f}}}\sinh\frac{d}{\lambda_{\mathrm{f}}} + \cosh\frac{d}{\lambda_{\mathrm{f}}}}, \tag{5.1}$$

where ϵ and ϵ_{f} are the dielectric constants in the bulk solution and the charged film, ϵ_0 is the vacuum permittivity, and λ_{D} and λ_{f} are the Debye length in the bulk solution and in the film, as given by Eq. 3.11. As the thickness $d \to 0$, this reduces to

$$\Delta V_{\mathrm{th}} = \frac{\lambda_{\mathrm{D}}\sigma}{2\epsilon\epsilon_0}, \tag{5.2}$$

which was used by Zhou *et al.* (2007) to explain their work with supported lipid bilayers.

In summary, capacitive gating has been much more convincingly demonstrated then charge transfer as the mechanism causing a threshold voltage shift in an electrolyte-gated nanotube sensor. Capacitive gating cannot, however, explain all of these sensing results; for example, the charge density of proteins is significantly lower than that of the polyelectrolytes used by Artyukhin *et al.* (2006), so the expected shift due to gating by a protein would be only a few millivolts. We will discuss these explanations further, as well as an alternative explanation for some of these experiments, in Chapters 7-9.

Chapter 6

Device Fabrication and Electrolyte Measurement Setup

Detecting a molecule with a carbon nanotube requires the combination of a number of experimental pieces: we need to connect the nanotube to the macroscopic world electrically, find some method of visualizing it, bring our solution of molecules to the nanotube in a controlled way, and have a method for measuring electrical changes in the nanotube. In this Chapter, we will discuss the details behind each of these pieces. Section 6.1 explains how the nanotube devices were fabricated and electrically contacted, Section 6.2 describes how the nanotubes could be visualized using an atomic force microscope or photocurrent measurements, Section 6.3 details the microfluidic setup used to bring a solution to the nanotube, and Section 6.4 discusses how electrical measurements were made through an electrolyte solution and how to reduce experimental problems like hysteresis and leakage currents.

6.1 Nanotube Device Fabrication

Fabrication of carbon nanotube devices was performed at the Cornell NanoScale Science & Technology Facility (CNF). A detailed recipe for device fabrication is given in Appendix B, and these fabrication steps are illustrated in Figure 6.1.

Two types of substrates were used for the experiments presented in this thesis: doped silicon wafers with a 0.2–1 μm oxide layer and transparent 170-μm thick fused silica wafers. The basic fabrication steps were the same for each substrate; there were only small differences in the processing recipe. Using a photoresist

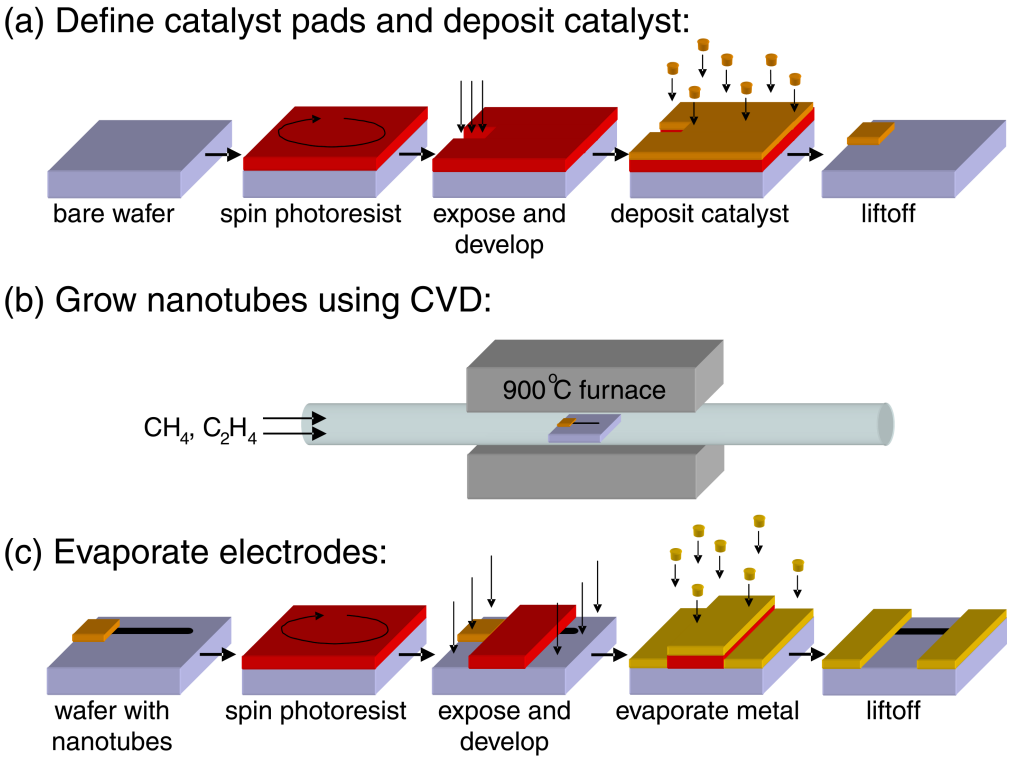

Figure 6.1: Nanotube device fabrication. (a) Catalyst was deposited in photolithographically defined catalyst pads. (b) Nanotubes were grown using a "fast heating" chemical vapor deposition method (Huang *et al.*, 2004). (b) Metal contacts were added lithographically on top of the nanotubes, with the source and drain electrodes separated by 5–15 μm.

mask, iron-based catalyst particles were deposited in defined places on the substrate. Nanotubes were then grown using a "fast heating" chemical vapor deposition method (Huang *et al.*, 2004). Gold, palladium, or platinum contacts were added lithographically on top of the nanotubes, with the source and drain electrodes separated by 5–15 μm. For the devices used for the experiments with DNA, the nanotubes were then suspended by wet-etching (with buffered oxide etch) a 1-μm-wide trench under them in the SiO_2. Critical point drying was necessary after etching to prevent the nanotubes from sticking to the bottom of the trench.

The devices were then electrically characterized using a setup that will be de-

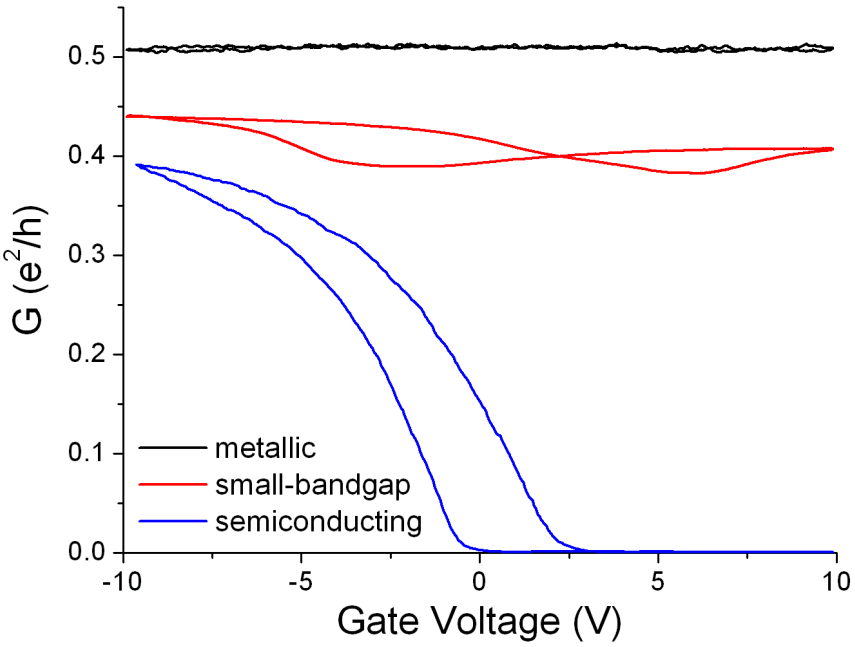

Figure 6.2: G vs. V_g for each of the three varieties of nanotubes: metallic, small-bandgap semiconducting, and moderate-bandgap semiconducting. For many devices, however, the conductance does not follow one of these simple relations to gate voltage, as a result of defects, crossing nanotubes, multiwalled nanotubes, etc., as we will see in Figure 6.4. The hysteresis in these curves will be discussed in Section 6.4.2.

scribed in more detail in Section 6.4.1. Briefly, we applied a 10–50 mV bias to each source electrode and checked for current through the drain electrode. With the Si/SiO_2 devices, we then measured this current as a function of the voltage applied to the back gate (swept from -10 V to 10 V at 500 mV/second) to determine whether the nanotube at that junction was semiconducting or metallic. Figure 6.2 shows examples of the G–V_g curve for each of the three flavors of nanotubes that were discuss in Section 2.2: metallic, small-bandgap semiconducting, and moderate-bandgap semiconducting. Metallic nanotubes were rare among our devices, since the presence of charges on the oxide, defects, and multiple (or mul-

tiwalled) nanotubes would generally lead to some gate dependence. Electrically characterizing the devices using the back gate was not possible for the fused silica devices, which we were only able to gate through an electrolyte.

6.2 Imaging Carbon Nanotubes

Single-walled carbon nanotubes are too small to see in an optical microscope. Large multiwalled nanotubes or nanotube bundles can be seen using differential interference contrast (DIC) or phase contrast microscopy (Prakash *et al.*, 2003), and single-walled nanotubes can be seen with the help of fluorescent molecules (Prakash *et al.*, 2003; Zhou *et al.*, 2007), but no one has optically observed bare individual single-walled nanotubes.

For most of the experiments in this thesis, we have visualized our nanotubes using an atomic force microscope (AFM), which can form a topographic picture of a surface that allows us to determine the nanotube diameters; we will discuss this technique in Section 6.2.1. It is also possible to image a large number of nanotubes more quickly in a scanning electron microscope (SEM), but the cleanliness of the sample is affected by carbonaceous deposits from the electron beam, so this technique is more useful for obtaining statistics about a particular nanotube growth recipe than for characterizing a sample for an experiment. A better method for quickly locating nanotube devices involves measuring the nanotube photocurrent, and we will discuss this technique in Section 6.2.2.

6.2.1 Atomic Force Microscopy

An atomic force microscope (AFM) can form a topographic image of a surface by measuring the force between an oscillating scan tip and the sample. For our

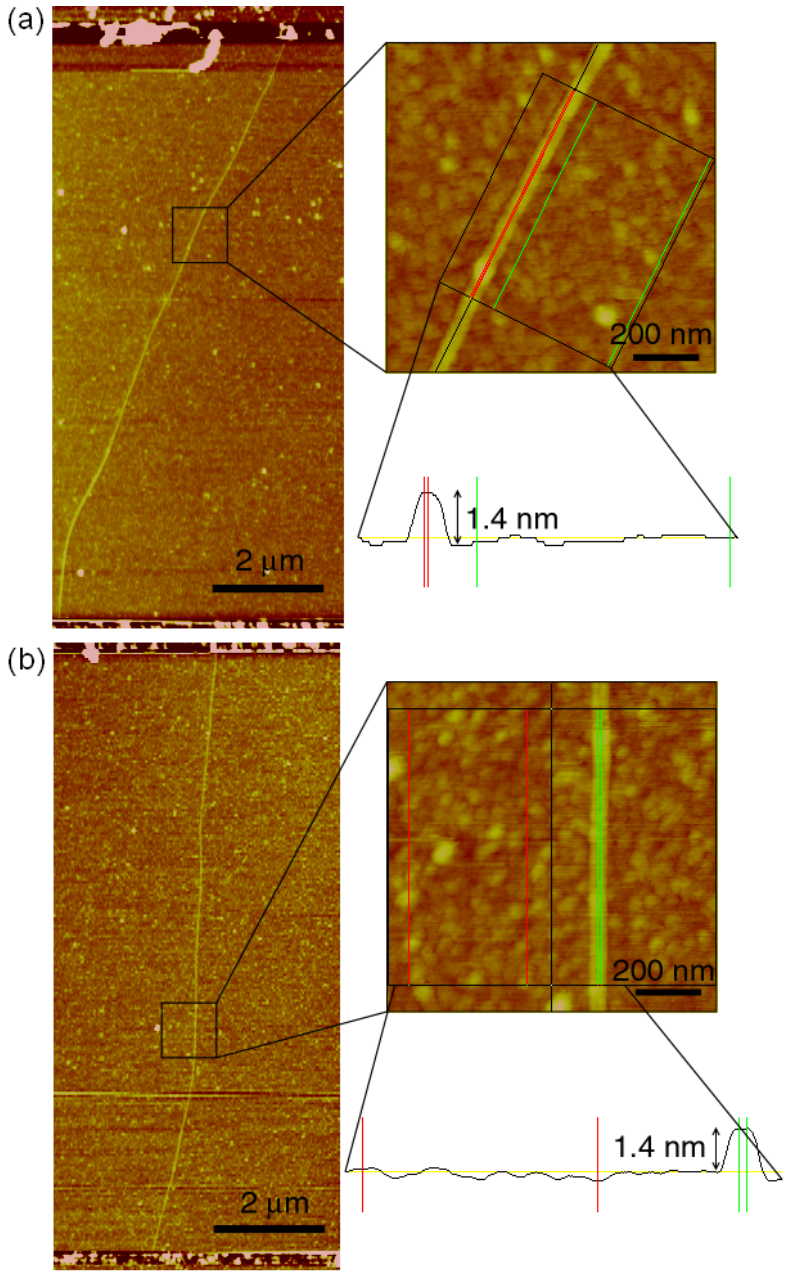

Figure 6.3: Measuring nanotube diameters with an atomic force microscope (AFM). The diameter of both nanotubes, (a) and (b), is about 1.4 nm, and the separation between the source and drain electrodes is about 10 μm.

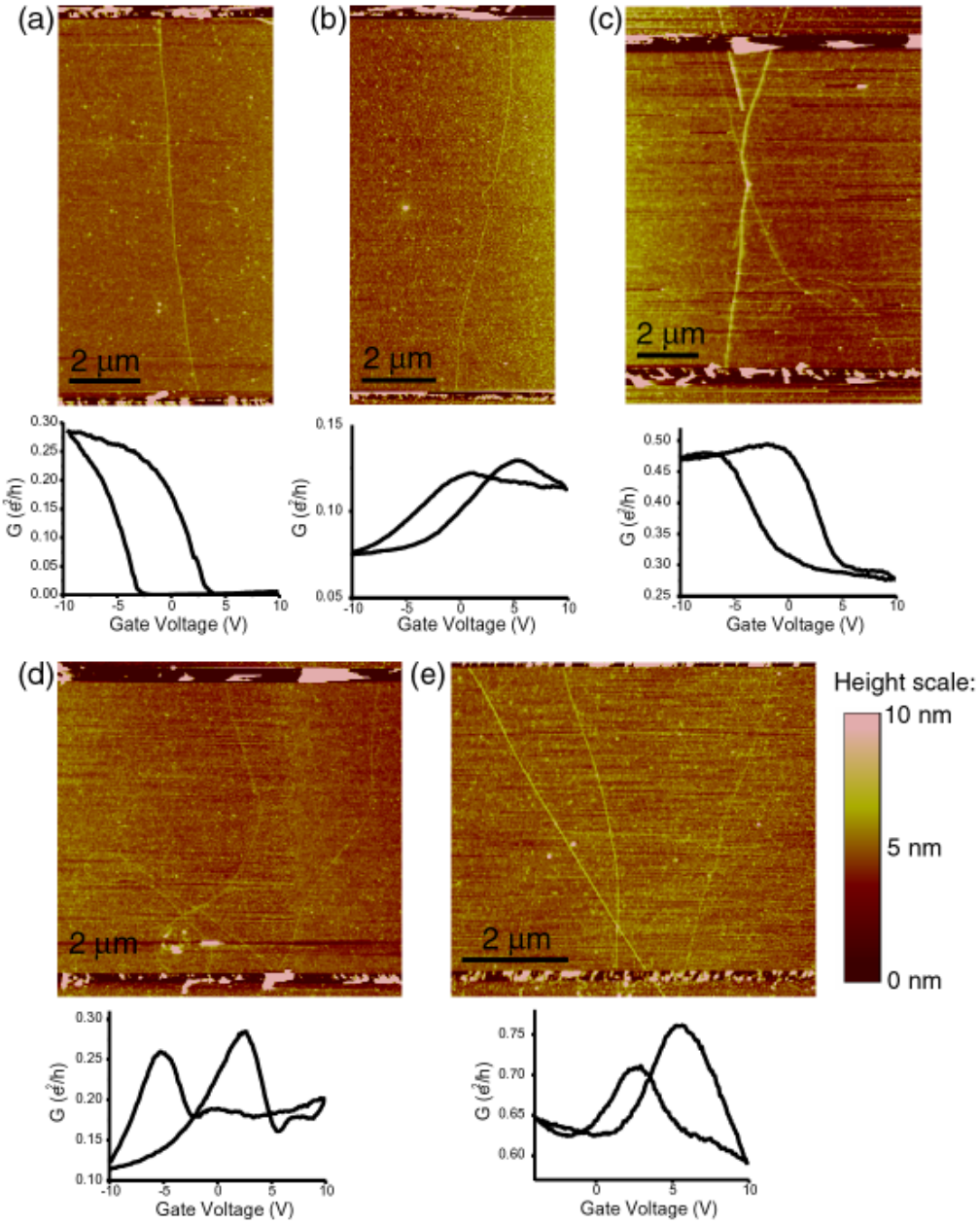

Figure 6.4: AFM images and G–V_g curves for different nanotubes. (a) An individual semiconducting single-walled carbon nanotube. (b-e) Defects, multiple nanotubes, and crossing nanotubes can cause G–V_g curves that deviate from the usual semiconducting behavior, but as long as there is some gate dependence to the conductance, these nanotubes can stil be used for sensing experiments.

measurements, we used a Dimension 3100 AFM from Digital Instruments (now Veeco Instruments) operated in tapping mode. Figure 6.3 shows how the location and diameter of two different nanotubes is determined using an AFM, and Figure 6.4 shows the AFM images along with the conductance versus back-gate voltage curves for five different nanotubes.

Many of our devices, like the one seen in Figure 6.4(a), contain individual semiconducting single-walled carbon nanotubes with G–V_{g} curves that we can easily understand in terms of the discussion of Section 2.3. Many others devices, however, contain multiple nanotubes, nanotubes with defects, or crossing nanotubes, which result in G–V_{g} curves that are more difficult to interpret, such as those shown in Figure 6.4(b-e). As long as these devices show some gate-dependence, however, they are still useful for sensing experiments.

6.2.2 Photocurrent Measurements

While an AFM is able to give very precise information about the nanotube location and diameter, these measurements can also be very time-consuming. The AFM images in Figures 6.3 and 6.4 also provide no information about whether or not the nanotubes imaged are actually electrically connected to the contacts (although an AFM can be used to obtain this information using a technique known as electrostatic force microscopy, or EFM).

A much faster technique for quickly locating the conducting nanotubes between two contacts with submicron resolution is known as scanning photocurrent microscopy, in which a diffraction-limited laser spot is scanned over the device and the photocurrent is measured as a function of position. A photocurrent signal will be observed where local electric fields allow generated electrons and holes to

separate, resulting in a map of the bends in the nanotube band structure. This signal has recently been used to study carbon nanotubes (Balasubramanian *et al.*, 2005; Ahn *et al.*, 2007) and silicon nanowires (Ahn *et al.*, 2005).

Our photocurrent measurements were performed with Jiwoong Park's setup in the Department of Chemistry and Chemical Biology at Cornell, with help from his graduate student Wei Wang and with Nathan Gabor from the McEuen group. We used a 530-nm 10-mW laser that was modulated at 20 kHz, and the photocurrent was measured through one electrode with a lock-in amplifier while we grounded the second electrode. The reflected light intensity was measured simultaneously; since the metal contacts are more reflective than the fused silica substrate, this allowed us to determine the spot location relative to the contacts.

Figure 6.5 shows two examples of suspended nanotube devices imaged with scanning photocurrent microscopy. In both cases, a large signal is seen where each nanotube touches a metal contact, which probably results from a thermoelectric effect: laser heating creates a temperature gradient, and thus a voltage bias, across the nanotube, resulting in a measurable current. This signal could be reduced by using laser with a different wavelength. A smaller photocurrent response is seen along each nanotube, with the most pronounced spots occurring on either side of the trench. This same effect has been observed in other photocurrent measurements of suspended nanotubes, which is indicative of the strong electric field at the trench edges (Ahn *et al.*, 2007).

We have also used scanning photocurrent microscopy to obtain the first images of nanotubes while they are in solution, as seen in Figure 6.6. The photocurrent signal along a nanotube does not change dramatically when the nanotube is wet, suggesting that these spots are more likely to be related to defects in the nanotubes

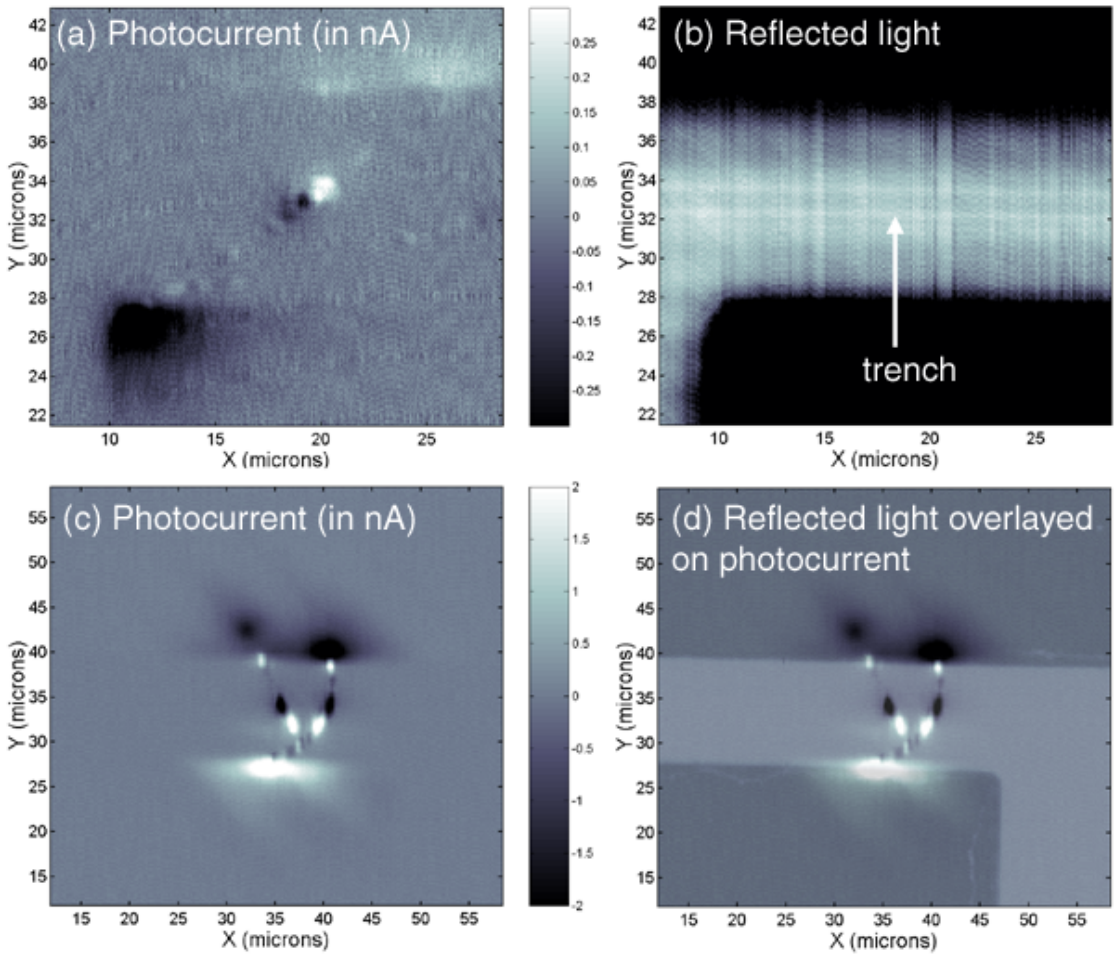

Figure 6.5: Photocurrent imaging of carbon nanotubes. (a) The photocurrent response in nA (for a 10 mW laser) is shown for a suspended carbon nanotube. Large thermoelectric signals are seen at the two metal contacts, and two dots are seen where the nanotube crosses the 1-μm-wide trench. (b) The metal contacts and the trench can also be seen in the reflected light signal, which is measured simultaneously with the photocurrent signal. (c) The two suspended nanotubes seen in this image show a stronger photocurrent response. The trench is 2.4 μm wide. (d) By overlaying the reflected light image on the photocurrent image, we can measure the position of the nanotubes relative to the contact edges.

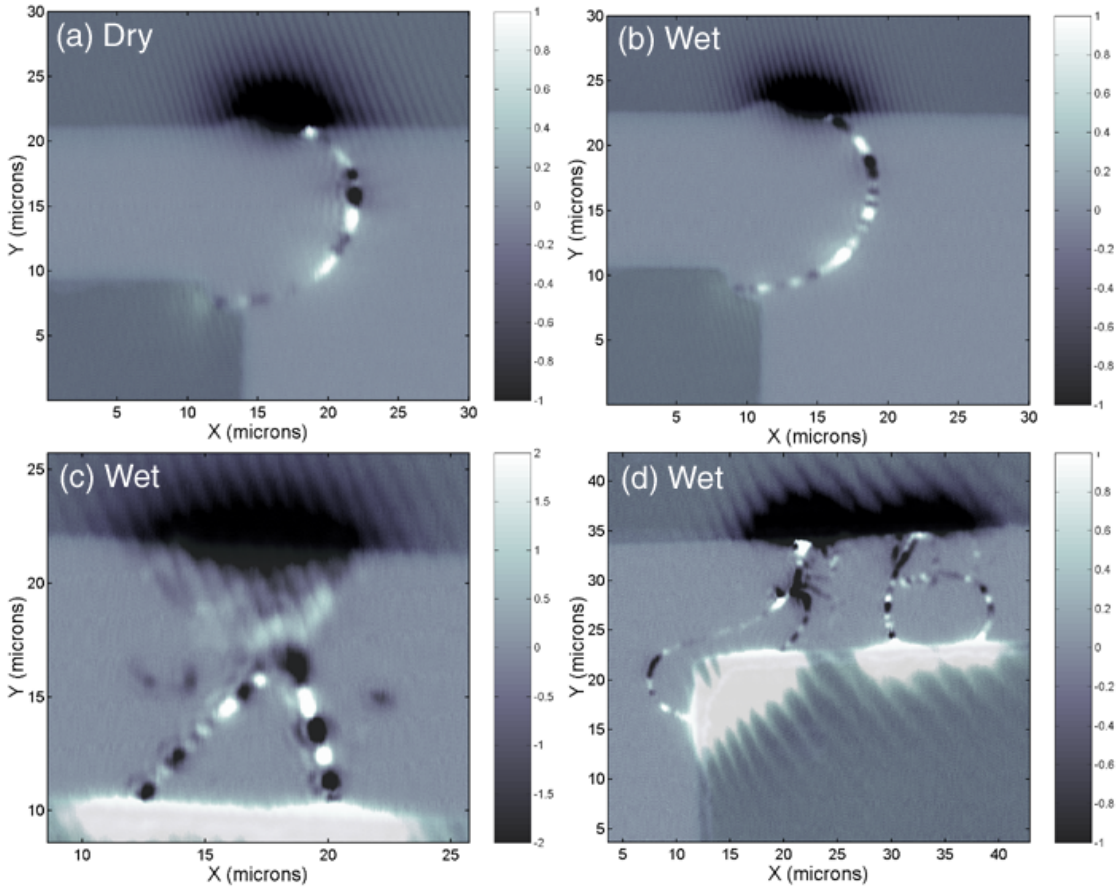

Figure 6.6: Photocurrent imaging of nanotubes in solution. In all of these images, the reflected light signal is overlaid on the photocurrent response (measured in nA), and the 1-μm trench is located between the two contacts. (a) The photocurrent response oscillates from positive to negative along this nanotube, as seen by the bright and dark spots. (b) When the nanotube is covered with 1 mM NaCl, the photocurrent is similar to the response of the dry nanotube seen in (a). (c) and (d) show other examples of nanotubes imaged in 1 mM NaCl.

than to charge variations on the substrate surface that would be screened by the presence of solution. The ability to image nanotubes in solution should prove an exciting tool for use during future experiments. For instance, if a nanotube is lifted off a substrate by a surfactant or a cell, we should see a change in the photocurrent response along the nanotube or a shift in the nanotube position, especially for nanotubes that curve between contacts. The changing photocurrent response will also allow us to determine how various analytes change the electric field around a nanotube. We will discuss these possibilities further in Section 9.2.5.

6.3 Microfluidics and Flow Control

Most of the measurements in this thesis were performed inside a microfluidic poly(dimethylsiloxane) (PDMS) channel. The process of fabricating these channels and setting up the measurements is shown in Figure 6.7.

The channels were made from an etched silicon wafer mold. For these experiments, the channels were 60–100 μm wide and 25–70 μm high. To make the PDMS, we mixed the components from the Sylgard 184 Silicone Elastomer Kit (15:1 base to curing agent), placed the mixture under vacuum to remove air bubbles, poured it in an etched silicon wafer mold, placed it under vacuum again, and then baked it at 70 °C for 70 minutes.

For each experiment, an individual channel was cut from the mold, and holes (0.25–1 mm diameter) were punched in either end. The PDMS was then oxidized in an air plasma (Harrick Scientific Basic Plasma Cleaner) for 30–90 seconds to make the surface hydrophilic by producing polar silanol groups (Ng *et al.*, 2002). The channel was aligned over the nanotubes and sealed to the device. If the nanotube device surface is also oxidized in a plasma, –OH functional groups would

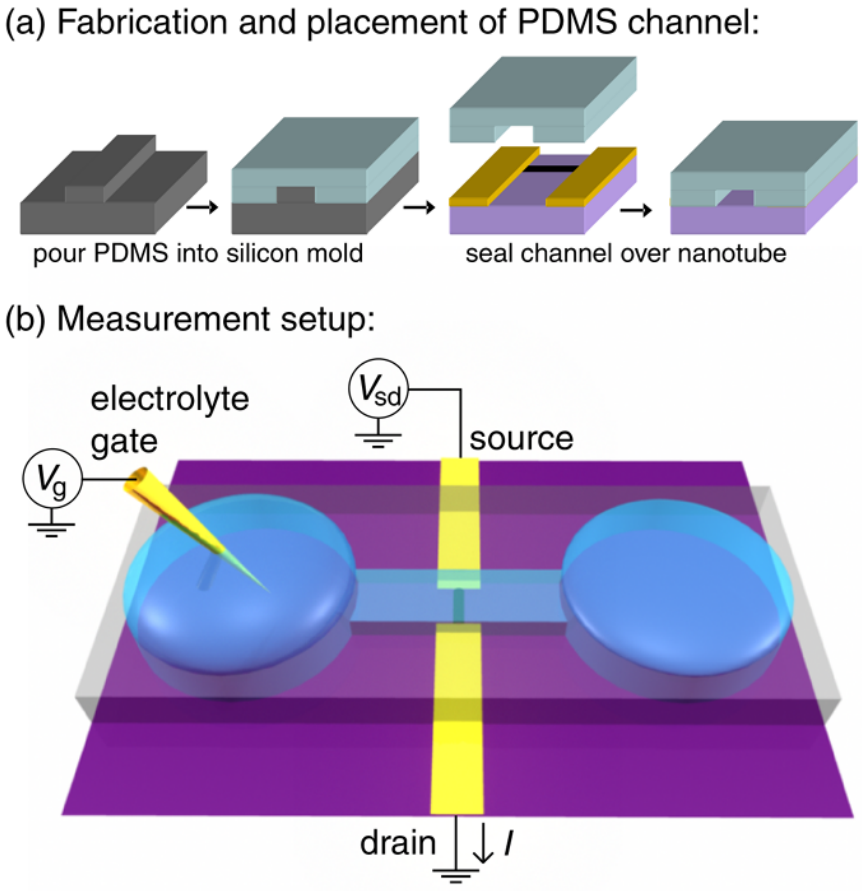

Figure 6.7: Setting up a measurement in a PDMS microfluidic channel. (a) A mold for the channel was formed photolithographically from a silicon wafer. The PDMS ingredients were then poured into the mold and baked until they set. Individual microfluidic channels could be cut from the mold and sealed over the nanotube device. (b) The PDMS channel had a reservoir punched on either end, allowing it to be filled with solution. An electrolyte-gate voltage V_g was applied to a gold wire placed in one of the reservoirs, and the source-drain current through the nanotube was measured while applying a voltage V_{sd}.

form on the oxide surface, which would form irreversible covalent –O-Si-O-bonds when sealed to the PDMS, but since exposure to plasma also destroys the carbon nanotubes, we could only form a weaker, reversible seal. Although this sometimes caused problems with solution leaking underneath the PDMS and breaking the cell, it also meant that the PDMS could be removed after each set of experiments, and each nanotube device could be reused repeatedly. On the fused silica devices, removing the PDMS channel would sometimes also remove parts of the metal contacts, since the adhesion of these contacts was weaker than on the Si/SiO_2 devices.

The simplest method of filling and emptying the PDMS channel was to use large reservoirs punched on either end. The flow direction could then be roughly controlled by varying the relative sizes of the droplets in each reservoir. Interestingly, gravity was not always dominant in controlling the flow direction: if one reservoir had a large droplet and the other had a medium droplet, the solution would flow towards the larger droplet. This is due to the important role of surface tension in microfluidics (see, *e.g.*, Hirsa *et al.*, 2005), and was relevant when the total volume of the two droplets was greater than a sphere with the diameter of one of the holes.

Microfluidic flows can also be controlled using a variety of external fields, including pressure, electric, magnetic, acoustic and capillary forces (Stone *et al.*, 2004). For all of these methods, the open reservoirs depicted in Figure 6.7(b) are not sufficient; microtubing must be used to connect the PDMS channel to an external forcing device, such as a syringe pump or an eletrokinetic pump. In typical microfluidic setups, this is accomplished by plasma-cleaning both the PDMS channel and the bottom cover slide so that they form an irreversible seal, which

is unperturbed by the attachment of the microtubing. Because nanotube devices are destroyed by plasma, however, we could only plasma-clean the PDMS channel, resulting in a weaker and reversible bond that was often destroyed by the stresses involved in inserting tubing. We had more success inserting tubing when the piece of PDMS was wider and thicker, which required larger nanotube device chips (and thus fewer devices per wafer), and when the PDMS was allowed to sit on the nanotube device and form a stronger bond for 10–15 minutes before the introduction of tubing.

When we were able to attach a PDMS channel to an external forcing device, we could obtain excellent control over the flow speed and direction. We had some success with a syringe pump, but the best forcing mechanism was a gravity-feed, in which the free end of the tubing was attached to an open syringe on a lab jack, as illustrated in Figure 6.8. By turning the crank on the lab jack to change the height of the free water surface relative to the channel, we could greatly increase the flow speed, reverse the flow, or stop it completely with a very fast response. For both the gravity-feed system and the syringe pump, it was critical to remove all air bubbles from the system before attaching the tubing, or their compressibility would introduce a time lag in the system.

A better method for attaching tubing to a PDMS channel would be to use a microport, which is a wider channel that can be lowered over a hole in the PDMS and held there using pressure applied by a micromanipulator (MFP Microport Interface from Cascade Microtech), although the forces applied by external pumps can still rupture the interface between the PDMS and the device. We have had the best success when the pump is used only to pull on the fluid in the channel, and not to push.

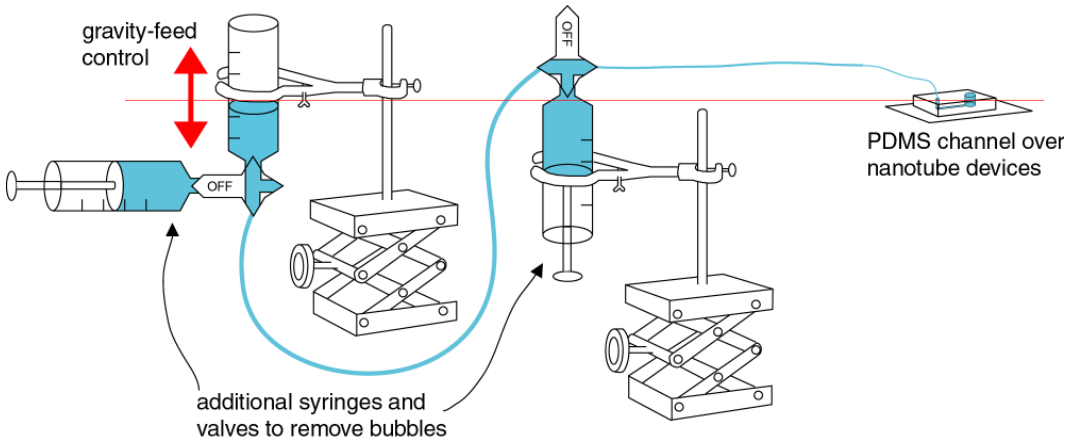

Figure 6.8: Setup for gravity-feed control of microfluidic flows. Tubing placed in the PDMS channel was attached to an open syringe on a lab jack. Raising and lowering the lab jack relative to the channel allowed for excellent control over flow speed and direction. Additional valves and syringes were used to remove air bubbles from the system, which was critical for successful operation.

6.4 Electronic Measurements with Electrolyte Gate

As discussed in Chapter 4 and illustrated in Figure 4.1(a), measuring an electrolyte-gated nanotube transistor involves placing a small voltage V_{sd} on the source electrode on one side of the nanotube and measuring the current through the drain electrode on the other side, all while sweeping the gate voltage V_g on an electrolyte-gate wire. In this section, we will discuss the experimental details of how these measurements are performed. We will also explore two complications of these measurements–hysteresis and leakage currents through the solution–and the methods used to reduce these problems.

6.4.1 Measurement Setup

Figure 6.7(b) shows a schematic of a basic measurement setup in a PDMS channel. The electronic measurements were controlled using the LabVIEW 7.1 program

Measureit 2.2, written by Vera Sazonova (Sazonova, 2006).[1] The program set and read voltages on a digital-to-analog DAQ card (PCI-6221), which was connected to a BNC connector block (BNC-2110), both from National Instruments. The electronic signals were transferred from BNC cables to the nanotube device using probes held by XYZ-300-TR micropositioners from Quater Research, as illustrated in Figure 6.9.

The voltage bias across the nanotube of $V_{\mathrm{sd}} = 5$–50 mV was applied either as a DC voltage using the DAQ card or as a roughly 100 Hz AC voltage (where 5–50 mV is the RMS value) using the output from a SR830 DSP Lock-In Current Preamplifier from Stanford Research. In both cases, the voltage applied at the source was actually 11 times higher than the desired 5–50 mV voltage across the nanotube, since it was typically first passed through a 10:1 voltage divider made with a 10 kΩ and a 1 kΩ resistor. For a DC bias, the current through the nanotube was measured using a current preamplifier from Ithaco (now DL Instruments), while for an AC bias, it was measured using the Stanford lock-in preamplifier. The DC gate voltage was applied using the DAQ card. The differences between the setups for AC and DC electronic measurements are shown in Figure 6.9. A 10 MΩ resistor was sometimes placed between the card and the gold gate wire for protection against large leakage currents, although this resistor can greatly increase the hysteresis of the device, as we will discuss below.

[1]More information about Measureit is available on its website: `http://measureit.team.googlepages.com/home`

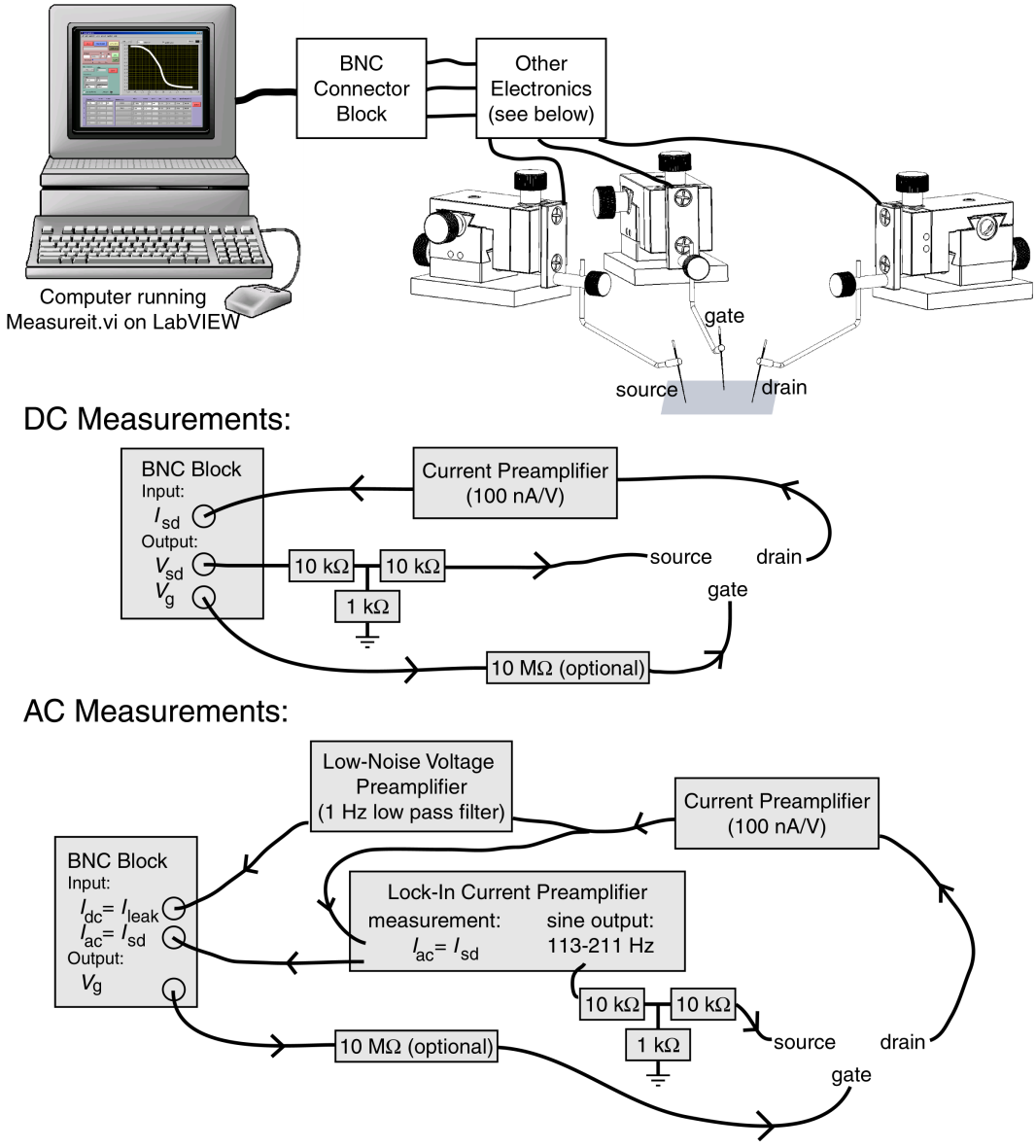

Figure 6.9: Electrical measurement setup. An AC or DC bias voltage, $V_{sd} = 5$–50 mV, was applied to the source while a LabVIEW program was used to sweep the gate voltage V_g and to measure the current I_{sd} passing through the drain. AC measurements also enabled simultaneous measurement of the leakage current I_{leak} between the gate and the drain.

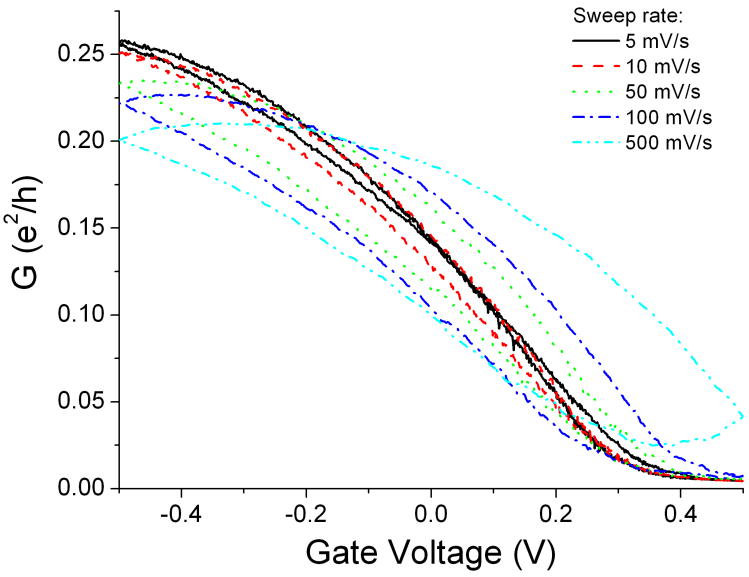

Figure 6.10: Effect of sweep rate on hysteresis, measured in 1 mM NaCl with an AC source-drain bias. The time constant on the lock-in amplifier was 100 ms for all but the 500 mV/second sweep, for which it was 10 ms. We generally used 30 mV/second in our experiments.

6.4.2 Hysteresis

In Section 4.2, we discussed the origin of hysteresis in electrolyte-gated nanotube transistors, and we have seen further examples of hysteretic conductance in some of the figures in Chapter 5 and in the G vs. V_g curves shown earlier in this Chapter. In this section, we will explore how we can reduce the hysteresis in our measurements.

In Figure 6.10, we see that the hysteresis can be decreased by decreasing the rate at which the gate voltage is swept. For the experiments presented in this thesis, we generally used a rate of 30 mV/second, which we chose as a balance between decreasing the hysteresis and decreasing the amount of time required for each G vs. V_g curve to be taken.

The hysteresis also depends on the concentration of ions in the solution. In

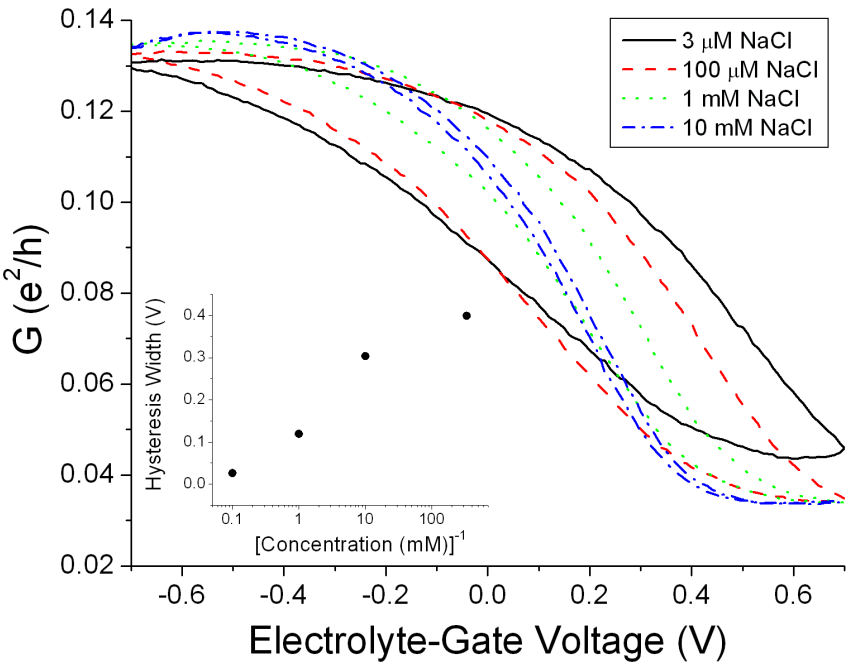

Figure 6.11: Effect of NaCl concentration on hysteresis. The conductance of a nanotube transistor is shown versus the electrolyte-gate voltage for various concentrations of NaCl electrolyte. For all curves, the gate voltage was swept at 30 mV/second and was applied through a 10 MΩ resistor. The inset shows that the width of these curves increases as the concentration decreases. The slight shift to the left as the NaCl concentration increases is due to the changing potential of the SiO_2 surface. Most of the data in Chapter 7 was taken in 1 mM NaCl.

Figure 6.11, we see that the hysteresis can be decreased dramatically by increasing the concentration of NaCl from 3 μM to 10 mM. The source of this hysteresis is the rearrangement of ions in solution: as illustrated in Figure 4.1(b), there is a resistance through the electrolyte solution, and a capacitance and resistance at each electrolyte-metal interface, resulting in a time constant $\tau \sim RC$. The capacitance is a roughly constant $C = (0.1\mathrm{F/m^2})A$ for solutions of different concentration, but the resistance through the solution and the contact resistance should both scale as $R \sim 1/\mathrm{concentration}$, so the time constant should also decrease as we increase

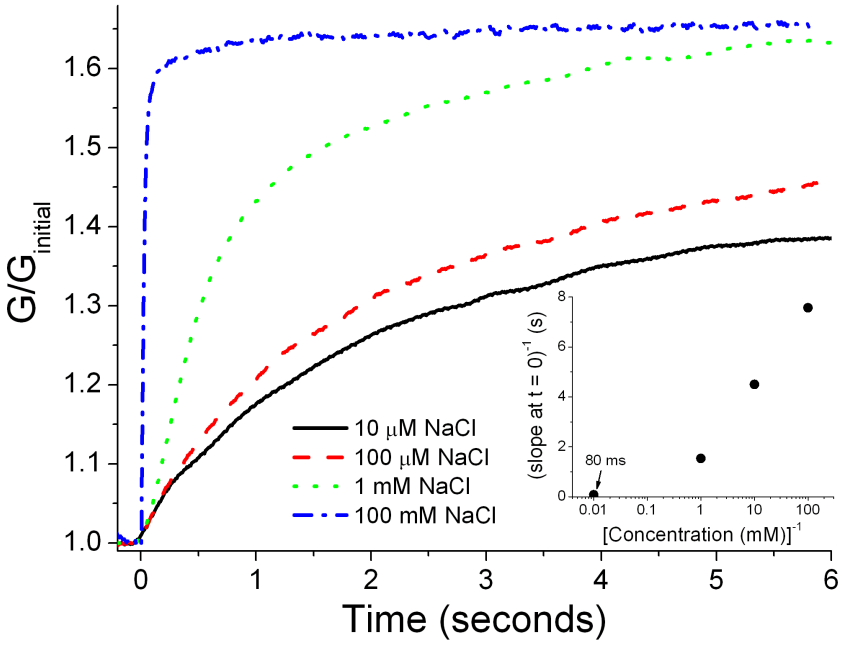

Figure 6.12: Nanotube response time in different NaCl concentrations. At $t = 0$, the gate voltage was switched from $V_g = 0$ to $V_g = -0.3$ V; the change in nanotube conductance is plotted as a function of time. This response is not a pure exponential, but we can extract the time constant for short times by taking the inverse of the slope at $t = 0$; this is plotted in the inset as a function of inverse concentration, and we see that the response time increases as the concentration decreases. These measurements were performed with the AC setup and without the 10 MΩ resistor. The time constant on the lock-in amplifier was 100 ms for all but the 100 mM solution, for which it was 10 ms.

the NaCl concentration. We can observe this in both Figure 6.11 and Figure 6.12, in which the nanotube response to a sudden change in gate voltage is plotted as a function of time.

The insets to Figures 6.11 and 6.12 show that for concentrations up to 10 mM, both the hysteresis width and the time constant at very short times increase roughly logarithmically with the inverse concentration, which is roughly proportional to the resistances in our circuit. Examining Figure 6.12 more closely, we

see that the conductance response is actually a complicated function of time: it is not a simple exponential or a power law. This reminds us that our circuit model in Figure 4.1 is simply an approximation for a more complicated electrochemical system.

Another important effect that we see in Figure 6.11 is that increasing the NaCl concentration causes a slight negative threshold voltage shift, or shift of the curve to more negative gate voltages. As mentioned in Section 5.3, Artyukhin *et al.* (2006) have explained this in terms of the changing potential of the SiO_2 surface. As the NaCl concentration increases, the Debye screening length decreases (see Eq. 3.11), resulting in an increased negative surface charge density as more silanol groups are able to ionize. At the same time, however, the Grahame equation says that the reduced screening length reduces the absolute value of the surface potential, causing it to become less negative. Models and experimental data both show that this second effect is stronger, so as the NaCl concentration increases, a more negative gate voltage is needed to compensate for this less negative surface potential.

These changes in the oxide surface properties must be considered in any sensing experiment. Artyukhin *et al.* (2006) found, for example, that coating their nanotube devices with a polyelectrolyte changed the ionic strength near the oxide surface, resulting in a large shift in the opposite direction as expected at 100 mM NaCl concentration. When the NaCl concentration was reduced to 1 mM, there was little change in ionic strength upon adsorption of the first polyelectrolyte layer, and the shift was in the expected direction. Experiments with suspended nanotube devices or nonionizable substrates would avoid these problems.

6.4.3 Leakage Currents

We saw in Section 4.3 that the leakage currents between the electrolyte-gate wire and the drain electrode are typically much larger for an electrolyte-gated nanotube than for a back-gated one. In this section, we will discuss ways to reduce the leakage currents in our experiments, after first estimating how large a leakage current we might expect.

The leakage current will be a combination of charging currents for the double layer capacitors ($C'_{\rm dl} \approx 0.1$ F/m^2) and charge-transfer currents through the resistors. We note that both $R_{\rm soln}$ and $R_{\rm ct}$ scale inversely with the solution concentration, so that their relative magnitude should remain approximately the same. If we take $\rho_{\rm soln} = 100\ \Omega \cdot$ m (for a 1 mM solution) and $R'_{\rm ct} = 0.1\ \Omega \cdot$ m^2 (a rough estimate based on the work of Li *et al.* (1992) with platinum), then for typical values used in our experiments[2] we would expect $R_{\rm soln}$ to be about 50 MΩ, and $R_{\rm ct}$ to be about 10 MΩ for the drain electrode and about 5 kΩ for the gate electrode. Based on the work of Li *et al.* (1992), the Warburg impedance that is in series with $R_{\rm ct}$ will be roughly equivalent to $R_{\rm ct}$, so the total resistance between the gate and drain is roughly 70 MΩ. When $V_{\rm g} = 0.5$ V, we would thus expect a resistive leakage current of about 7 nA. The value of $R'_{\rm ct}$ will change with electrode material (we typically used gold, not platinum), electrode potential, sweep rate, and solution composition, but this gives us a rough idea of the order of magnitude that we must deal with.

The electrolyte-gate leakage current is plotted in Figure 6.13(a) for several NaCl

[2]The gold electrolyte-gate wires used typically have diameters around 0.5 mm and exposed lengths around 1 mm. The exposed drain electrode area in a PDMS channel is about 10^3 μm^2. Typical cross-sections for our microfluidic channels are 50 μm $\times$ 50 μm.

concentrations, where we see that the leakage current increases with concentration as the solution resistance decreases. Note that the leakage currents are all a few nanoamperes, in agreement with our rough calculation above.

As noted in Section 4.2, although the voltage on a back gate can easily be swept from −10 V to 10 V, the voltage applied to an electrolyte gate must be kept in a much narrower regime, typically within ±0.7 V, to prevent the leakage currents from becoming too large. In addition to overwhelming the signal from the nanotube, large leakage currrents can shift the potential set by the electrolyte-gate wire, leading to inconsistent results. Furthermore, high gate voltages can caused undesired electrochemistry to occur on the electrodes; at 1.23 V, the electrolysis of water into hydrogen and oxygen gas will begin to occur.

Since we generally only want to measure the current through the nanotube, it is necessary to correct for this current by either ensuring that the nanotube current is much higher than this leakage current or separately measuring the leakage current and subtracting it from the data. We kept the leakage current low by limiting the magnitude of V_{g} to under 0.5–0.7 V during our experiments. The leakage current can also be reduced by aligning the PDMS channel at an angle, as in Figure 6.13(b), or passivating the source and drain contacts with self-assembled monolayers of hexadecanethiol, as in Figure 6.13(c). If an AC V_{sd} is used, then this DC leakage current due to the DC V_{g} will not be measured, but there is an AC leakage current that scales with V_{sd} due to conductance through the solution between the source and drain contacts, as shown in Figure 6.13(d).

All of the results thus far have been shown for a gold gate wire, but the kind of wire used will also affect the electrical measurements. Some of our measurements in Chapter 9 were performed with an Ag/AgCl gate wire, and in Figure 6.14 we

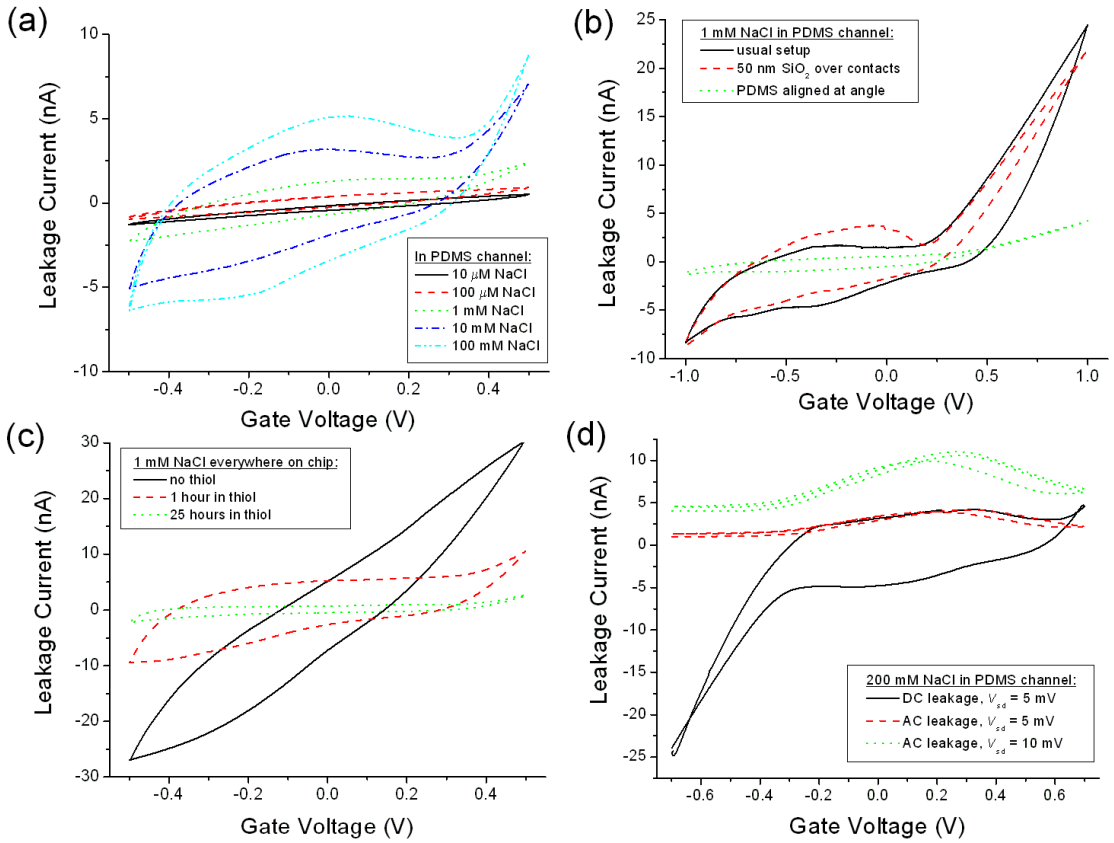

Figure 6.13: Leakage current through the electrolyte solution, measured with the 10 MΩ resistor. (a) The leakage current increases with concentration, as the solution resistance decreases. In this gate-voltage range, the leakage is mainly capacitive. (b) Evaporating SiO_2 on top of the gold source and drain electrodes did not reduce the leakage current, since the sides of the electrodes were still exposed, but it could be greatly reduced by aligning the PDMS channel at an angle to minimize the overlap between the solution and the drain electrode. (c) The leakage current could also be decreased by allowing a self-assembled monolayer of hexadecanethiol to form over the gold electrodes. (d) If an AC V_{sd} is used, the DC leakage current due to V_g will not be measured, but there is an AC leakage through the solution that scales with V_{sd}.

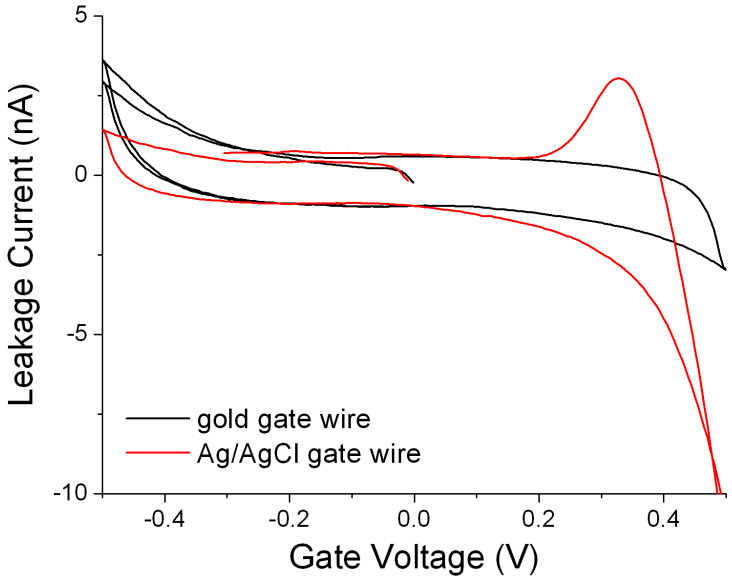

Figure 6.14: Leakage current for Au vs. Ag/AgCl gate wires. The current between the gate wire and the drain electrode is shown for both a solid gold wire and an Ag/AgCl pellet attached to a silver wire (E. W. Wright, Guilford, CT).

compare the leakage currents through the two kinds of wires. Although Ag/AgCl quasireference electrodes are often used to define a ground in electrophysiology experiments, the high leakage currents passing through our gate wires can cause their potential to drift over time, making them more problematic for our experiments.

Finally, we note that although the optional 10 MΩ resistor shown in Figure 6.9 can increase the hysteresis, this resistor also prevents these leakage currents from increasing too rapidly. This is important when performing initial measurements of back-gated nanotube devices, in case the back gate and drain were accidentally shorted together, but it is generally unnecessary for experiments with electrolyte-gated devices.

Chapter 7

Probing Electrostatic Potentials in Solution

The processes of oxidation (loss of electrons) and reduction (gain of electrons) are the basis of many chemical reactions, and the study of these oxidation-reduction (redox) reactions is the focus of the field of electrochemistry. A molecule that easily undergoes oxidation and reduction is known as redox-active. Redox reactions are involved in corrosion, batteries, and fuel cells, and they are also ubiquitous in biological systems. In our cells, for example, glucose is oxidized to store energy in ATP and NADH, and the NADH is oxidized in mitochondria to store energy in a chemical gradient. Chloroplasts use a different electron transfer chain in photosynthesis. Redox enzymes catalyze and control these reactions, causing them to happen quickly while still storing much of the released energy for the cell (Alberts *et al.*, 2002).

Electrochemists have developed a variety of tools for investigating and characterizing redox-active molecules in solutions. These techniques generally depend on the measurement or control of potential and current. Potentiometric techniques probe the electrochemical potential $\mu_{\mathrm{e-c}}$, which, as discussed in Section 3.1.3, is composed of the electrostatic (ϕ) and chemical (μ_{c}) potentials:

$$\mu_{\mathrm{e-c}} = e\phi + \mu_{\mathrm{c}}. \tag{7.1}$$

Amperometric techniques (*i.e.*, measurements of current) provide information related to reaction rates. The combination of current and potential measurements results in powerful techniques, such as cyclic voltammetry, for determining reac-

tion rates (current) as a function of driving force (applied potential) (Bard and Faulkner, 2001).

When a working electrode like a gold or platinum wire is placed in an electrolyte solution, it sets the electrochemical potential $\mu_{\mathrm{e-c}}$. The chemical potential μ_{c} is determined by redox-active molecules in the solution according to the Nernst equation, which is derived in Appendix C. For a single-electron redox couple ($\mathrm{Ox} + e^- \rightarrow \mathrm{Red}$) the Nernst equation is

$$\frac{\mu_{\mathrm{c}}}{e} = E^{0'} + \frac{k_{\mathrm{B}}T}{e} \ln \frac{[\mathrm{Ox}]}{[\mathrm{Red}]}, \tag{7.2}$$

where k_{B} is Boltzmann's constant, T is the temperature, e is the electron charge, and $E^{0'}$ is known as the formal potential, which is the chemical potential at $[\mathrm{Ox}]/[\mathrm{Red}] = 1$. The electrostatic potential ϕ in the solution is then determined by the difference between $\mu_{\mathrm{e-c}}$ (set by the metal electrode) and μ_{c} (set by the redox-active molecules). Electrochemists are also able to set or measure the electrostatic potential directly using a reference electrode, in which the electrode surface is protected from the redox-active molecules, *e.g.* by a porous frit that only allows smaller ions to pass through.

Reference electrodes are useful for measuring bulk solutions of redox-active molecules, but since it is difficult to find a true reference electrode with a width smaller than about 5 mm, it is not easy to perform electrochemical measurements on very small solution volumes. In recent times, there has been a drive towards ultraminiaturization of electrochemical systems for sensor applications and for studying small collections of molecules where the detection of discrete events might be possible, but electrochemists still lack the tools for performing many of these experiments. As we have seen throughout this thesis, carbon nanotubes could be the ultimate nanoscale electrodes, with excellent electronic properties, the ability to

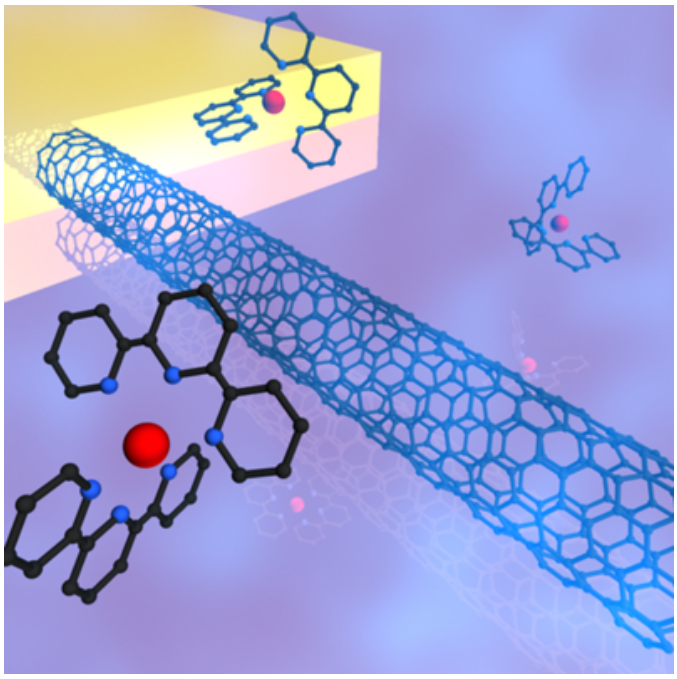

Figure 7.1: Artistic rendering of a carbon nanotube transistor in a solution of the redox-active molecules Co(2, 2′:6′, 2″-terpyridine)$_2^{+2}$.

operate in aqueous environments, and diameters of only a nanometer. Nanotubes are therefore promising candidates for performing nanoscale electrochemistry experiments, and the use of individual nanotubes as working electrodes has been demonstrated (Campbell *et al.*, 1999; Heller *et al.*, 2005).

In the experiments described in this chapter, we explored the response of electrolyte-gated single-walled carbon nanotube transistors to redox-active transition metal coordination complexes, a situation illustrated in Figure 7.1. As discussed in Section 5.3, carbon nanotubes have also been shown to be excellent sensors when used as transistors in an electrolyte environment. In most of these experiments, the analyte caused a shift in the gate-voltage dependence of the nanotube conductance, which was attributed to charge transfer from adsorbed molecules to the nanotube or a local electrostatic gating effect. Working with

redox-active molecules of a defined chemical potential, however, shows us that this explanation may not always be accurate.

We found that the nanotube acts similarly to a reference electrode and senses changes in the electrostatic potential of the solution. As we see from Eq. 7.1, these changes are directly related to the chemical potentials of the redox-active molecules, as measured in a traditional electrochemical cell. We show that although there may be some local interaction between the molecules and the nanotube transistor, the primary source of the signal is the electrochemical interaction between the molecules and the electrolyte-gate wire. This previously neglected effect is very important for interpreting the results of other nanotube sensing experiments in solution.

Before we discuss the response of our nanotubes to the redox-active molecules, we will begin in Section 7.1 with a description of the molecules used and the techniques for doing traditional electrochemical measurements. Then, in Section 7.2, we briefly describe the setup for the nanotube measurements before showing the nanotube response to redox-active molecules in Section 7.3. In Section 7.4, we combine these nanotube measurements with some traditional electrochemical measurements, which helps us interpret our results in Section 7.5. Section 7.6 contains some further results looking at how the nanotube response varies with the concentration of the redox-active molecules. Finally, in Section 7.7, we propose an experiment in which a nanotube could be used to measure changes in the oxidation state of even smaller solution volumes.

The work presented in this chapter was performed in collaboration with Suddhasattwa Nad, from Héctor Abruña's group in the Cornell Department of Chemistry and Chemical Biology, and most of the results in this chapter have been

published in Larrimore *et al.* (2006).

7.1 Electrochemical Molecules and Measurements

In this section, we will describe the redox-active molecules used in the experiments presented in this chapter, and we will discuss the standard tools used by electrochemists to learn more about a bulk solution of redox-active molecules. For example, when molecules that are initially in only an oxidized (or reduced) state are dissolved in solution, many of them will become reduced (or oxidized), and we would like to know the actual ratio of oxidized to reduced molecules, [Ox]/[Red]. We would also like to change this ratio. Here, we will show these kinds of measurements for the molecules that we studied with our carbon nanotube devices.

The preparation of the redox-active molecules as well as all the measurements in this section were performed by Suddhasattwa Nad.

7.1.1 Redox-active Molecules

Although the [Ox]/[Red] ratio for all of our solutions was generally within a few orders of magnitude of unity, the molecules were initially either entirely oxidized or entirely reduced before they were dissolved in solution. The molecules initially in an oxidized state were $[Co(bpy)_3]Cl_3$ (where bpy is $2,2'$-bipyridine), $K_3[Fe(CN)_6]$ (potassium ferricyanide), and $[Ru(NH_3)_6]Cl_3$ (hexaammineruthenium(III) chloride); the molecules initially in a reduced state were $[Co(tpy)_2]Cl_2$ (where tpy is $2,2':6',2''$-terpyridine), $[Co(atpy)_2]Cl_2$ (where atpy is $4'$-amino-$2,2':6',2''$-terpyridine), $[Co(bpy)_3]Cl_2$, $Na_4[Fe(CN)_6]$ (sodium ferrocyanide), and $[Ru(NH_3)_6]Cl_2$ (hexaammineruthenium(II) chloride). Table 7.1 lists these molecules and their formal potentials; we will describe how the formal potentials are

Table 7.1: Redox-active molecules used for nanotube electrochemistry experiments

Reduced Molecule	Oxidized Molecule	$E^{0'}$ (V)
$[Co(atpy)_2]Cl_2$		-0.14
$[Ru(NH_3)_6]Cl_2$	$[Ru(NH_3)_6]Cl_3$	-0.1085
$[Co(tpy)_2]Cl_2$		0.093
$[Co(bpy)_3]Cl_2$	$[Co(bpy)_3]Cl_3$	0.1405
$Na_4[Fe(CN)_6]$	$K_3[Fe(CN)_6]$	0.1815

obtained in Section 7.1.2.

$K_3[Fe(CN)_6]$ (Fisher Scientific, ACS grade), $Na_4[Fe(CN)_6]$ (Matheson, Coleman, and Bell, 99% min. assay), $[Ru(NH_3)_6]Cl_3$ (Aldrich Chemical, 95% assay), and $[Ru(NH_3)_6]Cl_2$ (Aldrich Chemical, 99.9+% assay) were used as obtained without further purification. To prepare $[Co(atpy)_2]Cl_2$, 4′-amino-2, 2′:6′, 2″-terpyridine was prepared from 4′-chloro-2, 2′:6′, 2″-terpyridine (Aldrich Chemical) using previously reported procedures (Mutai *et al.*, 2001). $[Co(atpy)_2]Cl_2$, $[Co(tpy)_2]Cl_2$, and $[Co(bpy)_3]Cl_2$ were then synthesized according to published procedures (Hogg and Wilkins, 1962).

7.1.2 Cyclic Voltammetry

All of our standard electrochemistry measurements were made using a technique called cyclic voltammetry. We measured cyclic voltammograms in a standard electrochemical cell, as illustrated in Figure 7.2. The current between a platinum working electrode and a platinum counter electrode was measured as a function of the voltage of the working electrode relative to a Ag/AgCl reference electrode. The reference electrode was filled with a NaCl solution that is separated from

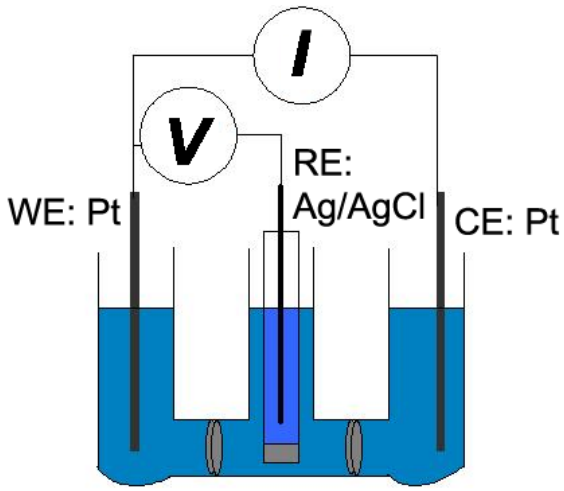

Figure 7.2: Standard electrochemical cell for cyclic voltammetry. The current between the platinum working electrode (WE) and counter electrode (CE) is measured as a function of the voltage of the WE versus the Ag/AgCl reference electrode (RE). The RE is filled with a NaCl solution that is separated from the analyte by a porous frit that allows small Na^+ and Cl^- ions to pass through but prevents the larger redox-active molecules from contaminating the RE. The three sections of the electrochemical cell here are also separated by frits (shown in grey), which are necessary for bulk electrolysis.

the analyte by a porous frit that allows small Na^+ and Cl^- ions to pass through but prevents the larger redox-active molecules from contaminating the Ag/AgCl electrode.

An example cyclic voltammogram is shown in Figure 7.3 for $[Co(tpy)_2]Cl_2$, where tpy is $2,2':6',2''$-terpyridine). As the potential difference between the working and reference electrodes increases, the measured current also increases as oxidation of the molecules occurs at the working electrode. As the potential passes the oxidation potential, the current begins to decrease as the reduced molecules near the working electrode are depleted. When the potential is reversed, the molecules are again reduced, taking electrons from the working electrode and causing a neg-

ative current through it. The formal potential for the redox-active molecule is the average potential between the two peaks; for $[Co(tpy)_2]Cl_2$, the formal potential is $E^{0'} = 93$ mV. A list of the formal potentials for all the redox-active molecules used in these experiments is given in Table 7.1.

To measure the ratio of oxidized to reduced molecules, [Ox]/[Red], we took cyclic voltammograms with a 25 μm platinum ultramicroelectrode as the working electrode; an example is seen in Figure 7.4. Because of the small size of the working electrode, the oxidation and reduction currents are limited by diffusion of the redox-active molecules to the electrode surface, which means that the current is related to the concentration of molecules available: the oxidation current is limited by the number of reduced molecules in solution, and the reduction current is limited by the number of oxidized molecules. Assuming that the rate of diffusion of the oxidized and reduced species is the same, which is a good approximation for the molecules we used, [Ox]/[Red] is simply the ratio of the reduction current to the oxidation current (Bard and Faulkner, 2001).

In the cyclic voltammograms discussed thus far, the number of molecules that are oxidized or reduced is small compared to the total number in solution, and so the measurement does not affect the bulk solution properties. We could change the [Ox]/[Red] value, however, by performing bulk electrolysis using a working electrode that is coiled to give it a very large surface area (Bard and Faulkner, 2001). To oxidize a solution, the potential of the working electrode was set to a large value relative to the reference electrode for several minutes, and the solution was stirred to maximize the number of reduced molecules reaching the electrode surface. Although oxidation at the working electrode is always accompanied by reduction at the counter electrode, these electrodes were separated by porous frits

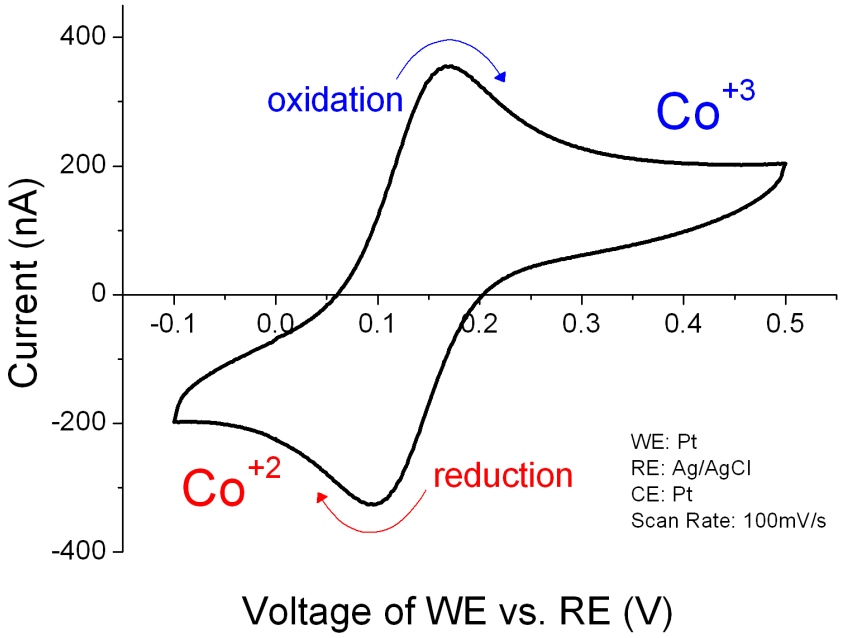

Figure 7.3: Standard cyclic voltammogram, shown for $[Co(tpy)_2]Cl_2$. The current between the platinum working and counter electrodes is measured as a function of the voltage of the working electrode relative to the Ag/AgCl reference electrode, which is swept at 100 mV/s. The current increases as the potential is swept upwards and oxidation of the redox-active molecule occurs at the working electrode, and then decreases as the reduced molecules near the electrode are depleted. When the potential is reversed, the molecules are reduced again, and a negative current is observed through the working electrode. The formal potential $E^{0'}$ is the average between the two peaks, which are separated by $k_B T/e \approx 59$ mV for a reversible one-electron process (Bard and Faulkner, 2001). For $[Co(tpy)_2]Cl_2$, we can measure from this plot that $E^{0'} = 133$ mV versus our reference electrode, which translates to $E^{0'} = 93$ mV versus a standard Ag/AgCl reference.

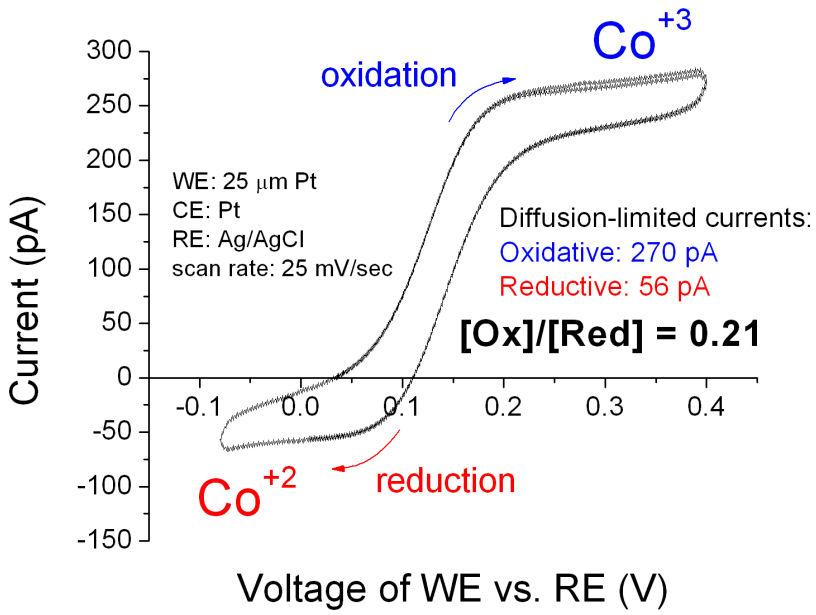

Figure 7.4: Determining [Ox]/[Red] from a cyclic voltammogram using an ultramicroelectrode. The [Ox]/[Red] ratio for a solution of $[Co(tpy)_2]Cl_2$ was determined from the limiting currents measured from a cyclic voltammogram at a sweep rate of 25 mV/s, using a 25 μm Pt working electrode, a large-area Pt counter electrode, and a Ag/AgCl reference electrode. Oxidative and reductive diffusion-limited currents in this example were 270 pA and 56 pA, respectively, giving an [Ox]/[Red] ratio of 0.21.

to prevent the solutions from mixing, as seen in Figure 7.2. Reduction of the solution was accomplished by the reverse process: setting the potential of the working electrode to a low value so that molecules are reduced at its surface. After this bulk electrolysis process, the new [Ox]/[Red] ratio was determined using an ultramicroelectrode; three cyclic voltammograms of the same solution in different oxidation states are shown in Figure 7.5.

7.2 Experimental Setup for Nanotube Measurements

Now that we have discussed the different types of redox-active molecules and the standard electrochemical techniques for studying them, we will describe the measurement setup used for our experiments with carbon nanotubes. Figure 7.6 shows a schematic of this setup. The nanotube devices were fabricated on Si/SiO_2 wafers as described in Chapter 6, and a PDMS channel (60 μm wide and 25 μm high) was sealed over the device and initially filled with an aqueous NaCl solution, which was also used as the supporting electrolyte for the redox-active molecules.

The nanotube transistor was gated through the electrolyte solution by applying a voltage V_g to a gold electrolyte-gate wire placed in one of the large reservoirs. A 10–50 mV source-drain bias was applied across the nanotube transistor, and the conductance was measured while sweeping the gate voltage, as discussed in Section 6.4.1. Using a high-impedance voltmeter, we could also measure the electrostatic potential in either reservoir using a Ag/AgCl reference electrode or the electrochemical potential using a second gold wire.

The redox-active molecules listed in Table 7.1 were dissolved at varying concentrations in the NaCl supporting electrolyte, and were then introduced into one of the PDMS reservoirs while measuring the conductance of the nanotube.

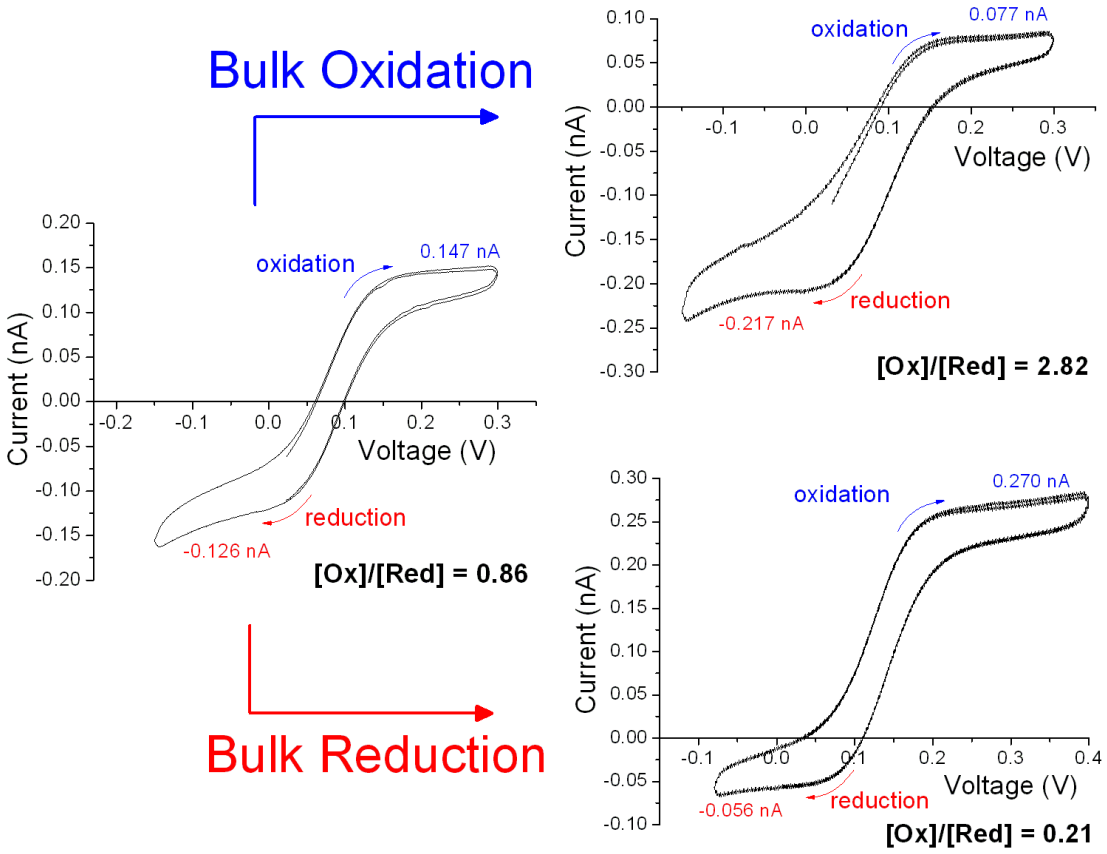

Figure 7.5: Changing [Ox]/[Red] with bulk electrolysis. Three cyclic voltammograms taking with an ultramicroelectrode are shown for the same solution of $[Co(tpy)_2]Cl_2$ in different oxidation states. The [Ox]/[Red] ratio was changed by performing bulk electrolysis with a large-surface-area working electrode before each of these microelectrode measurements. The electrodes and sweep rate are the same as in Figure 7.4.

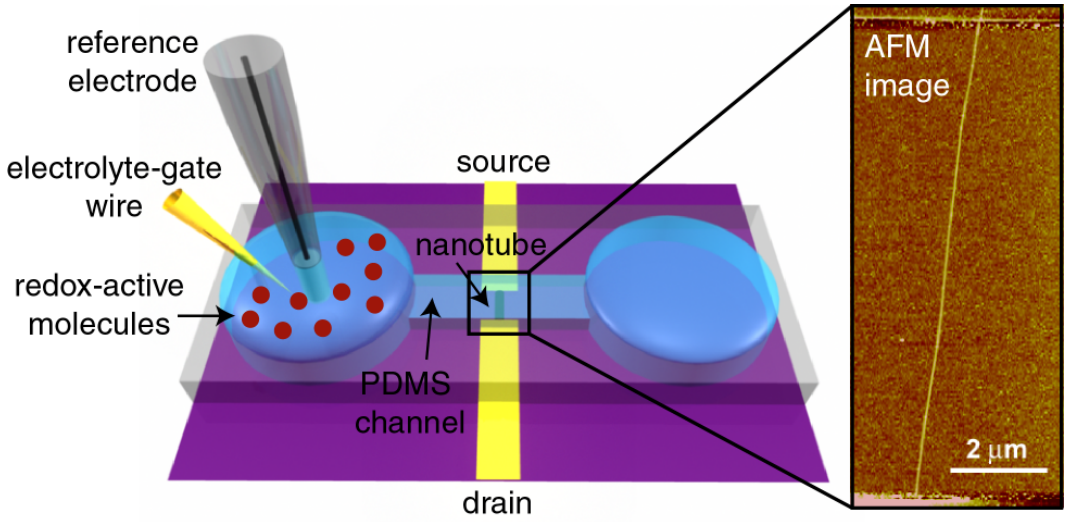

Figure 7.6: Measurement schematic for redox-active molecule measurements, including an AFM image of a single-walled carbon nanotube (diameter = 2.6 nm). The microfluidic PDMS channel that was sealed over the nanotube transistor had two large reservoirs (1 mm diameter) on either side, which were used to add or remove solution from the channel. An electrolyte-gate voltage V_g was applied to a gold gate wire placed in one of the reservoirs, and we measured the source-drain current through the nanotube while applying a 50 mV bias. Using a high-impedance voltmeter, we could also measure the electrostatic potential with a Ag/AgCl reference electrode.

7.3 Device Response to Redox-Active Molecules

Figure 7.7 shows the response of the nanotubes to redox-active molecules at a fixed electrolyte-gate voltage of $V_g = 0$. The conductance dramatically increases or decreases upon the addition of each molecule solution, with a time constant around 1 second. The direction of the change is not correlated with the overall charge of the molecule: both positively charged and negatively charged molecules cause both an increase and a decrease. It is correlated, however, with the oxidation state of the molecules: oxidizing molecules cause an increase in the conductance, while reducing molecules cause a decrease.

This change at $V_g = 0$ is due to a translation in the full G vs. V_g response, as shown in Figure 7.8 for the ferri/ferrocyanide redox couple. The translation can be described as a shift in the threshold voltage V_{th} at which the nanotube starts conducting. We see that the conductance change in Figure 7.7 is due to the direction of this translation: oxidizing molecules cause a positive shift, and reducing molecules cause a negative shift.

The method used to measure the threshold voltage shift is shown in Figure 7.9. The initial G-V_g curve in NaCl and the curve after adding the redox-active molecule are plotted on different horizontal axes, and the axes are shifted until the curves appear superimposed. Hysteresis is observed in both curves, as described in Section 6.4.1; these measurements were performed with V_g applied through the 10 MΩ resistor. Throughout the remainder of this chapter, we show only the negative sweep direction for clarity, although both directions were used when calculating ΔV_{th}.

Figure 7.10 shows that we see roughly the same threshold voltage shift if the redox-active molecules are near the nanotube as we do if they are confined by the

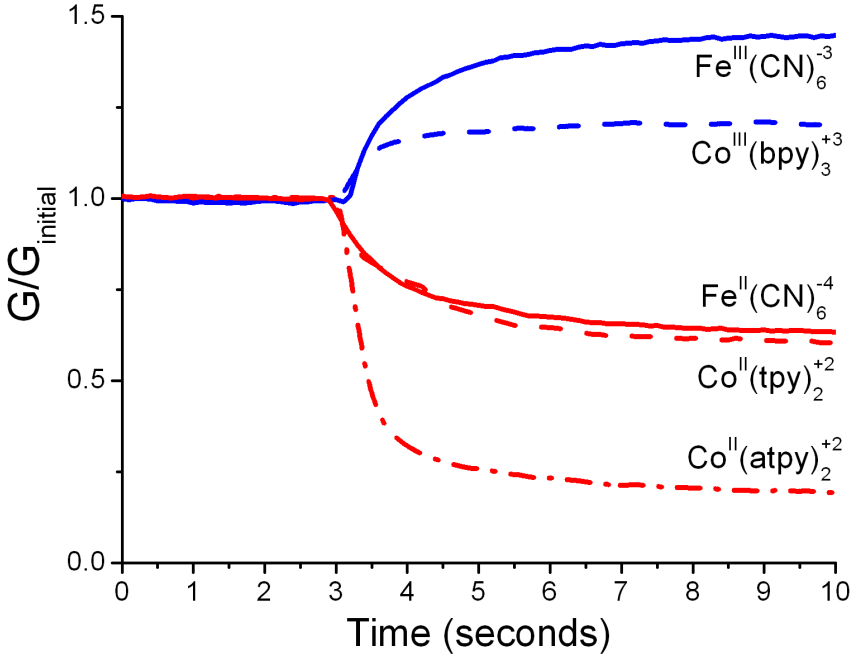

Figure 7.7: Conductance versus time during addition of redox-active molecules to the microfluidic channel. Adding 1 mM solutions of different redox-active molecules, all with the same 1 mM NaCl supporting electrolyte, causes the nanotube conductance to change dramatically at a fixed gate voltage ($V_g = 0$). The conductance began to change immediately upon adding the molecules, which occurred around 3 seconds. Oxidized molecules ($K_3[Fe(CN)_6]$ and $[Co(bpy)_3]Cl_3$) cause the conductance to increase, while reduced molecules ($Na_4[Fe(CN)_6]$, $[Co(tpy)_2]Cl_2$, and $[Co(atpy)_2]Cl_2$) cause the conductance to decrease. The time constants for the change range from 0.5 to 2 seconds. Note that this change is not correlated to the overall charge of the redox-active molecule.

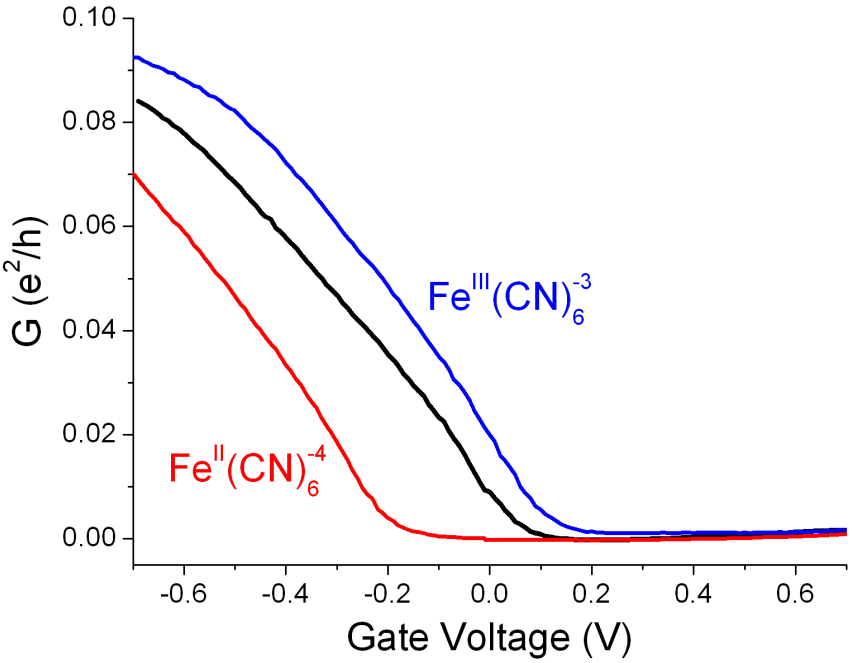

Figure 7.8: Conductance versus gate voltage for 1 mM ferricyanide and ferrocyanide in 1 mM NaCl supporting electrolyte. Ferricyanide ($Fe(CN)_6^{-3}$) causes a positive threshold voltage shift from the initial curve in 1 mM NaCl, while ferrocyanide ($Fe(CN)_6^{-4}$) causes a negative shift. Some hysteresis is observed in the reverse sweep direction. The leakage current between the electrolyte-gate wire and the drain electrode, which is typically 100 times smaller than the source-drain current, has been subtracted.

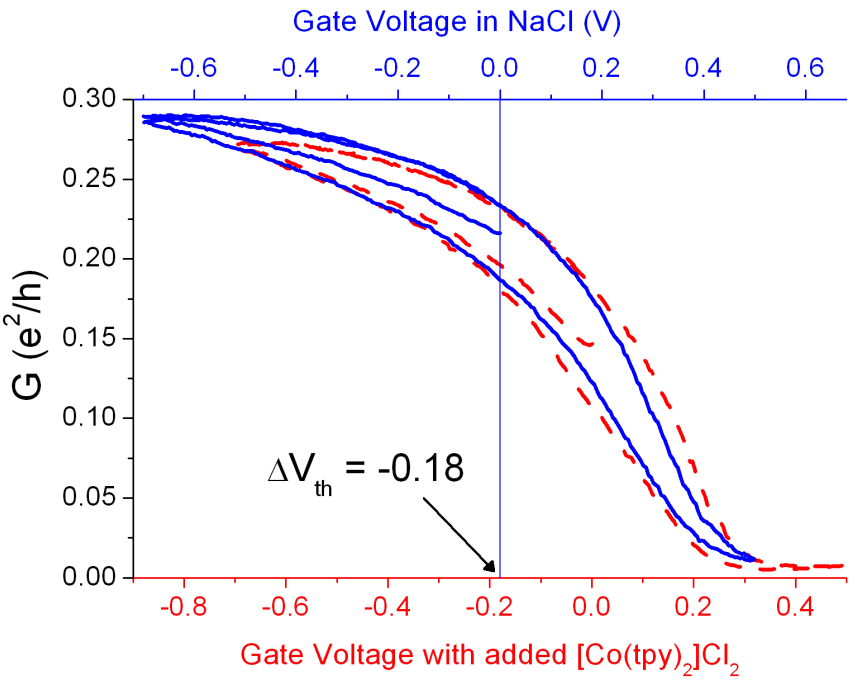

Figure 7.9: Measuring the threshold voltage shift. The conductance of a nanotube versus gate voltage is shown in 1 mM NaCl (blue, V_g on upper axis) and in 1 mM NaCl with 100 μM $[Co(tpy)_2]Cl_2$ (dashed red, V_g on lower axis). To calculate the threshold voltage shift ΔV_{th}, we measured the relative shift between the axes when the curves appear to be superimposed, as shown here. In this example, $\Delta V_{th} = -0.18$.

flow to the reservoir with the gate wire. The nanotube conductance changes as soon as the molecules are added to the reservoir with the gate wire, regardless of the flow speed or direction.[1] In particular, the conductance still changes even if the molecules have not reached the nanotube by either advection or diffusion: since a typical diffusion constant for a molecule in aqueous solution is $D = 5 \times 10^{-10}$ m^2/s (Bard and Faulkner, 2001, p. 147), it would take over 10 minutes for the root-mean-square displacement to equal the 1 mm distance between the reservoir and the nanotube, if there were no other forces on the molecules. Because advection by the flow pushes molecules back towards the reservoir, the actual time for any molecules to diffuse to the nanotube is much longer. In a separate experiment, we found that there is no change in the nanotube conductance if the molecules are confined by the flow only to the reservoir that does not contain the gate wire. We conclude that the observed signal depends only on the proximity of the molecules to the gate wire.

7.4 Combined Nanotube and Electrochemical Data

From the data in Section 7.3, we can say qualitatively that oxidizing molecules cause a positive threshold voltage shift, while reducing molecules cause a negative shift, and that this shift depends only on the proximity of the molecules to the electrolyte-gate wire. For a more quantitative understanding, however, we must turn to the electrochemical measurements described in Section 7.1.

By using those standard electrochemical techniques to change and measure the ratio of oxidized to reduced molecules in a bulk solution, we were able to

[1] We have also observed similar results when ammonia is added to the channel, suggesting that the signal observed by Bradley *et al.* (2003a) might also be related to interactions between the molecules and their gate wire.

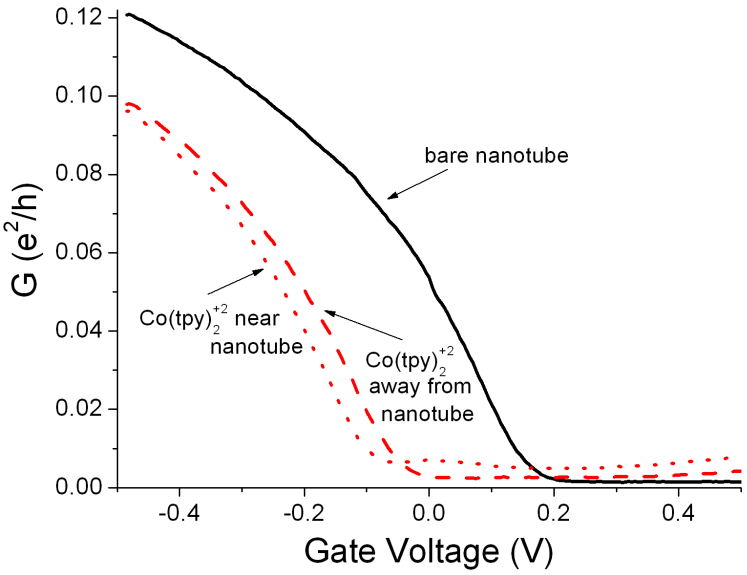

Figure 7.10: Dependence of ΔV_{th} on proximity of molecules to the nanotube. Adding 100 μM $[\text{Co(tpy)}_2]\text{Cl}_2$ to a 100 mM NaCl supporting electrolyte causes roughly the same shift from the initial curve (solid black) when the molecules fill the entire microfluidic channel (dotted red) as when they are confined by the flow to the reservoir containing the gate wire (dashed red). The small shift between the Co(tpy)_2^{+2} curves may be due to an interaction of the redox molecules with the nanotube or with the gold source and drain electrodes. The small current in the off state is likely caused by leakage through the electrolyte.

measure the threshold voltage shift as a function of [Ox]/[Red]. Figure 7.11(a) shows the threshold voltage shift for a 100 μM $[Co(tpy)_2]Cl_2$ solution at different [Ox]/[Red] ratios. This shift varies with the logarithm of [Ox]/[Red], with a slope of 61 ± 6 mV. This slope is also roughly 60 mV for $Ru(NH_3)_6$, but it is several times greater for the $Co(bpy)_3$ and $Fe(CN)_6$ redox couples, as seen in Figure 7.11(b).

The threshold voltage shift at [Ox]/[Red] = 1 was determined for all of the molecules. This is plotted in Figure 7.12 as a function of the formal potential $E^{0'}$ of each molecule, which is the potential at which oxidation or reduction occurs versus the potential of a Ag/AgCl reference electrode. Despite the scatter in the data, they are consistent with a linear dependence of the threshold voltage shift on $E^{0'}$ with unit slope, but further tests need to be done to confirm this relationship.

7.5 Interpretation Using the Nernst Equation

To develop a quantitative model to understand these data, we first recall that the Nernst equation, given in Equation 7.2, gives the chemical potential of the electrons in a solution of redox-active molecules with formal potential $E^{0'}$. We can substitute the Nernst Equation into Equation 7.1 to express the voltage V_g applied to the gold electrolyte-gate wire as

$$V_g = \frac{\mu_{e-c}}{e} = \phi + \left[E^{0'} + \frac{k_B T}{ne} \ln \frac{[Ox]}{[Red]} \right]. \tag{7.3}$$

If the nanotube behaves as a reference electrode and senses only the electrostatic potential ϕ, then the shift in the threshold voltage ΔV_{th} is the change in V_g needed to produce the same ϕ, which is just the change in μ_c/e. Since $n = 1$ for all our molecules, we can write the expected threshold voltage shift as

$$\Delta V_{th} = \Delta E^{0'} + (59.2 \text{ mV}) \log \frac{[Ox]}{[Red]}. \tag{7.4}$$

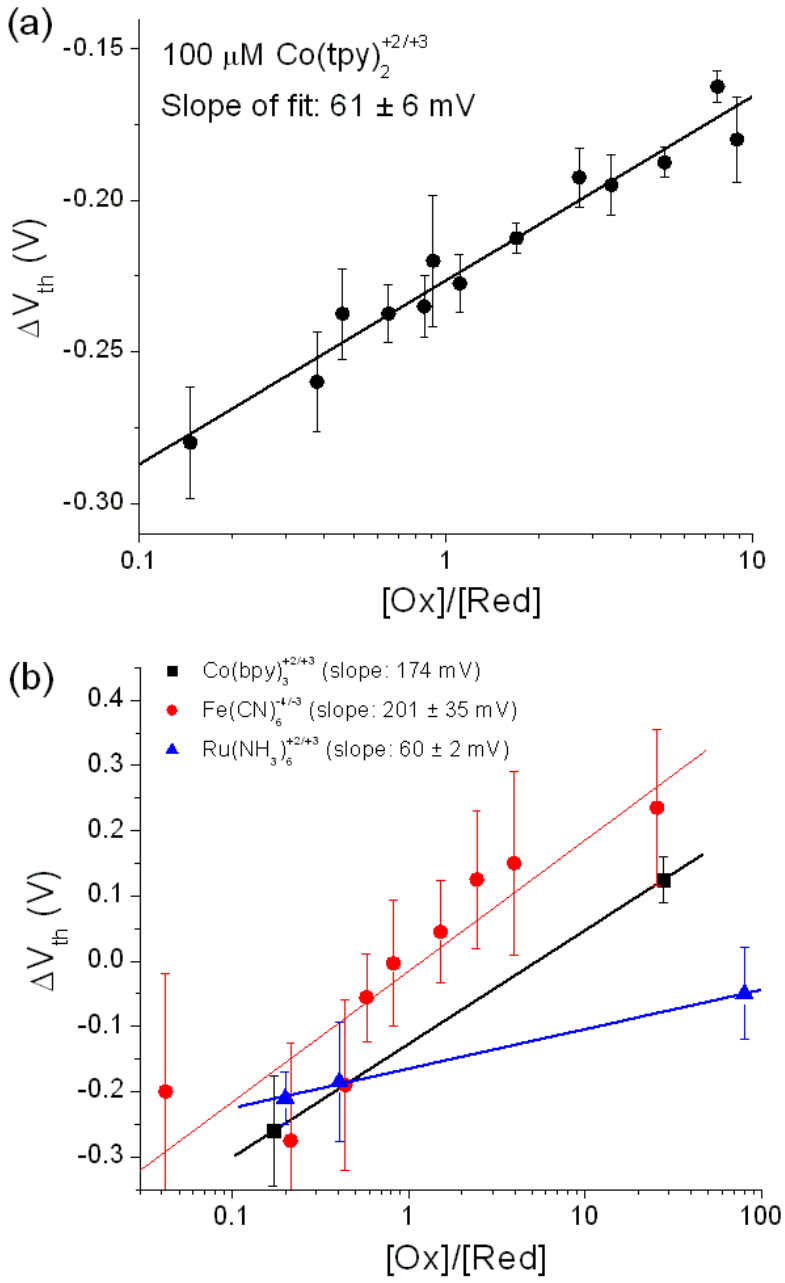

Figure 7.11: ΔV_{th} versus [Ox]/[Red]. (a) The threshold voltage shift for 100 μM $[Co(tpy)_2]Cl_2$ is shown for different [Ox]/[Red] ratios, which are set by bulk electrolysis. The supporting electrolyte was 1 mM NaCl. Error bars show the standard deviation from four different nanotubes. The slope of the linear fit is 61$\pm$6 mV. (b) For $Ru(NH_3)_6^{+2/+3}$, the slope is also 60 mV, but it is much higher for $Co(bpy)_3^{+2/+3}$ and $Fe(CN)_6^{-4/-3}$. These measurements were also performed in 1 mM NaCl.

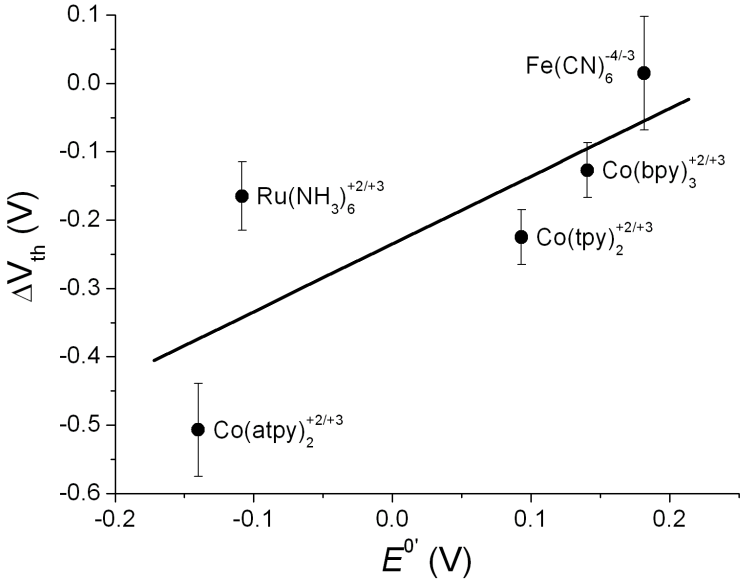

Figure 7.12: ΔV_{th} versus $E^{0'}$. The threshold voltage shift varies roughly linearly with $E^{0'}$, the formal potential of the redox-active molecules, which was measured by cyclic voltammetry with a Ag/AgCl reference electrode. The slope of the fit is 0.99 ± 0.49.

The observed gate-voltage dependence of the nanotube conductance follows this expected variation with the chemical potential of the redox-active molecules. Figure 7.11 shows that for $Co(tpy)_2^{+2/+3}$ and $Ru(NH_3)_6^{+2/+3}$, the threshold voltage varies as log [Ox]/[Red] with a slope within 3% of 59.2 mV.[2]

Figure 7.12 shows that the threshold voltage for all the molecules varies roughly linearly with $E^{0'}$ with a slope of approximately unity, although there is a large degree of scatter in these data. We reiterate that in this model, the local interaction is between the redox-active molecules and the gate wire, and the proximity of the molecules to the nanotube is irrelevant, and this result is confirmed by Figure 7.10.

Since the nanotube transistor, like a reference electrode, measures only the electrostatic potential ϕ, it should show no change relative to the potential measured with a reference electrode. To fully confirm this model, we measured the nanotube conductance versus the potential of a Ag/AgCl reference electrode before and after adding $[Co(tpy)_2]Cl_2$ to the system, as shown in Figure 7.13. The molecules shifted the conductance as a function of the electrolyte-gate voltage, but there is virtually no conductance change as a function of the reference potential.

It is worth noting that the gold source and drain contacts will interact with the molecules too, just like the gold electrolyte-gate wire. Since their exposed surface

[2]It is not clear why $Co(bpy)_3^{+2/+3}$ and $Fe(CN)_6^{-4/-3}$ showed a larger slope, but there are several possibilities to explain this effect, which were suggested by Suddhasattwa Nad. Some molecules are unstable under prolonged electrolysis conditions; for example, we observed a blue complex during our measurements of the ferricyanide/ferrocyanide couple. This was probably Prussian Blue (Beriet and Pletcher, 1993; Pharr and Griffiths, 1997), which adsorbs tenaciously to electrode surfaces (Itaya *et al.*, 1986; Winkler, 1995). We may therefore be observing a mixed potential due to different redox-active molecules in solution and adsorbed to the electrodes. Also, in the case of the $Co(bpy)_3^{2+/3+}$ couple, the [Ox]/[Red] ratio is very sensitive to dissolved oxygen in the solution (Abruña, 2006), which is difficult to control.

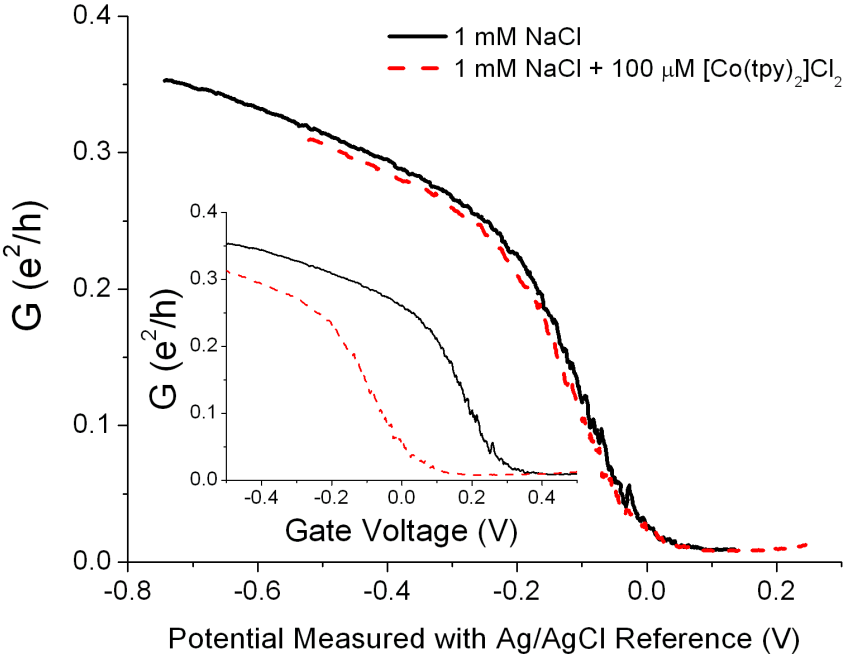

Figure 7.13: G vs. ϕ measured with reference electrode. The nanotube conductance is almost identical in 1 mM NaCl (solid black) and in 100 μM of $[Co(tpy)_2]Cl_2$ with a 1 mM NaCl supporting electrolyte (dashed red) when plotted versus the potential measured with a Ag/AgCl reference electrode. The reference was inserted in the reservoir containing the gold gate wire. Inset: When the conductance is plotted versus the voltage applied to the gate wire, it shows a threshold voltage shift after the $[Co(tpy)_2]Cl_2$ addition.

area is so much smaller than that of the gate wire (10^{-8} m^2 vs. 10^{-5} m^2), the gate wire will dominate in setting the electrochemical potential of the solution. To confirm this, we aligned our PDMS channel at an angle that minimized the exposed area of the source and drain contacts, and we also passivated the contacts on some devices with self-assembled monolayers of hexadecanethiol, but neither of these techniques changed the magnitude of the observed threshold voltage shift. Finally, as mentioned earlier, we used an additional gold wire attached to a high-impedance voltmeter to confirm that the electrochemical potential in the reservoir on the other side of the nanotube was the same as the potential we set with the gate wire. From all of these experiments, we conclude that we can safely neglect the effect of the exposed source and drain contacts on our results.

7.6 Concentration Dependence

In the previous sections, we have shown that a carbon nanotube acts as a nanoscale reference electrode and measures the electrostatic potential, which tells us about the chemical potential and thus about the redox state of the molecules in the solution. Nanotubes therefore open the door for new kinds of nanoscale electrochemistry experiments, and we are interested in how small a number of redox-active molecules a nanotube could detect. Equation 7.4 gives the expected threshold voltage shift of a nanotube in terms of the ratio [Ox]/[Red], but in this section, we will explore the response of nanotubes to the overall redox-active molecule concentration.

Figure 7.14 shows the threshold voltage shift of a carbon nanotube transistor as a function of the concentration of four different redox-active molecules. We see that ΔV_{th} scales logarithmically with concentration for all molecules, and then

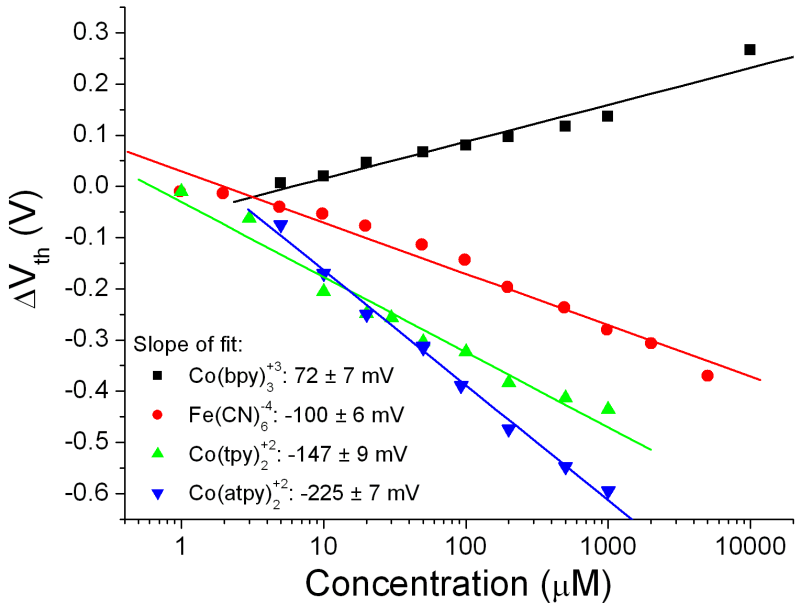

Figure 7.14: Concentration dependence of ΔV_{th} for redox-active molecules. ΔV_{th} varies linearly with the logarithm of the concentration for different redox-active molecules.

stops at zero for all four curves when there are less than a few μM of molecules in solution.

The lack of a threshold voltage shift below a few μM makes sense, because 1 μM is the practical lower limit for the ion concentration in a solution, as discussed in Section 3.1.5. Impurities are generally present at the 1 μM level, and it is likely that these impurities are dominating the chemical potential when we reduce the redox-active molecules to such low concentrations. Adsorption of molecules to the electrolyte-gate wire or residual oxygen in the solution could also be affecting these measurements.

The logarithmic dependence of ΔV_{th} on concentration is slightly more difficult to understand, since in the simplest picture, we might not expect changing the overall concentration to have any effect on [Ox]/[Red], which would make ΔV_{th}

constant as a function of overall concentration, rather than giving us the steep slope seen in Figure 7.14. This dependence of threshold voltage shift on concentration has previously been interpreted as a sign of a local molecule-nanotube interaction (Bradley *et al.*, 2003a). We can learn more, however, by again combining these nanotube measurements with some traditional electrochemical measurements.

Figure 7.15(a) shows $\Delta V_{\rm th}$ as a function of $[{\rm Co(tpy)_2}]{\rm Cl_2}$ concentration, along with measurements of the open circuit potential for these same solutions. The open circuit potential is measured with a high impedance voltmeter between a working and reference electrode. Since this is another measure of the chemical potential, it should follow the same form as $\Delta V_{\rm th}$. Just like in Figure 7.14, the threshold voltage shift varies logarithmically with concentration, but we also see that the open circuit potential does as well, and that both lines have roughly the same slope. Since $\Delta V_{\rm th}$ and the open circuit potential both measure $\mu_{\rm c}$, we conclude that their concentration dependence simply reflects a changing $\mu_{\rm c}$, and not molecule-nanotube adsorption. In other words, mixing a 10 μM $[{\rm Co(tpy)_2}]{\rm Cl_2}$ solution results in a higher [Ox]/[Red] ratio, or relatively more oxidized molecules, than mixing a 100 μM solution.

We have confirmed the variation of [Ox]/[Red] with concentration by separate ultramicroelectrode measurements, as seen in Figure 7.15(b). For this experiment, performed with a different set of dilutions of $[{\rm Co(tpy)_2}]{\rm Cl_2}$, we simultaneously measured [Ox]/[Red] and the open circuit potential. We see that lower concentrations do have a higher [Ox]/[Red] ratio, and that the slope of these data roughly agrees with that of the open circuit potential measurements. It is unclear whether the difference in slope is due to problems with the open circuit potential measurements (which are highly sensitive to the condition and history of the electrodes used) or

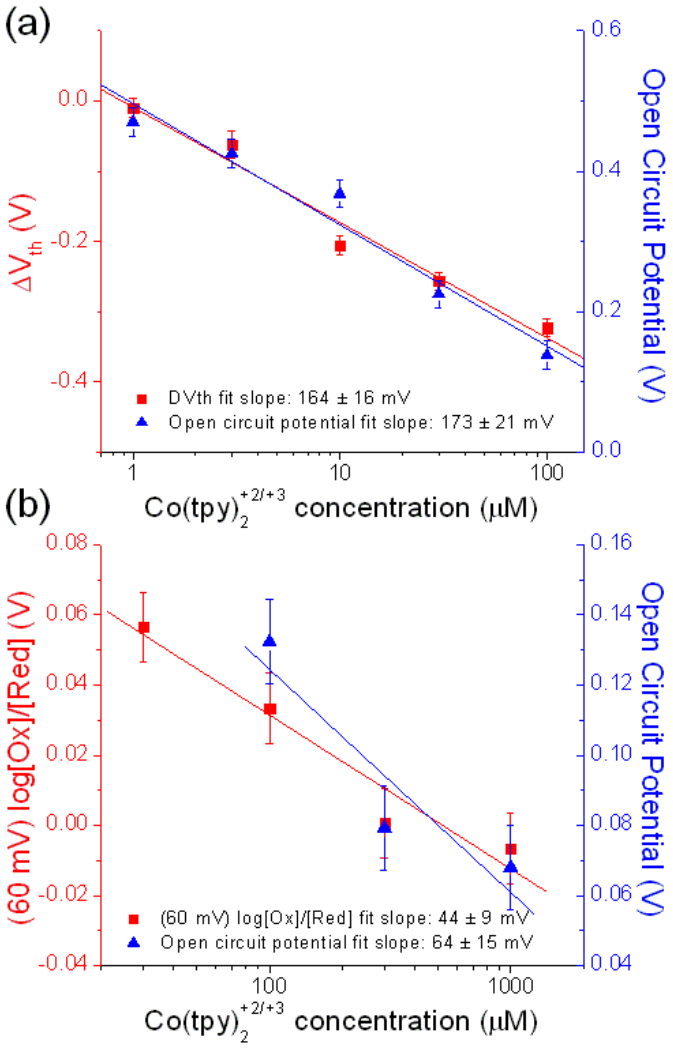

Figure 7.15: Relation of ΔV_{th}, open circuit potential, and [Ox]/[Red] to concentration. (a) ΔV_{th} (red squares, left axis) and open circuit potential (blue triangles, right axis) are plotted for $[\text{Co(tpy)}_2]\text{Cl}_2$ at different concentrations, all in a 1 mM NaCl supporting electrolyte. Fits to both data sets have roughly the same slopes of -170 mV. (b) Separate measurements with an ultramicroelectrode confirm that [Ox]/[Red] also varies with the concentration of dilutions of $[\text{Co(tpy)}_2]\text{Cl}_2$ (red squares, left axis). The slopes of this fit and of the open circuit potential data (blue triangles, right axis) for the same solutions are within each other's error, but it is unclear whether the changing [Ox]/[Red] accounts for the whole concentration dependence of μ_{c}.

whether the changing [Ox]/[Red] does not account for the whole concentration dependence of μ_c.

The variation of μ_c with the concentration of redox-active molecules means that a nanotube can be used to study these changes in concentration. We studied this possibility further using a different experiment, the results of which are shown in Figure 7.16. A small hole punched in a piece of PDMS was placed on top of a nanotube transistor, and the redox-active molecule $[Co(tpy)_2]Cl_2$ was added in increasing concentrations while monitoring the nanotube conductance at $V_g = 0$. When this molecule is dissolved in solution, the cobalt ion will start in the reduced state as Co^{2+}, but it can be oxidized (*e.g.*, by dissolved oxygen in solution) to Co^{3+}. We see in Figures 7.14 and 7.15(a) that ΔV_{th} decreases logarithmically with $[Co(tpy)_2]Cl_2$ concentration, and so when G varies linearly with V_g, we expect G to also decrease as log(concentration).

Figure 7.16 shows that the current through the nanotube decreased as we added $[Co(tpy)_2]Cl_2$ at increasing concentrations. When we plot the current as a function of concentration, we see that at low concentrations the current does vary logarithmically with the concentration. At higher concentrations, we may no longer be in the linear region of G vs. V_g, or leakage currents through the solution may cause problems.

After each addition of $Co(tpy)_2Cl_2$, especially at low concentrations, we also see that the current rises slowly over time. We may be seeing the gradual oxidation of this molecule over time, which we know occurs after the molecule is dissolved in solution. This suggests that we should be able to use a nanotube transistor to monitor changes in [Ox]/[Red]. In particular, we should be able to measure the activity of a redox enzyme as it oxidizes and reduces redox-active molecules.

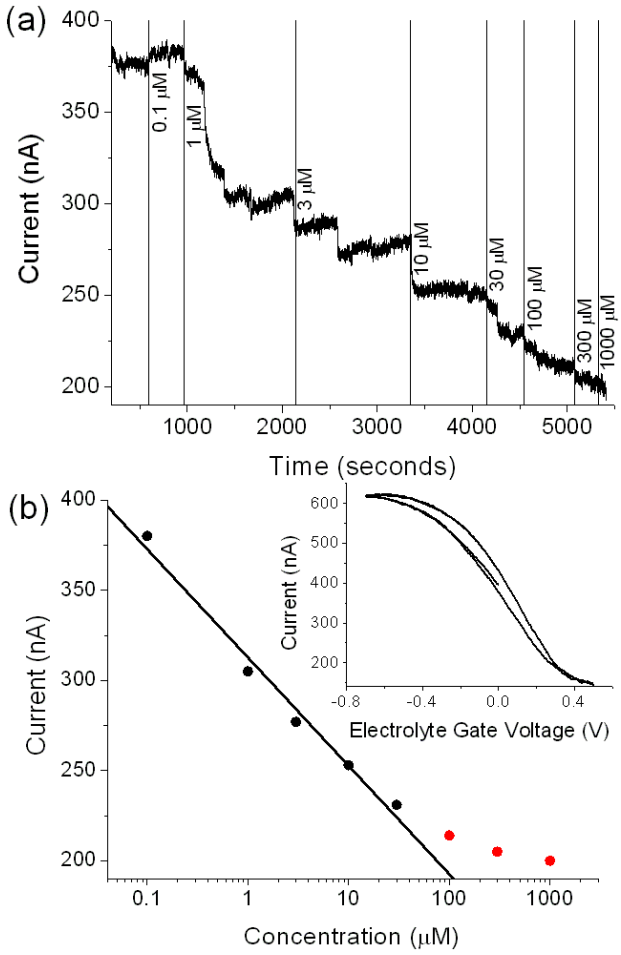

Figure 7.16: Effect on G of increasing concentration (at $V_g = 0$). (a) Current through a nanotube transistor while adding increasing concentrations of $[Co(tpy)_2]Cl_2$, with a source-drain voltage across the nanotube of $V_{sd} = 50$ mV (which can be used to convert between current and conductance). Since the entire solution could not be changed at once, multiple additions were made at each concentration until the current stopped decreasing (this is most noticeable at 3 μM). After each addition, especially at low concentrations, we also see that the current rises slowly over time. (b) The final current level at each concentration, plotted versus log(concentration). The fit, which excludes the last three points (red), has a slope of -60 ± 4 nA. Since dI/dV_g is roughly 0.75 nA/mV in the linear region (see inset), this corresponds to a threshold voltage shift of -80 mV per decade change in concentration. At high concentrations, dI/dV_g may no longer be constant, or large leakage currents could be a problem.

Some work in this area has recently been performed by Boussaad *et al.* (2006), who observed the conductance response of a nanotube transistor evolve in time in the presence of an oxidizing enzyme and its substrate.

7.7 Future Directions with Small Solution Volumes

The main advantage of a nanotube over a traditional reference electrode is its small size: since a traditional reference must be separated from the solution by a frit that allows ionic conduction but prevents contamination by the redox-active molecules of interest, it is difficult to miniaturize below the millimeter scale, limiting the size of electrochemical experiments. Since we have shown that a nanotube can be used to monitor the electrostatic potential of a solution, it should be possible to investigate nanoscale electrochemical systems. For example, given that we can detect threshold voltage shifts down to 5 mV and concentrations down to 1 μM, we estimate that with a microfabricated electrolyte-gate electrode, we could detect a single redox event in a [300 nm]^3 volume of solution. Bringing such a small volume of solution close to a nanotube may be possible with an emulsion (*e.g.*, aqueous droplets containing redox-active molecules in a background of oil), but it will be difficult. In the remainder of this section, however, we see how interesting effects could be studied with a 10 μm-high solution volume.

We can consider the effect of changing the voltage applied to the back gate of a nanotube device that is covered with a solution of redox-active molecules, as seen in Figure 7.17(a). Changing this voltage can change both the electrochemical potential $V_{\mathrm{soln}} = \mu_{\mathrm{e-c}}/e$ of the solution and [Ox]/[Red] for the molecules, so the

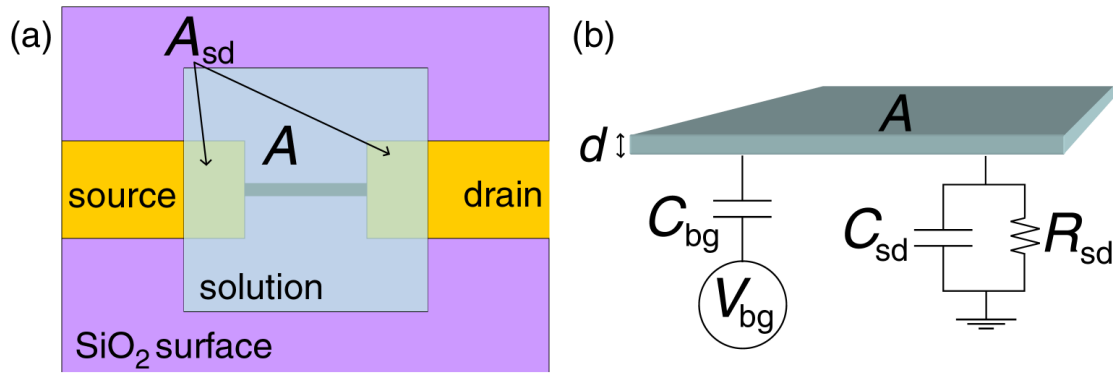

Figure 7.17: Proposed experiment for probing a small volume of redox-active molecules. (a) A solution of redox-active molecules is placed over a nanotube transistor, with area A of the solution overlapping the oxide surface. A_{sd} is the area of solution overlapping the metal electrodes. (b) The solution of area A and thickness d is capacitively coupled to the back gate, where a voltage V_{bg} is applied. It is also capacitively and resistively coupled to the source and drain electrodes.

conductance change of the nanotube can be written as

$$\Delta G = \frac{\mathrm{d}G}{\mathrm{d}V_{\mathrm{g}}}\Delta\phi = \frac{\mathrm{d}G}{\mathrm{d}V_{\mathrm{g}}}\left[\Delta\left(V_{\mathrm{soln}} - V_{\mathrm{NT}}\right) + \frac{k_{\mathrm{B}}T}{e}\Delta\ln\frac{[\mathrm{Ox}]}{[\mathrm{Red}]}\right], \tag{7.5}$$

where V_{NT} is the potential of the nanotube (roughly the average of the voltage applied to either side), which for a small enough voltage bias we can approximate as zero. For large solution volumes, changing the back gate voltage causes a only a negligible change in [Ox]/[Red], so any change in conductance will be due to the first term. For small enough volumes, however, the second term should become important.

For this geometry, as illustrated in Figure 7.17(b), the solution is capacitively coupled to the back gate with a capacitance $C_{\mathrm{bg}} = \epsilon_{\mathrm{SiO_2}}A/h = 2\times10^{-4}$ F/m^2 for an oxide of height $h = 200$ nm. The capacitance between the solution and the source and drain electrodes will be roughly $C_{\mathrm{sd}} = (0.1\ \mathrm{F/m^2})A_{\mathrm{sd}}$, and the resistance R_{sd} will scale inversely with the area of the contacts and will depend on

the concentration of ions in solution. If $A_{\rm sd} = A/5$ (roughly correct for our current nanotube devices), we can write the potential of the solution as

$$V_{\rm soln} = V_{\rm bg}\left(\frac{C_{\rm bg}}{C_{\rm bg}+C_{\rm sd}}\right)e^{-t/\left[R_{\rm sd}\left(C_{\rm bg}+C_{\rm sd}\right)\right]} = \frac{V_{\rm bg}}{100}e^{-t/\tau}, \tag{7.6}$$

where the time constant τ will depend on the solution concentration. Changing the back gate voltage from 0 V to 10 V will therefore cause $V_{\rm soln}$ to jump from 0 V to 100 mV, and then to decay back to 0 V with a time constant τ. The solution response could be much higher if $A_{\rm sd}$ were minimized, which could be accomplished by changing the device geometry or screening the contacts from the solution with an oxide coating.

For large solution volumes, switching the back gate voltage to 10 V will cause the nanotube conductance to initially jump by (100 mV)$\frac{{\rm d}G}{{\rm d}V_{\rm g}}$, and then to decay back to its initial value. If, however, the number of electrons added when you turn on $V_{\rm bg}$ is on the same order as the initial number of electrons in the solution, then the steady-state conductance will be different from the initial value, due to the second term in Equation 7.5.

We can write the number of electrons added, N_e, as

$$eN_e = C_{\rm bg}\left(V_{\rm bg}-\phi\right) - C_{\rm sd}\phi \tag{7.7}$$

$$= \left[C_{\rm bg}\left(V_{\rm bg}-V_{\rm soln}\right) - C_{\rm sd}V_{\rm soln}\right] + \left[\frac{\mu_{\rm c}}{e}\left(C_{\rm bg}+C_{\rm sd}\right)\right], \tag{7.8}$$

which starts at zero and grows to

$$eN_e(t\rightarrow\infty) = C_{\rm bg}V_{\rm bg} + \frac{\mu_{\rm c}}{e}\left(C_{\rm bg}+C_{\rm sd}\right) \tag{7.9}$$

in the steady state. If we assume that the solution initially contains N molecules, half oxidized and half reduced, then the chemical potential is

$$\mu_{\rm c} = \frac{k_{\rm B}T}{e}\ln\frac{\frac{N}{2}-N_e}{\frac{N}{2}+N_e}, \tag{7.10}$$

which can be put back into Equation 7.9 to solve for N_e, allowing μ_c and ϕ to be determined. For example, if the solution thickness is $d = 10$ μm, the concentration is 10 μM, V_{bg} is switched from 0 V to 10 V, and $A_{sd} = A/5$, the change in ϕ will be 15 mV, which should be measurable with our nanotube devices. (Because both N_e and N scale linearly with A, this total area of the solution drops out of the calculation.) Figure 7.18 shows the dependence on $\Delta\phi$ on the variables ΔV_{bg}, d, and concentration. We see that the expected signal diverges as the number of electrons added to the solution approaches $N/2$, the number of oxidized molecules that are able to accept an electron; it is not clear what experimental signal would be expected beyond this point.

To perform this experiment, it is necessary to confine a small volume of solution with a height of 10 μm or less. While this is easier than working with a [300 nm]^3 volume of solution, it is still not trivial. Simply placing a flat piece of PDMS over a solution droplet is not sufficient; we found that this results in a height closer to 100 μm. PDMS channels with low ceiling heights can be fabricated, but it would then be necessary to separate the solution in the channel from the input and output reservoirs. There are several kinds of valves that could be used to seal off part of a PDMS channel for this experiment, such as the pneumatic valves developed by the Quake group (Unger *et al.*, 2000) and the torque-actuated valves from the Whitesides group (Weibel *et al.*, 2005). We have not yet been able to successfully implement one of these methods in our channels, but they currently seem like the best ways to reach this small-solution-volume limit. With an improved microfluidic system, a carbon nanotube device will be a useful tool for investigating electrochemistry at smaller scales.

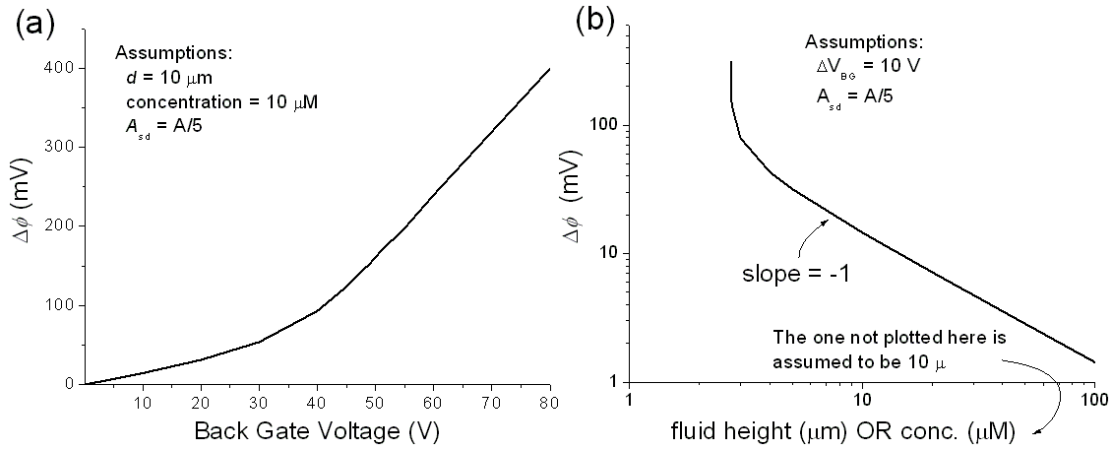

Figure 7.18: Expected change in the steady-state electrostatic potential ϕ due to an applied back-gate voltage for small solution volumes. (a) Change in ϕ as a function of the change in back gate voltage $V_{\rm bg}$, assuming that the solution of redox-active molecules has thickness $d = 10$ μm and concentration 10 μM. (b) Change in ϕ as a function of changing the solution thickness or concentration, assuming $V_{\rm bg}$ is switched from 0 V to 10 V. (ϕ has the same dependence on fluid height and concentration, and the one not plotted as the independent variable is assumed to be 10 μm or 10μM.) The curve diverges around a thickness of 2.7 μm (or a concentration of 2.7 μM) as the number of electrons N_e added to the solution approaches $N/2$, the number of oxidized molecules that are able to accept an electron.

7.8 Conclusions

We have demonstrated that nanotube transistors can be used as nanoscale reference electrodes to measure the electrostatic potential of a solution. They can therefore detect changes in the chemical potential of solution due to redox-active transition metal complexes, or in principle due to any potential-determining couple. These changes in potential shift the gate-voltage dependence of the nanotube conductance, and this shift depends linearly on the formal potentials of the molecules and logarithmically on their [Ox]/[Red] ratios. Although there may also be some local interaction between the molecules and the nanotube, the primary source of the observed signal is this non-local electrochemical effect, which must be considered in any electrolyte-gated nanotube sensing experiment. In particular, to confirm that a threshold voltage shift is due to a local nanotube-analyte interaction, one should use a reference electrode to monitor or set the electrostatic potential of the solution, and one should also examine the difference between the observed signal when the analyte is near the nanotube versus when it is confined to an area containing the gate electrode. We have also shown that using a nanotube as a reference electrode could lead to new kinds of nanoscale electrochemistry experiments, and we proposed an experiment in which a nanotube could measure changes induced by a back-gate voltage on the oxidation state of a thin volume of redox-active molecules.

Chapter 8

Searching for Local Nanotube-Analyte Interactions

In Chapter 7, we discussed an important non-local effect in nanotube sensing experiments: if a metal wire is used to set the electrochemical potential of the solution, then the nanotube will observe a signal simply due to the interaction of any potential-determining analyte and this gate wire. This effect must be considered in the design and interpretation of any sensing experiment involving an electrolyte-gated nanotube transistor, but this is not the only mechanism that could change a nanotube's conductance response in solution: local electrostatic gating could also result in a threshold voltage shift.

In the following two chapters, we will investigate the response of carbon nanotubes to local stimuli. This chapter describes experiments in which individual DNA molecules and highly-charged microspheres were brought in close proximity to carbon nanotubes, in the hope of seeing a change in the nanotube conductance. Although we were able to engineer a microfluidic setup to accomplish this task, no signal that correlated with individual DNA molecules or microspheres passing a nanotube was observed, probably due to screening of the charge by ions in the solution. The nanotube conductance did often show a series of spikes after the introduction of the molecules into the microfluidic channel, but we are unable to conclude that these spikes resulted from an electrostatic interaction between the DNA and the nanotube.

From the experiments, we conclude that confining the DNA closer to the nanotube is critical, and in Section 8.4 we suggest a number of ways in which this

might be accomplished. These results with DNA molecules also helped guide the experiments presented in Chapter 9, in which we looked at the interaction between nanotubes and living cells.

8.1 Setup for Experiments with DNA

DNA (deoxyribonucleic acid), the carrier of genetic information, is a polymer formed from stacked base pairs. Double-stranded DNA has a width of 2 nm and is one of the most highly charged linear polymers, with a net charge of $2e$ per base pair (0.34 nm), although the effective charge is reduced to $1e/(0.7\text{ nm})$ due to counterion condensation, as discussed in Appendix D. With this high charge and small size, DNA could be an interesting molecule to study with a carbon nanotube. The experiments presented in this chapter were carried out in collaboration with Yuval Yaish and Xinjian Zhou from 2002 to 2004.

In our experiments, we worked with four different kinds of DNA: λ-DNA, double and single-stranded DNA from the bacteriophage M13 (dsM13 and ssM13), and short DNA from a salmon. The properties of these different molecules, as well as experimental details on how they were prepared and visualized, are described in more detail in Appendix D.

The largest experimental hurdle in detecting DNA with a carbon nanotube arises because even though DNA is highly charged, it is also surrounded by counterions in solution. As discussed in Section 3.1.5, in a salty solution, charges are electrostatically screened from each other at distances greater than the Debye length λ_D, which scales inversely with the solution concentration. For a nanotube to see an electrostatic signal from a DNA molecule, we would therefore like to increase the Debye length by reducing the salt concentration as much as possible.

This was done with a semipermeable membrane that allowed salt, but not DNA, to pass through to a larger reservoir of deionized water (Slide-A-Lyzer Mini Dialysis Units, 3500 molecular weight cut-off, Pierce Biotechnology). We were unable to determine the concentration of the solution after dialysis, but as noted in Section 3.1.5, the practical lower limit on the concentration of an aqueous solution is about 1 μM, putting an upper limit on the Debye length of 300 nm.

Figure 8.1 shows a schematic of the microfluidic system used to bring DNA molecules to the nanotube. Since we wanted to bring the DNA as close as possible to the nanotube, we suspended the nanotubes over channels small enough that molecules in the channel would have a high probability of being near the nanotube, but large enough that DNA molecules will still flow into the channel. We chose 1-μm-wide and roughly 0.3-μm-deep channels that were wet-etched in the SiO_2 surface under the nanotubes as described in Appendix B (these devices were fabricated on Si/SiO_2 wafers with an oxide thickness of 1 μm to prevent the etch from exposing the back gate). These channels would sometimes become clogged with DNA or with other debris, but usually the DNA molecules were able to flow through. To bring the DNA to these small channels under each nanotube, we used a larger PDMS channel, which was aligned over the device. This channel could then be connected to our macroscopic plumbing system. We used a syringe pump to increase the flow speed, as discussed in Section 6.3, so that we would not have to wait too long between DNA molecules entering the channel.

Images of fluorescent DNA molecules flowing through this microfluidic system are seen in Figure 8.2. We were able to bring the DNA molecules to the suspended nanotube with high control, and the molecule speed was typically around 50 μm/s.

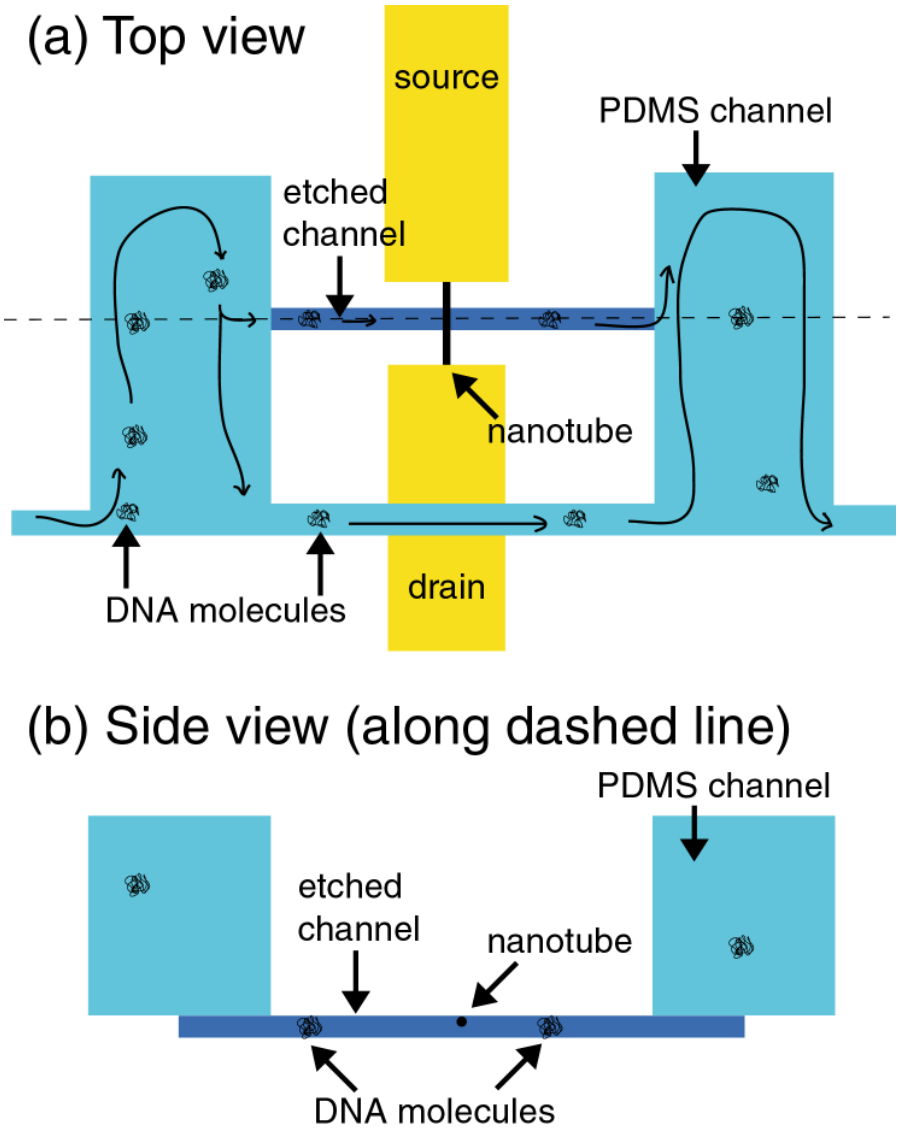

Figure 8.1: Schematic of microfluidic system for bringing DNA to a suspended nanotube. (a) Top view. A narrow channel is etched under the nanotube in the SiO_2 surface, and a larger PDMS channel is used to bring DNA molecules into this smaller etched channel. (b) Side view of the microfluidic setup along the dashed line in (a).

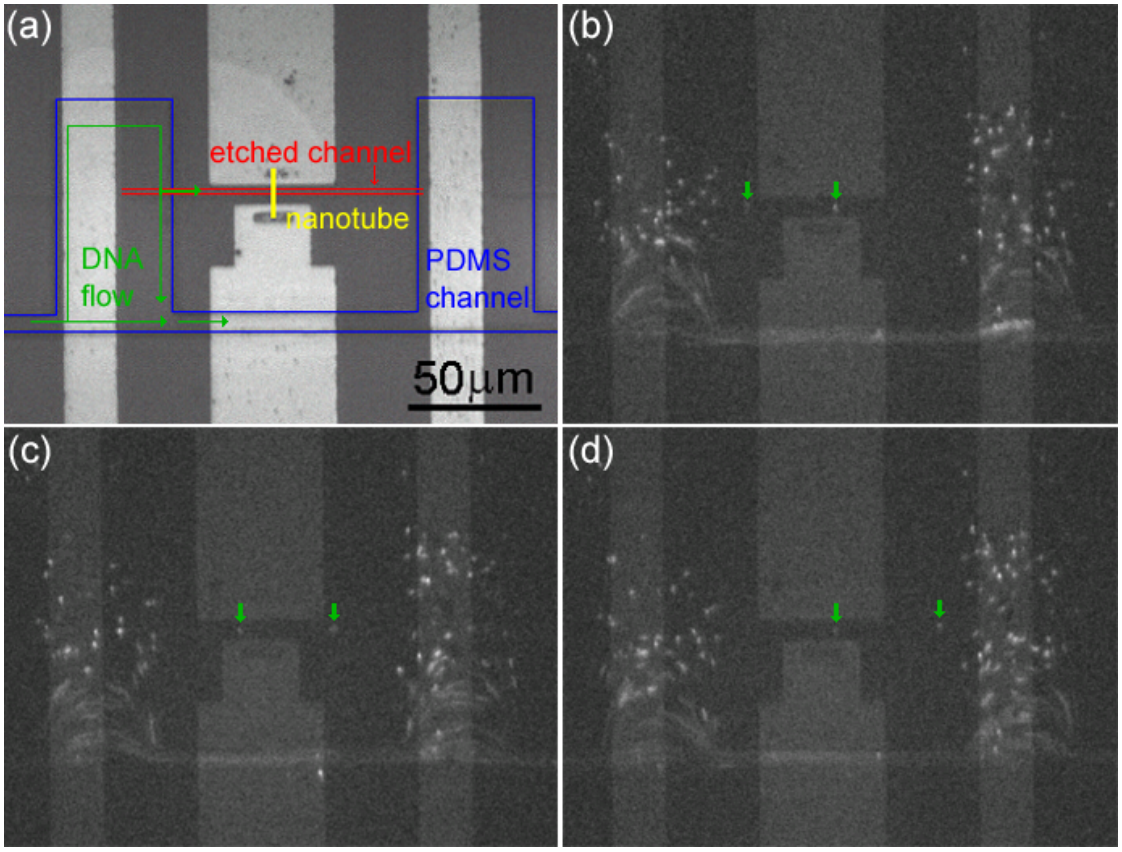

Figure 8.2: Fluorescence images of DNA near a suspended nanotube. (a) Bright-field image with added labels. The nanotube is grown between platinum source and drain electrodes and then suspended over a 1 μm-wide channel, and the larger PDMS channel is then aligned over the device. The metal contacts on either side of the nanotube can be used to set the potential of the solution in the PDMS channel. (b) Fluorescence image from a movie showing M13 DNA molecules flowing past the nanotube device. Two DNA molecules (marked with arrows) are seen inside the small etched channel. (c) 0.5 seconds later, the two DNA molecules have progressed farther within the channel. (d) 1 second after the frame in (b), the first DNA molecule has almost exited the channel, so we can estimate its speed to be around 50 μm/s.

8.2 Nanotube Response to DNA and Microspheres

Using the setup in Figure 8.1 to bring DNA molecules to the suspended nanotube transistor with high control, we performed a number of experiments in which the conductance of a nanotube was measured while different kinds of DNA flowed past it in the etched channel. Sometimes, there was no change in conductance, but other times, as seen in Figures 8.3 and 8.4, the conductance showed sharp spikes after the introduction of the DNA, which could be either upward or downward.

Figure 8.3(a) shows data from an experiment in which the nanotube conductance showed much more fluctuation after the introduction of dsM13 DNA. In Figure 8.3(b), we see that although the first spike in the conductance occurred at roughly the same time as the first DNA molecule passed the nanotube, there seems to be little correlation thereafter. In the one experiment shown in Figure 8.4, five of the initial downward spikes were correlated with DNA passing the nanotube (with the first DNA molecule causing the first spike), although subsequent spikes were again uncorrelated. It seems unlikely that this noise is due to a mechanical force, since the drag force on a dsM13 DNA molecule attached to a nanotube would be only 0.1 pN (using Eq. 3.17 with $a = R_{\rm h} = 130$ nm from Appendix D and $v = 50$ μm/s). This force is much smaller than > 1 nN required to change the nanotube bandgap through strain (Minot *et al.*, 2003), though it could possibly cause a weakening of the nanotube-metal contact. The spikes in conductance could also potentially be caused by unlabeled DNA molecules, since we do not know if all of our molecules were dyed.

We also performed similar experiments with the highly-charged 200-nm microspheres from Molecular Probes that are discussed in Appendix E. As with the DNA, we first used dialysis to make the salt concentration as low as possi-

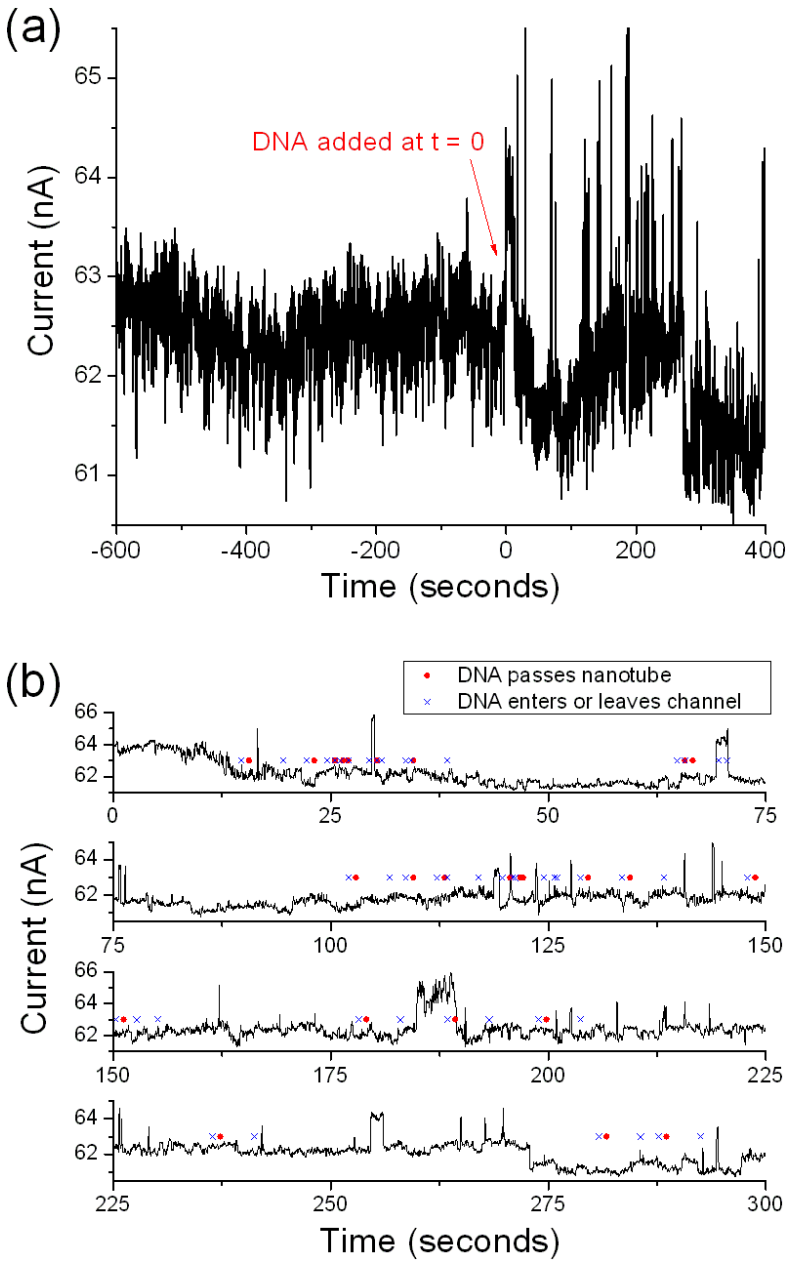

Figure 8.3: Electrical response of nanotube to DNA, with $V_{sd} = 10$ mV. (a) The nanotube current showed much more fluctuation after the introduction of dsM13 DNA to the PDMS channel. (b) Although the initial current spike occurred at roughly the same time as the first DNA molecule passed the nanotube, subsequent spikes were uncorrelated.

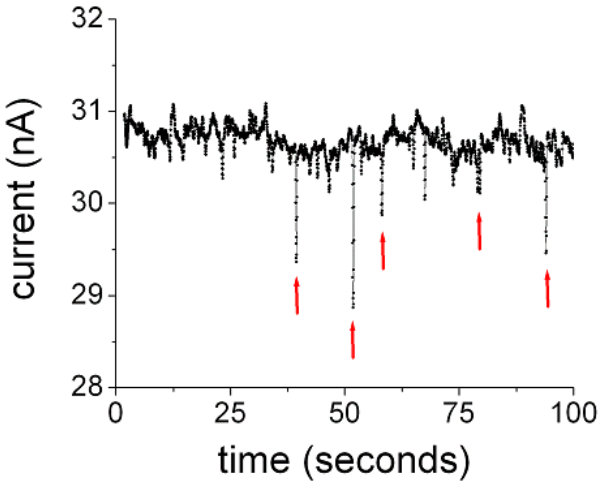

Figure 8.4: Second example of electrical response of nanotube to DNA. In this experiment (in which V_{sd} = 10 mV), five of the initial spikes (marked with red arrows) were correlated with a dsM13 DNA molecule passing the nanotube, but subsequent spikes were uncorrelated.

ble, and then we diluted the beads 1:100 in DI water before adding them to our PDMS channel. But as with the DNA experiments, we observed no correlation between the times when these beads passed a suspended nanotube and changes in the nanotube conductance.

8.3 Analysis

To our knowledge, a response from a nanotube transistor to an individual DNA molecule or charged microsphere has also not been reported by any other group. As discussed in Section 5.2, Star *et al.* (2006) and Tang *et al.* (2006) have explored the response of nanotube transistors to DNA that is dried on top of them, and Tang *et al.* found that the observed signal is due to DNA hybridization on the gold source and drain electrodes, and not on the nanotube itself. But DNA molecules

in solution have not been shown to electrostatically gate a nanotube.

Why has no response been observed when such a highly charged molecule is brought near such a sensitive device? The most likely reason is that even at low ion concentrations, many counterions remain around the DNA, screening most of its charge from the nanotube. And even with our small microfluidic channel, only small sections of the DNA were likely to come within a few nanometers of the nanotube.

To get a sense of how large a signal we might expect, we return to the Debye-Hückel theory discussed in Sections 3.1.5 and 5.5. If the DNA were a blanket directly coating the nanotube like the polyelectrolyte layers used by Artyukhin *et al.* (2006), then we would expect a huge potential change (over a volt), since the effective charge density (about 0.7 e/nm^2) is an order of magnitude larger than for the polyelectrolytes. This response will be greatly reduced, however, since only a small section of the nanotube and the DNA molecule will be in close proximity, and since the screening counterions will reduce the potential seen by the nanotube by a factor $e^{-r/\lambda_\mathrm{D}}$.

If the nanotube is 10 nanometers away from 10 base pairs of unscreened DNA (which have an effective charge of $5e$), then the potential change (as calculated from Eq. 3.10) is reduced to about 9 mV for $\lambda_\mathrm{D} \gg 10$ nm, and it would be further reduced to about 3 mV if $\lambda_\mathrm{D} = 10$ nm. Furthermore, since at most only the one-tenth of the nanotube that is suspended could be close to a DNA molecule, the threshold voltage shift would be at least 10 times smaller than this.[1] This value is much smaller than our minimum detectable threshold voltage shift of about 5 mV.

[1]Adding $N/10$ electrons to one-tenth of a nanotube will result in one-tenth of the resistance or conductance change as adding N electrons to the whole nanotube.

We can also consider the expected signal in terms of the charge sensitivity of the nanotube. In Section 4.1, we saw that the electrostatic capacitance of a 1-μm-long, 1-nm-diameter nanotube to an aqueous solution is about 0.3 fF, so in order for the threshold voltage of the suspended portion of the nanotube to shift by 5 mV, $Q_{\min} = (0.3\text{ fF})(5\text{ mV}) = 9e$ would need to be induced by the DNA. And to detect $\Delta V_{\text{th}} = 5$ mV for the entire 10-μm-long nanotube, $90e$ would need to be added, which is equivalent to the charge on a 60-nm-long (175 bp) piece of double-stranded DNA. To induce this much charge, this DNA would have to be held very close to the nanotube.

8.4 Conclusions and Future Prospects

From these results, it seems that a nanotube used in this configuration will not be an effective tool for single-molecule electronic detection. The spikes in the nanotube conductance after the introduction of DNA is promising, but we cannot yet conclude that this is related to an electrostatic interaction between the DNA and the nanotube. Even though we attempted to overcome the problems of the Debye screening length with our microfluidic design, we were unable to bring the DNA molecules close enough to observe a consistent signal.

We can see the importance of confining the DNA molecule by examining a different technique for electrostatic DNA detection: passing a DNA molecule through a nanopore while measuring the current inside the pore. The presence of DNA (or other molecules) inside the pore increases the pore's electrical resistance, causing a drop in the current. This has been demonstrated for easily-fabricated 200-nm PDMS pores (Saleh and Sohn, 2003), and much work has been done with 1.8-nm-diameter α-hemolysin protein channels (Kasianowicz *et al.*, 1996; Meller *et al.*,

2000) and with 5–15-nm solid-state nanopores (Li *et al.*, 2001; Storm *et al.*, 2005). Since DNA can be slowly pulled through these pores with optical tweezers (Keyser *et al.*, 2006), DNA sequencing may even be possible with this technique.

To measure an individual DNA molecule in solution with a nanotube, it will probably be necessary to provide a similar confinement. One possibility would be to make smaller fluidic channels. DNA has been electrophoretically driven into 30 by 40 nm channels (Reisner *et al.*, 2005), and current research is focusing on fabricating sub-20 nm channels for DNA flow (Mannion and Craighead, 2007), although the inability to plasma-treat nanotubes would prevent these fabrication methods from being used on our devices. Rather than confining the entire DNA strand in a channel, it may also be possible to use a novel device geometry to suspend a nanotube over a nanopore, which would both confine the DNA near the nanotube and allow simultaneous measurement of both the nanopore and the DNA electrical signals.

The DNA could also be brought closer to the nanotube using electrical forces such as DEP, as discussed in Section 3.2.2. The DEP electric field could be provided by nearby metal electrodes, as in the DNA-trapping experiments of Dewarrat *et al.* (2002), or by the nanotube itself, as Zheng *et al.* (2004a) demonstrated with nanoparticles. It may also be possible to use a different kind of DEP trapping known as optical tweezers, in which the electric field is provided by a focused laser. Optical tweezers have been used to unzip double-stranded DNA in a number of experiments (Koch and Wang, 2003), and if it is possible to position the DNA so that it unzips around a suspended nanotube, then an electrical response from the nanotube should be observed.

A final possibility for confining DNA near a nanotube is functionalization. Star

et al. (2006) at Nanomix, Inc. functionalized nanotubes with single-stranded DNA and measured the change in conductance when the nanotubes were then incubated with the complementary strands, although the solution was dried on the nanotube after each step of their experiment and the nanotube was measured using a back gate. Performing a similar experiment with DNA in solution may also yield an observable signal; Tang *et al.* (2006) showed, however, that the result of Star *et al.* is actually due to DNA hybridization on the contacts. A different functionalization scheme may therefore be necessary to observe a DNA-nanotube interaction.

In conclusion, we have found that controlling the nanotube/DNA geometry is critical in a DNA sensing experiment; it is necessary to confine or immobilize the DNA very close to the nanotube to prevent its charge from being screened by ions in the solution. Although we were unable to conclusively demonstrate electronic DNA detection with our nanotube geometry, some of the above suggestions may enable nanotubes to be used a effective single-molecule probes.

Chapter 9

Nanotube Interactions with Living Cells

In Chapter 8, we saw that simply bringing highly-charged molecules close to nanotube transistors is not sufficient to observe a response. Nevertheless, in the previous experiments discussed in Chapter 5, a number of researchers observed a response that is not simply due to a changing electrostatic potential in the solution. Artyukhin *et al.* (2006), for example, have convincingly shown that nanotubes respond to local electrostatic gating by alternating layers of charged polyelectrolytes. The work of Chen *et al.* (2004) suggests that adsorbed proteins can change the electronic properties of the metal-nanotube contact. In the McEuen group, Zhou *et al.* (2007) have found that the threshold voltage shift caused by covering a nanotube with a supported lipid bilayer is a local effect. And Patolsky *et al.* (2006) have shown that neuron cells can locally change the conductance of non-functionalized nanowires.

In this chapter, we will examine the response of nanotube transistors to living cells, extending the results for supported lipid bilayers of Zhou *et al.* (2007). As seen in Figure 9.1, a living cell membrane is much more complicated than a uniform supported lipid bilayer. In a cell, the bilayer contains a complicated structure of membrane proteins that are of critical importance for cellular functions such as communication with other cells, adhesion to external structures, and exchange of nutrients and wastes. It would be exciting to be able to locally probe this membrane structure, which would require a nanoscale probe such as a carbon nanotube. This chapter summarizes our initial results using a nanotube to probe several different types of cell membranes.

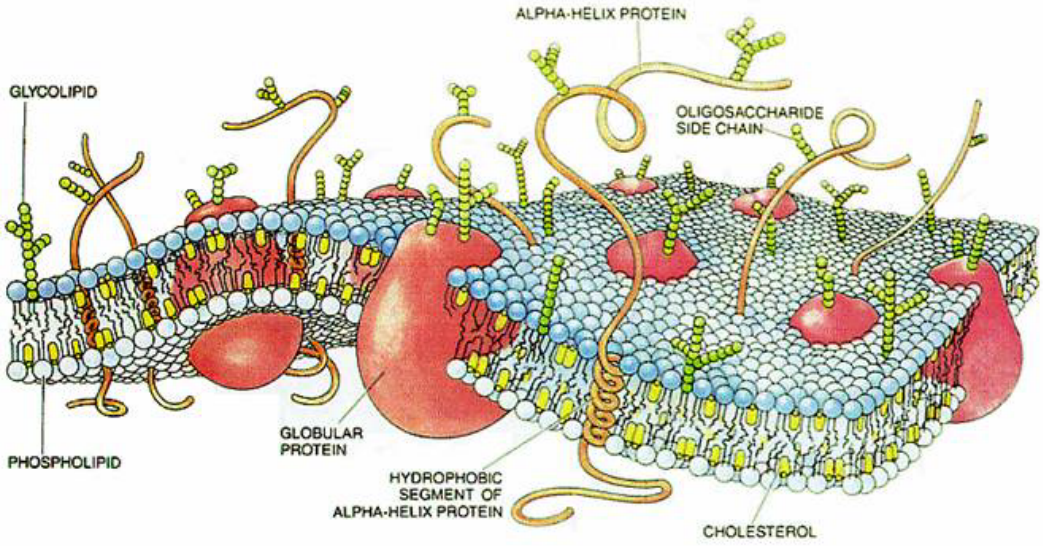

Figure 9.1: Cartoon illustration of a cell membrane, from Bretscher (1985). The plasma membrane is composed of many proteins embedded in a fluid bilayer of phospholipids.

For the experiments in Section 9.1, *Dictyostelium discoideum* amoebae were made to crawl across nanotubes that lay flat on a substrate, and for the experiments in Section 9.2, we used a piezo-controlled manipulator to pick up chromaffin and mast cells with a micropipette and to place them directly on the nanotube devices. For both of these experiments, due to the differences between a living cell and a supported lipid bilayer, the signal obtained with a bilayer was not observed when the cells were on top of non-suspended nanotubes. We will see in Section 9.2, however, that when cells were manipulated over suspended nanotubes, we often observed a negative threshold voltage shift in the device response. This effect may be due to lipid molecules from the membrane binding to the nanotube device. We discuss attempts to further understand these results as well as the future directions of this work in Section 9.3.

9.1 Amoebae Crawling over Nanotubes

In this section, we will discuss experiments in which the current through a nanotube transistor was measured while amoebae crawled over it. Just as the supported lipid bilayers used by Zhou *et al.* (2007) caused a large negative threshold voltage shift, one might expect a similar signal from a real cell membrane that is placed on top of an electrolyte-gated nanotube. These experiments were conducted in Eberhard Bodenschatz's group at the Max Planck Institute for Dynamics and Self-Organization in Göttingen, Germany; Carsten Beta and Katharina Schneider helped with the cell culture.

9.1.1 *Dictyostelium discoideum*

The soil-dwelling *Dictyostelium discoideum* is one of the most commonly studied amoebae; in 2005, for example, it became the first protist to have its genome fully sequenced (Eichinger *et al.*, 2005). *Dictyostelium* spends most of its life crawling around leaves and soil to feed on bacteria, but starving *Dictyostelium* will signal each other with cyclic adenosine monophosphate (cAMP) and will crawl together into a mound of 10^4–10^5 cells. This aggregate can form a slug to search for food elsewhere, or become a fruiting body with a sacrificial stalk supporting a mass of spores (Friedl *et al.*, 2001). Although this is a fascinating example of collective behavior, this mound is too large to probe with a nanotube. But because starving *Dictyostelium* cells will follow gradients in cAMP, a process known as chemotaxis (Haastert and Devreotes, 2004), we have a useful laboratory handle for making these cells walk where we want.

As mentioned above, a living cell's membrane is an uneven surface full of

membrane proteins. While a supported lipid bilayer can be in contact with the substrate, most of the cell membrane is actually 100–150 nm off the surface. Cell-substrate distances have been measured by interference-reflection microscopy (IRM) and electron microscopy: as illustrated in Figure 9.2(a), the cell can reach within 10–15 nm of the surface at focal contacts, and within 30 nm at close contacts (Verschueren, 1985; Giebel *et al.*, 1999). The actual adhesion mechanism at these contacts remains largely elusive for *Dictyostelium* (Titus, 2004), although at least one adhesion receptor protein, SadA, has been identified so far (Fey *et al.*, 2002). Uchida and Yumura (2004) have used IRM and confocal fluorescence microscopy to study the dynamics of actin filaments near the cell membrane, which are important in cell adhesion; their model of *Dictyostelium* migration is seen in Figure 9.2(b).

One might consider a nanotube to be an ideal tool to improve our understanding of *Dictyostelium* adhesion. The proteins involved in adhesion are typically only a few nanometers wide; for example, SadA is predicted to have a molecular weight of 105 kD (Fey *et al.*, 2002), so it should have a width of less than 5 nm. To study the behavior of nanoscale objects, one would like a probe that is at least that small; a nanotube is therefore a logical choice.

9.1.2 Measurement Setup

Dictyostelium cells are relatively easy to grow in culture, and the processes of culturing and counting them are described in Appendix F. The components of the HL5 medium used for cell culture and the phosphate buffer used for experiments are also presented there in Table F.1. The phosphate buffer has an ionic strength, as defined in Equation 3.12, of 100 mM.

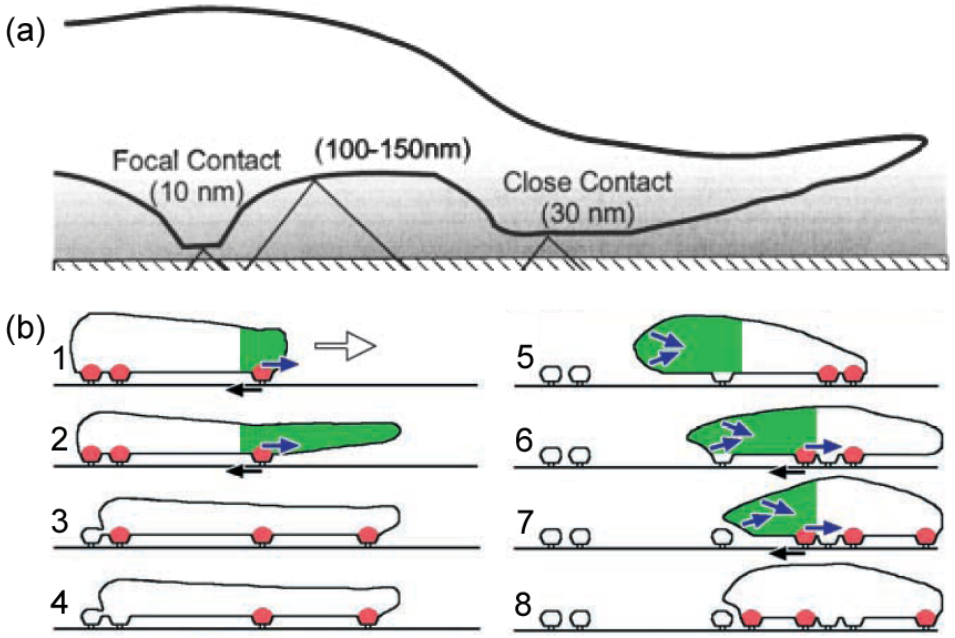

Figure 9.2: Cell-substrate distance and *Dictyostelium* adhesion model. (a) Most of a cell membrane is separated by 100–150 nm from a planar surface. The two types of contacts to the surface are focal contacts, in which a small cell region (1 μm wide and 2–10 μm long) reaches within 10–15 nm of the substrate, and close contacts, in which a larger area of the cell is 30 nm from the substrate. (Figure from Giebel *et al.*, 1999.) (b) A model of *Dictyostelium* migration, from Uchida and Yumura (2004). At the pink adhesion sites, actin filaments link the cell cytoskeleton to the substrate through putative transmembrane adhesion proteins. The role of the actin filaments in these cellular "feet" is not understood, but they suggest several possibilities, including the possibility that the actin foci may act as suction cups to mediate non-specific adhesion. Blue arrows represent the motive force applied when the cell's motor proteins contract its actin filaments, putting it under tension. Black arrows represent the traction force transmitted through the adhesion sites. There are separate extension (1–4) and retraction (5–8) phases.

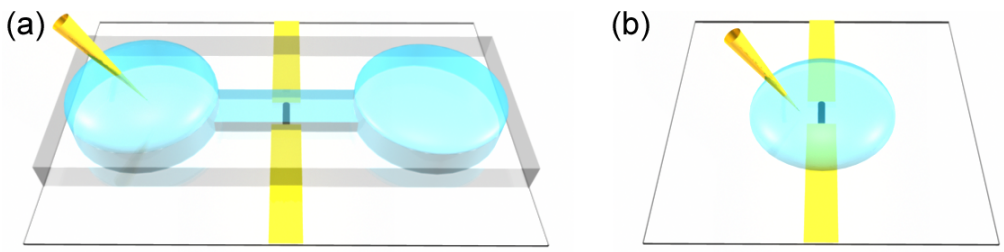

Figure 9.3: Measurement schematic for *Dictyostelium* measurements. The cells in buffer were either (a) placed in a PDMS channel that was sealed over the nanotube device or (b) placed directly over the nanotube with no PDMS.

Since we wanted to image the cells using an inverted microscope, we fabricated nanotube samples on 170-μm-thick fused silica wafers, as described in Section 6.1. As seen in Figure 9.3, for some experiments a PDMS channel (60–100 μm wide and 70 μm high) was sealed over the nanotube devices, while for others a drop of buffer was placed directly on the chip with no PDMS.

The nanotube was electrically measured using the AC setup described in Section 6.4, except without the current preamplifier. Instead, the current was calculated using the lock-in preamplifier to measure the voltage across a 10 kΩ resistor. The typical source-drain bias was $V_{\mathrm{sd}} = 50$ mV RMS.

9.1.3 Nanotube Response

When a large number of cells were introduced into a PDMS channel with a nanotube transistor gated by a gold wire, a threshold voltage shift of around $\Delta V_{\mathrm{th}} \approx -0.2$ V was typically observed. An example of this shift is seen from the black to the red curve in Figure 9.4, although we also see that this shift is observed whether or not there are cells over the nanotube devices.

From the results in Chapter 7, we know that interactions of an analyte with

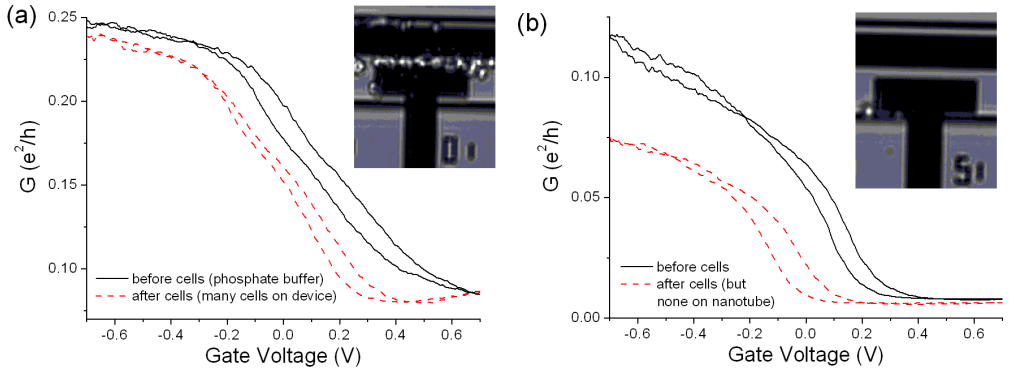

Figure 9.4: Conductance vs. gate voltage before and after large numbers of *Dictyostelium* cells are added to a PDMS channel over different non-suspended nanotube devices. A threshold voltage shift of $\Delta V_{\text{th}} \approx -0.2$ V was typically observed, whether or not there were cells over the nanotube devices (as seen in the insets). The background solution was phosphate buffer.

the gold gate wire can have a large effect on the nanotube conductance, even when the analyte is not close to the nantube, so we checked our results using a Ag/AgCl reference electrode. In Figure 9.5, we see that the threshold voltage shift observed with a gold gate wire disappears when the device is instead gated with the reference. This result suggests that the threshold voltage shift may be due to the cells (or some chemical released by them) interacting with the gold gate wire and changing the electrostatic potential of the solution.

To further investigate whether there is any local interaction between the nanotube and the *Dictyostelium* cells, we measured the nanotube conductance while the amoebae walked on top, as seen in Figure 9.6. These measurements were performed not in a PDMS channel, but in a large droplet of solution (around 10 μL) placed directly on the nanotube device. To make the cells walk over the nanotube, 10 μM cAMP was loaded in a micropipette (Eppendorf Femtotip, opening inner diameter of 0.5 μm), which was moved with a micromanipulator (Eppen-

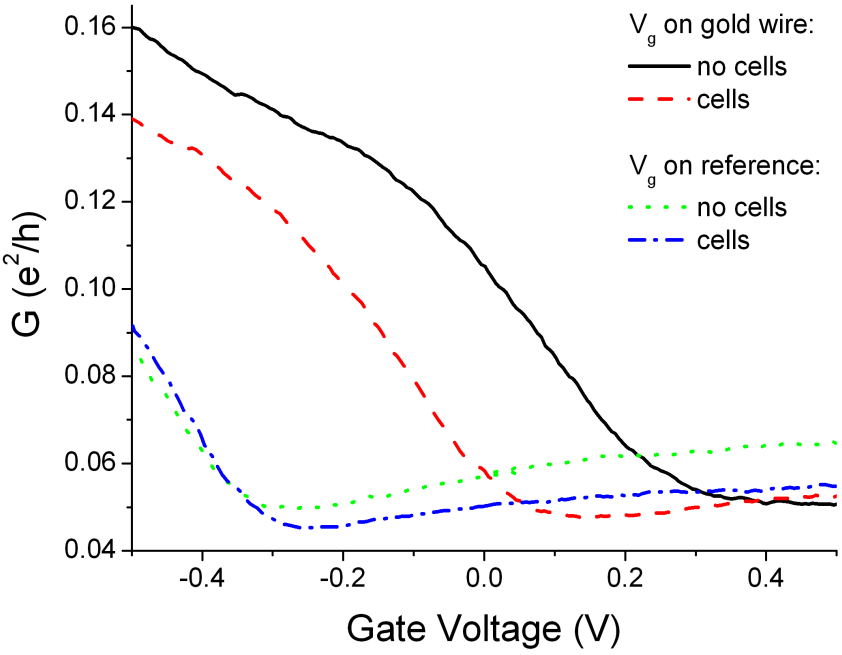

Figure 9.5: Conductance vs. gate voltage when *Dictyostelium* is added to a PDMS channel with a nanotube. The threshold voltage shift observed when the gate voltage is applied to a gold wire disappears when a Ag/AgCl reference electrode is used instead. The background solution was phosphate buffer.

dorf PatchMan) inside the solution droplet. After a few minutes, chemotactic cells would crawl towards the cAMP-filled pipette.

From the data in Figure 9.6, we see no noticeable change in the conductance as the cells walk on and off the nanotube, aside from a slow decay due to evaporation from the solution, which had to be periodically replenished.

The most likely reason for our lack of signal is that the cells did not get close enough to the nanotubes to cause any effect. These measurements were performed in phosphate buffer, which has an ionic strength of 100 mM, as seen in Table F.1, corresponding to a Debye length of less than 1 nm (Eq. 3.11). Although some portion of the cell (or an extracellular protein) must touch the substrate, when we look back at Figure 9.2(a), we see that almost all of the cell is at least 10 nm, and often 100 nm, away from the surface. Most of the cell charge will therefore be electrostatically screened from the nanotube. The parts of the cell that do touch the surface may be so widely spaced that they never happened to land on a nanotube, or so small that their effect on the nanotube is negligible.

9.2 Micropipette Cell Manipulation over Nanotubes

After observing no change in a nanotube's conductance due to *Dictyostelium* amoebae crawling overhead, we performed some similar experiments with non-motile chromaffin and mast cells. These cells were positioned over the nanotubes using a micropipette manipulator. As we will see in this section, when these cells were placed over non-suspended nanotube devices, we again observed no change in the nanotube conductance. When they were placed on suspended nanotubes, however, a large negative threshold voltage shift was sometimes observed, perhaps due to the nanotube interaction with the lipid molecules in the cell membrane.

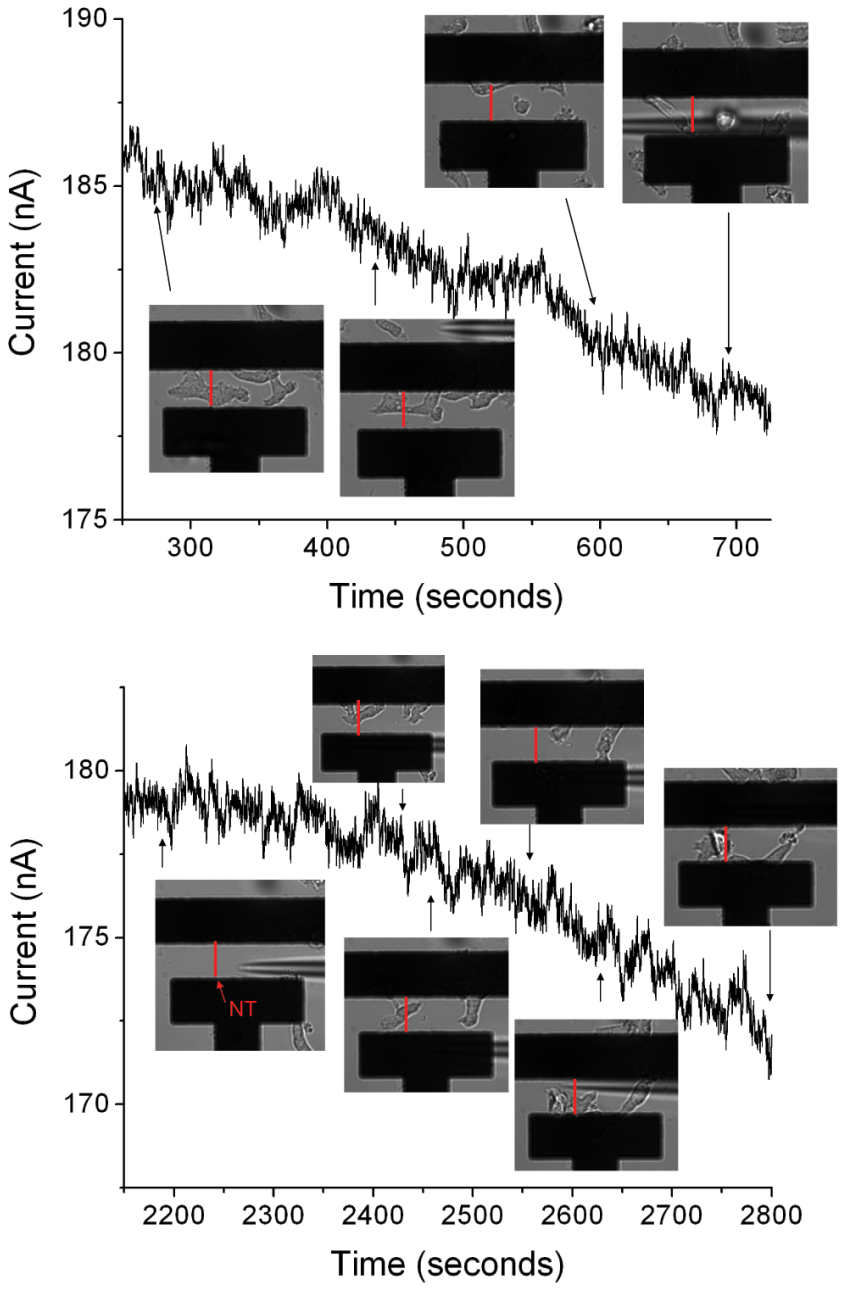

Figure 9.6: Current through a carbon nanotube (with $V_{\mathrm{sd}} = 50$ mV) as *Dictyostelium* cells crawled over its surface. The location of the nanotube, as determined by earlier AFM imaging, is shown in red. There is no observable change in the electrical response of the nanotube due to the cells, aside from a slow decay in the current due to evaporation from the phosphate buffer. The dark shadow observed in some images is the tip of the cAMP-filled micropipette that was used to induce the amoebae to walk over the nanotube.

The experiments in this section were performed in collaboration with Samantha Roberts from the McEuen group, who helped with the nanotube device fabrication and measurement, and Kassandra Kisler from Manfred Lindau's group in the Applied Physics Department at Cornell University, who was responsible for the cell manipulation.

9.2.1 Chromaffin and Mast Cells

Chromaffin and mast cells, unlike *Dictyostelium* amoebae, do not naturally live as individual organisms. Both are found inside humans and other animals, and they can be removed for experiments on individual cells. We used them for our experiments because they are widely available, so our collaborators at Cornell were experienced in culturing and manipulating them.

Unlike *Dictyostelium*, chromaffin and mast cells are non-motile. They will therefore not crawl away from wherever they are placed on a surface, and they will adhere to glass slides. Both kinds of cells are typically 10–20 μm in diameter.

Chromaffin cells are part of the endocrine system, which controls hormonal signaling in the body. They are found in the adrenal medulla and paraganglia, where they create and regulate hormones like adrenaline. They are also part of the sympathetic nervous system, which regulates involuntary behavior, and they are closely related to neurons. They have been widely used as a model system for studying neuronal processes like exocytosis, the extracellular discharge of vesicles (Carmichael and Winkler, 1985; Unsicker, 1993).

Mast cells are created in bone marrow and are found in tissues throughout the body. Their full biological function is not understood. They seem to play an important role in many diseases, but most mast cell investigations have related to

their role in allergic response (Metcalfe *et al.*, 1997).

9.2.2 Measurement Setup

Like for the experiments with *Dictyostelium*, nanotube devices were fabricated on fused silica wafers (500 or 170 μm thick), as described in Section 6.1. We performed experiments with both non-suspended and suspended nanotube devices. To make the suspended devices, we plasma-etched 1–2 μm trenches before the nanotube growth. The electrical measurements were performed using the AC measurement setup described in Section 6.4, typically using a source-drain bias of V_{sd} = 5–10 mV RMS.

The cells used in this section were picked up using glass micropipettes (pulled from glass capillaries by Kassandra Kisler) connected to a micromanipulator, which was controlled with an E-463 HVPZT piezo amplifier from Physik Instrumente. By applying suction to the micropipettes, Kassandra was able to pick up cells off the substrate and move them on top of nanotube devices. A brightfield microscope image of a micropipette holding a chromaffin cell over a suspended nanotube is seen in Figure 9.7.

In order for the micropipette to have access to the top of the nanotube devices, the setup shown in Figure 9.3(b) was used, in which a drop of solution was placed over the device without any microfluidic PDMS channel. The chromaffin cells were typically plated in the Lindau lab on small cover slips that were placed on the corners of the nanotube chips. A large drop of buffer was then used to connect the nanotube and the cover slip so that the cells could be moved over the nanotube while remaining in solution. The mast cells were provided in solution by Jose Moran-Mirabal from the Craighead lab. They were then spun down in a centrifuge

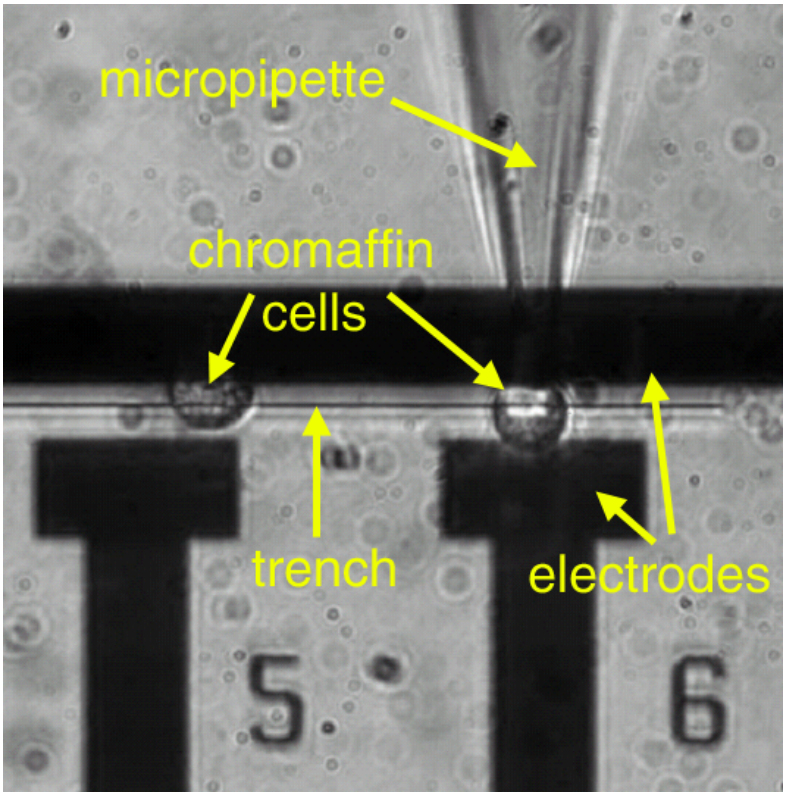

Figure 9.7: Brightfield image of a chromaffin cell over a suspended nanotube. The spacing between the source and drain electrodes is 10 μm. A micropipette is seen holding a cell over device 6, while a second cell is seen over device 5. The other smaller circles are dust in the microscope optics.

so that their medium could be removed, and they were resuspended in buffer for our experiments. This buffer was then deposited in a large drop over the nanotubes.

The buffer used in both cases is described in Appendix F. It has a total ionic strength of 176 mM; the Debye length in this buffer is about 0.7 nm (see Eq. 3.14). The cells would therefore need to be within a nanometer of the nanotubes for a signal to be observed.

For all of our experiments with nanotubes, we added the buffer containing the cells and measured the conductance as a function of gate voltage before and after a cell was placed on the nanotube. The gate wire was either a gold wire, as for the experiments in Chapters 7 and 8, or a Ag/AgCl pellet attached to a silver wire (E. W. Wright, Guilford, CT). Note that this Ag/AgCl pellet is different from the Ag/AgCl reference electrode used for the electrochemistry experiments in Chapter 7; it lacks a porous frit, and just like the gold wire it will set the electrochemical potential, not the electrostatic potential.

By measuring the initial G vs. V_{g} curve after the cells were in solution but before one was placed on the nanotube, we were able to avoid the false signal seen in Figure 9.4, in which simply adding the cells to the buffer caused a threshold voltage shift, regardless of whether the cells were on the nanotube. Since the electrolyte-gate wire sees the same solution whether a cell is on the nanotube or not, any threshold voltage shift would be due to the nanotube-cell interaction.

9.2.3 Nanotube Response

In our initial experiments, chromaffin and mast cells were placed on top of non-suspended carbon nanotube devices. As seen in Figure 9.8, however, the conductance versus gate voltage was unchanged by the presence of a cell over the

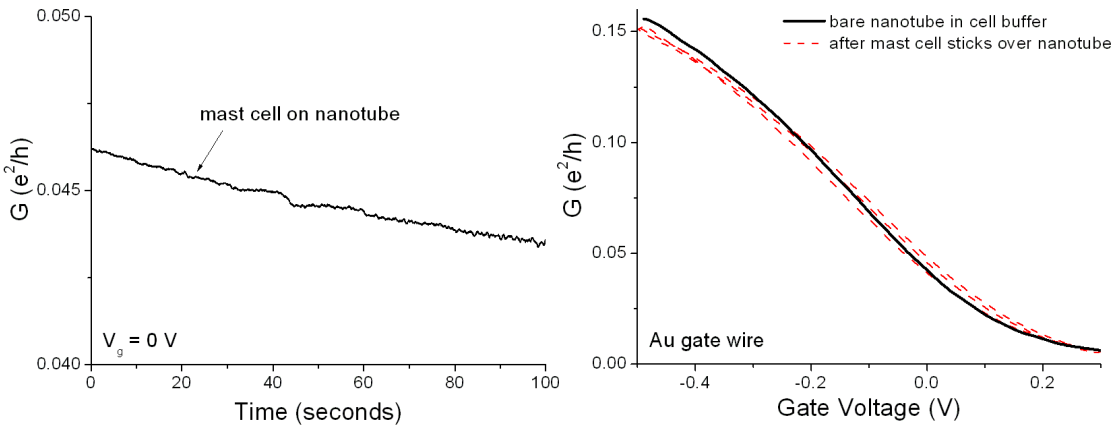

Figure 9.8: Response of a non-suspended nanotube to a mast cell. No dramatic change in the conductance occurred as a mast cell was lowered over the nanotube; there was simply a slow decay with time as the solution evaporated. The conductance versus gate voltage also remained the same before and after a mast cell was placed over the nanotube, even though the cell was firmly stuck to the surface above the nanotube.

nanotube, even when the cell was firmly stuck to the substrate.

When the nanotubes were suspended over 1–2 μm trenches, however, a negative threshold voltage shift was often observed, which corresponds to a decrease in conductance as the cell is placed over the nanotube for a p-type device. Figures 9.9 and 9.10 show six examples of this signal, with graphs of both the conductance as a function of time as the cell is lowered onto the nanotube and the conductance as a function of gate voltage before and after the cell was lowered. In at least four of these cases, the cell was difficult to remove from the surface and left behind a cellular residue that was visible with brightfield microscopy. After the cells were removed, the conductance curve did not shift back to its original position, as seen in Figure 9.9(a-b). Placing a second cell on the device resulted in no change or in a smaller second shift.

In one experiment, the reverse signal (a positive threshold voltage shift) was

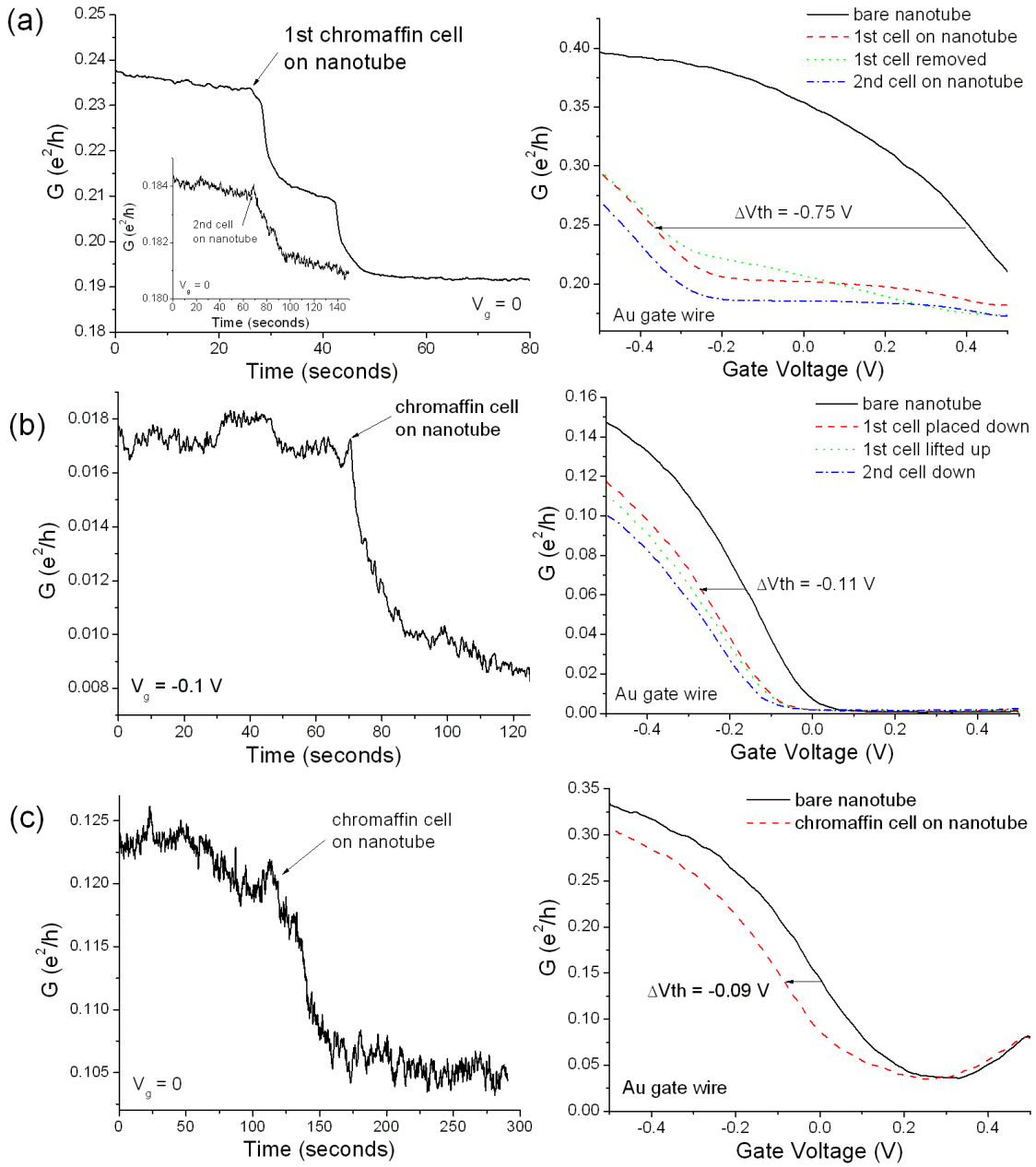

Figure 9.9: Response of suspended nanotubes to chromaffin cells. G vs. t and G vs. V_g are shown for three different nanotube devices, all of which show a negative threshold voltage shift after a cell is placed on top of them.

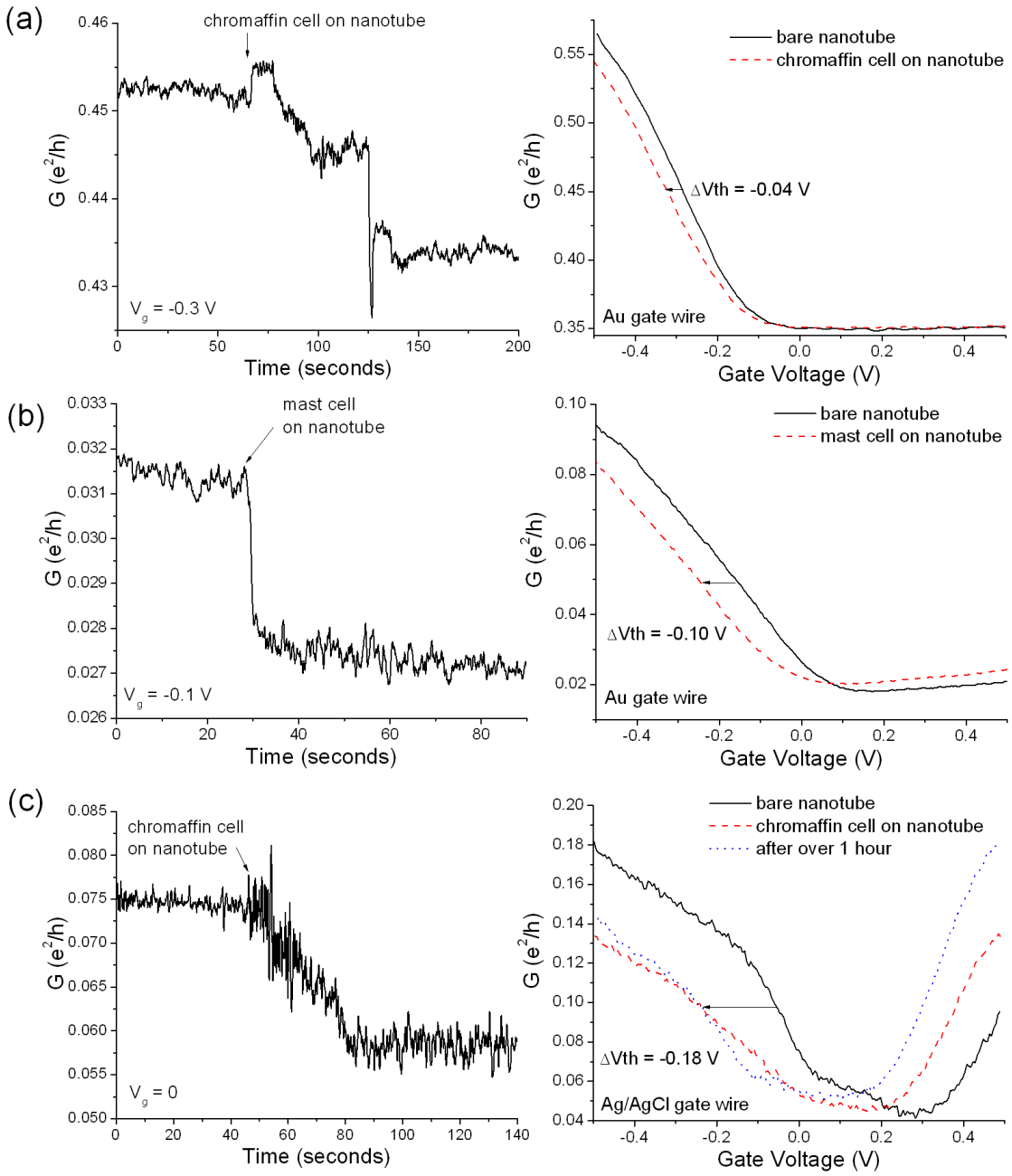

Figure 9.10: Response of suspended nanotubes to chromaffin and mast cells. As in Figure 9.9, G vs. t and G vs. V_g are shown for different nanotube devices, which show a negative threshold voltage shift after a cell is placed on top of them.

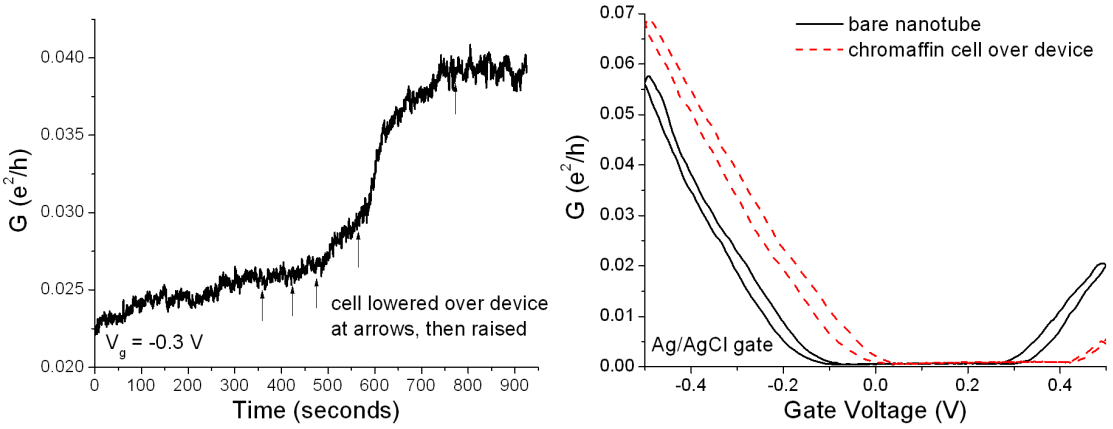

Figure 9.11: Atypical response of a suspended nanotube to a chromaffin cell. In this one experiment, a positive threshold voltage shift was observed after placing a chromaffin cell near the nanotube. Since the exact location of the nanotube was unknown, the cell was repeatedly lowered onto the substrate (at the locations marked by arrows), and then raised (shortly before the next arrow) and relowered. The conductance began increasing before a cell was placed on the device (usually the conductance slowly decays with time as solution evaporates), and then it increased more sharply after the cell was lowered the third and fourth time, which corresponded to a positive threshold voltage shift. A Ag/AgCl pellet was used as the electrolyte gate.

observed, as seen in Figure 9.11. It is unclear, however, if this reflects a real physical effect, since the nanotube conductance was increasing before any cell was lowered on the device, rather than slowly decaying as usual.

A response from the nanotube was not observed every time a cell was lowered over a conducting device. Sometimes, the experiment would fail for technical reasons, such as the nanotube ceasing to conduct or the solution over the nanotube evaporating. In most of the other cases when no signal was observed, the location of the nanotube was unknown, and it was necessary to guess where to put the roughly 15-μm-wide cell on the 40-μm-wide device. In other cases, dye molecules that were placed in the solution to image the cells better may have bound to the

nanotubes and prevented it from interacting with the cell. When an undyed cell was placed over a nanotube of known location, we did observe a signal, but we cannot yet say how reproducible this response is.

The nanotube response may also be related to the adhesion of the cell to the surface. In almost all of the experiments where a nanotube response was observed, we noticed that the cell seemed to stick firmly to the surface after being lowered over the nanotube: when the pipette holding the cell was lifted, either the cell remained on the surface instead of sticking to the pipette, or a visible residue remained on the surface, indicating that the cell was no longer intact. In most of the experiments where no response was observed, the cell was easily lifted intact from the surface, and it could also be slid along the surface with the pipette. These differences in cell adhesion can be related to both the surface properties of the substrate and of the cell, and are currently being investigated.

We also see in Figures 9.9–9.11 that the change in nanotube conductance generally occurs on a time scale of 20–40 seconds. This slow response is not due to the cell being slowly lowered over the nanotube with the pipette, since the pipette has always stopped moving before the conductance change is observed, at the locations marked by arrows in the conductance versus time graphs. The exception is the 2-second response to a mast cell in Figure 9.10(b); we do not have enough data, however, to state whether this faster response is caused by using a mast cell instead of a chromaffin cell, or whether it is an anomaly of that one experiment.

9.2.4 Analysis

From the experiments described in Section 9.2.3, we can conclude that placing a chromaffin or mast cell on a suspended nanotube device generally causes a negative

threshold voltage shift of about −0.1 V, and that this shift occurs over a time scale of about 30 seconds after the cell is placed on the device. This shift remains even after the cell is removed from the device. The mechanism behind this response, however, remains unclear. It may be related to the negative threshold voltage shift of around −0.2 V that Zhou *et al.* (2007) observed when they placed neutral supported lipid bilayers on non-suspended nanotubes, but the origin of their response was also unknown.

To better understand our results, we would like to know how the cell is interacting with the nanotube. As seen in Figure 9.12, there are three basic possibilities for the nanotube-cell configuration: the nanotube can remain outside the cell, it can be in the middle of the cell membrane, or it can be inside the cell. Because the lipid tails of the phospholipids making up the membrane are hydrophobic, the interfacial energy would be lowest if the nanotube were inside the membrane, as discussed in Section 3.2.4. The three different configurations are also all possible for the non-suspended section of the nanotube; if the suspended section moves into the middle of the cell membrane as in Figure 9.12(b), it could help the non-suspended sections overcome their van der Waals attraction to the surface and also move inside the membrane.

For the suspended nanotube to move inside the membrane, the energy required to transport the nanotube through the membrane would have to be overcome, either by the thermal energy of the nanotube's motion—there is typically 5–10 nm of slack in a 1-μm-long suspended nanotube (Minot *et al.*, 2003)—or the mechanical energy of pushing the cell over the nanotube with the pipette. There is little data, however, to help us determine how difficult it is for the nanotube to pass into the membrane. DNA-solubilized nanotubes cannot easily pass through a mem-

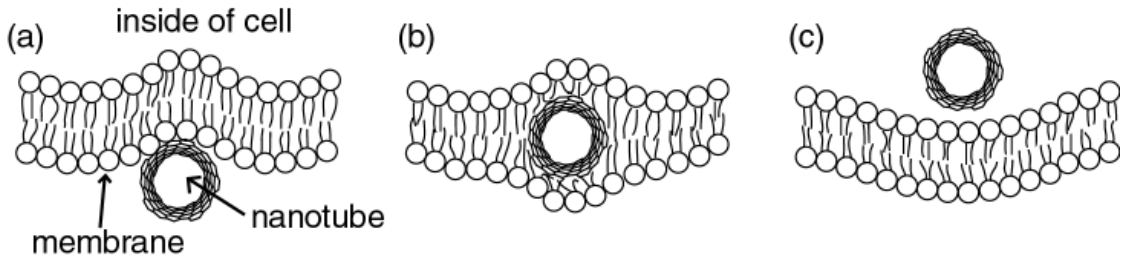

Figure 9.12: Possible configurations for the nanotube-cell interaction. When a cell is lowered onto a suspended nanotube, parts of the nanotube could be located (a) outside the cell membrane, (b) in the hydrophobic middle of the membrane, or (c) inside the cell.

brane: they are only internalized by cells through energy-dependent endocytosis, in which the cell membrane wraps itself around an object and pinches off a vesicle to transport it inside (Kam *et al.*, 2005). These DNA-solubilized nanotubes are hydrophilic, however, unlike our hydrophobic bare nanotubes, so one would expect an energy barrier for them to pass through the hydrophobic membrane. Multiwalled nanotubes (with diameters of 10–20 nm) have been used to pierce cell membranes and deliver quantum dots (also with diameters of 10–20 nm) without damaging the cells (Chen *et al.*, 2007). Our single-walled nanotubes should be able to pass through the membrane more easily than this, although they are passing through horizontally, while Chen *et al.* (2007) used an AFM tip to bring nanotubes perpendicular to their membranes.

9.2.5 Imaging Cells on Suspended Nanotubes

To determine whether the nanotube is preferentially located inside the membrane, we must have a better method of visualizing the cell than brightfield microscope images like the one in Figure 9.7. We have performed a number of experiments with total internal reflection fluorescence (TIRF) microscopy and confocal microscopy,

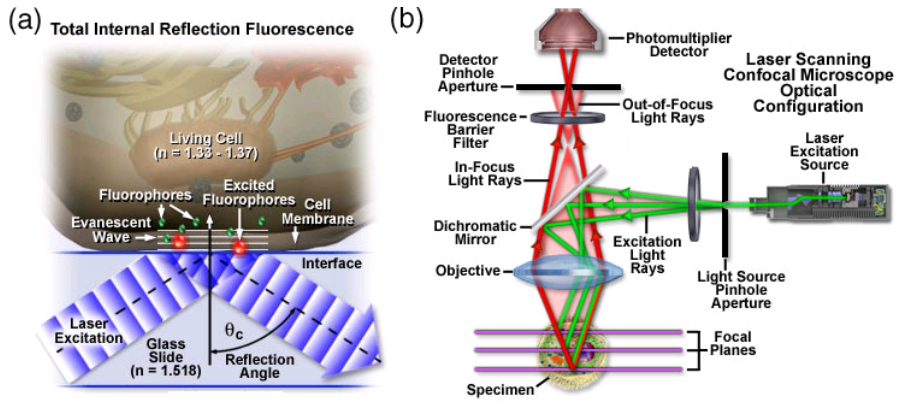

Figure 9.13: Cartoon illustrations of total internal reflection fluorescence (TIRF) and confocal microscopy, taken from `http://www.olympusmicro.com`. (a) In TIRF microscopy, only fluorophores within the penetration depth of the evanescent wave are excited, allowing imaging of a slice less than 100 nm thick. (b) In confocal microscopy, a pinhole is used to select the in-focus signal from. Slices can be imaged up to 500-μm deep in a sample, with diffraction-limited thicknesses around 500–800 nm.

which we will discuss below. We have found, however, that it is even difficult to tell if the cell is in the trench, much less whether the nanotube is inside the cell.

TIRF microscopy is the best microscopy technique for imaging a very thin slice of a sample that is next to a surface. As the cartoon in Figure 9.13(a) illustrates, an incident light beam totally internally reflects off a coverglass surface on which a sample is sitting. The evanescent wave generated during this reflection reaches a penetration depth given by

$$d_{\mathrm{p}} = \frac{\lambda}{4\pi\sqrt{n_{\mathrm{glass}}^2 \sin^2\theta - n_{\mathrm{sample}}^2}}, \tag{9.1}$$

where λ is the wavelength of the incident light, θ is the angle of incidence, and n_{glass} and n_{sample} are the indices of refraction of the coverglass and the sample. This evanescent wave excites fluorophores that are within d_{p} of the bottom of the sample, and the light they emit is observed. This produces an image of a section

of the sample that is less than 100 nm thick (Toomre and Manstein, 2001).

It becomes more difficult to interpret the results of TIRF microscopy, however, when the substrate contains a 1-μm deep trench, rather than being the flat coverglass illustrated in Figure 9.13(a), since the incident angle θ will change across the surface and not all of the light will be totally internally reflected. Figure 9.14 shows three examples of cells imaged with both brightfield and TIRF microscopy; two of the cells were stained with $DiIC_{18}(3)$, and one with FM1-43.[1] Because of the objective used, all devices that we wanted to examine with TIRF microscopy had to be fabricated on 170-μm-thick substrates. The trench is most visible in the TIRF image of the cell dyed with FM1-43, but we cannot conclude from this image whether or not the cell is going into the trench.

Another example of TIRF imaging is seen in Figure 9.15. In this case, the cell is on top of the carbon nanotube whose conductance response is seen in Figure 9.10(c). The location of the nanotube was determined earlier through photocurrent imaging, as seen in Figure 9.15(a). For this experiment, no dye was used on the cell, but water-soluble fluorescein dye was added to the buffer solution after observing the conductance response. In Figure 9.15(d), we see that the undyed cell shows up in the TIRF image as a dark circle surrounded by the fluorescent solution. The trench is brighter than the substrate surface both under the cell and far away from it, which makes sense if light was not totally internally reflected there so that more dye molecules were excited, and which also suggests that the cell may not be

[1] $DiIC_{18}(3)$ and FM1-43 (both available from Molecular Probes) are membrane dyes, and are only fluorescent when they are incorporated into a cell membrane. $DiIC_{18}(3)$ is a lipophilic dye with long hydrocarbon chains that allow it to incorporate itself inside a cell membrane. FM1-43 is amphiphilic, with a positively charged head and a hydrophobic tail, allowing it to line up next to the phospholipids in a membrane. It is also known as a voltage-sensitive dye, so that only dye molecules that are exposed to the potential difference across a cell membrane will fluoresce.

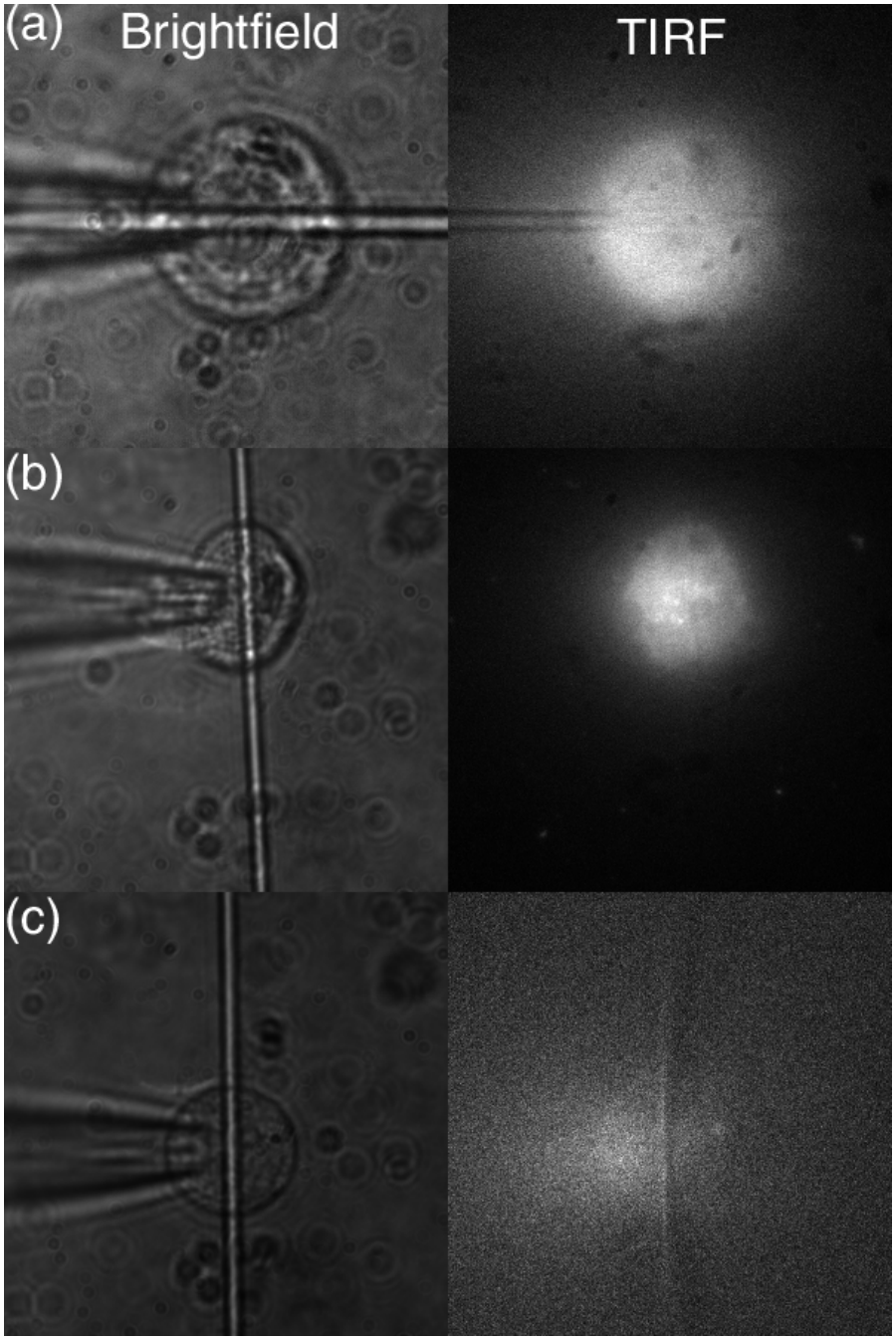

Figure 9.14: Brightfield and TIRF imaging of a cell over a 1-μm-wide trench. The three images on the left are brightfield pictures of a chromaffin cell held by a micropipette over a trench, and the three images on the right show the same cells imaged with TIRF microscopy. Cells (a) and (b) were dyed with $DiIC_{18}(3)$, and cell (c) was dyed with FM1-43. Cells were dyed and imaged by Kassandra Kisler.

occupying the trench fully.

A second microscopy technique that we investigated to determine whether the cells are inside the trenches is confocal microscopy. These experiments were performed using the Zeiss LSM Live Confocal Microscope in Itai Cohen's group; Mark Buckley and Jonathan McCoy provided microscope training. In a confocal microscope, a pinhole is used to select the in-focus signal preferentially, eliminating most of the background fluorescence, as seen in Figure 9.13(b). The focused laser is scanned across the sample, and a computer combines the fluorescence from different points (or lines, in the case of the Cohen group's microscope) to create a two-dimensional image of a slice through the sample. The thickness of this slice is diffraction limited to 500–800 nm, depending on the wavelength and optics used.

Figure 9.16 shows some of the images taken of our devices using a confocal microscope. When a fused silica substrate with a 4-μm-wide trench was coated with fluorescein dye, the trench fluoresced more brightly in the confocal images that the substrate surface. The fluorescence in the middle of the trench and away from the trench both decay as the confocal sections move down into the substrate, and these two decay curves line up when shifted 1.5 μm with respect to one another. The fluorescence decays more slowly than might be expected (5 μm deep into the substrate it has only dropped by a factor of two), but the dye concentration was very high. Because the decay curves can be simply translated on top of one another, we infer that the bottom of the trench is 1.5 μm lower than the substrate surface. AFM measurements showed that the trench depth is 1.6 μm, in excellent agreement.

When we repeated these measurements on a chromaffin cell that had been plated over a 4-μm-wide trench, as seen in Figure 9.16(d-f), the results are less

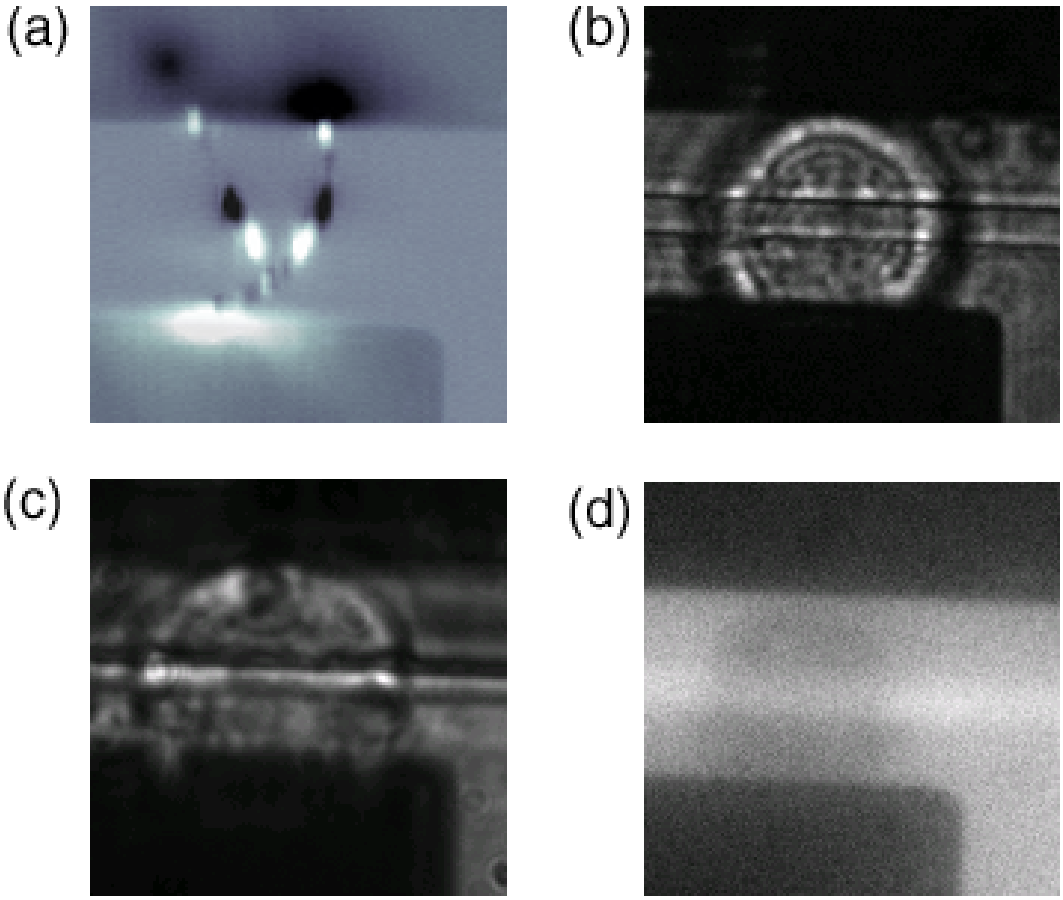

Figure 9.15: Brightfield and TIRF imaging of a cell over a nanotube. (a) Photocurrent signal showing nanotube locations, as discussed in Section 6.2.2, superimposed on reflected light signal showing metal electrodes. The spacing between electrodes is 10 μm. (b) Brightfield image of a chromaffin cell over these nanotubes. (c) Brightfield image of the same cell in a different focal plane. (d) TIRF image after adding fluorescein dye to solution around cell. The undyed cell is visible as a dark circle. Brightfield and TIRF images were taken by Kassandra Kisler.

clear. Away from the cell, the fluorescence in the trench is again brighter than outside the trench. The undyed cell is seen as a dark circle, and if it were fully occupying the trench, one would expect to see no difference in the fluorescence intensity inside or outside the trench underneath the cell. The trench is brighter under the cell, however, suggesting that there is dye in at least some of that area. It is difficult to tell from these images, however, whether the cell is halfway down the trench or simply resting on top of it. We also confocally imaged cells that had been dyed with FM1-43, but we were unable to gain any additional information from these images.

Other optical microscopy techniques that could be used to study our nanotube/cell configuration are phase contrast and differential interference contrast (DIC) microscopy, which are both used to provide contrast when imaging unlabeled transparent specimens like cells. In phase contrast microscopy, the phase of the light passing through the sample is collected, resulting in a (nonlinear) map of the optical path length through different parts of the sample. This optical path length depends on the specimen thickness and index of refraction, and since cells typically have a higher index of refraction than their surrounding medium (about 1.36 versus 1.335), they show up with much higher contrast than in brightfield microscopy (Murphy *et al.*, 2007a). In DIC microscopy, different optical techniques are used to obtain a map of the gradients in optical path length, or the derivative of a phase contrast image (Murphy *et al.*, 2007b). DIC is therefore a powerful technique for edge detection. As mentioned in Section 6.2, large multiwalled nanotubes and nanotube bundles in solution can be imaged equally well with DIC or phase contrast microscopy, although these techniques have not been used to see single-walled nanotubes (Prakash *et al.*, 2003). In principle, DIC microscopy could

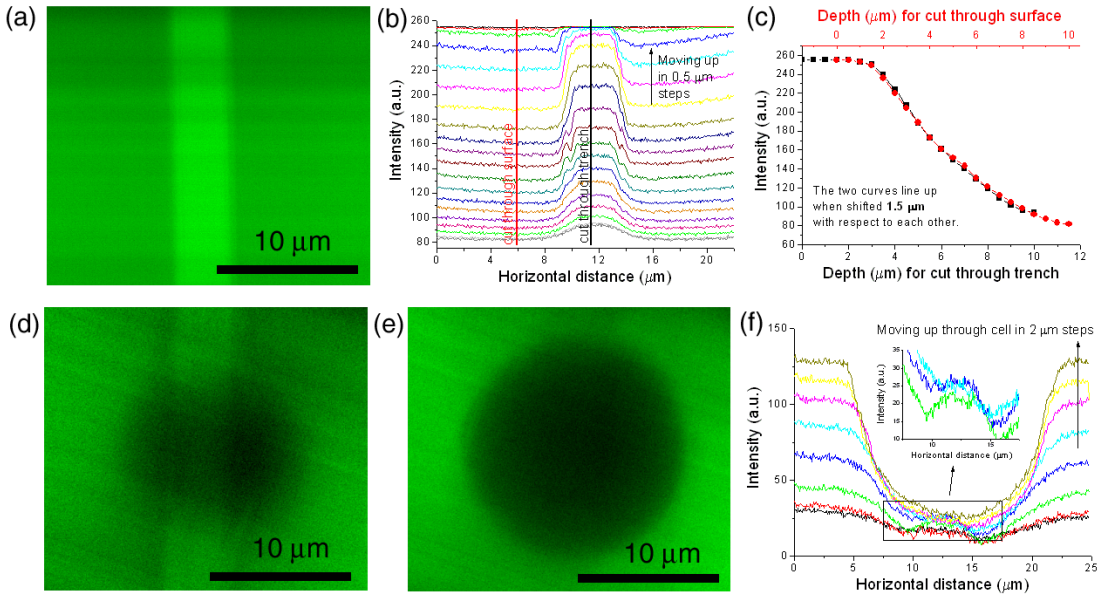

Figure 9.16: Confocal microscopy imaging of a cell on a trench. (a) Confocal image of a 4-μm-wide trench on a 170-μm-thick slide covered with fluorescein dye. The trench fluoresces more brightly than the bare surface. (b) The average intensity as a function of horizontal distance in a series of images like (a), separated by 0.5 μm. (c) Intensity as a function of vertical distance along the red and black lines through (b). The fluorescence seen in the trench and on the surface both decay as the focal plane moves deeper into the slide, and the two curves overlap when shifted by 1.5 μm with respect to each other. The trench depth measured with an AFM is 1.6 μm. (d) Confocal image like (a), but with a chromaffin cell plated over the trench and a lower fluorescein concentration. (e) When the focal plane is shifted higher than in (d), the undyed cell can be clearly seen as a dark circle. (f) Average intensity along a slice through the cell shown in (d) and (e) for images separated by 2 μm. We thank Itai Cohen's group in the Physics Department for the use of their confocal microscope.

be used to image diffraction-limited slices of a sample, but this technique is rarely used, and it is unlikely that we could gain more information from DIC than we have from confocal microscopy.

A more promising tool for obtaining useful information about our cells is a scanning electron microscope (SEM), which takes advantage of the very short wavelength of electrons (12.3 pm in a 10 kV SEM) to take much higher resolution images than are possible with any visible light microscope, making it possible to image single-walled carbon nanotubes. The main disadvantage of an SEM is the sample preparation required: the cells must be fixed and frozen, and our insulating fused silica substrate must be coated with a thin layer of metal to make it conducting. If these steps are taken after a cell is placed on a nanotube and the conductance signal is observed, then it may be possible to obtain a high-resolution image of the cell position relative to the nanotube and the trench.

Finally, a different and exciting option for imaging the nanotube/cell system is scanning photocurrent microscopy. As discussed in Section 6.2.2, these photocurrent measurements can be used to visualize conducting nanotubes even when the nanotubes are immersed in solution, and we observe a strong photocurrent signal wherever the nanotube bands bend, which tells us about the local electric fields. We would therefore expect the photocurrent signal to change if a nanotube is lifted up into a cell membrane, and we should be able to correlate these changes with the electrical signal. These measurements should also make it possible to determine whether the whole nanotube is lifted into the cell, or only the suspended portion.

9.3 Conclusions and Future Directions

We have shown that placing chromaffin or mast cells on a suspended carbon nanotube with a micropipette often causes a negative threshold voltage shift in the nanotube conductance, although these cells and crawling *Dictyostelium* amoebae give no response when they are on non-suspended nanotubes. This threshold voltage shift generally occurs over a roughly 30-second time scale after the cell is placed on the nanotube, and it is not reversed when the cell is removed from the nanotube. This removal is often difficult, due to the adhesion of the cells to the surface, and a visible cellular residue is often left behind on the surface.

The nanotube response may be related to the hydrophobic nanotube moving up into the middle of the cell membrane, although it is necessary to obtain more information about the cell configuration to verify this theory. We have attempted to visualize the chromaffin and mast cells using TIRF and confocal microscopy, but the resulting images have been difficult to interpret. It would probably be more fruitful to freeze a cell on a nanotube after an experiment, to coat the system with metal, and to examine it with an SEM. Scanning photocurrent microscopy should also provide useful information about the nanotube behavior, and has the advantage that it could be done concurrently with the placement of the cell on the nanotube.

Another possibility for determining whether the nanotube enters the cell is functionalizing the nanotube. If the nanotube were attached to a molecule that fluoresces when bound to something inside the cell or the cell membrane, then one could look for a line of fluorescence after the cell is placed on the nanotube. A difficulty with this technique, aside from the complications of functionalization, is that the bound molecules might change the nanotube behavior or its ability to fit

through the membrane.

If the nanotube response is due to its location in the middle of the cell membrane, then placing different amphiphilic molecules in solution, such as the membrane dye FM1-43, should also result in a negative threshold voltage as they bind around the nanotube. This would also explain why no threshold voltage shift was observed when placing cells on nanotubes in a solution containing FM1-43, since there would be no energetic advantage for the nanotubes to enter the cell membranes if they were already coated with dye molecules.

To understand the nanotube-cell interaction better, it could also be useful to begin with a simpler system. For example, before looking at the photocurrent response of a nanotube with a cell on top, it could be easier to use a supported lipid bilayer as a simpler artificial membrane. We could also examine the conductance response of nanotubes to giant unilamellar veiscles (GUVs), which are cell-sized phospholipid vesicles and can approximate the cell membrane without the membrane proteins or other complications. By seeing if a GUV produces the same threshold voltage shift as a cell when it is placed on a suspended nanotube we could determine whether the membrane structure is sufficient to account for the changes we see with cells.

Using GUVs or a different type of cell would also allow us to further investigate the adhesion of cells to the substrate, which has seemed to play an important role in our experiments thus far. It would also be useful to perform more experiments with chromaffin or mast cells on trenches without nanotubes and on bare substrates to determine whether the trenches or the nanotubes play a role in when the cells stick better to a surface or in when they rupture. If the trenches and substrate surface turn out to be a problem, then it would be possible to make longer nanotube

devices that are completely suspended over very deep trenches, so that the cell never touches the fused silica surface as it interacts with the nanotube. We could also learn more about cell adhesion and the nature of our signal by attempting to lift the cell immediately after the first conductance change is observed, rather than waiting 30 seconds for the full change, to see if the signal is still irreversible.

A final tool for investigating this system is to use an electrode inside the micropipette to measure or control the potential inside the cell. For our experiments thus far, we have picked up cells by sealing the pipette to the outside of the membrane, but for better electrical control of the inside of the cell we would want to enter a "whole-cell" patch clamp configuration in which the pipette breaks into the cell center, with the membrane sealed around its edges. The fragile nature of this seal would complicate the cell manipulation, but this configuration would allow us to perform more interesting experiments, such as measuring the change in nanotube conductance in response to an AC signal on the wire.

The electrical response that we have observed from semiconducting carbon nanotubes interacting with individual cells is an important step in the nanoscale electrical probing of biological systems. Through some of the experiments suggested in this section, we hope that the nature of this response will be elucidated, allowing nanotubes to be used for more advanced studies of cellular behavior.

Chapter 10

Conclusions and Future Directions

Carbon nanotubes, with their high electrical sensitivity, nanoscale dimensions, and ability to operate effectively in an electrolyte environment, can be excellent tools for probing the biomolecular world. As we saw in Chapter 5, electrolyte-gated nanotubes have already been used to detect chemicals, surfactants, proteins, and artificial cell membranes. All of these analytes shift the nanotube transistor threshold voltage, but the mechanisms behind this response are not always understood. In this thesis, we have attempted to improve our understanding of the nanotube response to different biochemical molecules and cells, and to use the nanotubes to learn more about these systems.

To perform these measurements, we fabricated a variety of single-walled nanotube devices on both Si/SiO_2 and fused silica wafers, as discussed in Chapter 6. We achieved average nanotube lengths of 10 μm, and many of these devices were suspended over trenches with widths of 1–2 μm. We integrated these devices with different PDMS microfluidic setups to bring the analytes to the nanotubes, and for some experiments, we were able to control the flow speed and direction of the analytes with high precision. We measured the conductance response of the nanotubes to these analytes using an electrolyte gate.

We first presented our results with redox-active transition metal complexes in Chapter 7. These molecules caused a large threshold voltage shift in our nanotube devices, and using a traditional electrochemical setup, we found that the magnitude and direction of the shift were directly related to the redox properties of the molecules as determined by the Nernst equation. We demonstrated that

this response is not related to a local interaction between the molecules and the nanotube; instead, it stems from changes in the chemical potential of the solution, which in turn affect the electrostatic potential that is measured by the nanotube.

In addition to having important implications for the interpretation of other nanotube sensing experiments that have generally not accounted for this effect, our results with redox-active molecules open the door to new kinds of nanoscale electrochemistry experiments. Because the nanotube acts as a nanoscale reference electrode in measuring the electrostatic potential of the solution, it could be used to probe tiny solution volumes that are inaccessible with a traditional reference electrode. We propose one such experiment to measure changes in the oxidation state of a 10-μm-high solution.

In Chapter 8, we discussed our experiments with DNA and highly-charged polystyrene beads, in which we were looking for a local interaction due to electrostatic gating of the nanotube by the analyte. Because the charge of these objects is screened by counterions in the solution at distances greater than the Debye length, it is necessary to bring them in very close proximity to the nanotube. We attempted to overcome this difficulty with our microfluidic design, but we were unable to bring the DNA or beads close enough to the nanotube to observe a consistent signal. Although we sometimes saw spikes in the nanotube conductance after DNA was introduced to the channel, we were unable to determine the cause of this response. We concluded that stronger confinement or immobilization of the molecule is necessary to detect DNA molecules in solution, and we suggest a number of ways this might be accomplished, including nanofluidics, DEP, optical tweezers, and functionalization.

We then described the results of our experiments with living cells in Chapter

9. We explored the response of nanotubes to crawling *Dictyostelium* amoebae and manipulated chromaffin and mast cells. In our experiments with non-suspended nanotube devices, no signal was observed, probably because most of the cell body was not in close contact with the substrate and was thus electrostatically screened from the nanotube. When we placed chromaffin or mast cells on suspended nanotubes, however, we often saw a large negative threshold voltage shift in the nanotube conductance that occurred on a 30-second time scale after the cell was placed on the device. This signal may be due to the nanotube moving into the hydrophobic center of the cell membrane, but we were unable to draw further conclusions without more information about the NT/cell configuration. We discussed attempts to image this configuration with TIRF and confocal microscopy, and we explained how an SEM or photocurrent microscopy might provide more information. We also discussed a number of other directions for this work, including controlling the potential inside the cell through a whole-cell patch clamp configuration, using GUVs or other cells to simplify the system, and suspending nanotubes over larger trenches to eliminate the effect of the substrate.

Our experiments have repeatedly demonstrated that to locally probe any object in solution, bringing it in very close proximity to the nanotube is of critical importance. We have developed a setup to achieve this with living cells and have discussed methods for bringing other molecules closer to our nanotube devices. We have shown that electrolyte-gated carbon nanotubes can be used effectively as nanoscale probes of biomolecular systems, and we have explored the exciting possibilities for these probes in many future experiments and applications.

Appendix A

Tight-Binding Calculation of Graphene Band Structure

As described in Section 2.2, the electronic properties of carbon nanotubes can be inferred from the band structure of graphene. In this Appendix, we calculate the band structure of graphene using the tight-binding approximation.[1] For pedagogical purposes, we neglect both the second-nearest-neighbor interactions and the wavefunction overlap, since this simplified calculation still gives the right qualitative behavior.

For this calculation, we will refer back to Figure 2.2, which shows the real-space lattice and reciprocal lattice of graphene. We recall that the real-space crystal is a honeycomb lattice of carbon atoms with lattice vectors $\vec{a}_1 = (\frac{a\sqrt{3}}{2}, \frac{a}{2})$ and $\vec{a}_2 = (\frac{a\sqrt{3}}{2}, -\frac{a}{2})$, and that the unit cell contains two carbon atoms, A and B. The spacing between nearest neighbors is $a_{\text{C-C}} = 1.42$ Å, so the lattice constant is $a \equiv |\vec{a}_i| = \sqrt{3}a_{\text{C-C}} = 2.46$ Å. The reciprocal graphene lattice is also a honeycomb, with reciprocal lattice vectors $\vec{b}_1 = (\frac{2\pi}{a\sqrt{3}}, \frac{2\pi}{a})$ and $\vec{b}_2 = (\frac{2\pi}{a\sqrt{3}}, -\frac{2\pi}{a})$.

The basis of the tight-binding approximation is the assumption that the interactions between carbon atoms only cause perturbations to electrons in atomic wave functions φ_j. We use functions of the form

$$\Phi_{j\vec{k}}(\vec{r}) = \frac{1}{\sqrt{N}} \sum_{\vec{R}} e^{i\vec{k}\cdot\vec{R}} \varphi_j(\vec{r} - \vec{R}), \tag{A.1}$$

which satisfy Bloch's theorem (Ashcroft and Mermin, 1976). Graphene is sp^2 hybridized, which means that the $2s$, $2p_x$, and $2p_y$ orbitals form linear combinations

[1] The content of this section is largely drawn from a term paper written in Spring 2003 for Professor Chris Henley's Solid-State Physics II class at Cornell.

(are "hybridized") to create three sp^2 orbitals. These orbitals, known as σ orbitals, bind each carbon atom to its three nearest neighbors. The $2p_z$ orbital is known as a π orbital, which is oriented perpendicular to the graphene plane. Since the π electrons are responsible for transport in the tube, we will calculate their energy levels (Saito *et al.*, 1998). The atomic wavefunction φ_j in Eq. A.1 is thus the wavefunction of the p_z atomic orbital.

The energy bands $E(\vec{k})$ in the tight-binding method are given by solving

$$0 = \det(H - ES), \tag{A.2}$$

where

$$H_{jj'}(\vec{k}) = \left\langle \Phi_{j\vec{k}} \left| \mathscr{H} \right| \Phi_{j'\vec{k}} \right\rangle \tag{A.3}$$

is known as the transfer integral matrix for Hamiltonian $\mathscr{H}$ and

$$S_{jj'}(\vec{k}) = \left\langle \Phi_{j\vec{k}} \middle| \Phi_{j'\vec{k}} \right\rangle \tag{A.4}$$

is known as the overlap integral matrix (Saito *et al.*, 1998). Since we have two carbon atoms in the unit cell, A and B, Equation A.2 becomes

$$\begin{aligned} 0 &= \begin{vmatrix} H_{AA}(\vec{k}) - E(\vec{k})S_{AA}(\vec{k}) & H_{AB}(\vec{k}) - E(\vec{k})S_{AB}(\vec{k}) \\ H_{BA}(\vec{k}) - E(\vec{k})S_{BA}(\vec{k}) & H_{BB}(\vec{k}) - E(\vec{k})S_{BB}(\vec{k}) \end{vmatrix} \\ &= \begin{vmatrix} H_{AA}(\vec{k}) - E(\vec{k})S_{AA}(\vec{k}) & H_{AB}(\vec{k}) - E(\vec{k})S_{AB}(\vec{k}) \\ H^*_{AB}(\vec{k}) - E(\vec{k})S^*_{AB}(\vec{k}) & H_{AA}(\vec{k}) - E(\vec{k})S_{AA}(\vec{k}) \end{vmatrix}, \end{aligned} \tag{A.5}$$

where the second equality uses the equivalence of carbon atoms.

If the atomic wavefunctions φ are normalized, $S_{AA} = 1$, and since we are neglecting the wavefunction overlap, $S_{AB} = 0$. Since we are neglecting all but nearest-neighbor interactions, H_{AA} only includes the interaction of an atom with itself:

$$H_{AA}(\vec{k}) = \langle \Phi_A \left| \mathscr{H} \right| \Phi_A \rangle = \epsilon_{2p}, \tag{A.6}$$

where ϵ_{2p} is the energy of the $2p$ orbital denoted by the p_z atomic wavefunction φ_A. H_{AB} is the transfer matrix between neighboring atoms, and for a crystal of N unit cells with atoms at R_A and R_B we can calculate it as

$$\begin{aligned} H_{AB}(\vec{k}) &= \langle \Phi_A \left| \mathscr{H} \right| \Phi_B \rangle \\ &= \frac{1}{N} \sum_{\vec{R}_A, \vec{R}_B} e^{i\vec{k}\cdot(\vec{R}_B - \vec{R}_A)} \left\langle \varphi_A(\vec{r} - \vec{R}_A) \left| \mathscr{H} \right| \varphi_B(\vec{r} - \vec{R}_B) \right\rangle \\ &\approx \frac{1}{N} \sum_{\vec{R}_A} \left(e^{i\vec{k}\cdot\vec{R}_1} + e^{i\vec{k}\cdot\vec{R}_2} + e^{i\vec{k}\cdot\vec{R}_3} \right) \gamma_0 \\ &= \left(e^{i\vec{k}\cdot\vec{R}_1} + e^{i\vec{k}\cdot\vec{R}_2} + e^{i\vec{k}\cdot\vec{R}_3} \right) \gamma_0 \\ &\equiv f(k)\gamma_0, \end{aligned} \tag{A.7}$$

where the last equality defines $f(k)$, γ_0 (the first-nearest-neighbor interaction energy) is defined by

$$\gamma_0 \equiv \left\langle \varphi_A(\vec{r} - \vec{R}_A) \left| \mathscr{H} \right| \varphi_B(\vec{r} - [\vec{R}_A + \vec{R}_{\text{n.n.}}]) \right\rangle, \tag{A.8}$$

and $\vec{R}_{\text{n.n.}}$ is any of $\{\vec{R}_1, \vec{R}_2, \vec{R}_3\}$, the three vectors pointing from atom A to its nearest neighbors.

Substituting these quantities, Equation A.5 becomes

$$\begin{aligned} 0 &= \begin{vmatrix} \epsilon_{2p} - E(\vec{k}) & \gamma_0 f(\vec{k}) \\ \gamma_0 f^*(\vec{k}) & \epsilon_{2p} - E(\vec{k}) \end{vmatrix} \\ &= (\epsilon_{2p} - E(\vec{k}))^2 - |f(\vec{k})|^2 \gamma_0^2. \end{aligned} \tag{A.9}$$

Solving for $E(\vec{k})$, we find

$$\begin{aligned} E(\vec{k}) &= \epsilon_{2p} \pm \gamma_0 |f(\vec{k})| \\ &= \epsilon_{2p} \pm \gamma_0 |e^{ik_x a/\sqrt{3}} + 2\cos\frac{k_y a}{2} e^{-ik_x a/2\sqrt{3}}| \\ &= \epsilon_{2p} \pm \gamma_0 \sqrt{1 + 4\cos^2\frac{k_y a}{2} + 4\cos\frac{k_y a}{2}\cos\frac{k_x a\sqrt{3}}{2}}, \end{aligned} \tag{A.10}$$

where we have expressed $|f(\vec{k})|$ in terms of the xy-coordinates of Figure 2.2(b), with the origin at the Γ point. The parameters ϵ_{2p} and γ_0 are determined by fitting experimental or first-principles results; common values are $\epsilon_{2p} = 0$ and -3 eV $< \gamma_0 < -2.5$ eV (Reich *et al.*, 2002). Plotting this expression gives the band structure of graphene shown in Figure 2.3(a).

In Equation A.10, $E(\vec{k})$ is measured with respect to the Γ point. In these coordinates, the K point is at $(\frac{2\pi}{a\sqrt{3}}, \frac{2\pi}{3a})$. If we measure $\vec{k}$ with respect to the K point, we find that in the limit $ka \ll 1$, $|f(\vec{k})| \approx \frac{\sqrt{3}}{2}ka$, where $k = |\vec{k}|$. When we take $\epsilon_{2p} = 0$ in Eq. A.10, we thus find that near the K points,

$$E(\vec{k}) = \pm\frac{\sqrt{3}}{2}\gamma_0 ka = \pm\frac{3}{2}\gamma_0 k a_{\text{C-C}}, \tag{A.11}$$

giving us the dispersion cones of Figure 2.3(c).

Appendix B

Nanotube Device Recipe

In this Appendix, we provide the recipe used to fabricate the nanotube devices that were used for the experiments in this thesis. The catalyst deposition and nanotube growth were performed in Paul McEuen's lab at Cornell University, and all other fabrication steps were performed at the Cornell NanoScale Science & Technology Facility (CNF). This recipe has evolved from years of experience with nanofabrication and nanotube growth accumulated by members of the McEuen group; we particularly thank Xinjian Zhou and Samantha Roberts.

1. **Create a mask for each photolithography step.**

   - Design masks using L-Edit. Refer to the 5x Stepper manual on the CNF website for size limitations and instructions on alignment marks.
   - Expose pattern on a new 5-inch photomask (glass coated with a thin layer of chrome and photoresist) in the GCA/MANN 3600F Optical Pattern Generator.
   - In the Hamatech Mask Plate Processor, develop (Program 2) and etch (Program 1) mask. Strip remaining resist in the resist hot strip baths, then run through the spin rinse dryer.

2. **Characterize wafer.** Start with a clean 4-inch wafer. This recipe has been developed for silicon wafers with a 200–1000 nm oxide or for 170–500 μm-thick fused silica wafers. With Si/SiO_2 wafers (from Nova Electronics), it is useful to check the thickness of the oxide layer using the Leitz MV-SP Spectrophotometer before beginning any processing. With fused silica

wafers (from Mark Optics), there is no film to measure (and one cannot use an interferometer anyway), but since both sides of the wafer look identical, it is useful to make a small scratch on one side to keep track of which side is up.

3. **Etch alignment marks and back-gate pads (and trenches, if desired).** Alignment marks must be added in the first lithographic step so that subsequent layers can be aligned to this first one. For Si/SiO_2 wafers, it is convenient to etch holes through the SiO_2 layer, known as back-gate pads, in the same step. To make suspended nanotubes, the trenches can be etched in this step if the nanotubes will be grown last, on top of the electrodes.

   - Prime the wafer (making it hydrophobic so photoresist will stick) by squeezing a full dropper of P20 primer on the wafer. Wait at least 10–20 s, and then spin the primer with Program 4 (4000 rpm for 60 s). (Alternatively, you can prime the wafer in the Vapor Prime Oven, which results in a more uniform photoresist layer, but this step takes 30 min and is generally unnecessary.)
   - Spin photoresist (S1813 for the 5x Stepper or SPR700-1.2 for the Autostep, both from Shipley Company) on the wafer at 4000 rpm.
   - Bake the wafer on a 115 °C hotplate for 60 s (Si/SiO_2) or 90 s (fused silica), and cool on a heat sink.
   - Expose the wafer using one of the wafer steppers:
     - GCA-6300 5x g-line Stepper: Load the mask with GCA keys in the stepper and expose wafer for 0.4–0.7 s. (The correct exposure varies over time, so making an exposure array at the beginning of

your processing may be necessary.) For 170-μm fused silica wafers, it is necessary to place the wafer on top of a 90-mm Whatman filter paper circle. The transparent/opaque switch and the focus offset (nominally 0 for Si/SiO_2, 77 for fused silica, but often as much as 70 higher than these) should be adjusted for the kind of wafer used. The 5x Stepper often provides inconsistent results on transparent wafers, with part of the pattern coming out nicely and parts not being exposed, sometimes within the same die.

  - GCA Autostep 200: The Autostep seems to provide more consistent results for transparent wafers. Load the GCA key mask and expose the wafer for about 0.3 s (the focus setting of 0 is usually accurate). For 170-μm fused silica wafers, a second wafer with holes drilled through it may be used to lift the wafer to the proper height. Note that wafers are loaded in the opposite direction as on the 5x Stepper.

- Develop wafer in MIF300 for 60–90 s, rinse with DI water, and blow dry with compressed N_2.

- Clean the Oxford PlasmaLab 80+ Reactive-Ion Etcher with O_2 plasma for at least 5 min before loading the wafer. Then run an O_2 plasma for 30 s (known as a "descum") before etching the oxide with the CHF_3/O_2 recipe. To measure the etch rate (nominally 25–30 nm/min), use the Leitz Spectrophotometer or the Tencor P10 Profilometer. (When measuring a substrate less than 400 μm thick with the P10 Profilometer, raise the substrate by placing a Beta Wipe underneath.) With a Si/SiO_2 wafer, etch through the oxide layer; with a fused silica wafer, etch deep enough to see the alignment marks (800 nm is more than sufficient).

With a Si/SiO_2 wafer, next etch into the Si substrate for 5 min with a CH_4 or SF_6 plasma. Finally, etch the remaining photoresist with an O_2 plasma.

4. **Evaporate electrodes (can also wait until after growth, unless nanotubes are grown over a trench).** Metal electrodes are patterned on the surface to make contact to both ends of the nanotubes and, on Si/SiO_2 substrates, to make contact to the Si back gate. If the nanotubes are grown over trenches, electrodes must be defined before growth, or the nanotubes will no longer be suspended; otherwise, the electrodes may be deposited after growth. If electrodes are deposited before growing nanotubes, the electrode metal must be platinum to survive the nanotube growth temperature.

   - Spin primer and photoresist as in Step 3, but at 2000 rpm (Program 2) instead of 4000 rpm, giving you a thicker layer for better liftoff.
   - Expose wafer in 5x Stepper or Autostep as in Step 3, but use the electrode mask and roughly double the exposure time. You should be able to see a faint outline of the exposed pattern under a microscope. (Be sure to use a microscope that uses yellow light!)
   - Place wafer inside the YES-58SM Image Reversal Oven and run the 80-min recipe.
   - Flood expose for 30 s in the HTG System III-HR Contact Aligner.
   - Develop in MIF321 for 60–75 s, rinse with DI water, and blow dry.
   - Descum the wafer with O_2 plasma for 30 s in the Oxford 80 Etcher or the Branson/IPC P2000 Barrel Etcher.

- Load devices in one of the CVC 4500 Evaporators and evaporate 2 nm Ti followed by 40–100 nm of Pt at about 1 Å/s.
- Liftoff photoresist and excess metal in 1165 for 3–8 hours, rinse with acetone and isopropanol, and blow dry. The devices are now ready for electrical characterization.

5. **Dice wafer.** Since fused silica wafers have no crystal axes, it is necessary to dice them using the K&S 7100 Dicing Saw. Since using the dicing saw is much messier than dicing by hand, this step must be done before defining the catalyst pads. Before dicing the wafer, spin a photoresist coating to protect the features made already. After dicing, scratch numbers in the upper left corner of each chip to distinguish them and keep track of which side is up. To remove the chips from the sticky blue paper that held them to the dicing frame, pull them off with tweezers or (for the more fragile 170-μm-thick pieces) use acetone to dissolve the paper.

6. **Define catalyst pads.** In this step, we coat the substrate with photoresist and make small holes in the resist in the places we want nanotubes to grow.

   - Spin primer and photoresist as in Step 3.
   - Expose devices in the 5x Stepper or Autostep as in Step 3, but using the catalyst pad mask. If exposing pieces in the 5x Stepper (rather than a whole wafer), center each piece on the standard wafer chuck on top of a piece of filter paper to provide enough vacuum.
   - Develop as in Step 3.
   - Clean the Oxford 80 Etcher with O_2 plasma for 5 min, load the wafer, and etch the photoresist with O_2 to the desired level (0.5–3.5 min).

7. **Deposit catalyst.** Nanotubes can be grown from a variety of catalysts, including iron nanoparticles mixed in hexanes, but the following method was found to be the most reproducible:

   - Following the recipe from Kong *et al.* (1998b), but using water as a base rather than methanol, mix 60 mg $Fe(NO_3)_3 \cdot 9H_2O$, 15 mg $MoO_2(acac)_2$, and 45 mg Al_2O_3 in 45 mL DI water inside a glass jar with a plastic-coated magnetic stir rod. Sonicate the mixture for several hours when first made, and again for 30–60 min before each use. Following sonication, magnetically stir the solution until ready to use.

   - If wafer is not already diced, do so by hand using a diamond-tipped scribe. Use the edge of a ruler to guide the scribe along a line that is aligned with the Silicon crystal axes (as indicated by the wafer flat), then gently pull the two pieces apart with two pairs of tweezers.

   - Add the catalyst solution in a large drop on each nanotube chip, wait 2–10 min, and then rinse off the excess catalyst with water.

   - Liftoff in acetone for 5–15 min, then rinse with acetone and isopropanol and dry with N_2 gas.

   - The chip may be cleaned using a plasma etch, ozone, or calcination (heating in an open furnace to 700 °C) before growth. These techniques may improve the surface cleanliness, but they do not have a dramatic impact on the growth.

8. **Grow nanotubes.** In order to grow long (5–15 μm) nanotubes, use a "fast heating" chemical vapor deposition method, similar to that of Huang *et al.* (2004).

- Clean the furnace tube (22-mm inner diameter, 25-mm outer diameter, 4 or 5-feet long, from Quartz Scientific) by scrubbing with glassware cleaner, rinsing with DI water, rinsing with acetone, and rising again with DI water, and then bake it out inside a 800 °C furnace. Each third of the tube should be inside the furnace for at least 10 min.
- Place one or two chips with catalyst particles inside the furnace tube, and push with a hooked metal rod to the center of the furnace. Make a mark on the furnace tube just outside the furnace to indicate where it should be such that the chips are in the center. (This mark must be on the part of the tube that will stay outside the furnace, or it will be burnt off inside.)
- Close the furnace lid, attach the gas flow connections, and flow 0.8 SLM (standard liters per min) Ar. Check for gas leaks.
- Heat the furnace to 700 °C while flowing 0.8 SLM Ar. Add 0.2 SLM H_2 to reduce the sample for 15 min.
- Slide the furnace tube so that the chips are outside the furnace, and increase the temperature setpoint to 1040 °C.
- Once the temperature reaches 1040 °C, add 0.2 SLM H_2 (if it is not on already), 0.8 SLM CH_4, and 5.5 SCCM (standard cubic cm per min) C_2H_4. Wait 2–3 min.
- Turn off the Ar, change the setpoint to 915–930 °C, slide to furnace tube back so that the chips are in the center of the furnace, and wait 10 min.
- Cool in 0.8 SLM Ar (and 0.2 SLM H_2, if desired), opening the furnace top once the temperature drops below 500 °C and removing the chips

below 100 °C.

- It is often worthwhile to examine several catalyst pads with an AFM to ensure that there are some nanotubes before continuing.

9. **If not done already, evaporate electrodes.** Follow the procedure in Step 4 to evaporate metal electrodes, but do NOT descum the devices in oxygen plasma, as this will destroy the nanotubes. When electrodes are deposited after growth, Pd is usually the best choice of metal, since it makes good contacts to the nanotubes and adheres well to the substrate. For Si/SiO_2, Au also works well, but Au will not stick easily to fused silica devices without an adhesion layer like Cr, which worsens the contact to the nanotube. These metals may be evaporated faster than Pt, at about 4-5 Å/s.

10. **Wet-etch trenches under nanotubes, if desired.** If the nanotubes were not originally grown over trenches, they may still be suspended using a chemical etch. Wet etches are isotropic, giving you little control over the aspect ratio of the finished trench, and making it a difficult technique to use for suspending very long nanotubes.

    - Spin primer and photoresist as in Step 3.
    - Expose devices in the 5x Stepper or Autostep as in Step 3, but using the trench mask.
    - Develop as in Step 3.
    - Etch the devices with buffered oxide etch (BOE) 6:1 for desired etch time (SiO_2 is etched at about 100 nm/min). Be sure to follow the necessary safety protocols for working with HF!

- Transfer repeatedly (about 8 times) between different baths of DI water until BOE is diluted, making sure chips are always coated with solution.
- Liftoff photoresist in acetone 5–15 min.
- Transfer repeatedly (about 4 times) between different baths of methanol until acetone is diluted, making sure chips are always coated with solution.
- Place the devices in the Critical Point Dryer to remove the methanol while keeping the devices suspended.

Appendix C

Deriving the Nernst Equation

In this Appendix, we derive the Nernst Equation, which is critical for the results in Chapter 7. First, in Section C.1, we provide a derivation using Boltzmann factors, which physicists will likely find intuitive. Then, in Section C.2, we explain the more rigorous derivation that is usually used by chemists.

C.1 Using Boltzmann Factors

Figure C.1 shows the energy diagram for redox molecules at different [Ox]/[Red] ratios, where we see that the chemical potential μ_c is the difference between the energy barriers for taking electrons from and for giving electrons to the gold electrolyte-gate wire. We can write [Ox]/[Red] in terms of the Boltzmann factors for these processes:

$$\frac{[\mathrm{Ox}]}{[\mathrm{Red}]} = \frac{\text{probability of being oxidized}}{\text{probability of being reduced}} \tag{C.1}$$

$$= \frac{\exp\left(-[\text{barrier for losing an } e]/k_\mathrm{B}T\right)}{\exp\left(-[\text{barrier for gaining an } e]/k_\mathrm{B}T\right)} \tag{C.2}$$

$$= \exp\left(\mu_c/k_\mathrm{B}T\right). \tag{C.3}$$

Taking the natural logarithm of both sides gives

$$\mu_c = k_\mathrm{B}T \ln \frac{[\mathrm{Ox}]}{[\mathrm{Red}]}. \tag{C.4}$$

If $\mu_c \neq 0$ at [Ox]/[Red] = 1, we need to add in this additional constant:

$$\mu_c = \mu_c^0 + k_\mathrm{B}T \ln \frac{[\mathrm{Ox}]}{[\mathrm{Red}]}. \tag{C.5}$$

This is the Nernst equation for the reaction $\mathrm{Ox} + e^- \rightarrow \mathrm{Red}$.

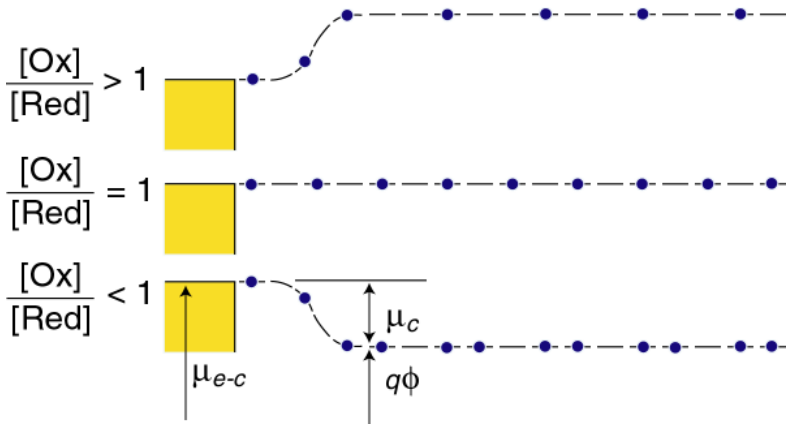

Figure C.1: Energy diagram for redox-active molecules, in which oxidized molecules are represented as empty states and reduced molecules are represented as full states. The gold electrolyte-gate wire sets the electrochemical potential μ_{e-c}, which is comprised of the electrostatic (ϕ) and chemical (μ_c) potentials. For simplicity, we are taking [Ox]/[Red] = 1 (when half of the available states are filled) to be the condition when the energy barriers for taking an electron or giving an electron to the gate wire are the same ($\mu_c = 0$). Changing [Ox]/[Red] changes this difference in energy barriers so that the net current flowing in or out of the solution is zero.

C.2 Using Entropy and the Gibbs Free Energy

Chemists generally derive the Nernst equation using entropy and the Gibbs free energy; the derivation here is largely adapted from Olmsted and Williams (1997). Quantities here are given per molecule, not per mole, and so Boltzmann's constant k and the electron charge e are used instead of the gas constant R and Faraday's constant F. To convert to the molar quantities given in most chemistry textbooks, it is simply necessary to multiply by Avogadro's number: $R = kN_A$ and $F = eN_A$.

The entropy a molecule is defined as

$$S \equiv k \ln \Omega, \tag{C.6}$$

where Ω is the number of states available to the molecule. The number of states must vary linearly with the volume V of the system, which is inversely proportional to the concentration c, so we can also write the entropy as

$$S = k \ln \text{ (constant} \times V) = -k \ln \text{ (constant} \times c). \tag{C.7}$$

The change in entropy from some state 1 to another state 2 is therefore

$$\Delta S = S_2 - S_1 = -k \ln \frac{c_2}{c_1}, \tag{C.8}$$

so that the entropy of state 1 is

$$S_2 = S_1 - k \ln \frac{c_2}{c_1}. \tag{C.9}$$

If state 1 is at standard conditions, in which c_1 is unity (*e.g.*, 1 atm or 1 M), it will merely cancel the units of c_2. We can therefore write the entropy of an arbitrary molecule A as

$$S(A) = S^0(A) - k \ln[A], \tag{C.10}$$

where S^0 is the entropy at standard conditions and $[A]$ denotes the concentration of A. The change in entropy for a reaction

$$aA + bB \rightarrow yY + zZ \tag{C.11}$$

is then given by

$$\Delta S_{\text{rxn}} = [yS(Y) + zS(Z)] - [aS(A) - bS(b)] \tag{C.12}$$

$$= \Delta S^0_{\text{rxn}} - k \ln \frac{[Y]^y [Z]^z}{[A]^a [B]^b}. \tag{C.13}$$

We define the ratio in the last term as the *reaction quotient*:

$$Q \equiv \frac{[Y]^y [Z]^z}{[A]^a [B]^b}. \tag{C.14}$$

In an electrochemical cell, the *cell potential* E is the chemical potential available from redox reactions ($E = \mu_{\text{c}}/e$). E is related to the *Gibbs free energy* change ΔG only by a constant: $\Delta G = -neE$, where n is the number of electrons transferred. (There is a negative sign because a spontaneous reaction has a negative ΔG and a positive E.) The Gibbs free energy is related to the entropy by $G = H - TS$, where H is the enthalpy and T is the temperature of the system. Using these relations, we can now use Eq. C.13 to write the change in Gibbs free energy,

$$\Delta G = \Delta H - T\Delta S = \Delta G^0 + k_{\text{B}} T \ln Q, \tag{C.15}$$

and the cell potential,

$$E = E^0 - \frac{k_{\text{B}} T}{ne} \ln Q. \tag{C.16}$$

This is known as the Nernst equation. For a redox reaction involving a single electron transfer,

$$\text{Ox} + e^- \rightarrow \text{Red}, \tag{C.17}$$

$Q = [\text{Red}]/[\text{Ox}]$, and Eq. C.16 becomes

$$E = E^0 + \frac{k_\text{B}T}{e} \ln \frac{[\text{Ox}]}{[\text{Red}]}. \tag{C.18}$$

Since $E = \mu_\text{c}/e$, this is equivalent to Eq. C.5. The cell potential at standard conditions E^0 is often replaced by the formal potential $E^{0'}$, which includes some small corrections to the logarithm and is the potential that is actually measured in an electrochemical cell.

Appendix D

DNA

DNA (deoxyribonucleic acid) was used for the dielectrophoretic trapping experiments in Section 3.2.2, as well as for the nanotube sensing experiments in Section 8. In this Appendix, we will review the relevant properties of DNA and discuss the particular kinds of DNA molecules and fluorescent labeling that were used for this thesis.

Double-stranded DNA is a flexible polymer with a width of 2 nm a length of 0.34 nm per base pair, and it has net charge of $2e$ per base pair. This charge, however, will be partially cancelled by Manning-Oosawa counterion condensation, an effect which prevents the effective charge of a linear polymer from being above $1e$ per Bjerrum length $\lambda_{\mathrm{B}} = e^2/4\pi\epsilon\epsilon_0 kT$ (O'Schaughnessy and Yang, 2005). The Bjerrum length, which is the length at which the electrostatic and thermal energy of a charge balance, is approximately 0.7 nm in a room-temperature aqueous solution, so the effective charge of DNA, either double-stranded or single-stranded, is $1e/(0.7\text{ nm})$.[1]

Because DNA is flexible, a long DNA molecule in solution will be a coiled ball; this flexibility is measured by the persistence length, which is around $\ell_{\mathrm{p}} = 50$ nm for double-stranded DNA. There are a number of methods for estimating the RMS end-to-end distance of a DNA molecule of length L and persistence length ℓ_{p}, including treating the DNA as a random walk (or a self-avoiding random walk) of $N = L/\ell_{\mathrm{p}}$ steps of length ℓ_{p}, but the best approximation seems to be treating

[1] Counterion condensation will only occur if the salt concentration is low enough that the Debye screening length is much greater than the polymer diameter. For DNA, this means that the ionic strength of the solution must be less than 10 mM, which was always the case for our DNA sensing experiments.

the DNA as a "worm-like coil" (Richards, 1980), giving an RMS length of

$$R_{\mathrm{RMS}} = \ell_{\mathrm{p}} \sqrt{2N \left[1 - \frac{1}{N} \left(1 - e^{-N} \right) \right]}. \tag{D.1}$$

This RMS end-to-end distance is not directly measurable, but one can measure the radius of gyration, $R_{\mathrm{g}} = R_{\mathrm{RMS}}/\sqrt{6}$, which is the RMS distance of the chain elements from their center of gravity. For DNA in solution, we are also interested in the hydrodynamic radius, $R_{\mathrm{h}} = \zeta R_{\mathrm{g}}$, which is the radius of a hypothetical hard sphere that diffuses with the same speed as DNA. The proportionality constant ζ, which varies with the flexibility and density of a polymer, is around 0.65 for DNA (Tinland *et al.*, 1997).

Single-stranded DNA has unpaired bases which bind to nanotubes (Zheng *et al.*, 2003a), so it might also be an attractive candidate for a sensing experiment. The parameters for single-stranded DNA are different from double-stranded DNA, since it is more flexible and can stretch farther, and these parameters depend more strongly on the concentration of ions around the DNA. The length per base pair is increased to around 0.43 nm, and for our low salt concentrations, the persistence length should be around $\ell_{\mathrm{p}} = 5$ nm (Tinland *et al.*, 1997).

In our experiments, we worked with four different kinds of DNA: λ-DNA, double and single-stranded DNA from the bacteriophage M13 (dsM13 and ssM13), and short DNA from a salmon. The radii R_{g} and R_{h} are shown in Table D.1 for these four DNA molecules. The DNA was labeled with YOYO-1 (490 nm excitation, 509 nm emission) or OliGreen (490 nm excitation, 518 nm emission) fluorescent dyes, both of which allowed single DNA molecules to be observed in our Olympus BX51WI microscope with a 40x objective and a U-MNB2 narrow-band blue filter (470–490 nm excitation, 520 nm emission) illuminated by a mercury arc lamp. The DNA molecules and dyes were obtained from Molecular Probes.

Table D.1: Experimental parameters for different DNA molecules

DNA	base pairs	length (μm)	R_{g} (nm)	R_{h} (nm)
λ	48,500	16.5	524	341
dsM13	7000	2.4	198	129
ssM13	7000	3.01	71	46
salmon	500	0.17	45	29

Appendix E

Microspheres: Polystyrene Beads and CU Dots

Submicron beads were used for both the DEP trapping experiments in Section 3.2.2 and the nanotube sensing experiments in Chapter 8. Here, we briefly describe the different kinds of beads used for this work.

We purchased negatively-charged 40-nm and 200-nm diameter polystyrene micropsheres from Molecular Probes (carboxylate-modified yellow-green fluorescent FluoSpheres). The surface charge of these microspheres was 0.1-2 moles of electrons per gram (meq/g), for a surface charge of over 5 $e/\text{Å}^2$, making them extremely highly charged. Like for DNA, however, this charge will be reduced by condensation of counterions from solution. The fluorescence from these microspheres is observable with our Olympus U-MNB2 narrow-band blue filter (470–490 nm excitation, 520 nm emission); they showed little photobleaching. The density of polystyrene is 1.05 g/cm^3, so they are roughly neutrally buoyant in water.

We also used fluorescent CU dots, which were prepared by Erik Herz in Uli Wiesner's group in Materials Science and Engineering at Cornell. These dots contained a silica core with a 15–20 nm gold shell, for a total diameter of about 150 nm. They absorb best at 540 nm and emit at 580 nm, so we were able to see them with our Olympus U-MNG2 narrow-band green filter (530-550 excitation, 590 emission). The density of silica is 2.2 g/cm^3, so sedimentation is more important for the CU dots than for the polystyrene microspheres.

Appendix F

Cell Culture and Buffer Solutions

F.1 *Dictyostelium discoideum*

Wild-type AX2-214 *Dictyostelium discoideum* cells were used for the experiments described in Section 9.1. Cells were grown in petri dishes in HL5 medium, the components of which are displayed in Table F.1.

These cells double every 8–10 hours, as seen in the growth curve in Figure F.1. To count cells in a dish, the cells were first washed off the bottom of the dish by squirting them with their medium with a 10 mL pipette. 10 μL of these cells were then diluted with 10–40 μL of Trypan blue dye, which stains dead cells to prevent them from being counted. 10 μL of this dilution was then counted in a calibrated chamber known as a hemocytometer.

After several days, a dish of cells will become confluent, meaning that all the cells are touching their neighbors. The cells were then washed from the bottom of the dish, and one drop of cells were placed in a new dish with 10 mL fresh HL5 medium. This process was repeated up to 10 times for any dish of cells, after which a new dish was started from the original frozen stock cells.

The experiments described in Section 9.1 were performed in phosphate buffer, which is also described in Table F.1. This buffer has a total ionic strength of 100.2 mM, giving a Debye length of 0.9 nm (see Eq. 3.14). The HL5 medium was removed from a dish and it was rinsed twice with phosphate buffer (without washing the cells off the bottom), before filling it with a final phosphate buffer solution. The cells could then be washed off the bottom and loaded into the nanotube device, or, for experiments with chemotactic cells, starved in the buffer for 7–9 hours before

Table F.1: Components of HL5 medium and phosphate buffer, with grams per liter, concentration, and ionic strength I

	HL5 Medium			**Phosphate Buffer**		
	g/L	conc. (mM)	I (mM)	g/L	conc. (mM)	I (mM)
KH_2PO_4	0.5	3.7	22.2	2.00	14.7	88.2
Na_2HPO_4	0.5	3.5	21	0.36	2.0	12
glucose	13.5	75	0.0			
yeast extract	7.0	-	0.0			
peptone	14.0	-	0.0			

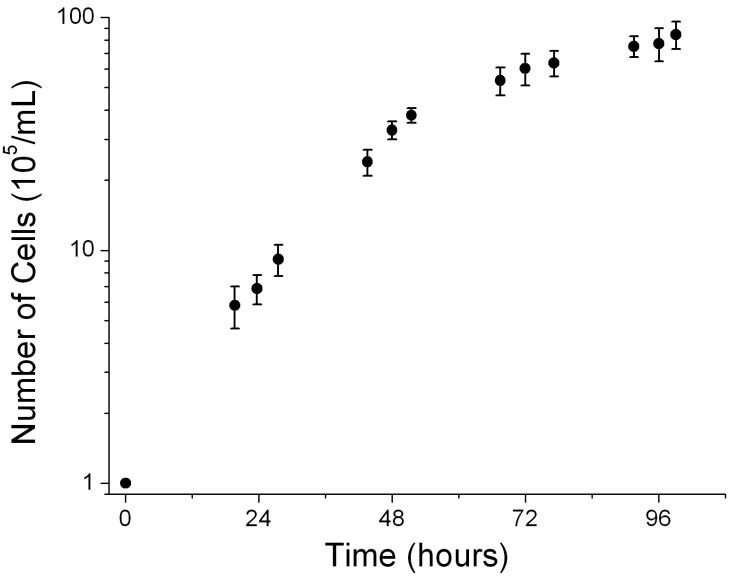

Figure F.1: Growth curve for AX2-214 wild-type *Dictyostelium*. Twelve petri dishes were prepared with an initial concentration of 10^5 cells/mL in HL5 medium, and the dishes were counted over a period of four days. Error bars represent the standard deviation from at least three countings.

Table F.2: Components of buffer used for experiments with chromaffin and mast cells, with concentration and ioninc strength I

	conc. (mM)	I (mM)
NaCl	150	150
KCl	5	5
$CaCl_2$	5	15
$MgCl_2$	2	6
HEPES	10	0

rinsing them with fresh buffer and beginning the experiments.

F.2 Chromaffin and Mast Cells

The experiments described in Section 9.2 were performed with chromaffin and mast cells. The chromaffin cells were provided by Kassandra Kisler in the Lindau lab in Applied Physics, and the mast cells were provided by Jose Moran-Mirabal in the Craighead lab in Applied Physics.

The experiments were performed in the buffer described in Table F.2, which has a total ionic strength of 176 mM (HEPES, or $C_8H_18N_2O_4S$, is uncharged, and thus does not contribute to the ionic strength). From Equation 3.14, we see that the Debye length in this buffer is 0.7 nm. The osmolarity is 313 mmol/kg, and the pH is 7.25.

REFERENCES

H. Abruña. Cornell University, 2006. Personal communication.

Y. Ahn, J. Dunning, and J. Park. Scanning photocurrent imaging and electronic band studies in silicon nanowire field effect transistors. *Nano Lett.*, **5**:1367, 2005.

Y. H. Ahn, W. Tsen, B. Kim, Y. W. Park, and J. Park. Photocurrent imaging of p-n junctions and local defects in ambipolar carbon nanotube transistors. Preprint, 2007.

B. Alberts, A. Johnson, J. Lewis, M. Raff, K. Roberts, and P. Walter. *Molecular Biology of the Cell*. Garland Science, New York, NY, fourth edition, 2002.

A. B. Artyukhin, M. Stadermann, R. W. Friddle, P. Stroeve, O. Bakajin, and A. Noy. Controlled electrostatic gating of carbon nanotube FET devices. *Nano Lett.*, **6**:2080, 2006.

C. L. Asbury, A. H. Diercks, and G. van den Engh. Trapping of DNA by dielectrophoresis. *Electrophoresis*, **23**:2658, 2002.

C. L. Asbury and G. van den Engh. Trapping of DNA in nonuniform oscillating electric fields. *Biophys. J.*, **74**:1024, 1998.

N. W. Ashcroft and N. D. Mermin. *Solid State Physics*. Saunders College Publishing, New York, NY, 1976.

P. Bagchi and S. Balachandar. Inertial and viscous forces on a rigid sphere in straining flows at moderate Reynolds numbers. *J. Fluid Mech.*, **481**:105, 2003.

K. Balasubramanian, M. Burghard, K. Kern, M. Scolari, and A. Mews. Photocurrent imaging of charge transport barriers in carbon nanotube devices. *Nano Lett.*, **5**:507, 2005.

A. J. Bard and L. R. Faulkner. *Electrochemical Methods, Fundamentals and Applications*. John Wiley & Sons, New York, NY, second edition, 2001.

J. M. G. Barthel, H. Krienke, and W. Kunz. *Physical Chemistry of Electrolyte Solutions: Modern Aspects*. Steinkopff, Darmstadt, Germany, 1998.

H. C. Berg. *Random Walks in Biology.* Princeton University Press, Princeton, NJ, 1993.

C. Beriet and D. Pletcher. A microelectrode study of the mechanism and kinetics of the ferro/ferricyanide couple in aqueous media: The influence of the electrolyte and its concentration. *J. of Electroanal. Chem.*, **361**:93, 1993.

K. Besteman, J.-O. Lee, F. G. M. Wiertz, H. A. Heering, and C. Dekker. Enzyme-coated carbon nanotubes as single-molecule biosensors. *Nano Lett.*, **3**:727, 2003.

M. Bockrath, D. H. Cobden, A. G. Rinzler, R. E. Smalley, L. Balents, and P. L. McEuen. Luttinger liquid behavior in carbon nanotubes. *Nature*, **397**:598, 1999.

J. O. Bockris, M. A. V. Devanathan, and K. Müller. On the structure of charged interfaces. *J. Am. Chem. Soc.*, **274**:55, 1963.

S. Boussaad, B. A. Diner, and J. Fan. Redox tuning of the electronic properties of single-walled carbon nanotubes. Preprint, 2006.

S. Boussaad, N. J. Tao, R. Zhang, T. Hopson, and L. A. Nagahara. *In situ* detection of cytochrome c adsorption with single walled carbon nanotube device. *Chem. Commun.*, **13**:1502, 2003.

K. Bradley, M. Briman, A. Star, and G. Grüner. Charge transfer from adsorbed proteins. *Nano Lett.*, **4**:253, 2004.

K. Bradley, A. Davis, J.-C. P. Gabriel, and G. Grüner. Integration of cell membranes and nanotube transistors. *Nano Lett.*, **5**:841, 2005.

K. Bradley, J.-C. P. Gabriel, M. Briman, A. Star, and G. Grüner. Charge transfer from ammonia physisorbed on nanotubes. *Phys. Rev. Lett.*, **91**:218301, 2003a.

K. Bradley, J.-C. P. Gabriel, A. Star, and G. Grüner. Short-channel effects in contact-passivated nanotube chemical sensors. *Appl. Phys. Lett.*, **83**:3821, 2003b.

M. S. Bretscher. The molecules of the cell membrane. *Sci. Am.*, **254**:86, 1985.

H.-J. Butt, K. Graf, and M. Kappl. *Physics and Chemistry of Interfaces.* Wiley-VCH, Berlin, 2003.

H. Cai, X. Cao, Y. Jiang, P. He, and Y. Fang. Carbon nanotube-enhanced electrochemical DNA biosensor for DNA hybridization detection. *Anal. Bioanal. Chem.*, **375**:287, 2003.

J. K. Campbell, L. Sun, and R. M. Crooks. Electrochemistry using single carbon nanotubes. *J. Am. Chem. Soc.*, **121**:3779, 1999.

S. W. Carmichael and H. Winkler. The adrenal chromaffin cell. *Sci. Am.*, **253**:40, 1985.

A. Castellanos, A. Ramos, A. González, N. G. Green, and H. Morgan. Electrohydrodynamics and dielectrophoresis in microsystems: scaling laws. *J. Phys. D: Appl. Phys.*, **36**:2584, 2003.

R. J. Chen, S. Bangsaruntip, K. A. Drouvalakis, N. W. S. Kam, M. Shim, Y. Li, W. Kim, P. J. Utz, and H. Dai. Noncovalent functionalization of carbon nanotubes for highly specific electronic biosensors. *Proc. Natl. Acad. Sci. U.S.A.*, **100**:4984, 2003.

R. J. Chen, H. C. Choi, S. Bangasaruntip, E. Yenilmez, X. Tang, Q. Wang, Y.-L. Chang, and H. Dai. An investigation of the mechanisms of electronic sensing of protein adsorption on carbon nanotube devices. *J. Am. Chem. Soc.*, **126**:1563, 2004.

X. Chen, A. Kis, A. Zettl, and C. R. Bertozzi. A cell nanoinjector based on carbon nanotubes. *Proc. Natl. Acad. Sci. U.S.A.*, **104**:8218, 2007.

P. A. Christensen and A. Hamnet. *Techniques and Mechanisms in Electrochemistry.* Blackie Academic & Professional, New York, NY, 1994.

P. G. Collins, K. Bradley, M. Ishigami, and A. Zettl. Extreme oxygen sensitivity of electronic properties of carbon nanotubes. *Science*, **287**:1801, 2000.

X. Cui, M. Freitag, R. Martel, L. Brus, and P. Avouris. Controlling energy-level alignments at carbon nanotube/Au contacts. *Nano Lett.*, **3**:783, 2003.

Y. Cui and C. M. Lieber. Functional nanoscale electronic devices assembled using silicon nanowire building blocks. *Science*, **291**:851, 2001.

Y. Cui, Q. Wei, H. Park, and C. M. Lieber. Nanowire nanosensors for highly sensitive and selective detection of biological and chemical species. *Science*, **293**:1289, 2001.

S. Datta. *Electron Transport in Mesoscopic Systems*. Cambridge University Press, New York, NY, 1995.

V. Derycke, R. Martel, J. Appenzeller, and P. Avouris. Controlling doping and carrier injection in carbon nanotube transistors. *Appl. Phys. Lett.*, **80**:2773, 2002.

F. Dewarrat, M. Calame, and C. Schönenberger. Orientation and positioning of DNA molecules with an electric field technique. *Biophys. J.*, **4**:189, 2002.

L. Eichinger *et al.* The genome of the social amoeba *Dictyostelium discoideum*. *Nature*, **435**:43–57, 2005.

P. Fey, S. Stephens, M. A. Titus, and R. L. Chisholm. SadA, a novel adhesion receptor in *Dictyostelium*. *J. Cell Biol.*, **159**:1109–1119, 2002.

P. Friedl, S. Borgmann, and E.-B. Bröcker. Amoeboid leukocyte crawling through extracellular matrix: lessons from the *Dictyostelium* paradigm of cell movement. *J. Leukocyte Biol.*, **70**:491–509, 2001.

Q. Fu and J. Liu. Effects of ionic surfactant adsorption on single-walled carbon nanotube thin film devices in aqueous solutions. *Langmuir*, **21**:1162, 2005.

M. Fuhrer, H. Park, and P. L. McEuen. Single-walled carbon nanotube electronics. *IEEE Trans. on Nanotech.*, **1**:78, 2002.

P. R. C. Gascoyne and J. Vykoukal. Particle separation by dielectrophoresis. *Electrophoresis*, **23**:1973, 2002.

K.-F. Giebel, C. Bechinger, S. Herminghaus, M. Riedel, P. Leiderer, U. Weiland, and M. Bastmeyer. Imaging of cell/substrate contacts of living cells with surface plasmon resonance microscopy. *Biophys. J.*, **76**:509, 1999.

J. Giles. Top five in physics. *Nature*, **441**:265, 2006.

D. C. Grahame. The electrical double layer and the theory of electrocapillarity. *Chem. Rev.*, **41**:441, 1947.

N. G. Green, A. Ramos, and H. Morgan. AC electrokinetics: a survey of sub-micrometre particle dynamics. *J. Phys. D: Appl. Phys.*, **33**:632, 2000.

G. Gruner. Carbon nanotube transistors for biosensing applications. *Anal. Bioanal. Chem.*, **384**:322, 2006.

M. S. Gudiksen, L. J. Lauhon, J. Wang, D. C. Smith, and C. M. Lieber. Growth of nanowire superlattice structures for nanoscale photonics and electronics. *Nature*, **415**:617, 2002.

T. Guo, P. Nikolaev, A. Thess, D. T. Colbert, and R. E. Smalley. Catalytic growth of single-walled nanotubes by laser vaporization. *Chem. Phys. Lett.*, **243**:49, 1995.

P. J. M. V. Haastert and P. N. Devreotes. Chemotaxis: signalling the way forward. *Nature Rev. Mol. Cell Biol.*, **5**:626, 2004.

J. Hahm and C. M. Lieber. Direct ultrasensitive electrical detection of DNA and DNA sequence variations using nanowire nanosensors. *Nano Lett.*, **4**:51, 2004.

N. Hamada, S. Sawada, and A. Oshiyama. New one-dimensional conductors: graphitic microtubules. *Phys. Rev. Lett.*, **68**:1579, 1992.

H. S. Harned and B. B. Owen. *The Physical Chemistry of Electrolytic Solutions*. Reinhold Publishing Corporation, New York, NY, third edition, 1958.

I. Heller, J. Kong, H. A. Heering, K. A. Williams, S. G. Lemay, and C. Dekker. Individual single-walled carbon nanoelectrodes for electrochemistry. *Nano Lett.*, **5**:137, 2005.

A. H. Hirsa, C. A. López, M. A. Laytin, M. J. Vogel, and P. H. Steen. Low-dissipation capillary switches at small scales. *Appl. Phys. Lett.*, **86**:014106, 2005.

R. Hogg and R. G. Wilkins. Exchange studies of certain chelate compounds of the transistion metals. Part VIII. $2, 2', 2''$-terpyridine complexes. *J. Chem. Soc.*, page 341, 1962.

R. Hölzel. Single particle characterization and manipulation by opposite field dielectrophoresis. *Biophys. J.*, **56**:435, 2002.

S. Huang, M. Woodson, R. Smalley, and J. Liu. Growth mechanism of oriented long single walled carbon nanotubes using "fast-heating" chemical vapor deposition process. *Nano Lett.*, **4**:1025, 2004.

M. P. Hughes. AC electrokinetics: applications for nanotechnology. *Nanotechnology*, **11**:124, 2000.

S. Ijima. Helical microtubules of graphitic carbon. *Nature*, **354**:56, 1991.

M. F. Islam, E. Rojas, D. M. Bergey, A. T. Johnson, and A. G. Yodh. High weight fraction surfactant solubilization of single-wall carbon nanotubes in water. *Nano Lett.*, **3**:269, 2003.

K. Itaya, I. Uchida, and V. D. Neff. Electrochemistry of polynuclear transition metal cyanides: Prussian Blue and its analogues. *Acc. Chem. Res.*, **19**:162, 1986.

A. L. Ivanovskii. Non-carbon nanotubes: synthesis and simulation. *Russ. Chem. Rev.*, **71**:175, 2002.

A. Javey, J. Guo, D. B. Farmer, Q. Wang, E. Yenilmez, R. G. Gordon, M. Lundstrom, and H. Dai. Self-aligned ballistic molecular transistors and electrically parallel nanotube arrays. *Nano Lett.*, **4**:1319, 2004.

A. Javey, J. Guo, Q. Wang, M. Lundstrom, and H. Dai. Ballistic carbon nanotube field-effect transistors. *Nature*, **424**:654, 2003.

A. Javey, H. Kim, M. Brink, Q. Wang, A. Ural, J. Guo, P. McIntyre, P. McEuen, M. Lundstrom, and H. Dai. High-κ dielectrics for advanced carbon-nanotube transistors and logic gates. *Nature Mater.*, **1**:241, 2002.

N. W. S. Kam, M. O'Connell, J. A. Wisdom, and H. Dai. Carbon nanotubes as multifunctional biological transporters and near-infrared agents for selective cancer cell destruction. *Proc. Natl. Acad. Sci. U.S.A.*, **102**:11600, 2005.

C. L. Kane and E. J. Mele. Size, shape, and low energy electronic structure of carbon nanotubes. *Phys. Rev. Lett.*, **78**:1932, 1997.

N. Kapouleas. Complete constant mean curvature surfaces in Euclidean three-space. *Ann. Math.*, **131**:239, 1990.

J. J. Kasianowicz, E. Brandin, D. Branton, and D. W. Deamer. Characterization of individual polynucleotide molecules using a membrane channel. *Proc. Natl. Acad. Sci. U.S.A.*, **93**:13770, 1996.

K. Keren, R. S. Berman, E. Buchstab, U. Sivan, and E. Braun. DNA-templated carbon nanotube field-effect transistor. *Science*, **302**:1380, 2003.

U. F. Keyser, B. N. Koeleman, S. van Dorp, D. Krapf, R. M. M. Smeets, S. G. Lemay, N. H. Dekker, and C. Dekker. Direct force measurements on DNA in a solid-state nanopore. *Nature Physics*, **2**:473, 2006.

W. Kim, A. Javey, O. Vermesh, Q. Wang, Y. Li, and H. Dai. Hysteresis caused by water molecules in carbon nanotube field-effect transistors. *Nano Lett.*, **3**:193, 2003.

A. Kitahara and A. Watanabe. *Electrical Phenomena at Interfaces*. Marcel Dekker, Inc., New York, NY, 1984.

C. Klinke, J. Chen, A. Afzali, and P. Avouris. Charge transfer induced polarity switching in carbon nanotube transistors. *Nano Lett.*, **5**:555, 2005.

S. J. Koch and M. D. Wang. Dynamic force spectroscopy of protein-DNA interactions by unzipping DNA. *Phys. Rev. Lett.*, **91**:028103, 2003.

J. Kong, A. M. Cassell, and H. Dai. Chemical vapor deposition of methane for single-walled carbon nanotubes. *Chem. Phys. Lett.*, **292**:567, 1998a.

J. Kong, M. G. Chapline, and H. Dai. Functionalized carbon nanotubes for molecular hydrogen sensors. *Adv. Mater.*, **13**:1384, 2001a.

J. Kong and H. Dai. Full and modulated chemical gating of individual carbon nanotubes by organic amine compounds. *J. Phys. Chem. B*, **105**:2890, 2001.

J. Kong, N. R. Franklin, C. Zhou, M. G. Chapline, S. Peng, K. Cho, and H. Dai. Nanotube molecular wires as chemical sensors. *Science*, **287**:622, 2000.

J. Kong, H. T. Soh, A. M. Cassell, C. F. Quate, and H. Dai. Synthesis of individual single-walled carbon nanotubes on patterned silicon wafers. *Nature*, **395**:878, 1998b.

J. Kong, E. Yenilmez, T. W. Tombler, W. Kim, H. Dai, R. B. Laughlin, L. Liu, C. S. Jayanthi, and S. Y. Wu. Quantum interference and ballistic transport in nanotube electron waveguides. *Phys. Rev. Lett.*, **87**:106801, 2001b.

M. Krüger, M. R. Buitelaar, T. Nussbaumer, C. Schönenberger, and L. Forró. Electrochemical carbon nanotube field-effect transistor. *Appl. Phys. Lett.*, **78**: 1291, 2001.

M. Krüger, I. Widmer, T. Nussbaumer, M. Buitelaar, and C. Schönenberger. Sensitivity of single multiwalled carbon nanotubes to the environment. *New J. Phys.*, **5**:138, 2003.

R. Krupke, F. Hennrich, H. v. Löhneysen, and M. M. Kappes. Separation of metallic from semiconducting single-walled carbon nanotubes. *Science*, **301**: 344, 2003.

L. Larrimore. Carbon nanotubes as diffraction microscopy mounts. Cornell University Admission to Candidacy Exam, 2005.

L. Larrimore, S. Nad, X. Zhou, H. Abruña, and P. L. McEuen. Probing electrostatic potentials in solution with carbon nanotube transistors. *Nano Lett.*, **6**:1329, 2006.

F.-B. Li, A. R. Hillman, and S. D. Lubetkin. A new approach to the mechanism of chlorine evolution: separate examination of the kinetic steps using AC impedance on a rotating thin ring electrode. *Electrochimica Acta*, **37**:2715, 1992.

J. Li, H. T. Ng, A. Cassell, W. Fan, H. Chen, Q. Ye, J. Koehne, J. Han, and M. Meyyappan. Carbon nanotube nanoelectrode array for ultrasensitive DNA detection. *Nano Lett.*, **3**:597, 2003.

J. Li, D. Stein, C. McMullan, D. Branton, M. J. Aziz, and J. A. Golovchenko. Ion-beam sculpting at nanometre length scales. *Nature*, **412**:116, 2001.

D. R. Lide, editor. *CRC Handbook of Chemistry and Physics*. CRC Press, Cleveland, OH, 87th edition, 2006.

Y. Lin, H. Skaff, T. Emrick, A. D. Dinsmore, and T. P. Russell. Nanoparticle assembly and transport at liquid-liquid interfaces. *Science*, **299**:226, 2003.

X. Liu, Z. Luo, S. Han, T. Tang, D. Zhang, and C. Zhou. Band engineering of carbon nanotube field-effect transistors via selected area chemical gating. *Appl. Phys. Lett.*, **86**:243501, 2005.

C. Lu, Q. Fu, S. Huang, and J. Liu. Polymer electrolyte-gated carbon nanotube field-effect transistor. *Nano Lett.*, **4**:623, 2004.

J. T. Mannion and H. G. Craighead. Nanofluidic structures for single biomolecule fluorescent detection. *Biopolymers*, **85**:131, 2007.

M. R. Maxey and J. J. Riley. Equation of motion for a small rigid sphere in a nonuniform flow. *Phys. Fluids*, **26**:883, 1983.

P. L. McEuen and J.-Y. Park. Electron transport in single-walled carbon nanotubes. *MRS Bulletin*, **29**:272, 2004.

A. Meller, L. Nivon, E. Brandin, J. Golovchenko, and D. Branton. Rapid nanopore discrimination between single polynucleotide molecules. *Proc. Natl. Acad. Sci. U.S.A.*, **97**:1079, 2000.

D. D. Metcalfe, D. Baram, and Y. A. Mekori. Mast cells. *Physiol. Rev.*, **77**:1033, 1997.

E. Minot. *Tuning the Band Structure of Carbon Nanotubes*. PhD thesis, Cornell University, 2004.

E. D. Minot, Y. Yaish, V. Sazonova, J.-Y. Park, M. Brink, and P. L. McEuen. Tuning carbon nanotube band gaps with strain. *Phys. Rev. Lett.*, **90**:156401, 2003.

J. A. Misewich, R. Martel, P. Avouris, J. C. Tsang, S. Heinze, and J. Tersoff. Electrically induced optical emission from a carbon nanotube FET. *Science*, **300**:783, 2003.

D. B. Murphy, R. Oldfield, S. Schwartz, and M. W. Davidson. Phase contrast microscopy: Introduction. http://www.microscopyu.com/articles/phasecontrast/phasemicroscopy.html, 2007a. Nikon MicroscopyU.

D. B. Murphy, E. D. Salmon, K. R. Spring, M. Abramowitz, and M. W. Davidson. Differential interference contrast: Fundamental concepts. http://www.olympusmicro.com/primer/techniques/dic/dicintro.html, 2007b. Olympus Microscopy Resource Center.

L. E. Murr, K. F. Soto, E. V. Esquivel, J. J. Bang, P. A. Guerrero, D. A. Lopez, and D. A. Ramirez. Carbon nanotubes and other fullerene-related nanocrystals in the environment: A TEM study. *JOM*, **56**:28, 2004.

T. Mutai, J.-D. Cheon, S. Arita, and K. Araki. Phenyl-substituted $2,2':6',2''$-terpyridine as a new series of fluorescent compounds—their photophysical properties and fluorescence tuning. *J. Chem. Soc. Perkin Trans. 2*, **7**:1045, 2001.

D. L. Nelson and M. M. Cox. *Lehninger Principles of Biochemistry*. W. H. Freeman & Company, New York, NY, fourth edition, 2004.

J. M. K. Ng, I. Gitlin, A. D. Stroock, and G. M. Whitesides. Components for integrated poly(dimethylsiloxane) microfluidic systems. *Electrophoresis*, **23**:3461, 2002.

Y. Nosho, Y. Ohno, S. Kishimoto, and T. Mizutani. n-type carbon nanotube field-effect transistors fabricated by using Ca contact electrodes. *Appl. Phys. Lett.*, **86**:073105, 2005.

J. P. Novak, E. S. Snow, E. J. Houser, D. Park, J. L. Stepnowski, and R. A. McGill. Nerve agent detection using networks of single-walled carbon nanotubes. *Appl. Phys. Lett.*, **83**:4026, 2003.

M. J. O'Connell, P. Boul, L. M. Ericson, C. Huffman, Y. Wang, E. Haroz, C. Kuper, J. Tour, K. D. Ausman, and R. E. Smalley. Reversible water-solubilization of single-walled carbon nanotubes by polymer wrapping. *Chem. Phys. Lett.*, **342**: 265, 2001.

T. W. Odom, J.-L. Huang, P. Kim, and C. Lieber. Atomic structure and electronic properties of single-walled carbon nanotubes. *Nature*, **391**:62, 1998.

J. Olmsted and G. M. Williams. *Chemistry: The Molecular Science*. Wm. C. Brown Publishers, Dubuque, IA, second edition, 1997.

B. O'Schaughnessy and Q. Yang. Manning-Oosawa counterion condensation. *Phys. Rev. Lett.*, **94**:048302, 2005.

F. Patolsky, B. P. Timko, G. Yu, Y. Fang, A. B. Greytak, G. Zheng, and C. M. Lieber. Detection, stimulation, and inhibition of neuronal signals with high-density nanowire transistor arrays. *Science*, **313**:1100, 2006.

F. Patolsky, G. Zheng, O. Hayden, M. Lakadamyali, X. Zhuang, and C. M. Lieber. Electrical detection of single viruses. *Proc. Natl. Acad. Sci. U.S.A.*, **101**:14017, 2004.

C. M. Pharr and P. R. Griffiths. Infrared spectroelectrochemical analysis of adsorbed hexacyanoferrate species formed during potential cycling in the ferrocyanide/ferricyanide redox couple. *Anal. Chem.*, **69**:4673, 1997.

R. Prakash, S. Washburn, R. Superfine, R. E. Cheney, and M. R. Falvo. Visualization of individual carbon nanotubes with fluorescence microscopy using conventional fluorophores. *Appl. Phys. Lett.*, **83**:1219, 2003.

P. Qi, O. Vermesh, M. Grecu, A. Javey, Q. Wang, and H. Dai. Toward large arrays of multiplex functionalized carbon nanotube sensors for highly sensitive and selective molecular detection. *Nano Lett.*, **3**:347, 2003.

A. Ramos, H. Morgan, N. G. Green, and A. Castellanos. AC electrokinetics: a review of forces in microelectrode structures. *J. Phys. D: Appl. Phys.*, **31**:2338, 1998.

A. Ramos, H. Morgan, N. G. Green, and A. Castellanos. AC electric-field-induced fluid flow in microelectrodes. *J. Colloid Interface Sci.*, **217**:420, 1999.

M. Reibold, P. Paufler, A. A. Levin, W. Kochmann, N. Pätzke, and D. C. Meyer. Carbon nanotubes in an ancient Damascus sabre. *Nature*, **444**:286, 2006.

S. Reich, J. Maultzsch, and C. Thomsen. Tight-binding description of graphene. *Phys. Rev. B*, **66**:035412, 2002.

W. Reisner, K. J. Morton, R. Riehn, Y. M. Wang, Z. Yu, M. Rosen, J. C. Sturm, S. Y. Chou, E. Frey, and R. H. Austin. Statics and dynamics of single DNA molecules confined in nanochannels. *Phys. Rev. Lett.*, **94**:196101, 2005.

E. G. Richards. *An introduction to the physical properties of large molecules in solution*. Cambridge University Press, New York, NY, 1980.

A. Robert-Peillard and S. V. Rotkin. Modeling hysteresis phenomena in nanotube field-effect transistors. *IEEE Trans. on Nanotech.*, **4**:284, 2005.

J. A. Robinson, E. S. Snow, Ş. C. Bădescu, T. L. Reinecke, and F. K. Perkins. Role of defects in single-walled carbon nanotube chemical sensors. *Nano Lett.*, **6**:1747, 2006.

S. Rosenblatt. *Pushing the limits of carbon nanotube transistors*. PhD thesis, Cornell University, 2006.

S. Rosenblatt, Y. Yaish, J. Park, J. Gore, V. Sazonova, and P. L. McEuen. High performance electrolyte gated carbon nanotube transistors. *Nano Lett.*, **2**:869, 2002.

R. Saito, G. Dresselhaus, and M. S. Dresselhaus. *Physical Properties of Carbon Nanotubes*. Imperial College Press, London, 1998.

R. Saito, M. Fujita, G. Dresselhaus, and M. S. Dresselhaus. Electronic structure of chiral graphene tubules. *Appl. Phys. Lett.*, **60**:2204, 1992.

R. Saito and H. Kataura. Optical properties and Raman spectroscopy of carbon nanotubes. *Topics Appl. Phys.*, **80**:213, 2001.

O. A. Saleh and L. L. Sohn. An artificial nanopore for molecular sensing. *Nano Lett.*, **3**:37, 2003.

V. Sazonova. *A Tunable Carbon Nanotube Resonator*. PhD thesis, Cornell University, 2006.

V. Sazonova, Y. Yaish, H. Üstünel, D. Roundy, T. Arias, and P. L. McEuen. A tunable carbon nanotube electromechanical oscillator. *Nature*, **431**:284, 2004.

G. P. Siddons, D. Merchin, J. H. Back, J. K. Jeong, and M. Shim. Highly efficient gating and doping of carbon nanotubes with polymer electrolytes. *Nano Lett.*, **4**:927, 2004.

R. E. Smalley, Y. Li, V. C. Moore, B. K. Price, R. Colorado, Jr., H. K. Schmidt, R. H. Hauge, A. R. Barron, and J. M. Tour. Single wall carbon nanotube amplification: En route to a type-specific growth mechanism. *J. Am. Chem. Soc.*, **128**:15824, 2006.

E. S. Snow and F. K. Perkins. Capacitance and conductance of single-walled carbon nanotubes in the presence of chemical vapors. *Nano Lett.*, **5**:2414, 2005.

E. S. Snow, F. K. Perkins, E. J. Houser, Ş. C. Bădescu, and T. L. Reinecke. Chemical detection with a single-walled carbon nanotube capacitor. *Science*, **307**:1942, 2005.

H.-M. So, K. Won, Y. H. Kim, B.-K. Kim, B. H. Ryu, P. S. Na, H. Kim, and J.-O. Lee. Single-walled carbon nanotube biosensors using aptamers as molecular recognition events. *J. Am. Chem. Soc.*, **127**:11906, 2005.

T. Someya, J. Small, P. Kim, C. Nuckolls, and J. T. Yardley. Alcohol vapor sensors based on single-walled carbon nanotube field effect transistors. *Nano Lett.*, **3**: 877, 2003.

S. Sotiropoulou and N. A. Chaniotakis. Carbon nanotube array-based biosensor. *Anal. Bioanal. Chem.*, **375**:103, 2003.

A. Star, J.-C. P. Gabriel, K. Bradley, and G. Grüner. Electronic detection of specific protein binding using nanotube FET devices. *Nano Lett.*, **3**:459, 2003a.

A. Star, T.-R. Han, J.-C. P. Gabriel, K. Bradley, and G. Grüner. Interaction of aromatic compounds with carbon nanotubes: correlation to the Hammett parameter of the substituent and measured carbon nanotube FET response. *Nano Lett.*, **3**:1421, 2003b.

A. Star, T.-R. Han, V. Joshi, J.-C. P. Gabriel, and G. Grüner. Nanoelectronic carbon dioxide sensors. *Adv. Mater.*, **16**:2049, 2004a.

A. Star, V. Joshi, T.-R. Han, M. V. P. Altoé, G. Grüner, and J. F. Stoddart. Electronic detection of the enzymatic degredation of starch. *Org. Lett.*, **6**:2089, 2004b.

A. Star, D. W. Steuerman, J. R. Heath, and J. F. Stoddart. Starched carbon nanotubes. *Angew. Chem. Int. Ed.*, **41**:2508, 2002.

A. Star, E. Tu, J. Niemann, J.-C. P. Gabriel, C. S. Joiner, and C. Valcke. Label-free detection of DNA hybridization using carbon nanotube network field-effect transistors. *Proc. Natl. Acad. Sci. U.S.A.*, **103**:921, 2006.

H. A. Stone, A. D. Stroock, and A. Ajdari. Engineering flows in small devices: Microfluidics toward lab-on-a-chip. *Annu. Rev. Fluid Mech.*, **36**:381, 2004.

A. J. Storm, C. Storm, J. Chen, H. Zandbergen, J.-F. Joanny, and C. Dekker. Fast DNA translocation through a solid-state nanopore. *Nano Lett.*, **5**:1193, 2005.

X. Tang, S. Bangsaruntip, N. Nakayama, E. Yenilmez, Y.-I. Chang, and Q. Wang. Carbon nanotube DNA sensor and sensing mechanism. *Nano Lett.*, **6**:1632, 2006.

S. J. Tans, A. R. M. Verschueren, and C. Dekker. Room-temperature transistor based on a single carbon nanotube. *Nature*, **393**:49, 1998.

B. Tinland, A. Pluen, J. Sturm, and G. Weill. Persistence length of single-stranded DNA. *Macromolecules*, **30**:5763, 1997.

M. A. Titus. The role of talin and myosin VII in adhesion—A FERM connection. In A. Ridley, M. Peckham, and P. Clark, editors, *Cell Motility: From Molecules to Organisms*. John Wiley & Sons, Chichester, England, 2004.

D. Toomre and D. J. Manstein. Lighting up the cell surface with evanescent wave microscopy. *Trends Cell Biol.*, **11**:298, 2001.

D. J. Tritton. *Physical Fluid Dynamics*. Oxford University Press, New York, NY, second edition, 1988.

S. Tuukkanen, J. J. Toppari, A. Kuzyk, L. Hirviniemi, V. P. Hytönen, T. Ihalainen, and P. Törmä. Carbon nanotubes as electrodes for dielectrophoresis of DNA. *Nano Lett.*, **6**:1339, 2006.

K. S. K. Uchida and S. Yumura. Dynamics of novel feet of *Dictyostelium* cells during migration. *J. Cell Sci.*, **117**:1443–1455, 2004.

M. A. Unger, H.-P. Chou, T. Thorsen, A. Scherer, and S. R. Quake. Monolithic microfabricated valves and pumps by multilayer soft lithography. *Science*, **288**: 113, 2000.

K. Unsicker. The chromaffin cell: paradigm in cell, developmental and growth factor biology. *J. Anat.*, **183**:207, 1993.

H. Verschueren. Interference reflection microscopy in cell biology: methodology and applications. *J. Cell. Sci.*, **75**:279, 1985.

P. R. Wallace. The band theory of graphite. *Phys. Rev.*, **71**:622, 1947.

S. G. Wang, Q. Zhang, R. Wang, and S. F. Yoon. A novel multi-walled carbon nanotube-based biosensor for glucose detection. *Biochem. Bioph. Res. Co.*, **311**: 572, 2003.

D. B. Weibel, M. Kruithof, S. Potenta, S. K. Sia, A. Lee, and G. M. Whitesides. Torque-actuated valves for microfluidics. *Anal. Chem.*, **77**:4726, 2005.

J. W. G. Wildöer, L. C. Venema, A. G. Rinzler, R. E. Smalley, and C. Dekker. Electronic structure of atomically resolved carbon nanotubes. *Nature*, **391**:59, 1998.

I. Willner. Biomaterials for sensors, fuel cells, and circuitry. *Science*, **298**:2407, 2002.

K. Winkler. The kinetics of electron transfer in $Fe(CN)_6^{4-/3-}$ redox system on platinum standard-size and ultramicroelectrodes. *J. of Electroanal. Chem.*, **388**: 151, 1995.

L. Yang and J. Han. Electronic structure of deformed carbon nanotubes. *Phys. Rev. Lett.*, **85**:154, 2000.

G. Zhang, P. Qi, X. Wang, Y. Lu, X. Li, R. Tu, S. Bangsaruntip, D. Mann, L. Zhang, and H. Dai. Selective etching of metallic carbon nanotubes by gas-phase reaction. *Science*, **314**:974, 2006.

G. Zheng, F. Patolsky, Y. Cui, W. U. Wang, and C. M. Lieber. Multiplexed electrical detection of cancer markers with nanowire sensor arrays. *Nat. Biotechnol.*, **23**:1294, 2005.

L. Zheng, S. Li, J. P. Brody, and P. J. Burke. Manipulating nanoparticles in solution with electrically contacted nanotubes using dielectrophoresis. *Langmuir*, **20**:8612, 2004a.

L. X. Zheng, M. J. O'Connell, S. K. Doorn, X. Z. Liao, Y. H. Zhao, E. A. Akhadov, M. A. Hoffbauer, B. J. Roop, Q. X. Jia, R. C. Dye, D. E. Peterson, S. M. Huang, J. Liu, and Y. T. Zhu. Ultralong single-wall carbon nanotubes. *Nature Mater.*, **3**:673, 2004b.

M. Zheng, A. Jagota, E. D. Semke, B. A. Diner, R. S. McLean, S. R. Lustig, R. E. Richardson, and N. G. Tassi. DNA-assisted dispersion and separation of carbon nanotubes. *Nature Mater.*, **2**:338, 2003a.

M. Zheng, A. Jagota, M. S. Strano, A. P. Santos, P. Barone, S. G. Chou, B. A. Diner, M. S. Dresselhaus, R. S. Mclean, G. B. Onoa, G. G. Samsonidze, E. D. Semke, M. Usrey, and D. J. Walls. Structure-based carbon nanotube sorting by sequence-dependent DNA assembly. *Science*, **302**:1545, 2003b.

C. Zhou, J. Kong, and H. J. Dai. Intrinsic electrical properties of individual single-walled carbon nanotubes with small band gaps. *Phys. Rev. Lett.*, **84**:5604, 2000.

X. Zhou, J. M. Moran-Mirabal, H. G. Craighead, and P. L. McEuen. Supported lipid bilayer/carbon nanotube hybrids. *Nature Nanotechnology*, **2**:185, 2007.

X. Zhou, J.-Y. Park, S. Huang, J. Liu, and P. L. McEuen. Band structure, phonon scattering, and the performance limit of single-walled carbon nanotube transistors. *Phys. Rev. Lett.*, **95**:146805, 2005.

J. M. Zou, I. Vartanyants, M. Gao, R. Zhang, and L. A. Nagahara. Atomic resolution imaging of a carbon nanotube from diffraction intensities. *Science*, **300**:1419, 2003.